THE UNIVERSITY OF HULL

Laser processing of transparent conducting films for use in flexible electronics

being a Thesis submitted for the degree of Doctor of Philosophy

in The University of Hull

by

Jack Eden, MPhys. (Hons.)

February 9, 2020

"The important thing is not to stop questioning. Curiosity has its own reason for existence. One cannot help but be in awe when he contemplates the mysteries of eternity, of life, of the marvelous structure of reality. It is enough if one tries merely to comprehend a little of this mystery each day."

- Albert Einstein, 1955

Abstract

Transparent conducting films based on novel materials have been laser processed on glass and flexible polyethylene terephthalate (PET) substrates in order to increase their electrical conductivity. The goal was to reduce the amount of indium used in display and photovoltaic applications by printing the indium containing compounds, hence only depositing material where it is required, or by using non indium-based materials. Two systems were considered: an ink containing indium tin oxide (ITO) nano particles with a polymer binder and organic solvent, and an ink containing aluminium doped zinc oxide (AZO) nanoparticles in a titanium dioxide solution.

The conductivity of the as-deposited material was thought to have been improved in two ways: UV-induced photopolymerization of binder material and the removal of non conductive material from within the inks. The first shrinks the polymer binder bringing the conductive particles closer together and the second decomposes or vapourizes the organic components. Consequently, laser sources covering the UV and the infrared were used. These were the argon fluoride, xenon chloride, and helium cadmium lasers (193nm, 308nm, and 325nm wavelengths respectively) and the Yb:YAG and CO_2 lasers (1030nm and 10.6µm wavelengths respectively).

Thermal measurements confirmed low temperature processing in the UV and each of the ultraviolet lasers increased the electrical conductivity of the films by at least 3 orders of magnitude. The XeCl laser gave the best result of $\sim$1.5kΩ/sq. Higher temperature processing with the CO_2 laser gave $\sim$250Ω/sq but substrate damage occurred on temperature sensitive substrates. The current state of the art ITO films used in commercial devices are $\sim$10Ω/sq. Absorption spectra were used to not only obtain evidence that polymerisation was occurring (even with the IR laser) but also to quantify the charge carrier density and band gap.

The intrinsic conductivity of the AZO compounds was found to be very poor and so fine silver grids were manufactured by laser ablation to provide additional current pathways. Carbon dioxide laser irradiation of the AZO films gave a lowest sheet resistance of 2.3MΩ/sq whereas the use of an underlying silver grid resulted in 3Ω/sq.

Acknowledgements

Firstly, I would like to thank my supervisor, Howard Snelling, for his continuous support throughout the project and always having time to share thoughts and demonstrate techniques in the lab.

The work in this thesis was conducted as part of the INFINITY project, funded by the European Union's Horizon 2020 research and innovation programme under the grant agreement 641927. I would like to thank all the partners involved in the INFINITY project for the insight given at project meetings, with special thanks to Thiago M. Amaral and Sabine Heusing from INM for providing the many samples used throughout this thesis.

I'd also like to thank the other members of the department for their kindness in sharing equipment, as well as the technical support staff for the help received in setting up and getting parts made for experiments.

I would like to thank my colleagues in the postgraduate physics office for some of the most entertaining times during my time at Hull University. I'm especially grateful to Andrew Clarke who assisted in the temperature measurements and simulations used in this thesis.

Finally, I would like to thank Gemma for keeping me sane during the final year of my PhD.

Contents

Chapter 1

Introduction

Transparent, electrically conductive, thin films have seen an increase in interest with the recent market growth of photovoltaic cells, LCD televisions and smart-phones. Indium tin oxide (ITO) is the most commonly used transparent conductor in industry having a 93% market share.[1] ITO currently has the most ideal material properties to be used as a transparent conducting film, boasting sheet resistances down to $10\Omega/\text{sq}$ whilst maintaining greater than 85% transparency in the visible wavelength region. Current methods to produce ITO films are not ideal however. The conventional methods is sputtering of an ITO target, which besides requiring a very high vacuum system, also wastes a lot of the ITO material as much of it does not reach the substrate. In addition, further patterning of the films to form suitable electrode structures is necessary, providing further loss of material. Poor usage of ITO is to be avoided because of the very high price and limited supply of indium. This problem has encouraged research to be conducted for alternate methods for the deposition of ITO films. More recently, ITO films have been prepared onto substrates using so-called 'wet-processing'. This method wastes very little material since any lost material can be simply put back into solution and reused. The wet-processed films do, however, contain a lot of unwanted solvents and organic compounds that are detrimental to electrical conductivity and therefore need to be removed. In this thesis, laser irradiation of wet processed ITO films to increase their conductivity has been studied as an alternative to conventional furnace treatments. This potentially allows the use of temperature sensitive substrates, such as polymers, and in turn facilitate the production of flexible electronics. The ultimate aim of this research was to reduce the electrical conductivity to below 100Ω/sq of wet-processed indium-free transparent conducting films on temperature sensitive substrates using laser processing.

For this thesis the wet processed ITO films have been optically characterised and then irradiated under different conditions with the resulting electrical, optical and morphological effects measured and analysed. The initial optical characterisation was performed in order to understand which laser systems can be used to deposit energy into the films. Since the films are transparent in the visible range, lasers in the infrared (IR) and ultraviolet (UV) parts of the electromagnetic spectrum have been used. The morphological properties of the films have been measured using profilometers and microscopy to see how the surface is changing due to irradiation by the laser. From this we can see if the films are becoming damaged or cracked, which would negatively impact the optical and/or electrical properties. The optical properties were measured after irradiation to make sure transparency is maintained in the visible region. In addition, observation of the cut-off wavelengths allows quantification of the band-gap and plasma edge of the laser modified material. Finally, the electrical properties of the ITO films were measured. The electrical properties included Hall measurements which enabled us to determine how the electrical properties are changing due to laser irradiation.

The structure of the thesis is as follows. Chapter 2 contains the literature review. The literature review describes the current state of the art of ITO processing as used in industry to produce commercially available devices. It follows on to show some of the methods currently used to produce laser processed transparent conducting films based on indium-tin oxide, as well as some indium-free transparent conductors. The literature review also contains background information on the measurement techniques adopted in this thesis that quantify the electrical properties of thin films of various geometries.

In chapter 3 a description of the ITO films provided by the Leibniz Institute for New Materials (INM) is given, and a brief explanation on how they were manufactured. The ITO films were then characterised before being laser irradiated, in order to quantify their initial electrical conductivity. The optical properties were also measured to ascertain the optical transparency throughout the visible region, as well as being able to determine which wavelengths are suitable for the coupling of laser radiation into the films. Also presented in chapter 3 is a summary of the laser systems used throughout the thesis. This includes details of how each of the laser systems was setup and the parameters of the laser, including any pulse duration and beam size measurements if applicable. The final parts of chapter 3 include descriptions of the purpose built setups for measuring the sheet resistance of thin films in the low and high resistivity regimes, the Hall voltage measurement system used for the charge carrier density measurements and the optical system for measuring the haze of the transparent samples.

In chapter 4 the irradiation of ITO films by ultraviolet laser sources is described. The lasers considered include a xenon chloride laser, argon fluoride laser and a helium cadmium laser. By using ultraviolet radiation, polymerisation reactions were initiated by the high photon energies which densified the binder material via shrinkage in volume, pulling the ITO nanoparticles together and increasing electrical conductivity. The ITO electrical and optical properties were characterised after laser irradiation. By using photochemical processes in the ITO films, cold temperature processing ($\Delta T < 10^{\circ}\mathrm{C}$) was achievable and it was possible to increase the electrical conductivity on both glass and flexible PET substrates without damage.

In chapter 5 the same type of ITO films were irradiated by 3 different CO_2 laser sources in the infrared. Processing by the CO_2 laser was predominantly photothermal in nature and large temperature rises in the films and substrates occurred. Three regimes of laser radiation delivery were examined: continuous wave, low pulse rate with high energy, and finally high pulse rate with low energy. The ITO films were irradiated with each of the laser regimes and their resulting properties were measured and reported. Because the primary process with the CO_2 laser was the generation of high temperatures, avoiding laser-induced damage of temperature sensitive substrates was very difficult.

In chapter 6 laser-induced conductivity increases in indium free transparent conducing films were investigated. Using the techniques learned from the ITO films, indium free AZO films were prepared in a similar way and then laser irradiated. Both ultraviolet and infrared lasers were used. Due to the intrinsically poor conductivity of the AZO nanoparticles used in the films, the use of a silver grid underneath the film was investigated to improve the electrical conductivity. To create the silver grids with small enough features so as not to be visible, laser ablation was used.

In chapter 7 a final summary of the results in the thesis is given, along with some suggestions for future work.

Chapter 2

Literature Review

2.1 Introduction

Many of the electrical devices used today that require some form of light emission or absorption rely on a transparent layer on the front of the device that can carry electrical power whilst also transmitting visible light (400nm - 700nm wavelength). These thin films are known as transparent conducting coatings (TCC's). The most notable of these devices which require a TCC are photovoltaic panels and liquid crystal displays. Figure 2.1 shows an example of when a transparent conductor is required for a device that emits light.

The transparent conductor on top of the device has to have a certain level of conductivity for the device to work effectively. This level of conductivity requirement changes depending on the type of device in use. For example, a typical touch-screen requires between $400\Omega/\text{sq}$ and $700\Omega/\text{sq}$, whereas a typical photovoltaic cell will require between $8\Omega/\text{sq}$ and $80\Omega/\text{sq}$.[2]. This level of conductivity can easily be achieved with thin metallic films of gold at a

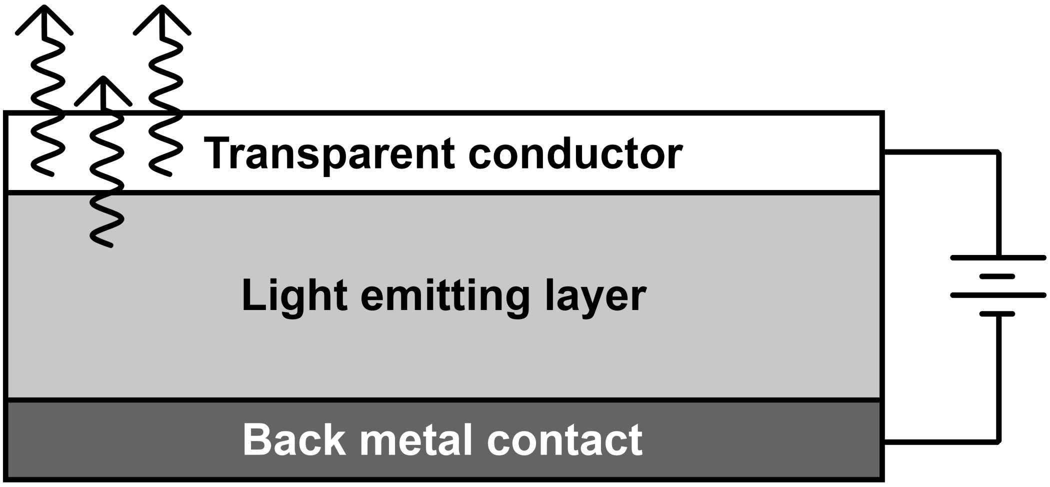

FIGURE 2.1: A diagram showing a typical cross section of a light emitting device requiring a transparent conducting contact at the top of the device that allows transmission of light

thickness of 40nm,[3] but the transparency of metallic films is not high enough to be used as a transparent conductor unless they are made extremely thin (<10nm).[4, 5] If the metallic films are made too thin, the electrical properties degrade, so a trade-off between high transparency and high conductivity is required. Therefore, the use of thin metallic films is not ideal. Even though they offer the best conductivity, they are characteristically reflective in the visible part of the spectrum. Instead of using metallic films thin enough to be transparent, an easier solution is to use a material that is intrinsically transparent in the visible part of the spectrum. Such a material would have to be a semiconductor, having a band gap of at least 3.1eV to allow the transmission of the shortest wavelength of visible light at 400nm. Ideally, the semiconductor material should also allow the transmission of as much near infrared radiation as possible, which allows photovoltaic devices to take advantage of more of the solar spectrum. Here lies a problem, however, since a transparent material has a completely filled valance band with an empty conduction band.[6]

With no electrons located in the conduction band, there cannot be any electrical conductivity. For this reason, a transparent conductor can neither be as conductive as a metal, nor be 100% transparent. Getting the best performance out of a transparent conducting film is therefore very challenging due to the complex interplay between both the optical and electrical properties of the semiconducting material. Even with all the challenges involved, transparent conducting materials exist, and are used in countless devices.

2.2 Indium tin oxide

The most commonly used transparent conductor is currently indium tin oxide (ITO) with a 93% market share.[1] ITO is a degenerately doped n-type semiconductor, which if deposited in the right way can have electrical conductivities of the order of $10\Omega/\mathrm{sq}$ with a thickness range in the 100's of nanometres (corresponding to a resistivity as low as $9 \times 10^{-5}\Omega\,\mathrm{cm}$).[7–10] ITO films can also boast greater than 85% transmission over the visible region, and extend that transparency into the near infra-red. [11, 12] The composition of typical ITO films is mainly the element indium, making up around 75% of the mass. Due to the scarcity of indium, coupled with the rising demand for use in large screen displays and solar panels, the price is very high with volatile market prices. [13]

A common method of producing ITO films is to use sputtering, and this is the method used in the majority of commercial applications. Sputtering is a type of physical vapour deposition where the material to be deposited is ejected

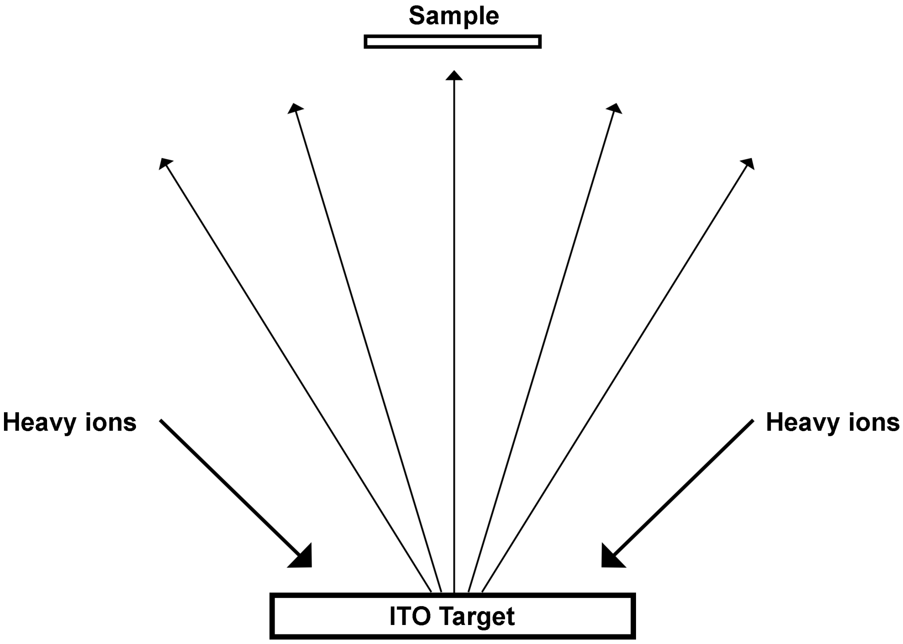

FIGURE 2.2: A typical sputtering chamber with an ITO target. The charged heavy ions are attracted to the oppositely charged target holder which bombard the ITO. This causes the ITO to be ejected and redeposited onto the sample and chamber walls.

from a target in vapour form and condenses onto a substrate, as shown in figure 2.2.

Sputtering, and other physical vapour deposition methods, create very electrically conductive and uniform ITO films but come at a cost. For uniform and contaminent free deposition, the process must be performed in high vacuum. Typically, pressure levels below the order of 10^{-6}mbar are required for acceptable film depositions.[14] When vacuum levels below the 10^{-6}mbar range are required, great care and attention has to be taken in order to achieve and maintain such a low vacuum. This equipment is very expensive and requires regular maintenance to ensure reliable operation of the sputter system in an industrial process. Another problem with using a sputtering system is wasted material. As can be seen in figure 2.2, as the material is ejected from the ITO target it is not only deposited on the sample, it is also deposited onto the inside of the vacuum chamber walls. When we consider that only between 20 and 25% of the ITO sputter target is typically used, coupled with the wasted material deposited onto the chamber walls, sputtering is a very inefficient use of an expensive material. [15] Furthermore, it is necessary to pattern the films post-deposition into the required structures leading to more material loss.

A more economic way to deposit thin films is to use a solution based material, which can then be deposited onto substrates using a method such as spin coating, known as wet deposition. This method has been used for the deposition of ITO in the past, giving uniform films without the need for expensive vacuum systems and more importantly a reduction in the wasted materials. There is 2 methods to achieve this. A film of ITO can be produced directly from chemical reactions within a solution leaving behind a continuous ITO film,[16, 17] or, using ITO nano-particles dispersed into a solution leaving discontinuous films on the substrate. [18, 19]

However, wet deposition of solution based ITO films is not without its problems. In order to get the solid ITO material into a form that can be spin coated, it must first be made into compounds that can be dissolved. Putting the ITO into solution with other non-conducting materials heavily restricts the electrical conductivity, and post processing of the films is required to get the resistivity low enough to be useful in devices that require a transparent conductor. Typically, the ITO films are heated in a furnace at over 500°C to crystallize the films, whist also removing any remaining unwanted material left over from the reactions. As shown by Jing *et al.*, [20] using indium nitrate and tin chloride, 100nm ITO films were produced and after annealing at 600°C a sheet resistance of just below 2kΩ/sq could be achieved. The change in electrical conductivity was due to increasing the crystallinity of the films. The optical transparency was also improved by this heat treatment. Hammad [21] used a sol-gel method to produce 200nm ITO films, which were first dried at 130°C to remove any solvents and organic compounds, then annealed at 550°C to reduce the resistivity down to $1.1\times10^{-3}\Omega\,\mathrm{cm}$ (55Ω/sq). Again, the resistivity was shown to reduce because of the increasing crystallinity, but also, it is presented that the high annealing temperatures give rise to deficiency of oxygen in the films, which increases the number of charge carriers due to oxygen vacancies. [21] Hwang *et al.*, [22] used nanoparticle based ITO inks that could be ink-jet printed onto substrates directly into the pattern required with zero material wastage. After annealing at a temperature of 400°C the ink-jet printed ITO reached a sheet resistance value of 500Ω/sq. As well as a reduction in waste achieved by moving to wet processing, this also opens up the possibility of printing electrode patterns. This avoids the need for post-deposition patterning and increases utilisation of the material. Development of ITO-based inks suitable for gravure and ink-jet printing has been conducted as part of the INFINITY project.

The ITO films used in the INFINITY project were created using ITO nanoparticles suspended in solution containing a polymerisable organic binder. The organic binder used was 3(Trimethoxysi- lyl)propyl methacrylate (MPTS), and played a key role for improving the conductivity of the films. As demonstrated by Al-Dahoudi and Aegerter [23, 24], under ultraviolet light the MPTS binder polymerises and can be seen to pull the ITO nanoparticles together under TEM, increasing the electrical conductivity of the films. Also demonstrated by Al-Dahoudi [25] is the sintering of the ITO nanoparticles when heated. When the temperature of the ITO films was increased up to 1000°C, the crystallite size of the ITO films increased by 24% when measured by XRD. With SEM images showing an increase in particle size with higher temperatures, it is concluded that the ITO nanoparticles are sintering together.

2.3 Alternative TCC's

With the high cost and scarcity of indium, alternative materials have been investigated to replace it using cheaper and more available materials. Many of the potential alternatives are known as transparent conducting oxides (TCOs), which are based on doped metal oxides. [26] The most common alternative materials are currently based on cadmium oxide, zinc oxide and tin oxide. [27]

Tin doped cadmium oxide films deposited via pulsed laser deposition have been shown to have resitivities as low as $2.38\times10^{-5}\Omega\,\mathrm{cm}$. [28] Using pulsed filtered cathodic arc deposition of indium doped cadmium oxide also showed impressive resistivity results which went down to around $7.23\times10^{-5}\Omega\,\mathrm{cm}$. [29] This level of resistivity is lower than can be achieved by commercially available indium tin oxide and uses little to no indium in the process, since indium is either omitted from the process altogether, or used as a dopant in small percentages. Even though cadmium oxide has outstanding electrical properties, the optical properties are not as good. The optical band gap of cadmium oxide is relatively low, and with certain dopant levels can be seen to be as small as 2.5eV. [30–32] This leads the cadmium oxide films to have a poor transparency in the lower wavelength range below 500nm. The biggest concern with cadmium oxide based films is the toxicity of cadmium. Cadmium is classified as a carcinogenic to humans, and has been identified as causing direct problems with the kidney and respiratory systems. [33, 34]

Tin oxide based transparent conductors have also been studied, often doped with antimony. Antimony doped tin oxide films often have a higher resistivity when compared with indium tin oxide ranging between $4\times10^{-4}\Omega\,\mathrm{cm}$ and $3\times10^{-3}\Omega\,\mathrm{cm}$. [35–37]. The optical properties of tin oxide are very good in comparison to cadmium oxide however. With a band gap of 3.75eV, which increases with doping levels, the transparency of tin oxide films is high, and extends into the ultraviolet range. [38]

Other alternatives include zinc oxide based transparent conductors. Two common dopants used in zinc oxide are silicon and aluminium. As shown by Minami *et al.*, [39] using silicon doped zinc oxide (SZO) deposited via magnetron sputtering electrical resitivities as low as $3.8\times10^{-4}\Omega\,\mathrm{cm}$ can be reached whilst remaining above 85% optical transparency in the visible range. Using aluminium zinc oxide (AZO) resitivities down to $1.4\times10^{-4}\Omega\,\mathrm{cm}$ have been measured with the same level of optical transparency. [40, 41]

Transparent conducting films based on graphene have also been investigated as an alternative for ITO in commercial devices. Graphene is a layer of carbon one atom thick, which makes the optical transparency of the layer between 97-98%, making it ideal for use as a transparent conductor. [42] As shown by P.Nayak [43], using a 4 layer graphene film deposited via CVD shows sheet resistance values at $40\Omega/sq$ whilst keeping the optical transmission at 90%. Graphene films have also been deposited with additional materials in an attempt to reduce the sheet resistance down to ITO levels. I.Khrapach *et al.*[44] successfully deposited 5 layer graphene films interlaced with ferric chloride and reached a sheet resistance value of $8.8\Omega/sq$ with a transparency of 84%. The films were only stable in air for up to a year, but demonstrates that graphene films can be as conductive and transparent as commercially available ITO films.

2.4 Laser processing of TCO's

Instead of using the conventional furnace treatments to post process TCO films, lasers have been used to deliver energy directly into the films to increase electrical conductivity. In order to laser process thin film materials it is necessary to either deposit the optical radiation directly into the film or to indirectly heat the film via absorption into the substrate. This requires careful choice of laser wavelength and consideration of absorption, reflection, scattering and coherent effects such as thin film interference. In the literature, two approaches have been used for the laser processing of TCO films. Since by definition TCO films are transparent in the visible wavelength range, either ultraviolet or infrared lasers are used to deposit energy into the films.

In the case of ultraviolet laser irradiation of TCO films, a combination of two processes can be achieved. Using high repetition rate neodymium-doped yttrium aluminium garnet (Nd:YAG) lasers in the third harmonic at 355nm, ultraviolet radiation can be absorbed into the films and used to create a photothermal effect. [45–47] Here, the laser radiation is absorbed directly into the films to create a heating effect. Using this method, the crystallinity of the films increases which reduces the grain boundary scattering, making the electron mobility higher and hence reducing the resistivity. The second method is to use the high photon energies of ultraviolet to create photochemical changes within the films. Excimer lasers are pulsed and are capable of outputting large fluences in the ultraviolet. [48] Excimer lasers have been used extensively for irradiation of transparent conducting films, especially when temperature sensitive substrates are used. [49–54] Pulses from excimer lasers are typically between 5ns and 35ns in length, and have pulse repetition rates below 100Hz. [55] This makes them ideal for irradiation of films on temperature sensitive substrates. The heat affected zone (HAZ) caused by a laser pulse, shown in figure 2.3, is related to the thermal diffusion length, and is calculated from equation 2.1 [56, 57]

$$\delta = 2\sqrt{D_H \tau} \tag{2.1}$$

From equation 2.1, we see that the thermal diffusion length, δ, is related to the laser pulse length, τ and the thermal diffusivity, D_H. This means for short laser

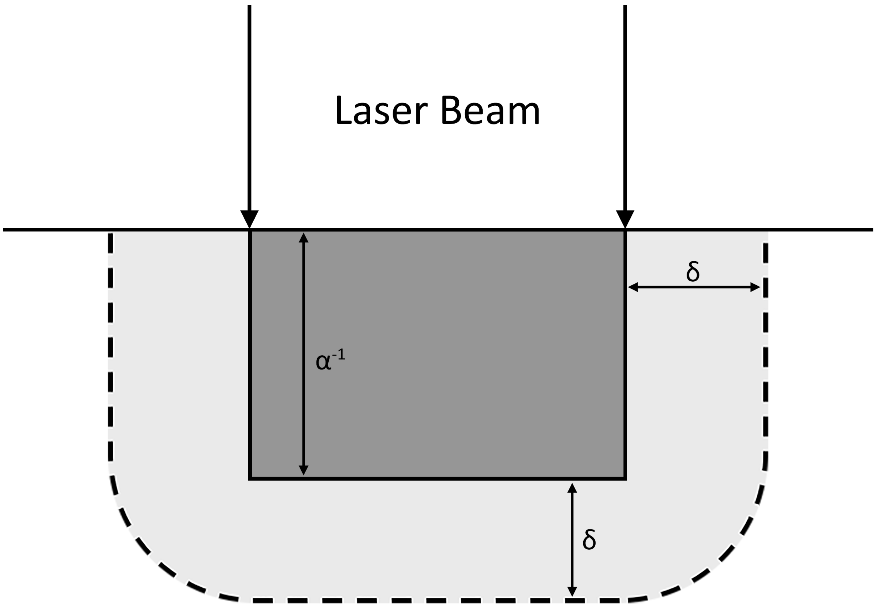

FIGURE 2.3: Heat affected zone of a laser pulse incident onto the surface of a material. $\alpha^{-}1$ is the absorption depth of the laser pulse, and δ is the thermal diffusion length which is related to the pulse length

pulses such as those from excimer lasers, the thermal diffusion length is going to be very small. Coupled with the low repetition rates at which excimer lasers can be operated, the heat accumulation between pulses is minimised, making them ideal for laser processing of temperature sensitive substrates. [58, 59]

Because excimer laser processing of transparent conductors relies chiefly on photochemical processes, ultraviolet radiation has to be absorbed throughout the film, and not just at the surface. The rate at which laser light is absorbed into a material is given by the absorption coefficient, α. A large α value results in the deposition of laser energy being located at the surface leaving the bulk of the film unirradiated by sufficient fluence to affect the film all the way down to the substrate. [56, 60] The Beer-Lambert law determines how far the optical radiation will penetrate into the material, and is given in equation 2.2. [61]

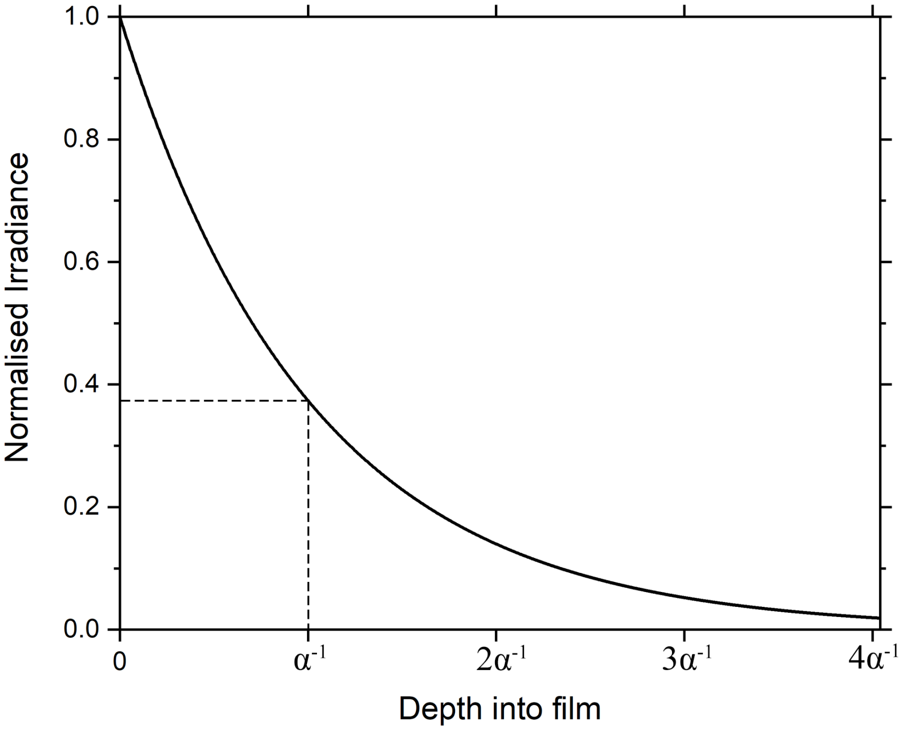

FIGURE 2.4: The Beer-Lambert law for optical absorption. At one absorption depth, α^{-1}, the irradiance drops to 37% (1/e) of the initial value.

$$I(z) = I_0 e^{-\alpha z} \tag{2.2}$$

The Beer-Lambert law shown in equation 2.2 shows an exponential decay of the laser irradiance, $I(z)$, as a function of depth, z, starting at the surface ($z = 0$). At a depth equal to α^{-1}, the laser irradiance has dropped to e^{-1} of its surface value as shown in figure 2.4. For indium tin oxide, as the incident light moves further into the ultraviolet, the absorption depth decreases dramatically. [62, 63] This makes the choice of ultraviolet laser crucial if the entire thickness of the film needs to be processed. An example of this can be seen in figure 5.2, where the attenuation coefficient, α, of the ITO films used in this thesis is plotted against wavelength in the ultraviolet.

Using a furnace is the conventional method for curing transparent conducting films at temperatures often exceeding 500°C for hours at a time. [20, 21, 64]. Instead, infrared lasers can be used to couple energy directly into the films in a localised area to create similar temperature rises. The lower photon energy of the infrared light has no photochemical effect on the films, and acts purely as a localised heating source. Two commonly used infrared sources are the CO_2 laser at $\lambda = 10.6\mu m$ and the fundamental wavelength of the Nd:YAG laser at $\lambda = 1.064\mu m$. The CO_2 laser has been used in the literature to process transparent conducting films to make them more conductive, [65–68] along with the Nd:YAG laser [69–71]. Coupling infrared radiation into transparent conducting films is more challenging than ultraviolet. As the transparent films become more conductive, they also become increasingly reflective at lower infrared wavelengths, until becoming transparent at the plasma frequency. [72–74] As shown by Hamberg *et al.*, [72] ITO films have a reflectivity greater than 70% at the CO_2 laser wavelength and increases with higher charge carrier densities to around 90%. With up to 90% of the energy reflected, high irradiances are required to process the films, with potentially dangerous levels of reflected energy coming from the sample. The opposite problem occurs at Nd:YAG laser wavelengths, where the films are quite transparent. This is shown by Askari *et al.*, [73] where the transmittance at 1μm is around 80%, making the coupling of energy into the films low.

2.5 Electrical measurements on thin films

Measuring the resistivity of bulk materials can be a simple task. If the geometry is known, and total resistance is measured, then the resistivity, ρ can be found using equation 2.3

$$\rho = Resistance \times \frac{Area}{Length} \tag{2.3}$$

When measuring bulk materials the geometries are generally straight forward to measure, with the length much greater than the height or width. This becomes more difficult when measuring thin films which are usually less than 1µm in thickness with large areas in the length and width. In this case, we cannot simply make 2 contact points on the sample and assume that the current will flow through all of the material. An example of this problem is seen in figure 2.5, leading to incorrect resistivity measurements. From figure 2.5, it can be seen that the longer you make the length of the probes in relation to the width, the errors become smaller and smaller until they can be neglected.

One solution to this problem is to force a known geometry for the current path. This can be achieved in two ways. By using a metal busbar across both ends of the sample the current will flow across the whole sample uniformly, assuming there is an ohmic contact with the sample all the way along the busbar. Or alternatively, by isolating a long thin area of the sample, the errors can be made to be negligible, at a cost of having to destroy part of the sample.

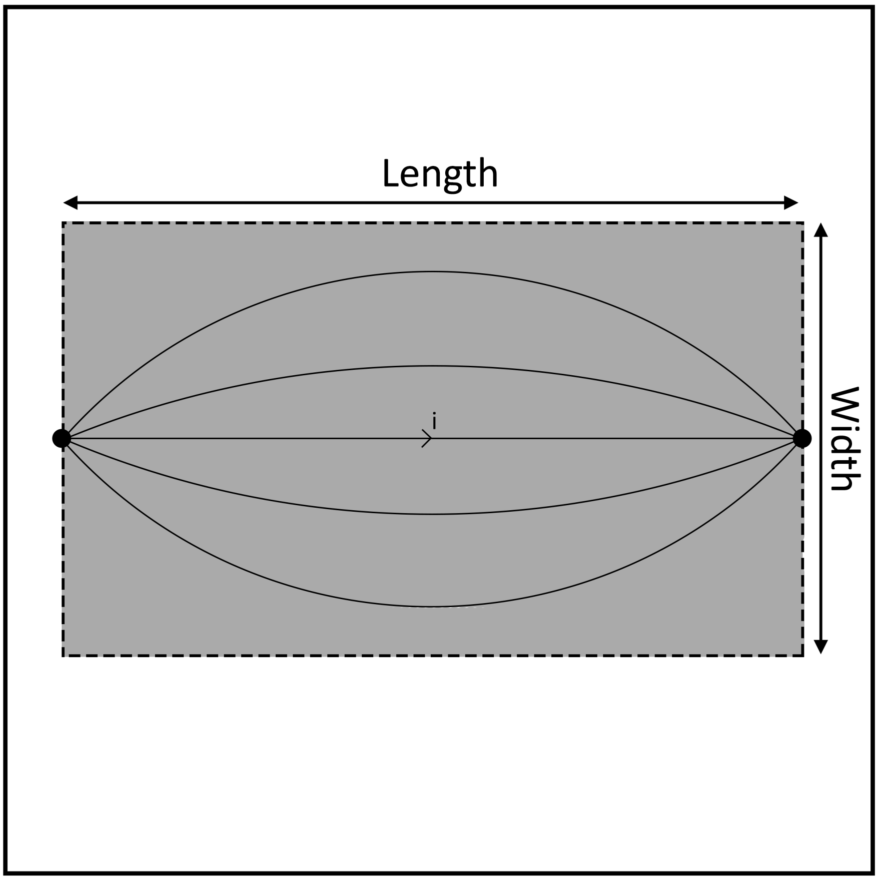

FIGURE 2.5: Incorrect resistivity value obtained from unknown geometry. The current path will be defined by the electric field and local material properties. Even for a homogeneous film, the field is non-uniform and consequently the width of the current path is ill-defined.

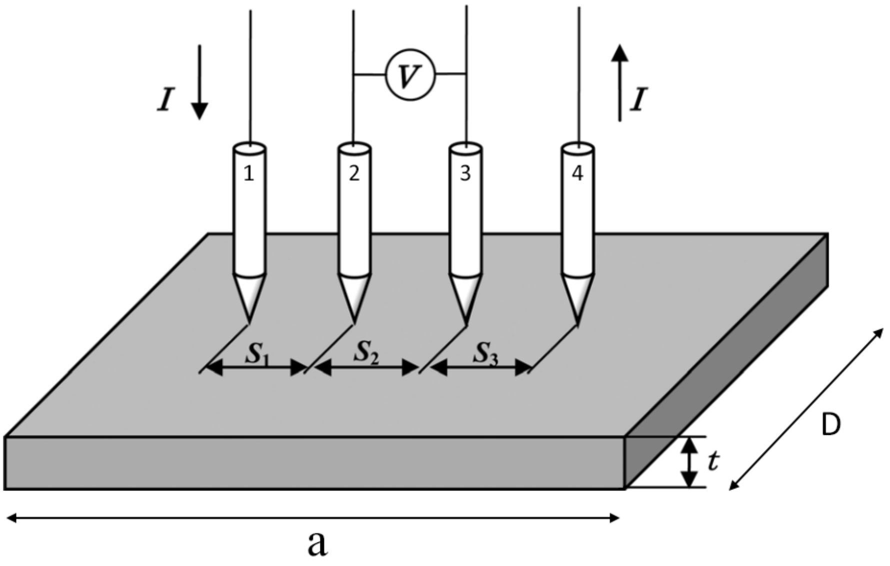

FIGURE 2.6: The arrangement for the linear 4-point probe method. [75] For the probe used in this work, $S_1 = S_2 = S_3$ and is referred to as S without a subscript.

These two approaches come with problems other than just potentially damaging the sample however. When using a 2 point probe electrical measurement, parasitic resistances are present. These include the resistances of the wires and probes, contact resistance between the probes and the material, and any internal resistance of the measurement equipment. These parasitic resistances can be removed by separating the current and voltage measurements through using 4-probes. The arrangement of a linear 4-point probe setup is shown in figure 2.6. Since the voltage measurement is made from a separate voltmeter with an ideally infinite resistance, the parasitic resistance values in the system become insignificant in comparison, giving a more accurate resistivity reading. The 4-point probe method becomes more useful as the resistance of the sample being measured becomes lower and more comparable to the parasitic resistance.

When measuring the resistivity of a sample using the linear 4-point probe method, it is traditional to represent the value obtained as Ohms per square (Ω/sq). Ohms per square is simply the resistivity divided by the thickness of the film, from equation 2.4, and is known as the "sheet" resistance.

$$R_{sheet} = \frac{\rho}{thickness} \tag{2.4}$$

Using the linear 4-point probe method gives the sheet resistance directly. The sheet resistance can be calculated using equation 2.5, where I_{14} is the current flowing through probes 1 and 4, and V_{23} is the voltage measured across probes 2 and 3, shown in figure 2.6. Equation 2.5 gives the sheet resistance, with the value of 4.5324 being a correction factor, but this correction factor is only suitable for sheets which are infinite in size. [76]

$$R_{sheet} = \frac{V_{23}}{I_{14}} \frac{\pi}{\ln 2} \approx 4.5324 \frac{V_{23}}{I_{14}} \tag{2.5}$$

When infinite films cannot be approximated, other correction factors need to be used instead, which depend of the geometry of the sample being measured. Table 2.1 shows the correction factors used when the linear 4-point probe is used in different geometries assuming the probe spacings are all equal. [76] For these correction factors to be applicable, it is important that the geometry constraints of Table 2.1 are observed. There are also further correction factors needed to be used if the probes are located perpendicular to non-conducting boundaries, which makes this measurement increasingly difficult. [77]

TABLE 2.1: Table showing correction factors for various geometries of 4-point probe spacings. The definition of D, S and a are given in figure 2.6.

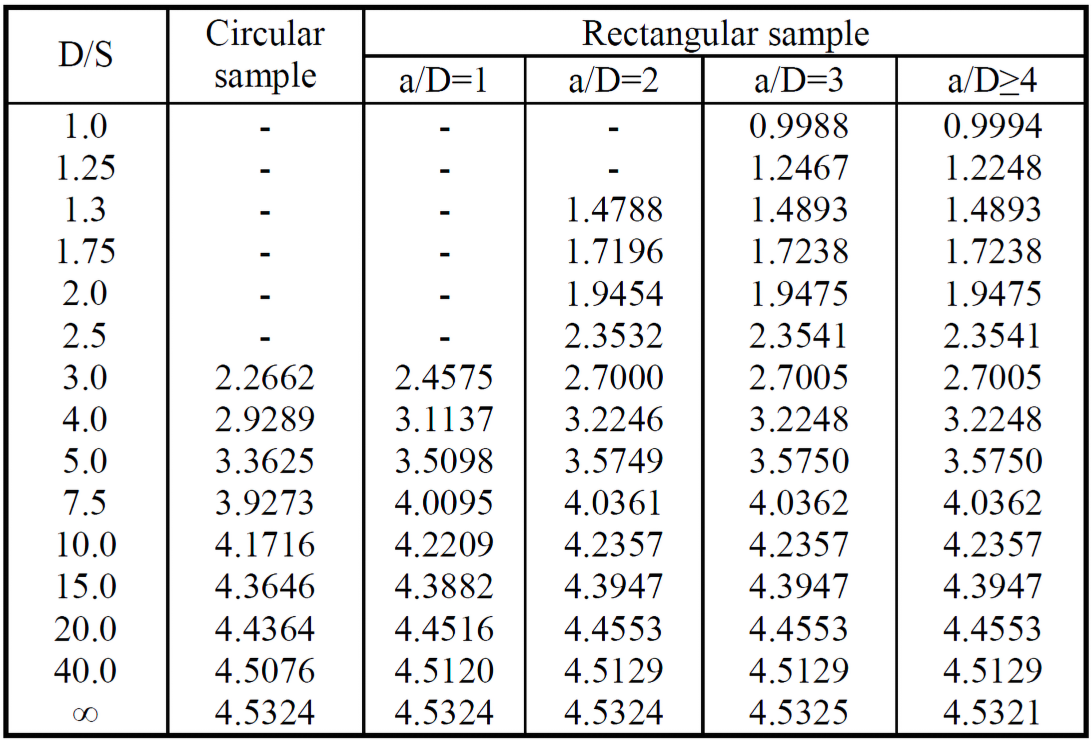

D/S	Circular sample	Rectangular sample			
		a/D=1	a/D=2	a/D=3	a/D≥4
1.0	-	-	-	0.9988	0.9994
1.25	-	-	-	1.2467	1.2248
1.3	-	-	1.4788	1.4893	1.4893
1.75	-	-	1.7196	1.7238	1.7238
2.0	-	-	1.9454	1.9475	1.9475
2.5	-	-	2.3532	2.3541	2.3541
3.0	2.2662	2.4575	2.7000	2.7005	2.7005
4.0	2.9289	3.1137	3.2246	3.2248	3.2248
5.0	3.3625	3.5098	3.5749	3.5750	3.5750
7.5	3.9273	4.0095	4.0361	4.0362	4.0362
10.0	4.1716	4.2209	4.2357	4.2357	4.2357
15.0	4.3646	4.3882	4.3947	4.3947	4.3947
20.0	4.4364	4.4516	4.4553	4.4553	4.4553
40.0	4.5076	4.5120	4.5129	4.5129	4.5129
∞	4.5324	4.5324	4.5324	4.5325	4.5321

To overcome these issues, a second measurement can be made whilst the 4-point probe is on the sample. This technique is called the dual configuration 4-point probe method. Here, the first measurement is made as usual in the 4-point probe method as setup in figure 2.6. Then the outer two probes are swapped, so that the current flows through probes 1 and 3, and the voltage is measured across probes 2 and 4. [78] The resistance from the two sets of measurements can then be calculated using equations 2.6 and 2.7.

$$R_{single} = \frac{V_{23}}{I_{14}} \tag{2.6}$$

$$R_{dual} = \frac{V_{24}}{I_{13}} \tag{2.7}$$

Using the above two equations, the sheet resistance of the sample is finally obtained from equation 2.8. [79]

$$R_{sheet} = R_{single} \times (-14.696 + 25.173\left(\frac{R_{single}}{R_{dual}}\right) - 7.872\left(\frac{R_{single}}{R_{dual}}\right)^2) \tag{2.8}$$

Using the dual 4-point probe technique removes the need for a correction factor, and makes the measurement independent of geometrical effects such as non conducting boundaries. [79–81]

Chapter 3

Methods and Materials

3.1 Methods

3.1.1 Optical

3.1.1.1 Transmission

To measure the optical transmission of the ITO films, two systems were used to cover the spectrum from the ultraviolet to the infrared. A ThermoScientific Evolution 220 spectrophotometer [82] was used to measure the transmission in the wavelength range from 190nm to 1100nm. To measure the transmission further into the infrared a Bruker IFS 66/S FTIR spectrophotometer [83] was used, which could measure the transmission in the wavelength range from 700nm to upwards of 20µm. To calculate the transmission of the sample, the incident intensity, I_0, and the intensity after the sample, I, can be substituted into equation 3.1.

$$Transmission(\%) = \frac{I}{I_0} \times 100 \tag{3.1}$$

To measure I_0, the transmission of the substrate by itself was taken in both instruments which takes into account any absorption in the substrate. Then, the film located on the substrate was measured to find I. In the case for the ThermoScientific Evolution 220, a diffraction grating is used to scan through each individual wavelength, measuring the transmission at each step. The Bruker IFS 66/S uses a technique called Fourier-transform infrared spectroscopy, in which all the wavelengths are simultaneously sent through the sample and then Fourier transforms turn the raw data into transmission data. From the transmission data it is possible to calculate the absorption coefficient for the sample, α, as long as the thickness is known. The Beer-Lambert law defined in equation 2.2 can be arranged into equation 3.2, and the absorption coefficient can be calculated if the thickness, d, and transmittance, T, is known. The transmittance is simply the transmission divided by 100.

$$\alpha = \frac{-\ln(T)}{d} \tag{3.2}$$

Following on from the calculation of the absorption coefficient, it is also possible for a Tauc plot to be created which indicates the optical band gap of the material, and is explained later on in this chapter in section 3.3.

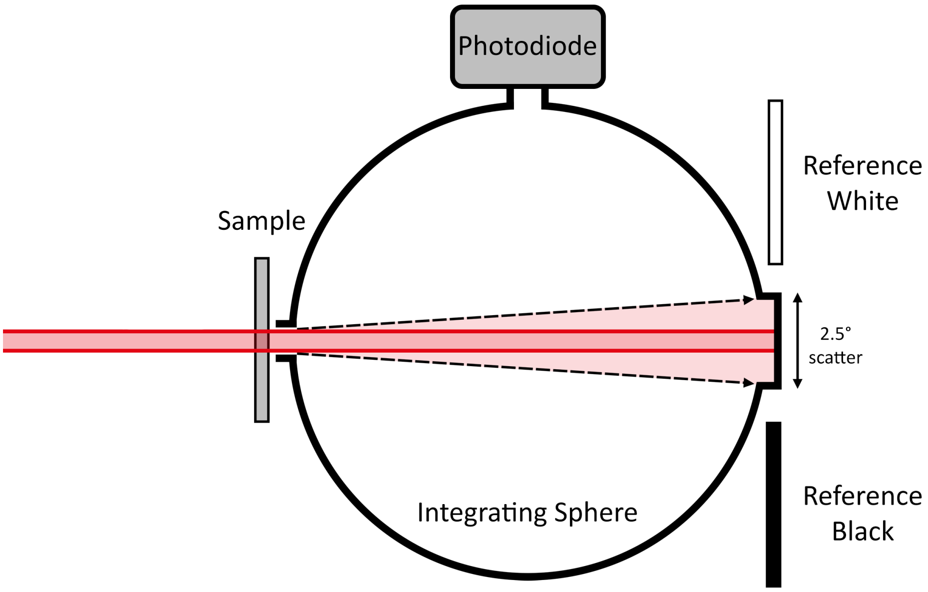

FIGURE 3.1: Haze measurement setup using an integrating sphere. The reference white or black could be inserted into the back of the sphere depending on which measurement was been taken.

3.1.1.2 Haze

Optical transmission measurements are a good indicator of how much light passes through a material, however, they do not indicate how hazy the material is. A hazy material will look foggy, even though the optical transparency might be very high. One of the main uses for ITO films is in display technologies. If the transparent conductor in displays exhibited signs of haze, screens would look foggy, which is undesirable. Haze has two distinctive regimes, wide angle scattering and narrow angle scattering. For ITO films used in displays the more important regime is the wide angle scattering, since it will affect the way the display looks more drastically. Measuring the wide angle haze is standardised by the American Society for Testing and Materials D1003-13. [84]

Following the ASTM D1003-13 guidelines, a haze meter was constructed using an integrating sphere and a unidirectional beam. The light source used was a helium neon laser of around 1mW of power. From ASTM D1003-13, the wide angle scattering is defined as scattered light at a greater angle than 2.5° normal from the beam. The setup is shown in figure 3.1. Any light scattered beyond 2.5° from the sample will impinge on the white surface of the integrating sphere, creating a voltage reading on the photodiode.

In order to calculate the haze, 4 measurements have to be taken with the integrating sphere. The readings are read as a voltage developed by the photodiode. With the sample removed and the standard white inserted, the first reading was recorded from the photodiode, T_1, making sure that it was not saturated with too much light. Keeping the sample removed and inserting the standard black, the second reading, T_3, was recorded. Now, inserting the sample into the setup, with the standard black inserted the third measurement, T_4, is taken. Finally, with the sample inserted as well as the standard white final reading, T_2 was recorded. To calculate the haze, equation 3.3 is used.

$$Haze = \frac{T_4 - T_3(T_2/T_1)}{T_1} \times \frac{T_1}{T_2} \tag{3.3}$$

The end result gives the haze as a percentage, at a wavelength of 633nm. The hazemeter constructed for use in this thesis could only measure the haze at a single wavelength (633nm), whereas a commercial hazemeter would have used a collimated white light source and been able to measure the haze as an average throughout the visible spectrum. The university did not own such a

FIGURE 3.2: The Jandel Veeco 4-point probe used for the resistivity measurements throughout this thesis.

device to measure the haze, and the budget did not allow us to purchase one. Therefore, an in house constructed hazemeter was used for the measurements as closely to the ASTM D1003-13 guidelines as possible.

3.1.2 Electrical

3.1.2.1 Resistivity

For the resistivity measurements to be the same for all the samples, a specific resistivity measuring setup was created for the purpose. Because some of the measurements required 4 points of contact, a 4-point probe was purchased from Jandel and can be seen in figure 3.2. [85] The 4-point probe featured spring loaded tips (so that the pressure on the films was constant throughout measurements), a tip radius of 100µm, and a spacing of 1mm between probes. To make sure the 4-point probe was aligned onto the isolated areas, a long working distance microscope was used so that the points of contact could be viewed from the side. Using the microscope ensured the probes were

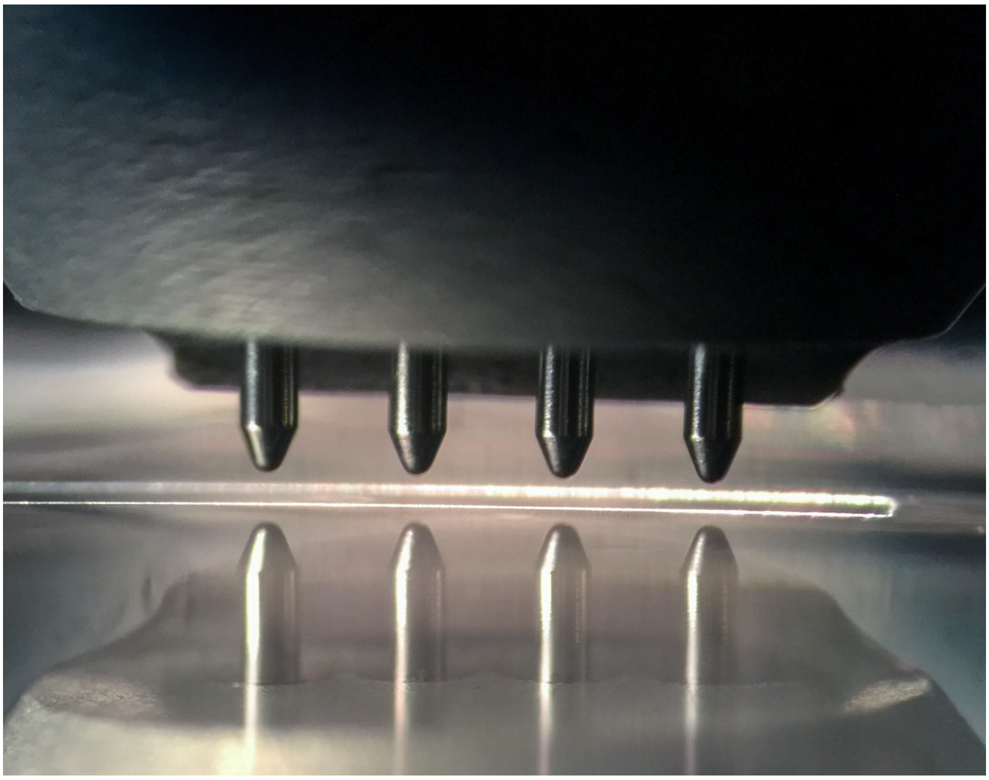

FIGURE 3.3: View through the long working distance microscope of the 4-point probe aligned just above an isolated area in an ITO film.

all situated on the laser irradiated line. Figure 3.3 shows a view through the microscope. The sample was situated on an XYZ micrometer-controlled stage beneath the 4-point probe so that fine adjustments were possible.

The 4-point probe setup was used in two different ways depending on the geometry of the isolated areas. In the case of the long and thin 6x1mm areas, a more simple approach could be used due to the lack of current spreading errors. In this approach, seen in figure 3.3, the 4-points are aligned in the centre of the 6x1mm line. Since the geometry is well defined a simple resistivity calculation can be performed using equation 3.4.

$$\rho = Resistance \times \frac{Width \times Thickness}{Length} \tag{3.4}$$

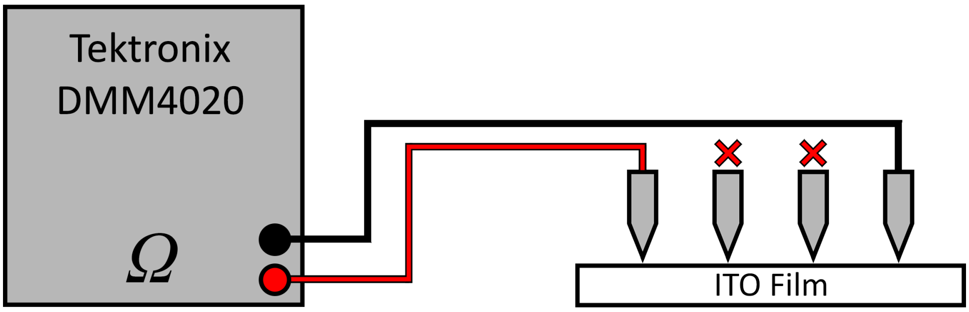

FIGURE 3.4: Resistivity setup used for samples with resistance greater than 1kΩ. The inner two probes were not connected in this case.

The resistance in this case was measured in one of two ways. Firstly, the resistance was measured using a Tektronix DMM4020 in a 2-probe configuration, shown in figure 3.4. With the DMM4020 set into resistance mode, it directly measures the resistance between the two probes. In this setup, the resistance of the wires, probes and any contact resistance is also included in the measurement. If the resistance of the sample was above 1kΩ then the % error caused is insignificant as the parasitic resistance values were small in comparison. However, in the case where the resistance of the sample was below 1kΩ the parasitic resistances stopped being negligible and needed to be accounted for. In this situation, the resistance was measured using all 4 contacts of the probe. The outer 2 probes had a known current passed through them and the voltage drop across the middle 2 probes was measured with a separate voltmeter. Using a voltmeter with very high internal resistance makes the parasitic resistances negligible, and therefore any errors due to them are minimised. The setup used in this situation is shown in figure 3.5.

To validate both the systems, known resistance values were measured. In the first setup using the 2-point probe system, a 2.4kΩ resistor with a 1% tolerance

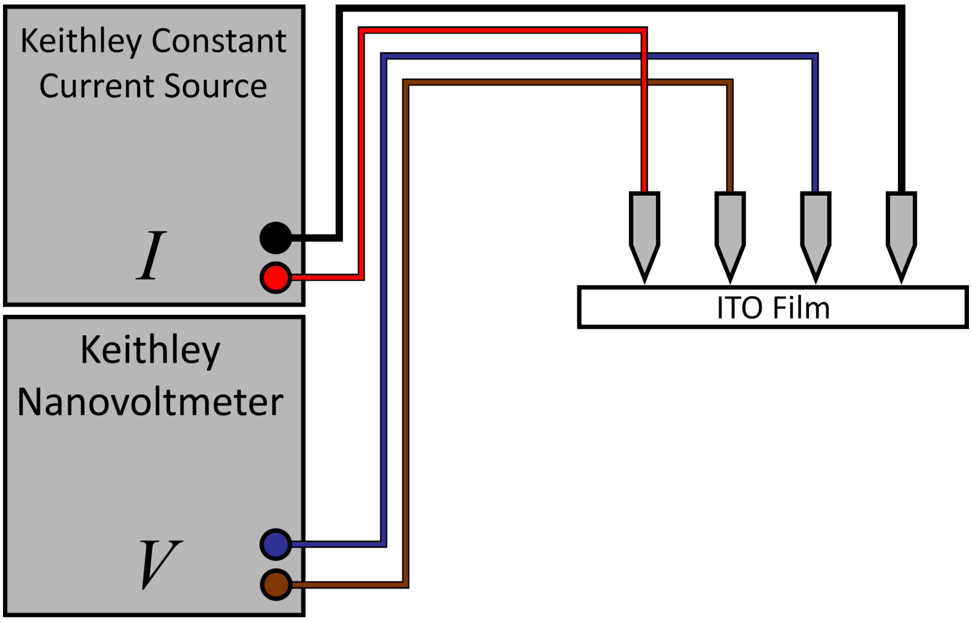

FIGURE 3.5: Resistivity setup used for samples with resistance lower than 1kΩ. Having a separate current supply and voltmeter eliminates parasitic resistances and reduces errors, but it takes longer to make a measurement.

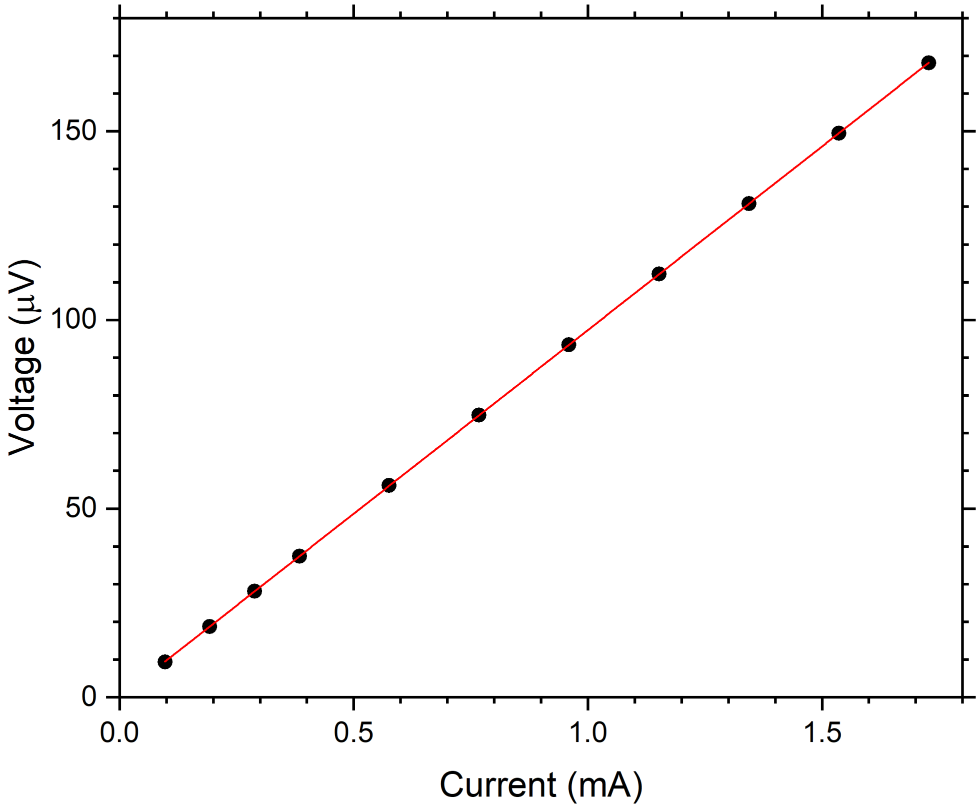

FIGURE 3.6: System validation using the 4-point probe system. The linear fit gives a resistance of 97.30 ± 0.03 mΩ. Well within the tolerances of the resistor.

was used. For the second setup using the 4-point probe, a 100mΩ resistor with a 5% tolerance was used. The Tektronix DMM4020 correctly measured the 2.4kΩ resistor within the tolerance levels at 2403Ω, and the 4-point probe system results are shown in figure 3.6. Here we see that the 100mΩ resistor was measured to be 97.30 ± 0.03mΩ, which is within the tolerance levels of the resistor and has a small uncertainty equivalent to $\sim$0.03%.

The second method to measure resistivity was used in the cases of the larger 6x6mm and 12x12mm areas. For these samples, current spreading becomes an issue and the simple resistivity calculation fails due to unknown geometries involved. For this situation, the setup used is shown in figure 2.6. It uses the same equipment used in the 6x1mm area measurements, keeping the 4-point probe, current source and nanovoltmeter but different measurements are taken. In this situation, the dual 4-point probe sheet resistance measurement was employed. As shown in the literature review, this method directly measures the sheet resistance of a film of unknown geometry using equations 2.6 - 2.8. To test this setup, a known sample had to be used. A commercial sheet of ITO was chosen for this. The ITO sample itself was not known to a high degree of accuracy, since it was in a batch with hundreds of other samples. However, the batch of samples was known to lie between 10 and 15Ω/sq.

To take the measurement, IV curves were plotted for both R_{single} and R_{dual} which can be seen in figure 3.7. The values measured for R_{single} and R_{dual} were 3.20Ω and 2.63Ω respectively. The sheet resistance for the dual configuration was calculated from equation 3.5.

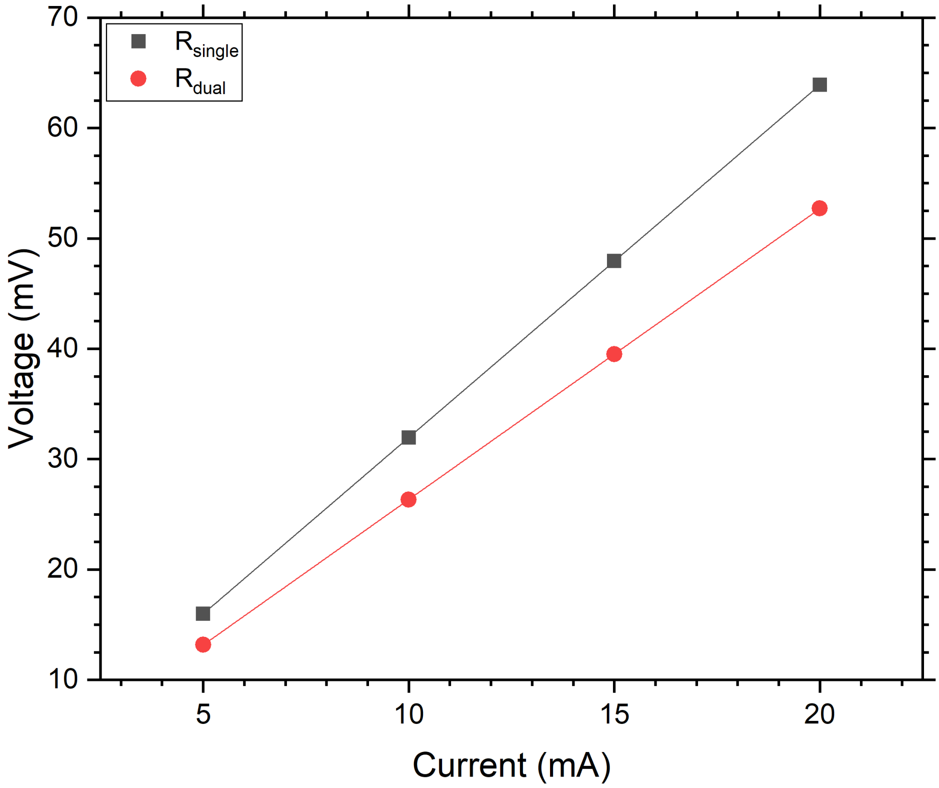

FIGURE 3.7: IV curves measured for commercial ITO films. The corresponding resistance values for R_{single} and R_{dual} are $3.20 \pm 0.04\Omega$ and $2.63 \pm 0.03\Omega$ respectively.

$$R_{sheet} = R_{single} \times (-14.696 + 25.173\left(\frac{R_{single}}{R_{dual}}\right) - 7.872\left(\frac{R_{single}}{R_{dual}}\right)^2) \tag{3.5}$$

Using the measured resistances and equation 3.5 gave a sheet resistance for the ITO films of (13.6±0.2)Ω/sq. This value lies within the stated sheet resistance range for the batch of ITO films we used.

Using this data it was also possible to test for the validity of the dual configuration setup by checking what the sheet resistance would be if R_{single} was measured alone and coupled with one of the correction factors shown in table 2.1 in the literature review. The ITO films that were used were 12x12mm

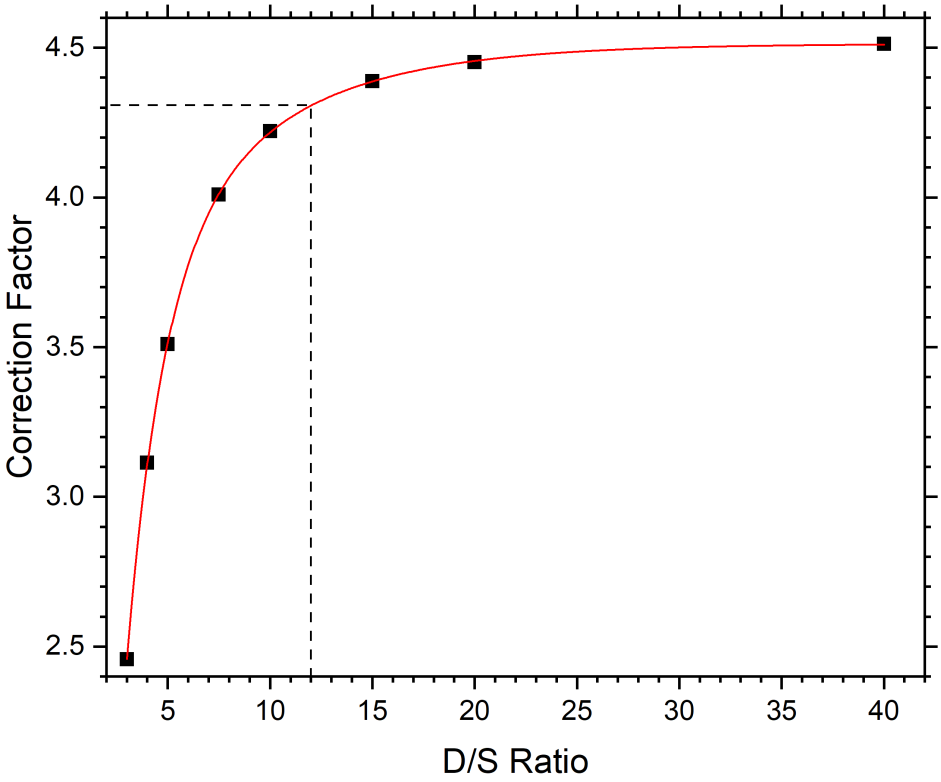

FIGURE 3.8: Correction factors for single configuration 4-point probe measurements from table 2.1. With a curve fitted, we can interpolate values not shown in the table. At a ratio of 12, the correction factor is 4.304.

square, giving a D/S ratio of 12. From figure 3.8, the correction factor for a D/S ratio of 12 is 4.304. Using R_{single} multiplied by this correction factor gives a sheet resistance of $13.7 \pm 0.2\Omega/\text{sq}$. Hence, the dual configuration and correction factor method agree when used properly.

3.1.2.2 Mobility

To compliment the resistivity measurements, a Hall voltage measurement system was constructed. Being able to measure the Hall voltage also enabled measurement of the charge carrier density and charge carrier mobility. These values are useful to explore why the electrical properties are changing due to laser irradiation, and can give insight into what laser-induced processes

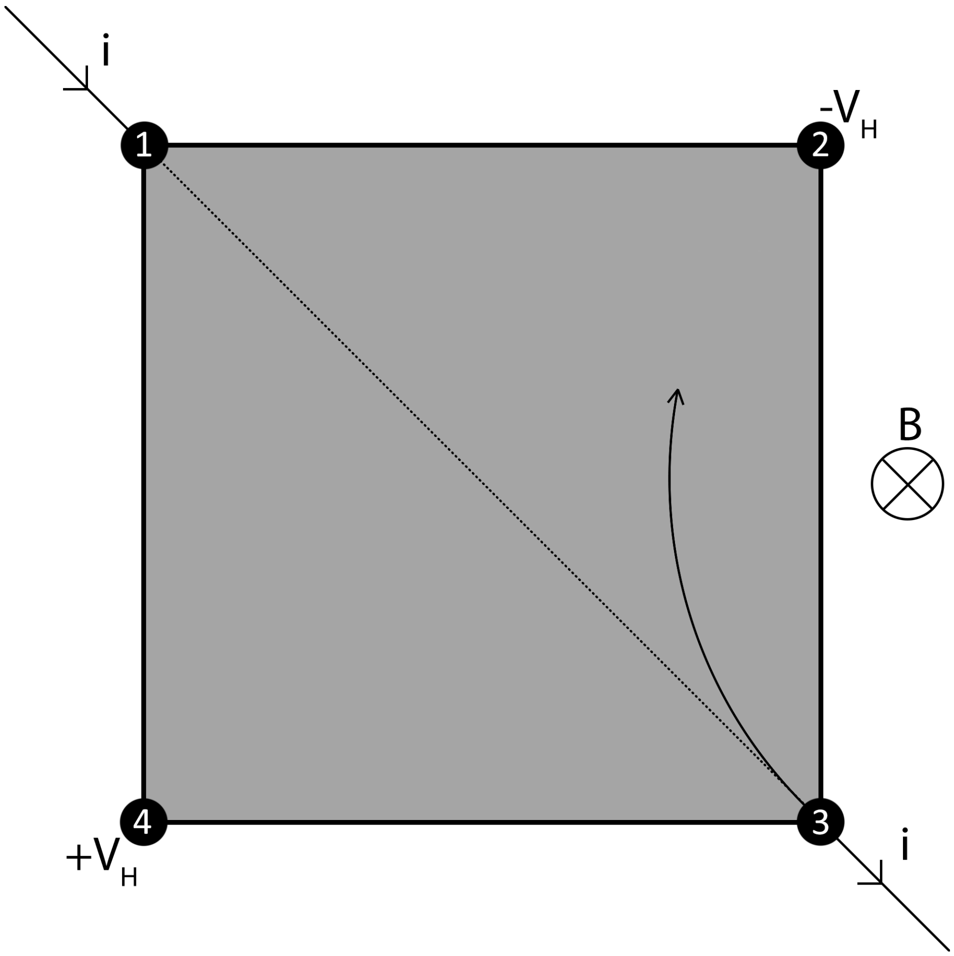

FIGURE 3.9: Hall voltage setup in the Van der Pauw arrangement. Current flows through opposite corners and the voltage is measured across the other corners. In the presence of a magnetic field the electrons will deflect to one side and create a potential, V_H.

are occurring. The setup for a Hall voltage system is similar to the resistivity measurements. We used the same Keithley constant current source and nanovoltmeter, and used 4 sprung loaded probes to contact the sample. The probe arrangement was different however, and can be seen in figure 3.9. The Hall measurement was setup following the NIST guidelines. [86]

In the Van der Pauw arrangement, the current flows diagonally through the sample and the voltage difference is measured across the other two corners. When a magnetic field is applied perpendicular to the direction of current flow, electrons will be deflected towards one of the corners and a potential difference can be measured across the device, known as the Hall voltage. Since the probes, sample holder and connectors all had to be situated in a magnetic field greater than 1T, great care had to be taken to ensure non magnetic parts were used. The Hall effect is very small, creating voltage differences of typically microvolts or smaller. Due to the small effect, electrical shielding was necessary. To mount the sample, 4 spring loaded probes spaced in a 12x12mm square were used and enclosed in an aluminium box. The sample holder was placed in between two electromagnet poles bigger than the entire sample holder, making sure a homogeneous magnetic field could be maintained across the sample. The electromagnet used could generate a maximum magnetic field of 1.2T, and could be set to any desired field below this by adjusting the current supplied to the coils.

To measure the Hall voltage, the sample was placed in a magnetic field, B. Current, I, was allowed to flow through probes 1 and 3, and the Hall voltage, V_H, was measured across probes 2 and 4. From these values, the charge carrier density was calculated from equation 3.6, where e is the electron charge. [86] Importantly, when using equation 3.6 the sheet charge carrier density, η_s, is calculated in units of cm^{-2}.

$$\eta_s = \frac{IB}{e|V_H|} \tag{3.6}$$

To test the system, a known calibration sample of ISOTAN was used. ISOTAN is an alloy of copper and nickel, making the resistivity very low. Having such

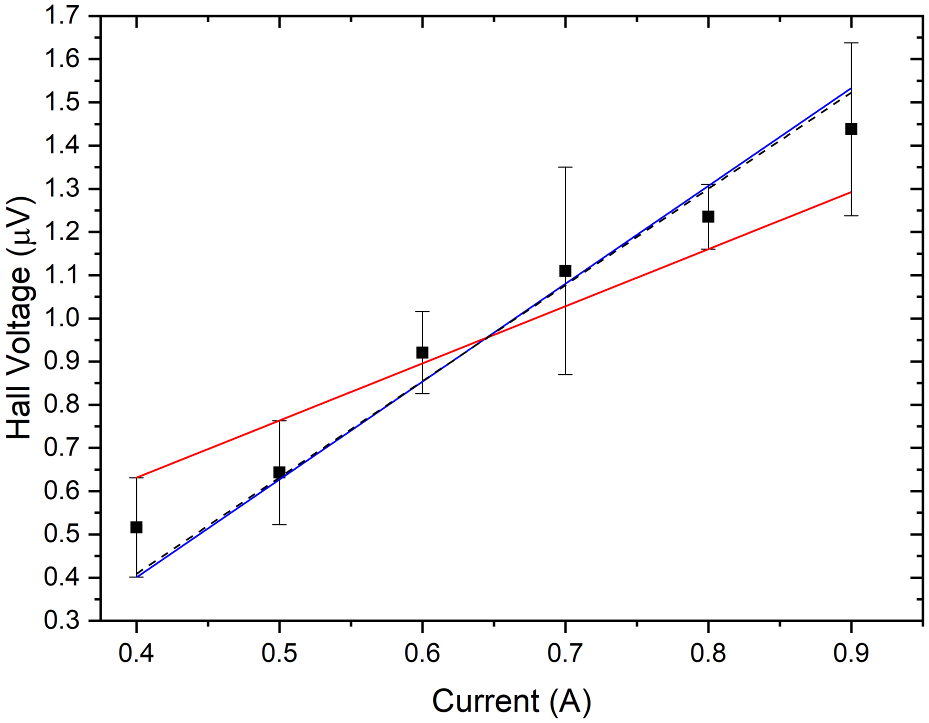

FIGURE 3.10: Measured Hall voltage of ISOTAN against current. The magnetic field strength in this case was 1T. The red and blue lines represent the lowest and highest gradient value within errors, with the dashed line the accepted value of the ISOTAN sample.

a low resistivity made the voltage drop across the device extremely small. Figure 3.10 shows the Hall voltage plotted against a range of currents through ISOTAN. As can be seen, the voltage drops were as small as 500nV even with 400mA of current flowing through the sample. The large errors were due to fluctuating voltages on the nanovoltmeter, which could not be improved upon when measuring such small voltages. The measured charge carrier density of the ISOTAN sample was $3.31 \pm 0.55 \times 10^{20}\text{cm}^{-2}$, which just agrees with the ISOTAN value of $2.8 \times 10^{20}\text{cm}^{-2}$. [87] From the sheet charge carrier density, η_s, we can infer the charge carrier mobility, μ_e, if we know the sheet resistance using equation 3.7. [86]

$$\mu_e = \frac{1}{eR_{sheet}\eta_s} \tag{3.7}$$

Measuring the sheet resistance of the ISOTAN sample using the dual configuration 4-point probe method, gave a value of 4.08mΩ/sq. Using the the values measured and using equation 3.7 gives a sheet carrier mobility of $4.61\text{cm}^2\text{V}^{-1}\text{s}^{-1}$. Consequently, by measuring the Hall voltage, we now have a complete picture of the electrical characteristics for the material

The ISOTAN sample used was an extreme. The resistivity was very low, and not comparable to the values expected here. To test the system on a more realistic sample, the commercial ITO films used to verify the 4-point probe resistivity system was also used in the Hall voltage setup. The same technique was used with this ITO sample. A 1T magnetic field was used. The current flow through the ITO sample was much lower, since the resistivity of the ITO

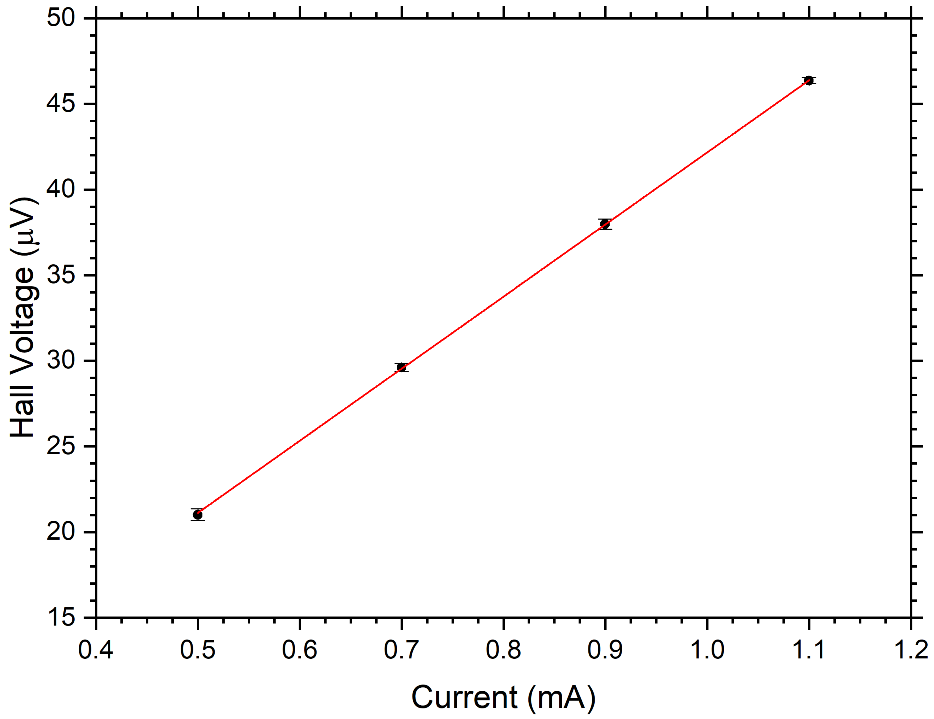

FIGURE 3.11: Measured Hall voltage of a commercial ITO films on glass against current. The magnetic field strength in this case was 1T.

was much higher than the ISOTAN sample. Figure 3.11 shows the Hall voltage as a function of current for the ITO sample.

As seen from figure 3.11, even though the current supplied was much lower than for the ISOTAN sample, the Hall voltage is more easily measured, being at least 20× higher in comparison. With the lower current and higher Hall voltage, the measurement became much more stable and a linear graph was obtained with uncertainties too small to represent as error bars. Again, using equation 3.6, the sheet charge carrier density is measured to be $14.8 \pm 0.7 \times 10^{15}\text{cm}^{-2}$. The sheet resistance of the commercial ITO sample was already measured in the previous section as being $13.6\Omega/\text{sq}$, and when substituted into equation 3.7, gives the charge carrier mobility of the ITO as $31.0\text{cm}^2\text{V}^{-1}\text{s}^{-1}$.

The commercial ITO films did not have a known carrier mobility, so for an approximate comparison the mobility values for various ITO films were identified in the literature. Values from 3 sources put a typical value for the mobility of ITO films between 20 and 50cm^{2}V^{-1}s^{-1}. [10, 88, 89] Consequently, our measurements are within the range of common values for ITO films.

As with the hazemeter, the device used here to measure the Hall voltage was built in house. The cost for a commercial Hall voltage measurement system was high, and was not possible to be purchased, but all the equipment used within a typical commercial system was available separately. Following the NIST guidlines, a sample holder with contact probes was designed and built that was able to be mounted in the 1T electromagnet. The system was then calibrated against a known sample, and was able to correctly measure the charge carrier density and mobility to within the errors of the sample.

3.2 Materials

3.2.1 Ink

The ITO films used in this thesis were prepared by the Leibniz Institute for New Materials in Germany. [90] The films consisted of ITO nano-particles suspended in a solution containing a polymer based binder, 3(Trimethoxysilyl)propyl methacrylate (MPTS), along with a solvent (isopropoxyethanol) to achieve the correct viscosity for spin deposition. [91] To make the ITO nanoparticles, a solution of indium(III) chloride and tin (IV) chloride was added

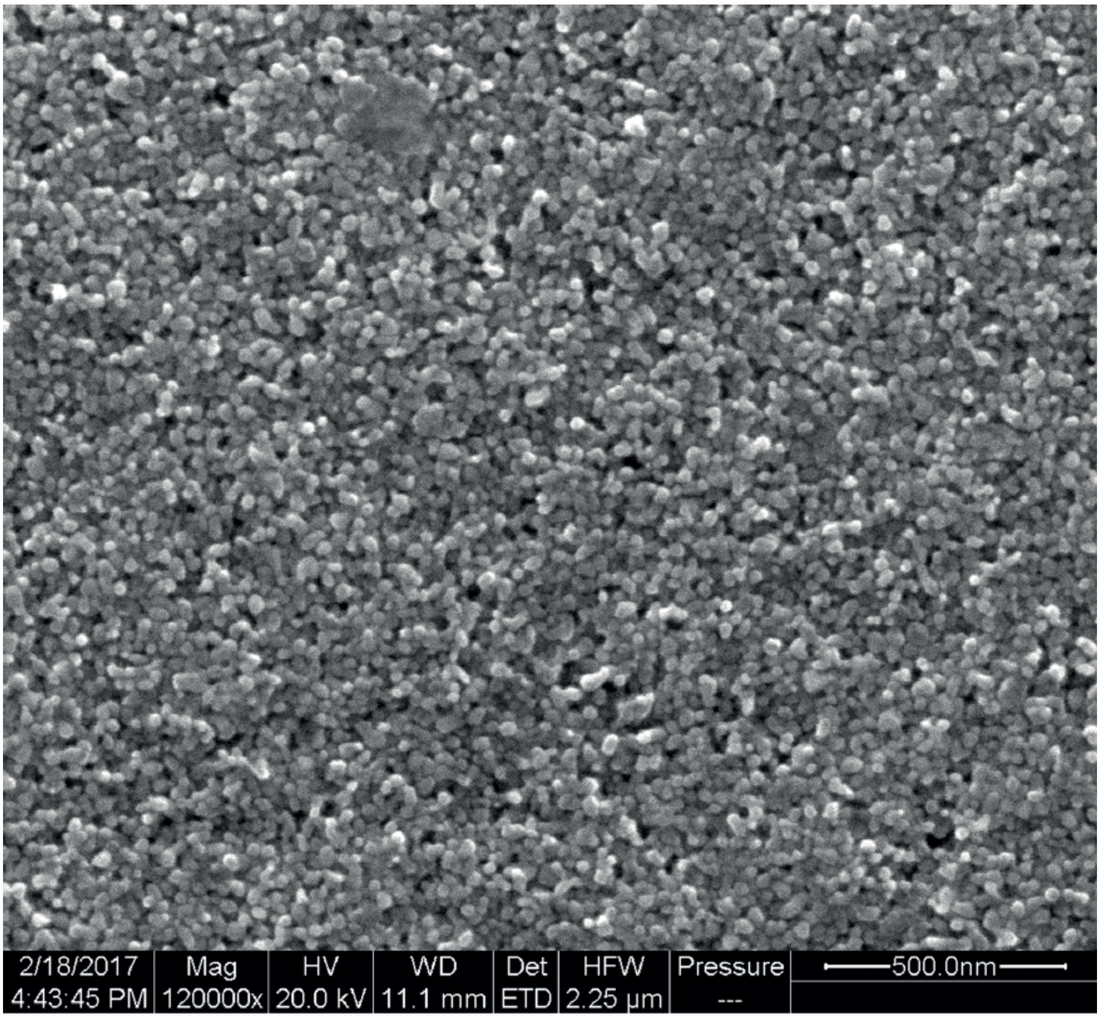

FIGURE 3.12: SEM picture of the ITO nano-particles suspended in MPTS on a glass substrate.

to an ammonia solution then dried to leave a powder which was annealed at 250°C in forming gas (92% N_2, 8% H_2). [92] The resulting nano-particles have an average size of 15-20nm. An SEM image of the nano-particles as received can be seen in figure 3.12. The MPTS binder and solvent mixed in with the ITO nano-particles act as a dielectric medium between neighbouring nano-particles, as shown in figure 3.13.

In a typical sputtered ITO film, the conductivity is dependant on the charge carrier density and the mobility of the electrons in the film as seen in equation 3.8, where σ_e is the conductivity, η_e is the electron density, μ_e is the electron

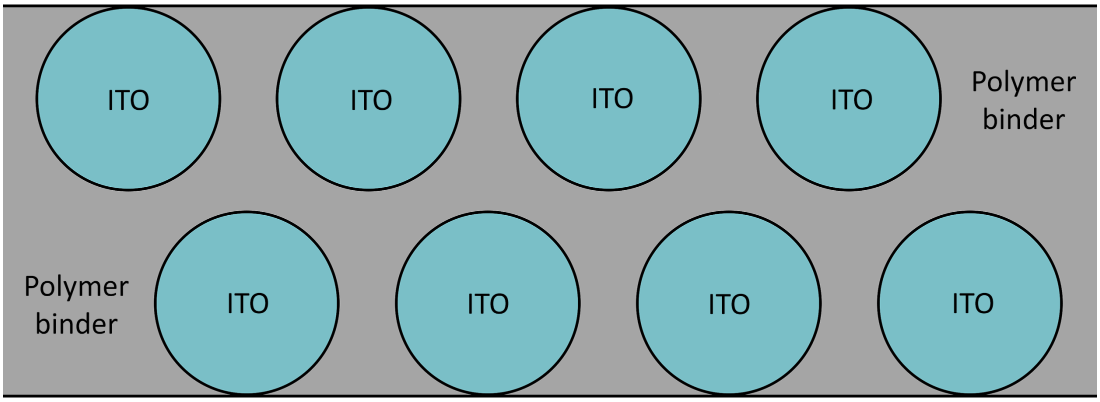

FIGURE 3.13: ITO nano-particles suspended in a polymer binder. The binder inhibits electrical conduction with a dielectric barrier between neighbouring particles.

mobility and e is the electron charge. Sputtered ITO films are continuous, and hence do not have any dielectric material that can interfere with the conductivity of them, though grain boundaries can still scatter electrons increasing the resistivity.

$$\sigma_e = \eta_e \mu_e e \tag{3.8}$$

In INM's nano-particle based films, the overall conductivity is dominated by the electron tunnelling current that can pass through the dielectric barrier formed by the polymer binder. This severely limits the electrical conductivity, even if the ITO nano-particles themselves have a very high value.

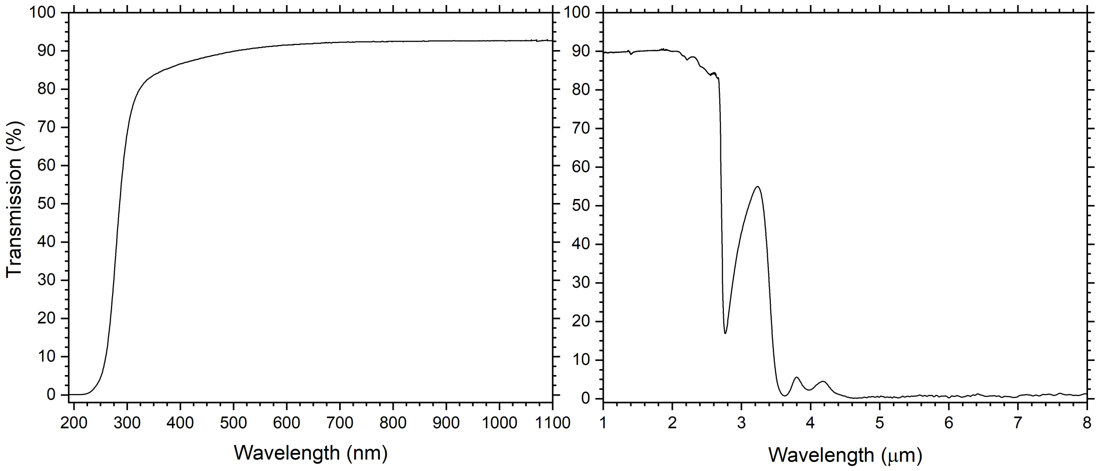

FIGURE 3.14: Optical transmission spectra for borofloat 33 substrates in the **Left** UV to NIR and **Right** NIR to MIR. Data at 10.6µm could not be measured due to the instrument limitations.

3.2.2 Substrates

3.2.2.1 Borosilicate Glass

The majority of the samples used for irradiation in this thesis were taken on Schott Borofloat 33 substrates. [93] The borofloat substrates were used over conventional soda lime glass due to the higher resistance to thermal cracking, having a coefficient of linear thermal expansion of $3.25\times10^{-6}K^{-1}$. This meant higher temperatures could be reached during laser processing of the ITO films without substrate damage, with the upper temperature limit of 500°C. The optical transmission of the borofloat substrates is shown in figure 3.14.

The optical properties show that the borofloat substrates are transparent above 80% from $\lambda = 320$nm and above. This make measuring the transmission of the ultraviolet wavelengths difficult if the films are on borofloat substrates. The borofloat substrates start to absorb again in the infrared at around $\lambda = 3$µm, meaning the CO_2 laser wavelength at 10.6µm will be fully absorbed into the

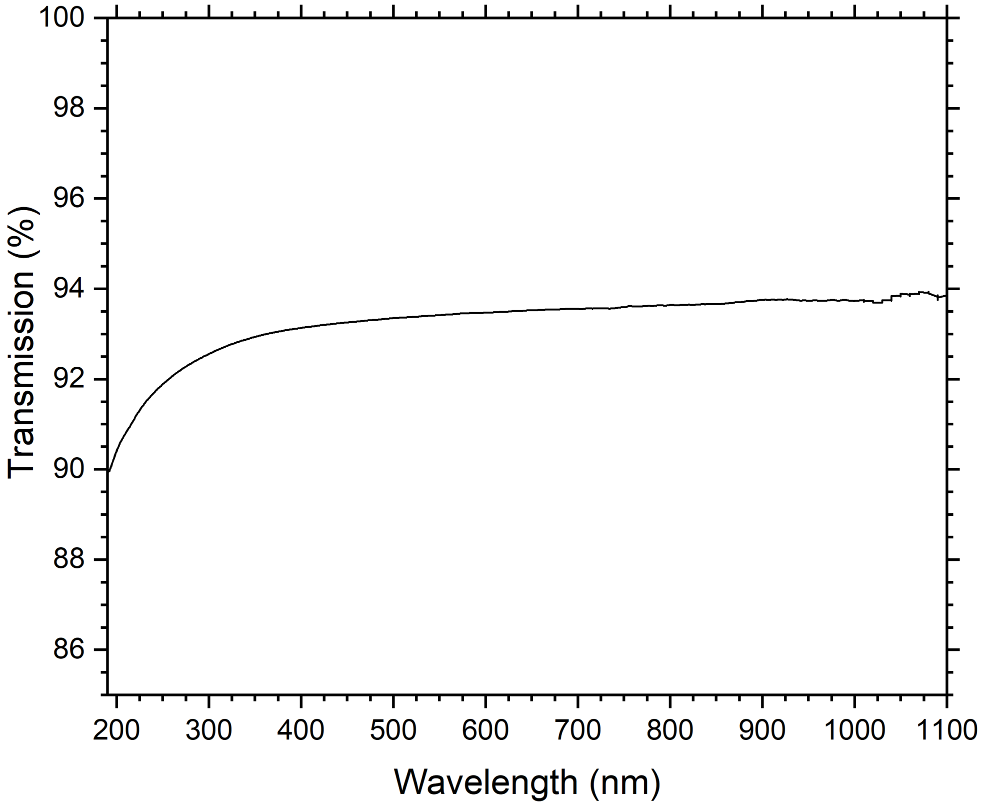

FIGURE 3.15: Optical transmission spectra for spectrosil 2000 substrates from 190nm to 1100nm.

substrate if not absorbed into the ITO films. The thermal conductivity of the borofloat substrates is low at 1.2$\text{Wm}^{-1}\text{K}^{-1}$, meaning any energy deposited into the substrate is not going to spread, concentrating temperature rises into small areas.

3.2.2.2 Fused Silica

The second type of glass substrate that was used were made from Heraeus spectrosil 2000 fused silica. [94] The main use for the fused silica substrates were for the ability to take transmission data further into the ultraviolet. As can be seen in figure 3.15, the transmission of the fused silica substrates remains above 90% at $\lambda = 190$nm. The thermal conductivity and coefficient of linear thermal expansion values for spectrosil are $1.4\mathrm{Wm}^{-1}\mathrm{K}^{-1}$ and $5.9\times10^{-7}\mathrm{K}^{-1}$ respectively. The thermal conductivity of the spectrosil is very similar to that of the borofloat samples, thus, it is expected that the laser treated samples using the CO_2 laser will heat the ITO samples in the same way. The spectrosil substrates do have a lower coefficient of linear thermal expansion and are expected to have a higher tolerance to thermal damage, and the upper working temperature was higher at 1350°C. Both the borofloat and spectrosil substrates absorb heavily in the infrared beyond $\lambda = 3\mu\mathrm{m}$ and neither substrate are favoured for the transmission measurements taken in the infrared. The spectrosil substrates would have been the better choice for all the glass samples due to the superior thermal expansion properties and better ultraviolet transmission, however, due to the high cost associated with the substrates it was not possible.

3.2.2.3 PET

For the ITO films deposited on flexible substrates, polyethylene terephthalate (PET) substrates were used. PET has a melting point of ∼260°C [95], which is substantially lower than that of the glass substrates used. Irradiation of the ITO films on the PET films is expected to be difficult when photothermal processes are required due to this low melting temperature. In an attempt to combat this issue, Melinex heat stabilized PET films [96] were used to increase the upper working temperatures of the substrates. PET has a thermal conductivity of $0.19\mathrm{Wm}^{-1}\mathrm{K}^{-1}$, which is around a 15% of that seen in the glass substrates. [97] The PET substrates were not used for any of the optical measurements

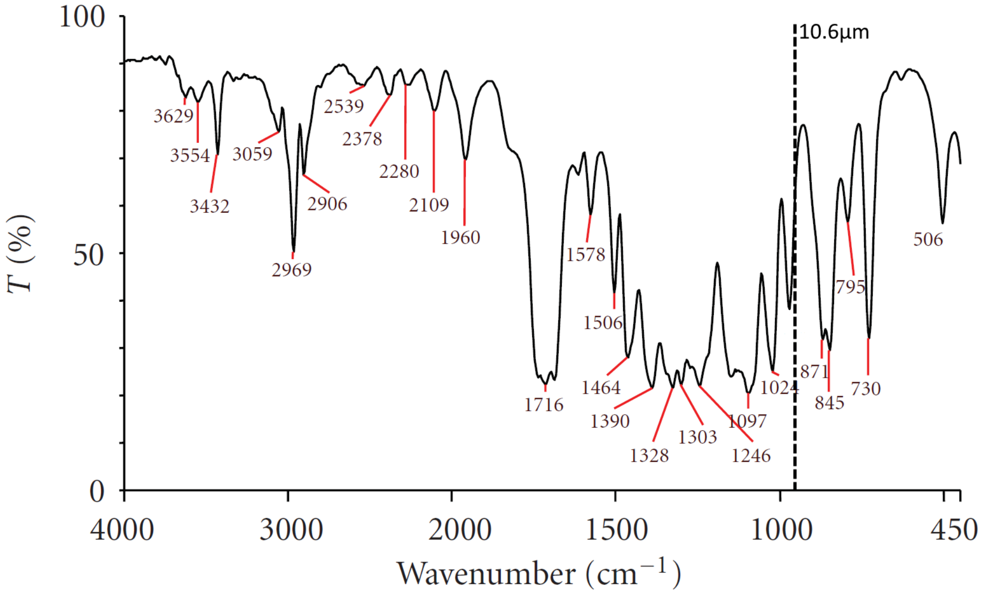

FIGURE 3.16: FTIR spectra for PET from from wavenumbers 4000cm^{-1} to 450cm^{-1} showing absorption peaks throughout. [99]

due to the poor transmission near the ultraviolet [98], as well as absorption peaks located throughout the infrared parts of the spectrum as seen in figure 3.16.

3.3 Initial Characterisation

The ITO films as received were typically greater than 100Ω cm (2MΩ/sq), which is over 6 orders of magnitude higher than commercially available sputtered ITO films.

The inks were deposited in one of three ways. On Borofloat substrates inkjet printed lines were supplied for irradiation and characterisation. The inkjet printed films were deposited using a Microdrop AD-P-8000 printer using nozzle sizes ranging from 70µm to 9µm. [100] Each ink-jet printed line was

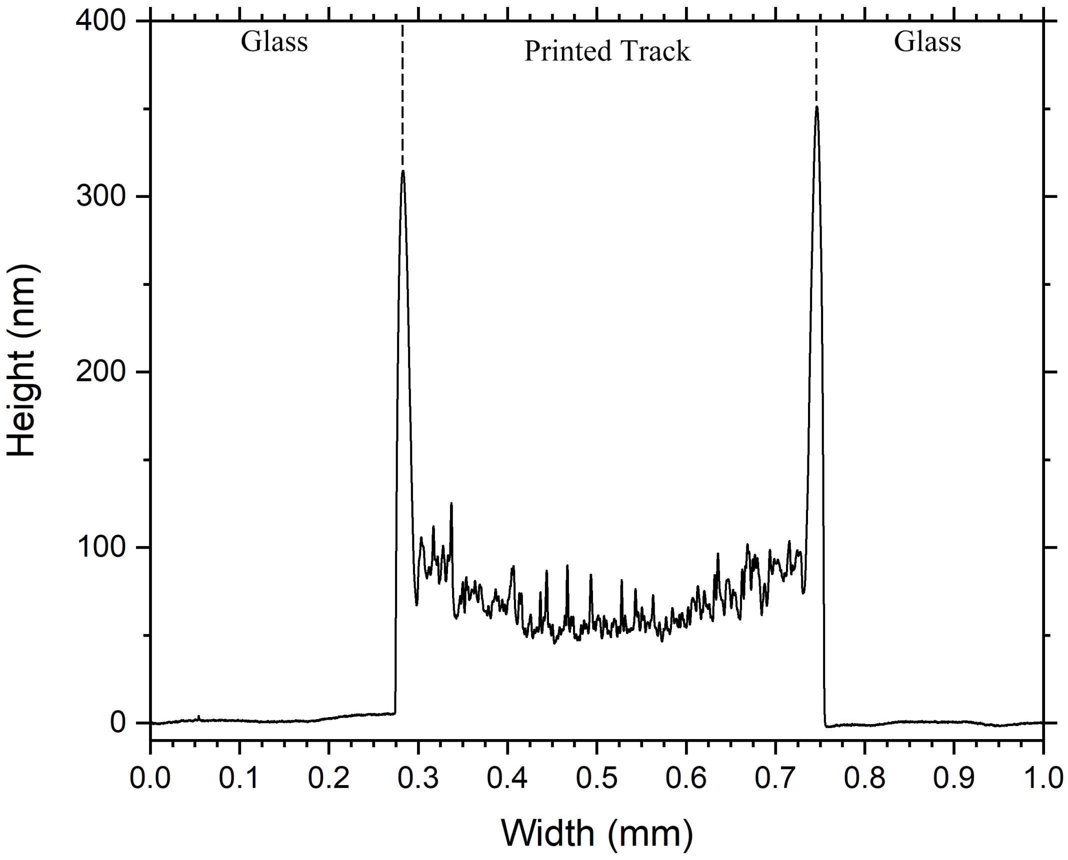

FIGURE 3.17: Surface profile taken across one of the ink-jet printed lines on a Borofloat 33 glass substrate using the Bruker Dektak XT stylus profilometer.

500µm wide and 40mm long, and each 50x50mm glass substrate contained 25 printed tracks.

To measure the thickness and width of each line, stylus profilometry using a Bruker Dektak XT was employed. The thickness and width of one of the ink-jet printed lines can be seen in figure 3.17.

As can be seen from figure 3.17, the tracks are non-uniform in thickness and have two spikes in thickness at the edge of the sample. This is known as the 'coffee ring effect' and is a result of capillary flow caused by varying evaporation rates across the printed track. [101, 102] The coffee ring effect makes

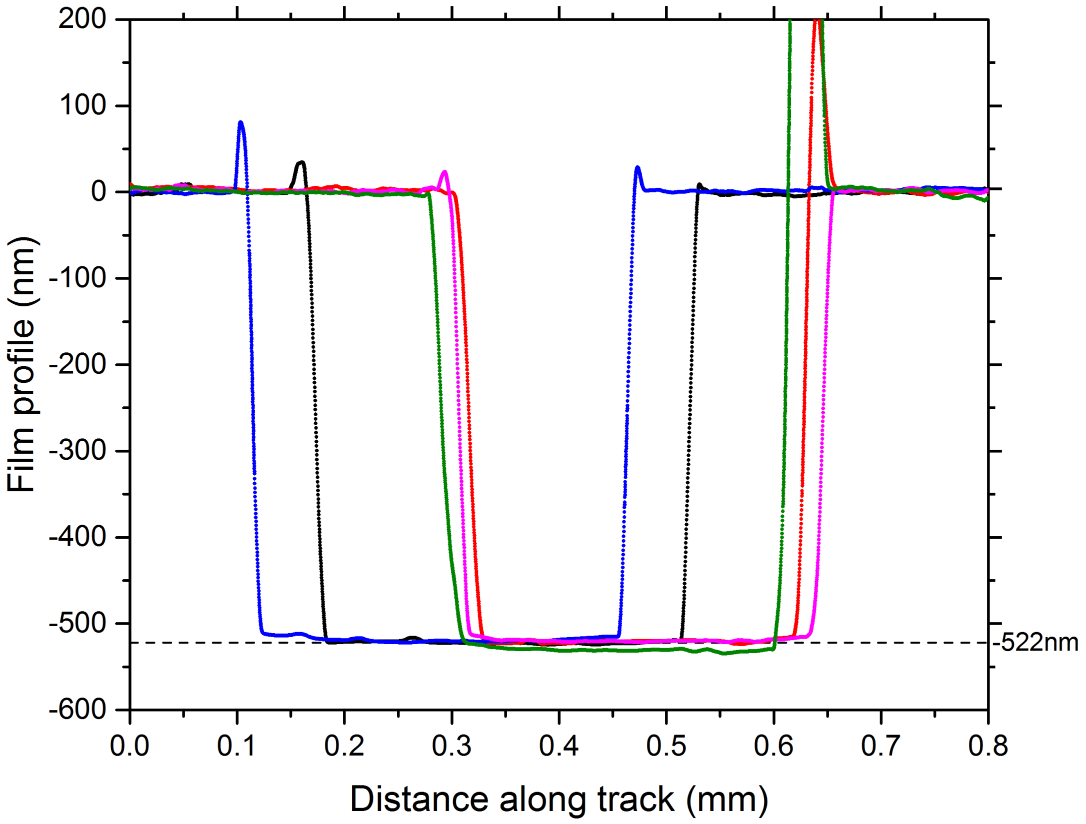

FIGURE 3.18: Surface profile of 5 different spin coated ITO films which were scratched using a pair of tweezers to generate a gap in the film which allowed the thickness to be measured.

the printed tracks very difficult to characterise because of their variable thickness across the width. Another problem with the printed tracks is the small width. To measure the transmission spectra of the tracks, it would be necessary to align the 500µm wide track to the spectrophotometer optical beam. This would have been very difficult to achieve perfectly every time, and so it was decided that the ink-jet printed tracks would not be the best choice for our experiments.

Spin coated samples were prepared on 50x50mm Borofloat 33 glass substrates, and measured approximately 520nm thick as shown in figure 3.18. The thickness was measured by scratching the ITO films with a pair of tweezers, and then using the Bruker Dektak to measure the profile of the scratch. Care was taken to not scratch the glass by using a pair of plastic tweezers for this purpose.

The thickness measured across different samples was consistent, as well as for different areas of the 50x50mm coatings (excluding the very edges). Having such a large area of continuous film made the spin coated samples suitable for many measurements including electrical, optical and surface morphology. As mentioned earlier, the electrical resistivity of our films before irradiation were of the order of $100\Omega\,\mathrm{cm}$ ($2\mathrm{M}\Omega/\mathrm{sq}$), although this value could vary from sample to sample. This was measured using an in-house 4-point probe measuring setup, details of the equipment and techniques are given in section 3.1.2.

To measure the optical transparency of the films, a ThermoScientific Evolution 220 spectrophotometer was used which has a wavelength range of 190nm to 1100nm. This covers the visible wavelength range required for characterising transparent conducing films. For the ultraviolet transmission measurements we used Spectrosil 2000 fused silica substrates in place of the Borofloat 33. Before irradiation, figure 3.19 shows the transparency of the films in the UV-VIS. A blank fused silica slide was used as a reference sample, so reflection losses and absorption from the substrate were accounted for. In order to measure the transmission further into the infrared, a Bruker IFS 66/S FTIR spectrometer was used. Using this source, the sample transmission in a wavelength range from 800nm to beyond 20μm could be measured. Borofloat substrates could be used up to 2.7μm wavelength since their transparency was in excess of the films, as can be seen in figure 3.20.

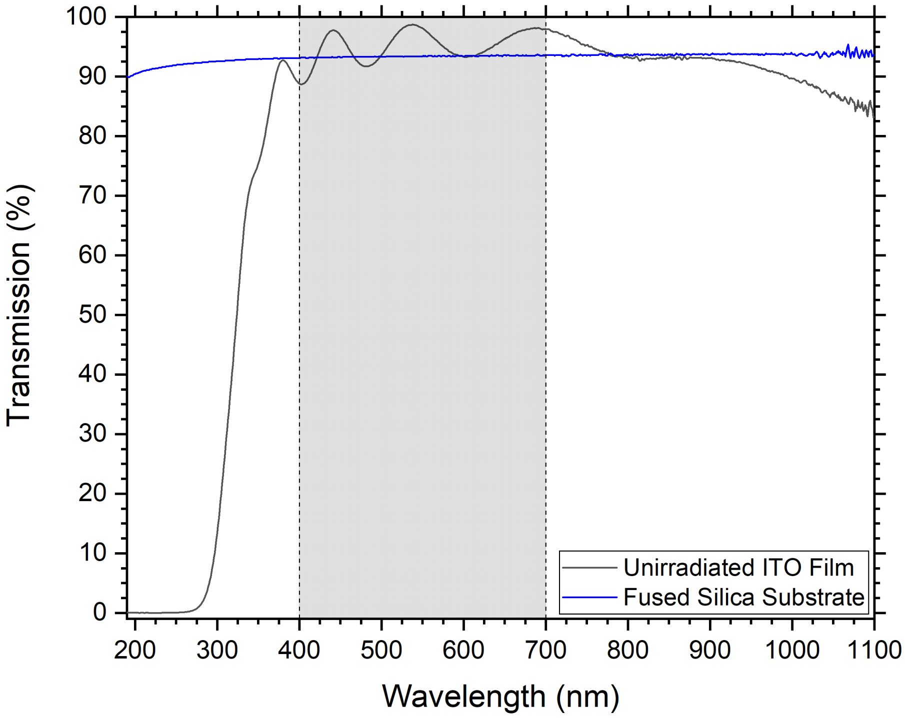

FIGURE 3.19: UV-VIS transmission spectra of the unirradiated ITO films. The sample had a fused silica substrate to allow measurement the UV transmission. The grey shaded area represents the visible spectrum. The oscillation of the transmission is attributed to thin film interference.

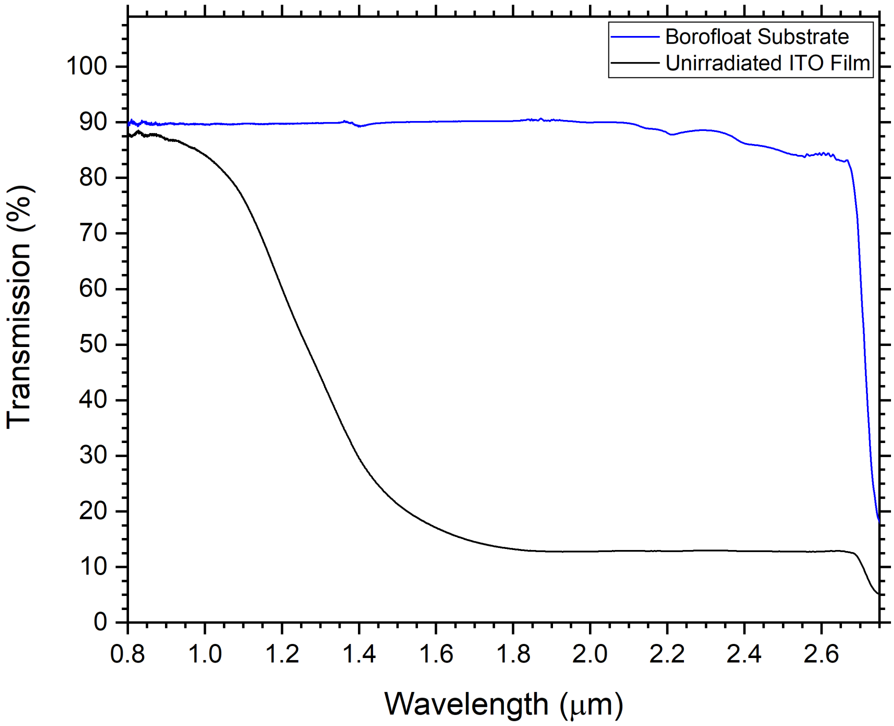

FIGURE 3.20: Infrared transmission spectra of the unirradiated ITO films. Borofloat substrates were used since they were transparent in this wavelength range.

From the transparency measurements in figures 3.19 and 3.20, a few properties of the ITO films can be determined. In the visible range of wavelengths, the ITO films remain greater than 90% transmissive for almost the entire range. Having greater than 90% visible transmission makes the films ideal for displays. The oscillation in transmission in the visible range is attributed to thin film interference, and can be used to measure the refractive index of the films using equation 3.9

$$n = \frac{\lambda_1 \lambda_2}{2d\Delta\lambda} \tag{3.9}$$

Where λ_1 and λ_2 are the wavelengths of 2 adjacent peaks of the interference pattern, d is the thickness of the films, and $\Delta\lambda$ is the difference between λ_1 and λ_2. Using the first two peaks in the visible part of the spectrum, $\lambda_1 = 441$nm and $\lambda_2 = 538$nm, the refractive index of the ITO films, n, is measured at ~ 2.4.

Their transparency also continues quite far into the near infrared, remaining greater than 50% to around 1.3µm wavelength. Being transparent in the near infrared does not benefit a display, but for photovoltaic devices, the infrared photons up to around 1.1µm can increase the efficiency of the device by contributing to the generation of charge carriers.

In the ultraviolet, the films start to absorb at wavelengths shorter than 350nm. From this absorption edge it is possible to create a Tauc plot to find the band gap of the material. [103] Although the Tauc plot gives the optical band gap, we are treating this as the same as the transport gap, within measurement uncertainty, as the exciton binding energy is of the order of 10's meV in comparison to several eV.

$$(\alpha \times h\nu)^{\frac{1}{n}} = A(h\nu - E_g) \tag{3.10}$$

In equation 3.10, α is the absorption coefficient, $h\nu$ is the photon energy, A is a constant of proportionality and E_g is the optical band gap. The constant n is dependant on the material being measured. For ITO, a semiconductor with direct allowed transitions, $n = \frac{1}{2}$. [63, 104, 105] Therefore, a plot of $(\alpha h\nu)^2$ as a function of $h\nu$ will be zero when $h\nu = E_g$, and the constant $''A''$ does not need to be known. The absorption coefficient as a function of wavelength was obtained from the optical transmission data via equation 3.11.

$$T(\lambda) = \frac{I_T(\lambda)}{I_0(\lambda)} = e^{-\alpha(\lambda)d} \tag{3.11}$$

Where T is the transmittance, I_0 is the incident irradiance, I_T is the transmitted irradiance and d is the sample thickness. Equation 3.11 can be arranged to find the absorption coefficient, α, as shown in equation 3.2. Finally, the connection between wavelength (in metres) and photon energy (in electronvolts) is simply given by equation 3.12.

$$eV = \frac{hc}{\lambda e} \tag{3.12}$$

Where h is Planck's constant, c is the speed of light, and e is the electron charge.

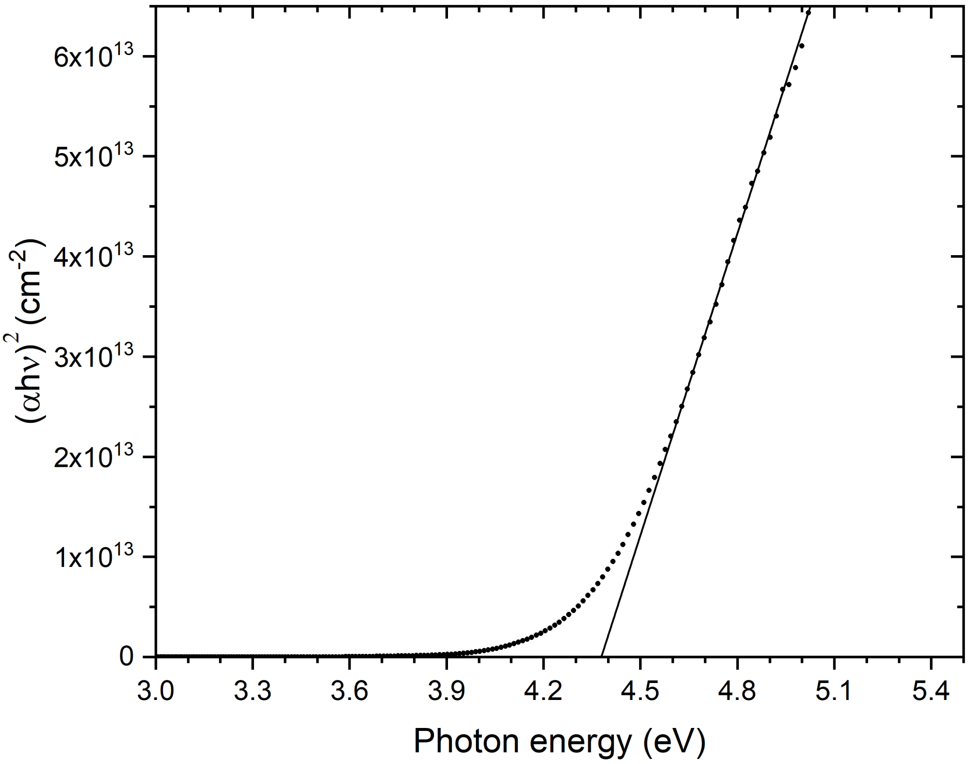

FIGURE 3.21: Tauc plot for unirradiated ITO films on Spectrosil2000 fused silica substrates.

Utilizing equations 3.10, 3.11 and 3.12, the transmission graph in figure 3.19 was transformed into the Tauc plot in figure 3.21.

The trend line for the linear portion of figure 3.21 was added by fitting a line of best fit for just the linear regime of the data, and this was used to find the intercept of the $y = 0$ line which tells us the value of E_g for the material. Whilst the data points in figure 3.21 contain a number of experimental uncertainties, the linearity of the data near the absorption edge is good, leading to a value of $E_g = (4.38 \pm 0.05)$eV. This is slightly higher than published data for the general band gap of ITO that gives E_g in the range 3.8-4.3eV. [106]

At the NIR end of the spectrum, we see that there is also a transmission edge lying between 1.2 and 1.4μm wavelength. This is known as the plasma edge, or the plasma frequency of the electrons in the ITO films. The plasma frequency of the electrons can be calculated by equation 3.13 [107–109]

$$\omega_p = \sqrt{\frac{n_e e^2}{m\varepsilon_0}}, [rad/s] \tag{3.13}$$

Here, n_e is the electron carrier density, e is the electron charge, m is the effective electron mass, and ε_0 is the permittivity of free space. The plasma frequency of the ITO films lies between 2.07×10^{14} and 2.85×10^{14}Hz (1.30×10^{15} and 1.78×10^{15}rad/s). By assuming that the effective electron mass can be approximated to the rest mass of an electron, we can estimate the charge carrier density, n_e, of the films. The unirradiated ITO films have an estimated charge carrier density of between 2.8×10^{16} and $5.2 \times 10^{16}\text{cm}^{-2}$. Typically, sputtered ITO films have charger carrier densities between 1×10^{16} and $6 \times 10^{16}\text{cm}^{-2}$. [110, 111] Hence, even though the spin coated ITO films have very poor overall electrical conductivity, the plasma edge indicates that the ITO nanoparticles have a charge carrier density comparable to commercially sputtered ITO films. From equation 3.8, the electrical conductivity is proportional to the charge carrier density, η_e, and the charge carrier mobility, μ_e. We must conclude that because our ITO films have a charge carrier density that is comparable to commercial ITO, that the charge carrier mobility of our ITO films is significantly lower.

Most of the laser irradiation of ITO was conducted on films deposited on Schott Borofloat 33 substrates, since borosilicate glass is more resilient to heat damage as well as being transparent into the near ultraviolet. The ITO films were also produced on flexible polyethylene terephthalate (PET) substrates. Laser irradiation of ITO films on PET substrate without causing damages was expected to be more difficult, since PET has a melting point much lower than borosilicate glass. PET also does not transmit light shorter than 300nm wavelength. [112] This makes transmission spectra of the ITO difficult to take, since the PET starts to absorb light whilst the films are still transparent. Hence, all of the optical transmission data were taken on the glass substrates. The ITO ink that was deposited onto the PET substrates is exactly the same as the one used on the glass substrates, but instead of using spin coating, the films are deposited via a gravure printing technique. The ITO ink developed by INM for use in this project had already been gravure printed onto PET substrates by Puetz *et al.*. [113] The as-deposited ITO on PET had the same resistivity before irradiation as when the glass substrates were used, typically exceeding $100\Omega\,\mathrm{cm}$. The films were 400nm thick as measured with the Bruker Dektak XT.

Chapter 4

Laser Systems

4.1 Laser Systems

In this section, the laser systems used throughout this thesis to irradiate the ITO films are characterised and the beam delivery systems are described. Photochemical processes were investigated using ultraviolet lasers. Infrared systems allowed exploration of laser-induced photothermal effects. Therefore, in the following sections , the lasers are grouped by their spectral characteristics.

4.1.1 Ultraviolet Laser Systems

4.1.1.1 Xenon Chloride Laser

The Lumonics Excimer-500 laser was used is a multigas laser and can operate with several different excimer mixtures. Here it was filled with helium, hydrogen chloride and xenon to generate the XeCl* exciplex. The XeCl laser outputs light in the ultraviolet at a wavelength of 308nm. This laser is a pulsed system,

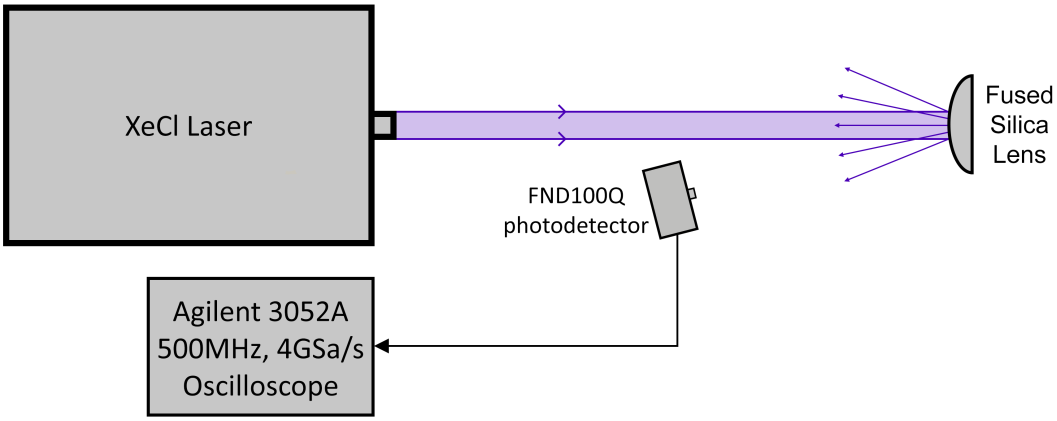

FIGURE 4.1: Experimental setup used for measuring the XeCl laser pulse length. The detector, coaxial cable, and oscilloscope were all matched at 50Ω.

being able to operate at a maximum repetition rate of 50Hz. The pulse length was measured by a FND100Q photodetector with a 90V bias applied. [114] The FND100Q photodetector has a bandwidth of 350MHz leading to a rise time of around 1ns when coupled into a matched 50Ω load. With the quartz window on the front of the detector, it has a spectral response between 200nm and 1150nm making it ideal for the XeCl laser pulse.

Figure 4.1 shows the experimental setup used to measure the XeCl laser pulse. The laser pulse was incident onto a plano-convex quartz lens, and the 4% reflection from the curved face was used to generate a heavily attenuated beam to measure the pulse length. The FND100Q photodetector was placed in the diverging beam at a distance to ensure that it was not saturated. Using an Agilent 3052A 500MHz oscilloscope terminated with 50Ω impedance gave a system rise time of around 1ns. The measured pulse was averaged 10 times, and as shown in figure 4.2, has a FWHM of 4.1ns. The pulse contains a tail which extends to beyond 10ns, but has approximately a third of the intensity of the main pulse.

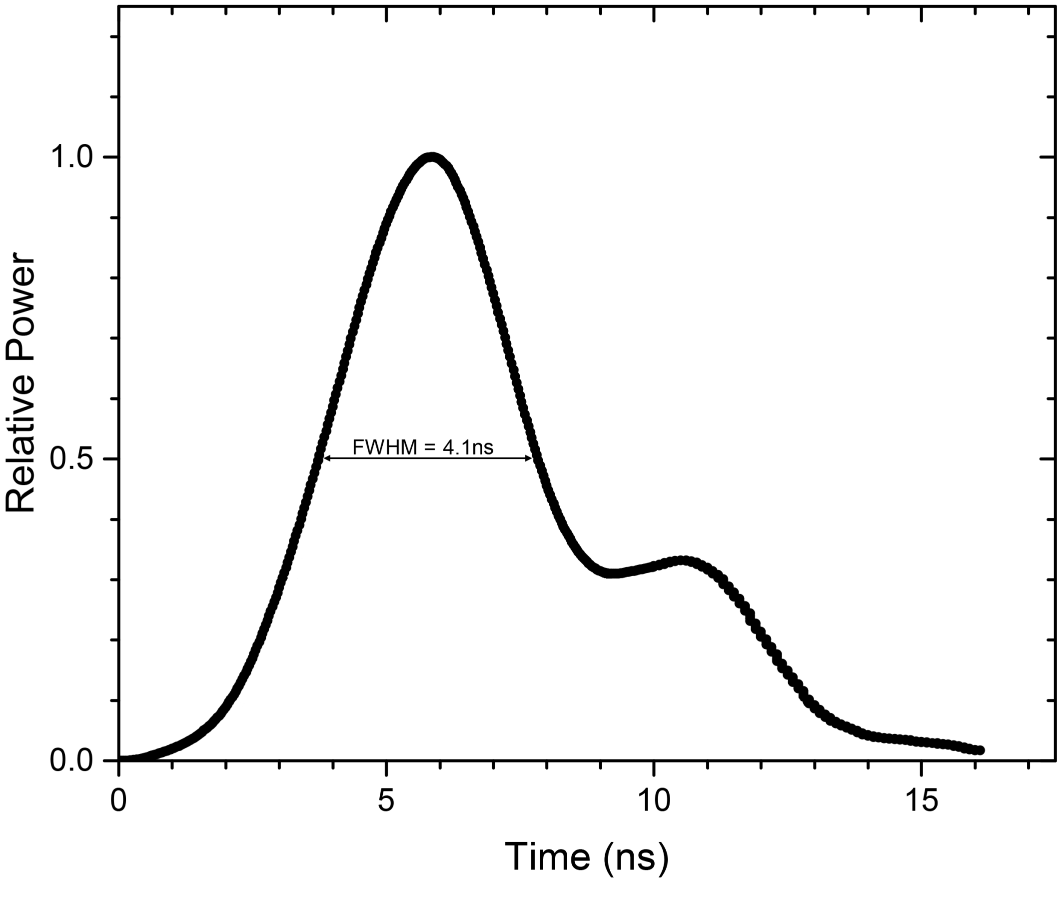

FIGURE 4.2: Measured pulse length of the XeCl laser using the FND100Q photodetector, 90V reverse bias, and 50Ω termination Together with the 500MHz oscilloscope bandwidth, this gave a system rise time of roughly 1ns.

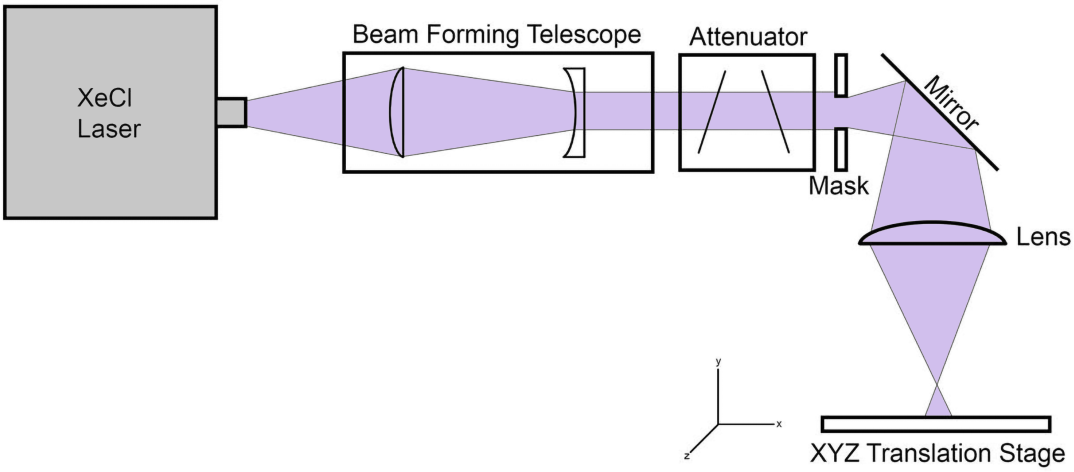

FIGURE 4.3: Optical setup used with the XeCl laser for irradiation of the ITO films. The beam forming telescope has cylindrical optics to transform the rectangular laser output into a square profile at the mask.

The transverse irradiance profile of the XeCl laser system was highly multimode, having a 2×1cm cross-section. Because of the large area rectangular beam, an imaging system as used with a square aperture mask to irradiate the ITO films. The optical setup used for irradiation with the XeCl laser is shown in figure 4.3.

The beam forming telescope (Fig. 4.3) consisted of two cylindrical lenses (one convex and one concave) and a 2x2 lenslet array to transform the rectangular beam into a square one at the mask. This made more efficient use of the energy and ensured a flat irradiance profile at the target located in the image plane. The attenuator in the optical setup comprised of two quartz plates, one of which has an angle dependent reflective coating. Changing the angle of the first plate increases the reflection losses, and the second plate corrects for the beam path deviation. Typically, a 2× or 3× demagnification imaging system was used after the attenuator, depending on what fluence was required

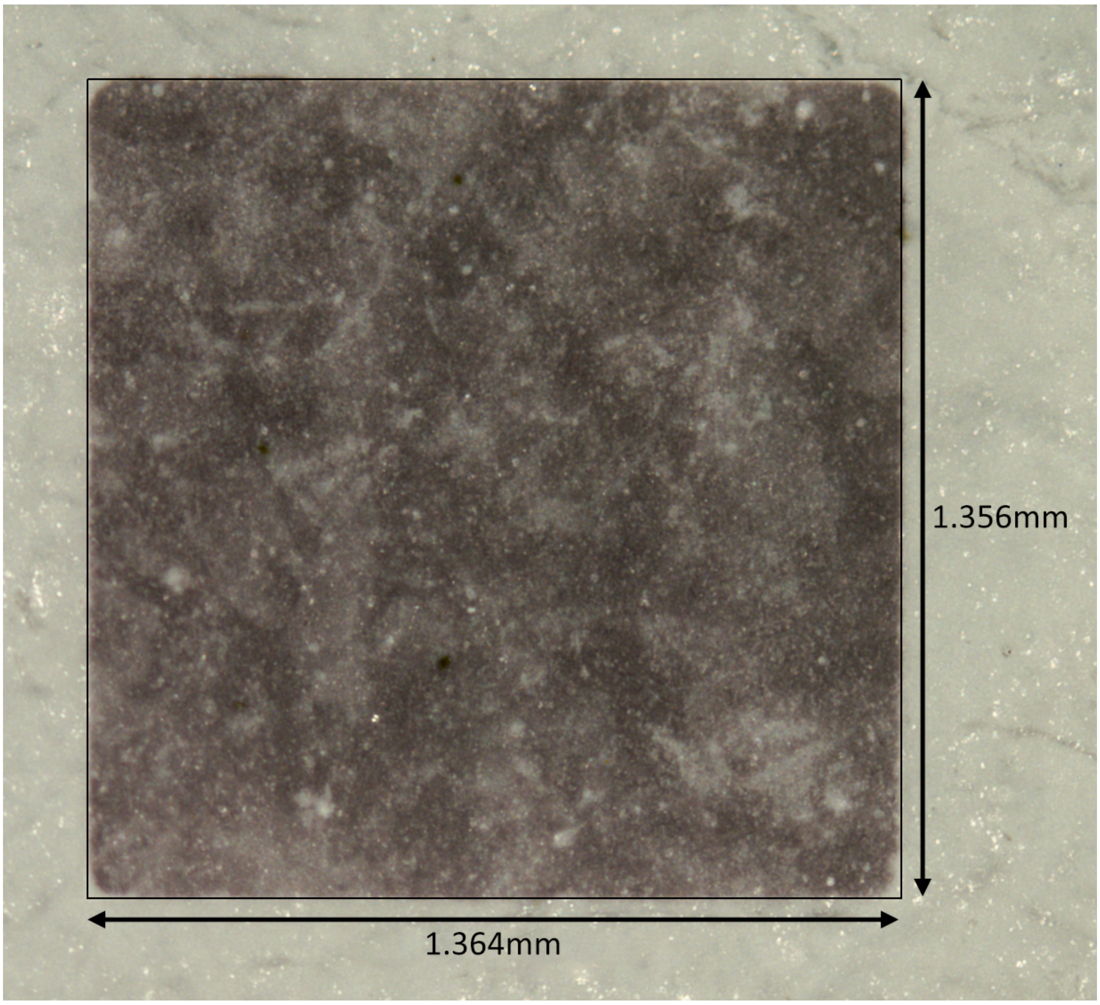

FIGURE 4.4: Projected image from a 2.75mm square mask onto a piece of thermal paper with a 2× demagnification.

at the sample. Figure 3.11 shows an example of the final projected image into thermal paper.

4.1.1.2 Argon Fluoride Laser

The argon fluoride (ArF) laser used was a Lambda-Physik LPF202, emitting light in the ultraviolet at 193nm. The ArF laser has the highest photon energy of the ultraviolet lasers used here at 6.42eV. As with the XeCl excimer laser, this is a pulsed system with nanosecond pulse lengths. The same technique

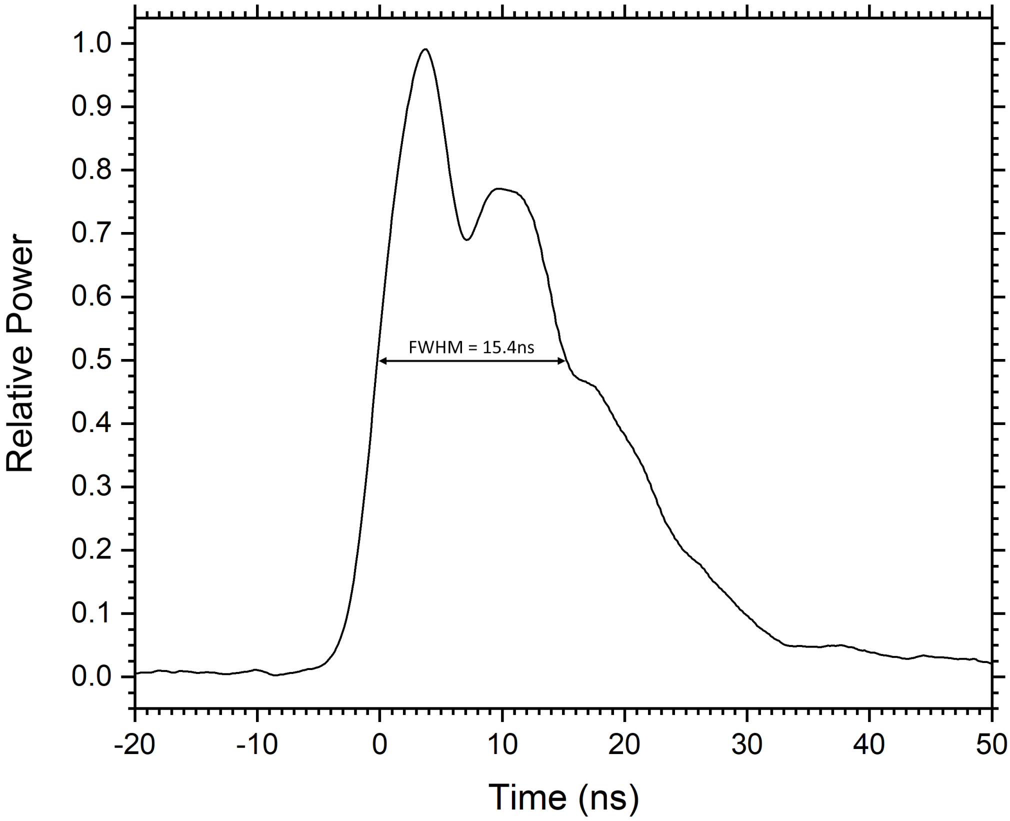

FIGURE 4.5: Pulse length of the ArF laser as measured with the FND100Q photodetector. The detector, coaxial cable, and oscilloscope were all matched at 50Ω.

and setup was used for the pulse length measurement, where the reflection from the front of a fused silica lens were measured with the FND100Q photodetector. The pulse length was measured to have a FWHM of 15.4ns, and can be seen in figure 4.5.

The transverse irradiance profile emitted from the ArF laser is very similar to the XeCl beam, in that it is a highly multimode rectangular beam of around 2×1cm size. The optical setup was different however, Here, a contact mask was used that was flood illuminated. This simplified the arrangement as it was found that increasing the fluence via demagnification was unnecessary. The setup is shown in figure 4.6.

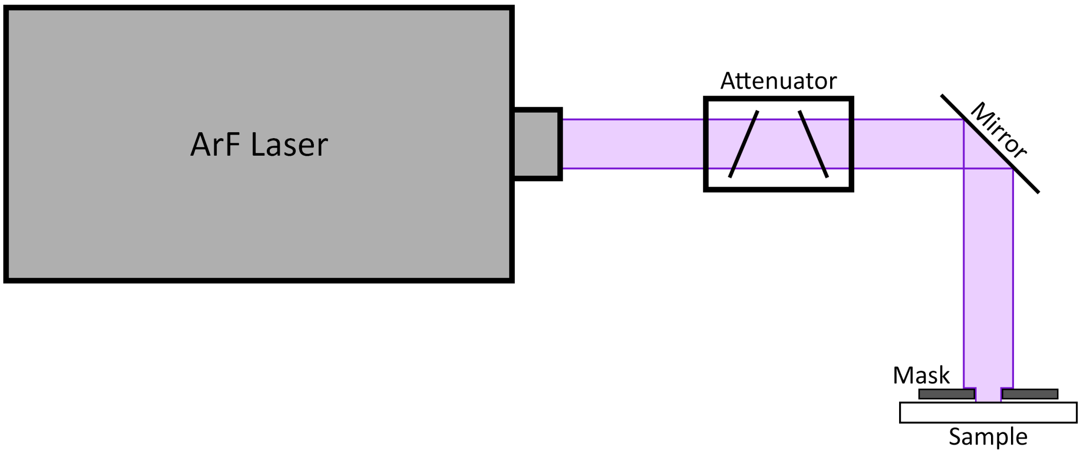

FIGURE 4.6: Optical setup used to irradiate ITO samples with the ArF laser. A direct contact illumination mask was used to define the irradiated area.

4.1.1.3 Helium Cadmium Laser

The helium cadmium (HeCd) laser used was an IK3552R-G from Kimmon Koha Co. Ltd. This laser source is of the continuous wave type and emits at only 325nm, since the 442nm laser line is internally inhibited. The output beam is circular and highly multi-mode with a diameter of around 1.5mm as it exits the laser. The output power of the laser was measured to be around 46mW at the sample after all the optical elements. The power was measured with a ThorLabs PM100D power meter, with a ThorLabs S350C sensor attached capable of measuring the power at 325nm wavelength.

With the laser having a small circular beam, the optical setup comprised of a simple lens and mirror, as seen in figure 4.7. The irradiance of the beam was controlled by raising or lowering the translational stage, which changed the size of the laser spot on the film. Typically, the spot was chosen to be 1mm diameter so that it fit inside the 1mm isolated tracks that are discussed later in

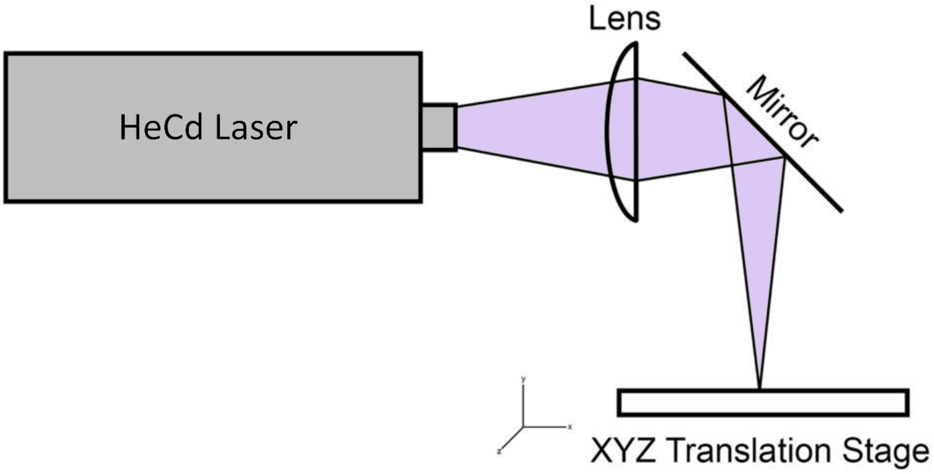

FIGURE 4.7: Optical setup used with the HeCd laser. A front surface mirror with a UV enhanced aluminium coating was used. The plano-convex focussing lens was fused silica.

section 4.1.3.1.

4.1.2 CO_2 Laser Systems

For the infrared irradiation of the ITO films, three types of CO_2 laser were used: a radio-frequency excited CO_2 laser (RF:CO_2), a transversely excited atmospheric pressure CO_2 laser (TEA:CO_2) and an Q-switched RF:CO_2 laser (QSW:CO_2). All three of the CO_2 lasers operated at the same wavelength of 10.6µm, but delivered the laser energy in different ways.

4.1.2.1 RF:CO_2 Lasers

For both the RF:CO_2 and the QSW:CO_2 lasers, the basic operation principle was the same. They both have narror gas discharges excited by a radio-frequency AC power supply. The output of the RF supply could be modulated with a

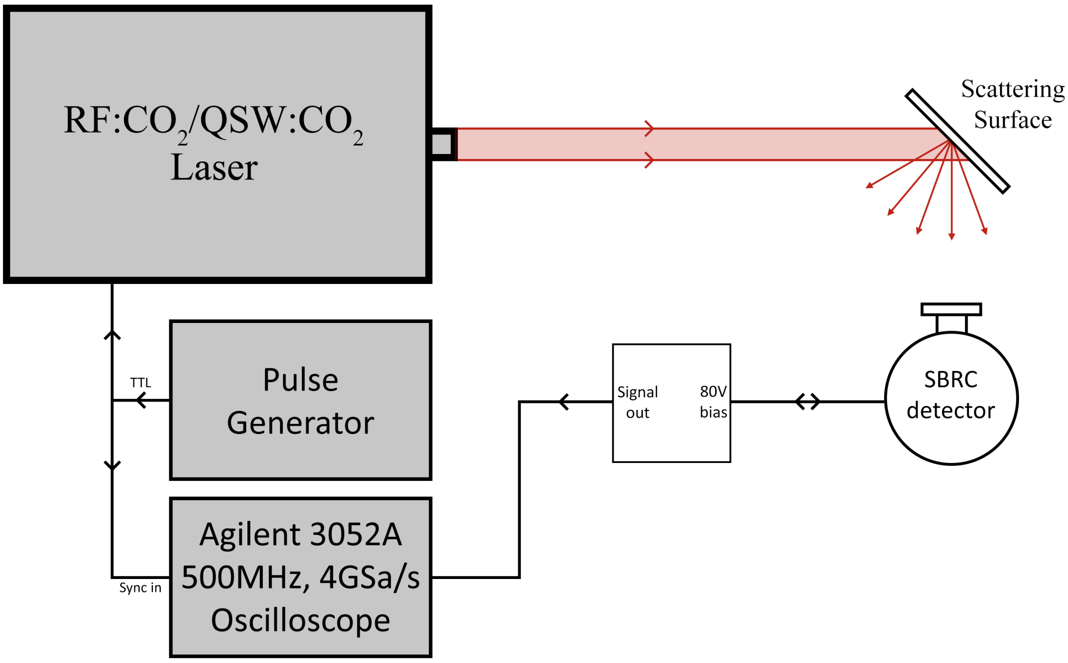

FIGURE 4.8: Optical setup used to measure the RF:CO_2 and QSW:CO_2 laser pulses. The scattering surface used was a brushed copper plate for the QSW:CO_2 laser and steel wool for the RF:CO_2 laser.

TTL signal. The only difference was the addition of an acousto-optic modulator (AOM) just before the output coupler on the QSW:CO_2 laser. The AOM enabled very fast switching of the laser cavity loss (Q-factor) between a high and low state, generating sub-microsecond pulses from the laser. To measure the pulse lengths from these two lasers, a Santa Barbara Research Corporation (SBRC) gold doped germanium detector was used. The SBRC detector had to be cryogenically cooled with liquid nitrogen, and the 80v reverse bias was only applied once at approximately 77K as indicated by a very low boil off rate from the cryostat. The experimental setup is shown in figure 4.8.

To measure the pulse of the RF CO_2 laser, the pulse generator was set to generate a 100µs pulse every second, as this was the shortest pulse the laser could output on demand reliably at this low repetition rate. The SBRC detector was

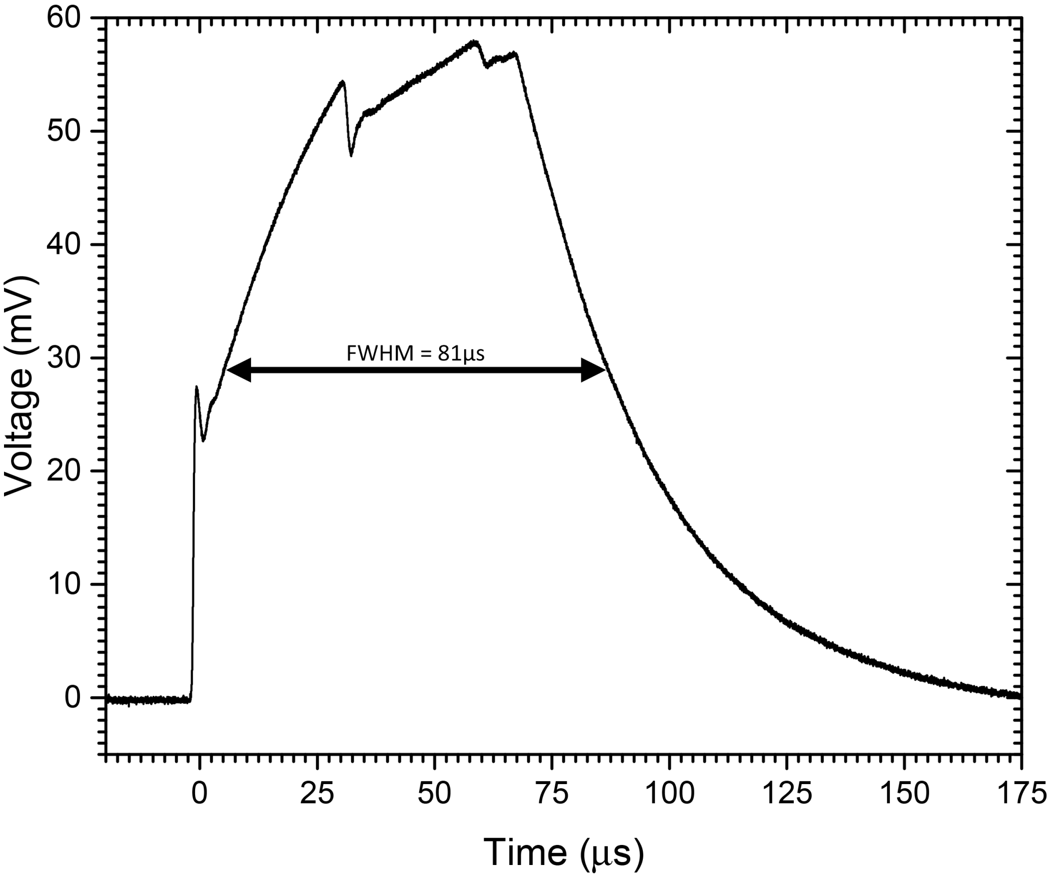

FIGURE 4.9: RF:CO_2 pulse measured with the SBRC detector. The laser was modulated at 1Hz with 100μs pulses via TTL from the pulse generator.

terminated at the oscilloscope with a 5kΩ resistor. This value was chosen as a compromise between the magnitude of the signal and the rise time of the system. The bandwidth of the system was estimated to still be around 100ns but of the order of 100 times the increase in voltage generation. When the RF supply was modulated with a pulse of 100μs, the FWHM of the optical pulse was ≈81μs (fig. 4.9). As seen from figure 4.9, the pulse does contain a tail that extends the pulse by more than 60μs beyond the FWHM level.

For the QSW:CO_2 laser the AOM frequency sets the repetition rate of the output pulses within the TTL pulse from the trigger pulse generator. For example, if the trigger pulse generator was set to 1Hz with 1ms pulses, and the AOM was set to 50kHz, the AOM would output 50 pulses within the 1ms window, every second. It was noted that for optimal laser operation the AOM should be set to 50kHz and so the frequency throughout the experiments used this AOM frequency. The pulse measurement from the QSW:CO_2 laser is shown in figure 4.10. From figure 4.10, the pulses from the laser can be seen to grow in energy until around 130µs, then halve in intensity. The pulses then remain at this lower energy until the TTL signal ends, when the pulses increase to the original energy before decaying back to nothing. It should be noted, for the pulse measurements made on the QSW:CO_2 laser, the termination at the oscilloscope was switched to 50Ω for the ability to resolve the shorter pulse widths.

In order to explore the behaviour seen in figure 4.10, the individual pulses were examined over shorter timescales. Figure 4.11 shows 3 examples of pulses at various times along the pulse train. Looking at figure 4.11 explains why the reduction in pulse energy seen in figure 4.10 was occurring. The highest energy pulse, often the one just before the pulse energy reduction, has a FWHM of 120ns and is a singular pulse. The following pulse after that, which appeared to have half the energy, was in fact two individual pulses located very close together in time. Both of the double pulses had increased pulse lengths, reducing their peak power. However, it was found that later in the pulse train, the pulses returned to being singular. This can be seen to occur at around 700µs and stays this way until the pulse train stops, and another one begins from the next TTL signal.

Both the RF:CO_2 and the QSW:CO_2 lasers had Gaussian beam profiles, and the

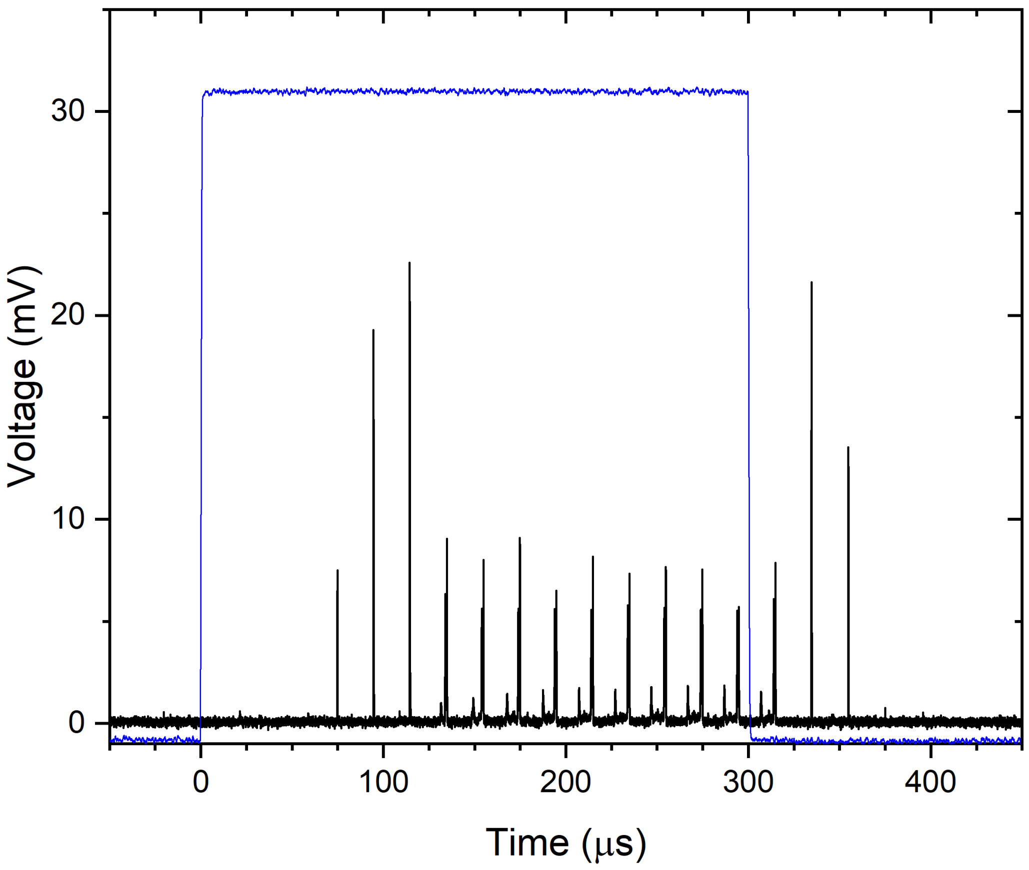

FIGURE 4.10: Pulse train from the QSW:CO_2 laser when a 300μs burst of pulses is requested from the laser. The blue line shows the trigger pulse of 300μs duration and the black line is the optical output.

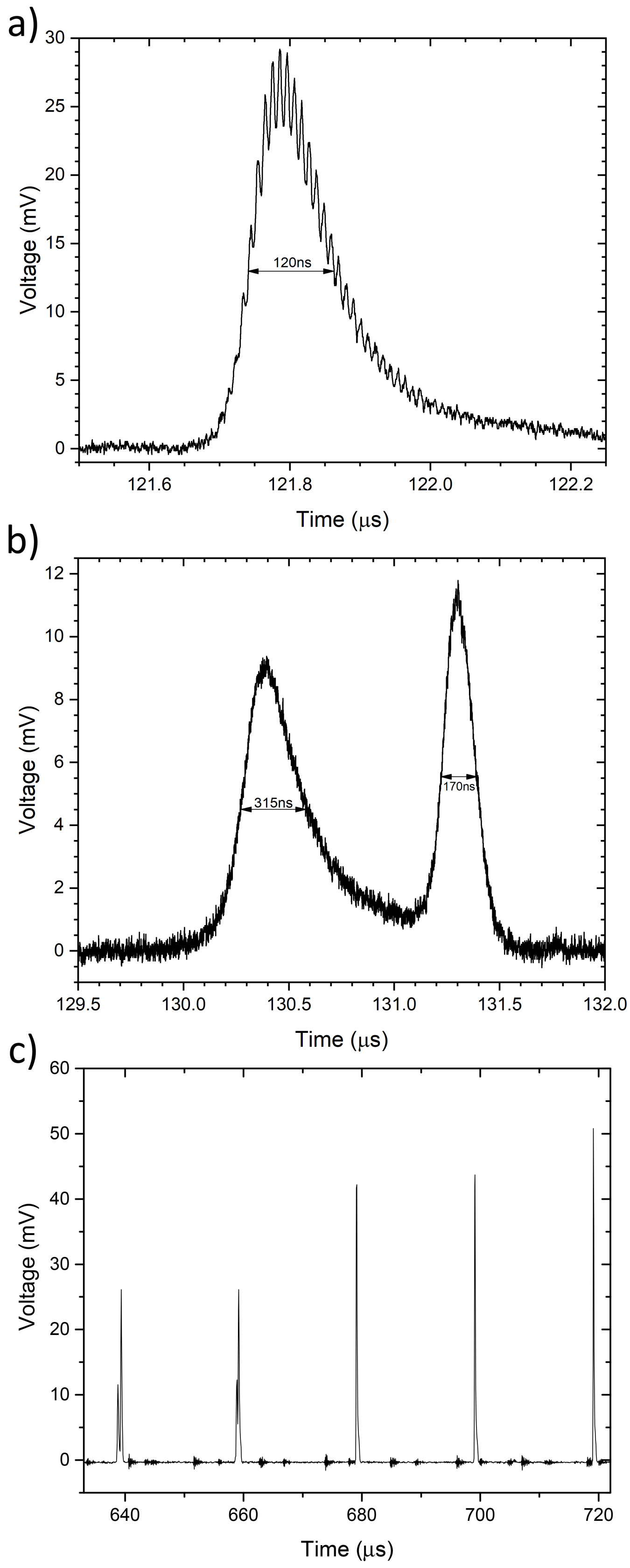

FIGURE 4.11: QSW:CO$_2$ laser pulses at various times along the pulse train. **a)** The pulse with highest energy. **b)** The first pulse that separates into a double pulse. **c)** At around 700μs into the pulse train where the pulses return into single pulse operation.

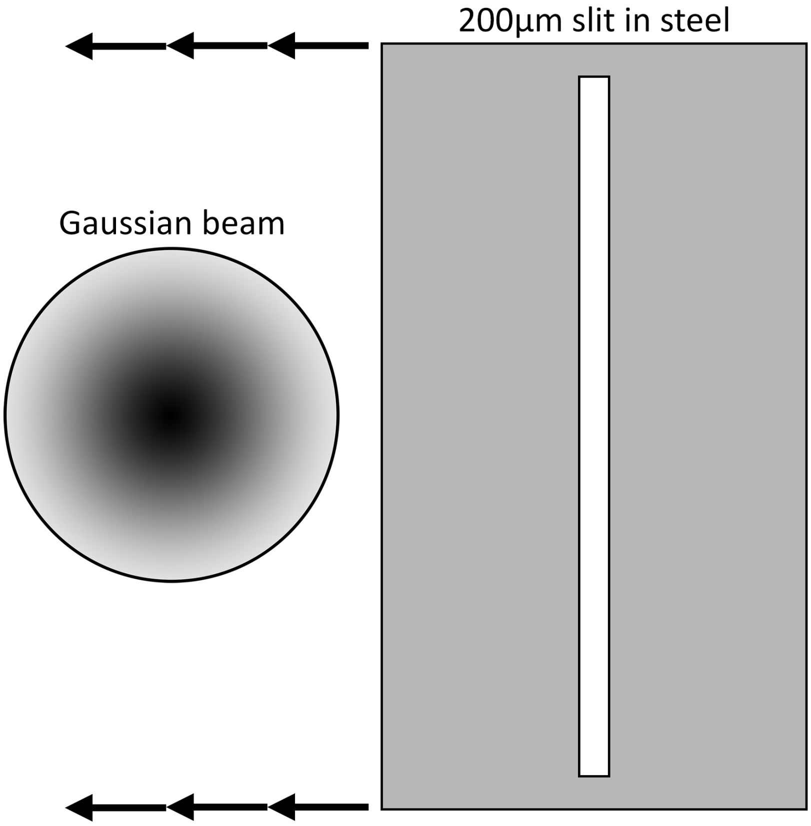

FIGURE 4.12: Scanning aperture setup used to measure the beam profile of the RF:CO_2 laser.

optical setup selected was the same as for the HeCd laser (fig. 4.7). The only differences were the materials used for the lens and mirror, which were zinc selenide and gold coated brass respectively. The beam profile of the RF:CO_2 laser was measured using a scanning aperture technique, with a 200µm wide slit. Care was taken to make sure the metal holding the slit was much larger than the beam, so that no beam could be incident on the detector unless going through the slit. Also, the slit was made much taller than the beam diameter to ensure that it was not clipped in the axis of the slit. Figure 4.12 shows the setup, and figure 4.13 shows the measured beam diameter.

The transverse beam profile of the QSW:CO_2 laser had unwanted features arising from the AOM in the laser cavity. In order to clean the beam shape up, a

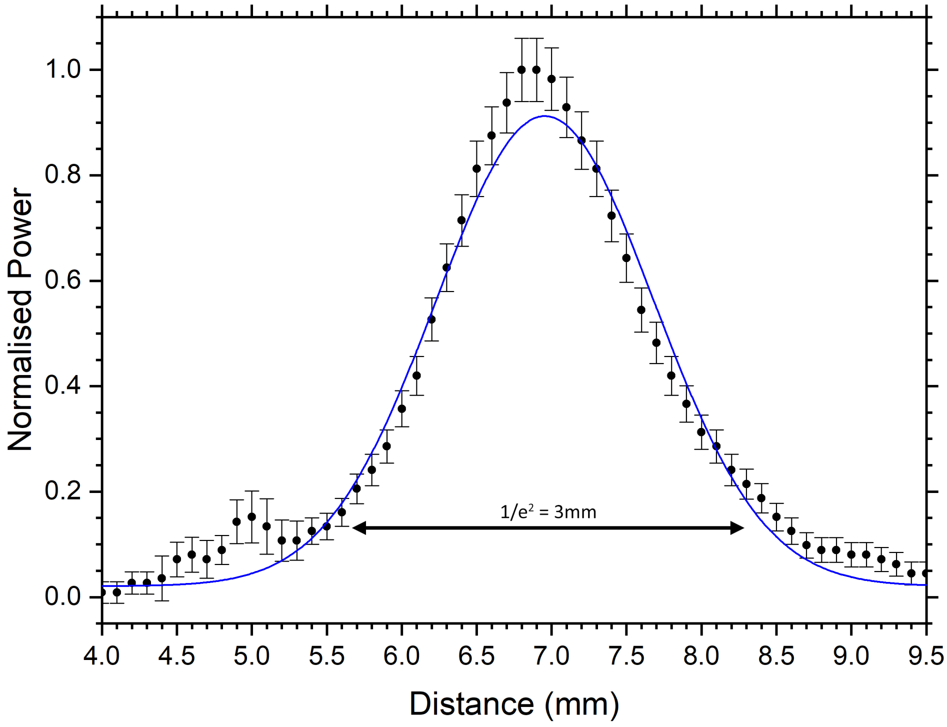

FIGURE 4.13: Data taken from the scanning aperture beam profile technique. The blue line is a Gaussian profile that has been fitted to the data giving a $1/e^2$ beam diameter of 3mm.

6mm diameter steel aperture was placed before the lens to block the unwanted parts. The spot sizes of the RF:CO_2 and QSW:CO_2 lasers were made to be as small as possible, with the use of a lens, without damaging the films and/or substrates.

4.1.2.2 TEA:CO_2 Laser

The third type of CO_2 laser used, the TEA:CO_2 laser, operates in a similar way to the ultraviolet excimer lasers. It is a pulsed laser system with low repetition rates (maximum of 20Hz). The laser pulses from the TEA CO_2 laser have two parts. The initial gain switched pulse is around 100ns in length and contains roughly 50% of the total pulse energy, this is then followed by a tail at much less intensity that extends to beyond 1µs containing the remaining 50% of the pulse energy. [115, 116] The TEA laser pulse energy was measured using a pyroelectric joule meter placed in the beam where it had diverged sufficiently such that the fluence did not damage the device. The pulse energy from the TEA laser was measured to be 2.5J, contained in a beam that was highly multimode in a 2x2cm square. With the laser beam being highly multimode and large in area, irradiation of the films was carried out in the same way as the ArF laser setup 4.6. The use of a contact mask was mainly due to the lack of a translational stage, however, the use of an imaging system that has an intermediate focal point with this laser was also made difficult by the large pulse energy which could ionize the air when focused into smaller areas.

4.1.3 Ultrafast Laser Systems

4.1.3.1 Titanium Sapphire Laser

The titanium sapphire (Ti:Sapphire) laser used was a Spectra-Physics Hurricane. Being a regeneratively amplified mode locked laser system, the laser was able to output a maximum repetition rate of 1kHz with each pulse containing 750µJ of energy. The optical bandwidth of the Hurricane laser allows pulse lengths down to 100fs to be generated. The laser comes equipped with a variable path length compensator on the stretcher/compressor module inside the cavity and by adjusting this the pulse length can be made as short as possible.However, dispersion in the system means a transform limited pulse

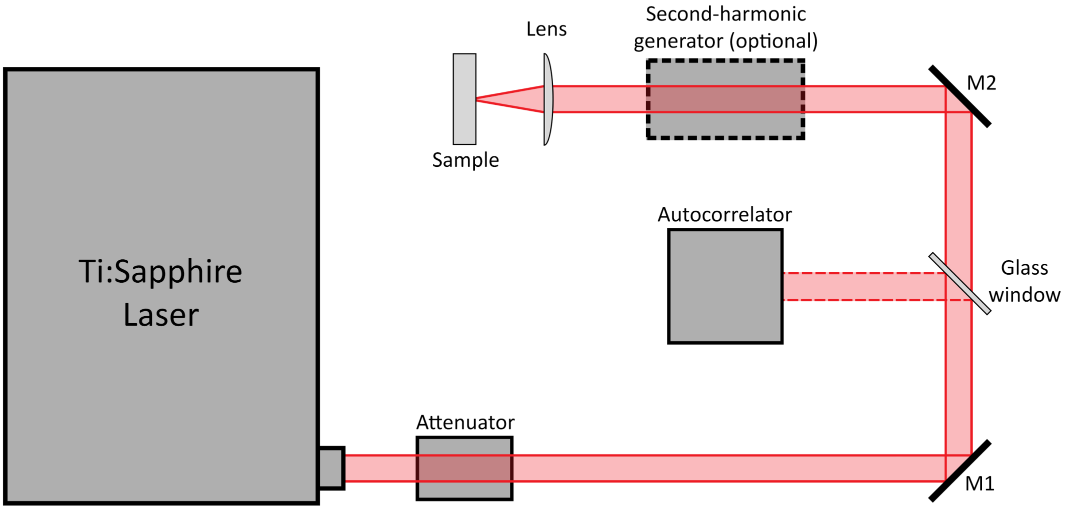

FIGURE 4.14: Optical setup used for the Ti:Sapphire laser. The glass window was mounted on a flip down optic holder, and switched between passing the beam to the sample or the autocorrelator for pulse length measurements.

is difficult to achieve and, in general, it was found to be longer than 100fs. The optical setup used for the Ti:Sapphire laser is shown in figure 4.14.

To measure the pulse length of femtosecond length pulses, an autocorrelator needed to be used. As shown in figure 4.14, a flip down glass window could be used to direct the beam into the autocorrelator for easy maintenance of the pulse length. The regeneratively amplified laser pulses have very high peak power and can damage optical components very easily, so a glass window was used to reflect only a small amount of the pulse into the sensitive autocorrelator. Adjusting the compressor module inside the laser cavity gave us a shortest reading of around 170fs on the autocorrelator. This is the autocorrelation function, and is $\sqrt{2}$ times larger than the actual pulse length when a Gaussian temporal shape is assumed. [117] This means that the shortest pulse obtained from by the laser was 120fs.

The primary use of the laser was to ablate and electrically isolate smaller areas

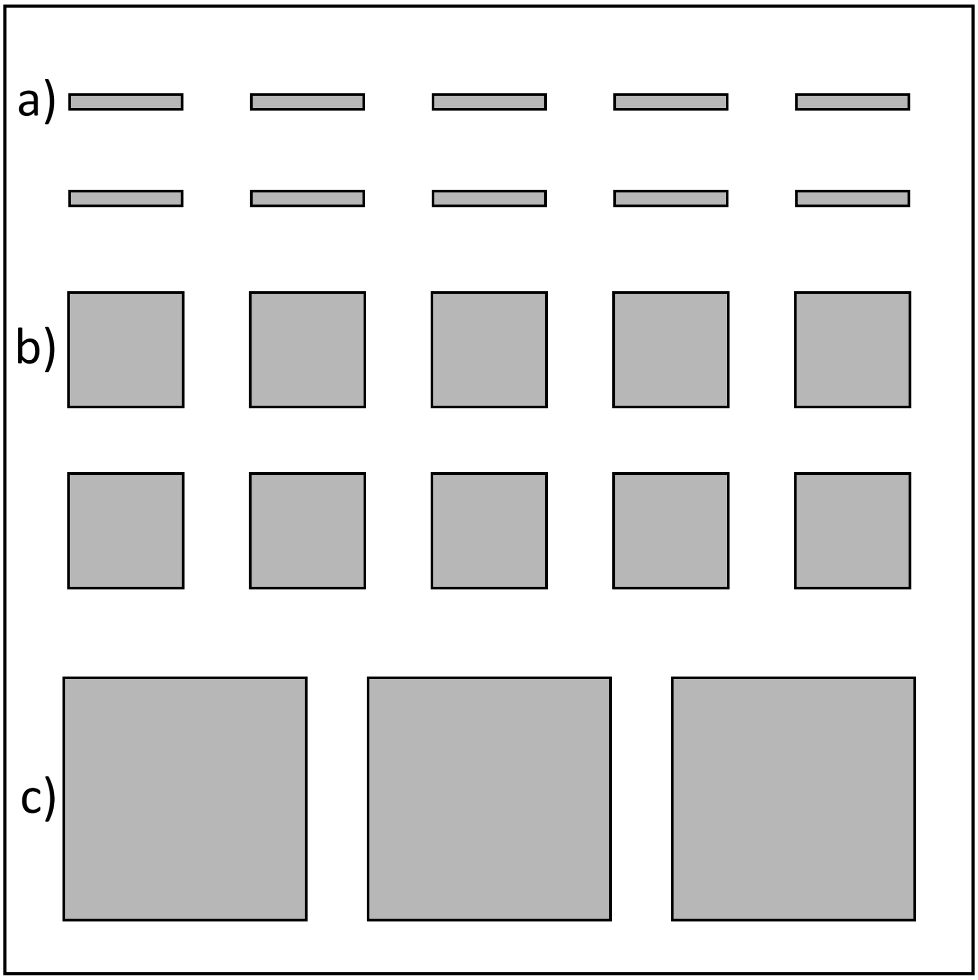

FIGURE 4.15: Electrically isolated areas laser ablated into the ITO films on 50x50mm substrates. **a)** 6x1mm areas, **b)** 6x6mm areas and **c)** 12x12mm areas

into the large 50x50mm square samples. For the isolation of smaller areas, the laser was focussed into a small spot, and then the attenuator was used to reduce the average power until there was a plasma just forming at the focal point in air. This meant that when the ITO films were placed at this focal point, the ITO could be ablated, to generate gaps in the film where current could not conduct through. Figure 4.15 shows the different ablated patterns used and figure 4.16 shows the surface profile across the ablated edge.

Following isolating the areas, they were irradiated either in the UV ir IR to change their electrical properties. The area was enclosed by the isolating etch

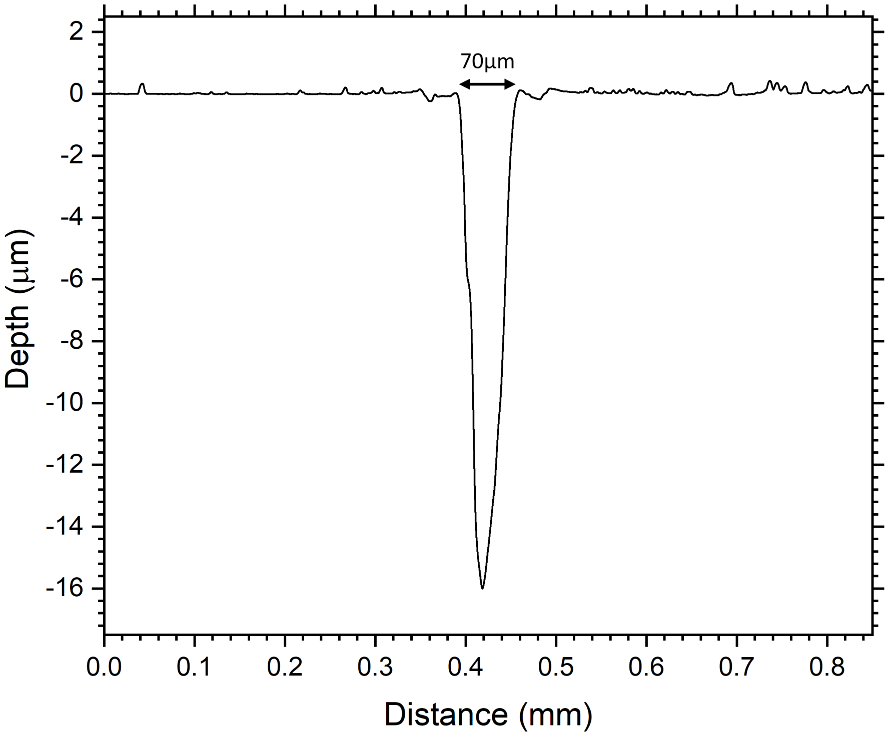

FIGURE 4.16: Dektak surface profile across a laser ablated line in the ITO film on a glass substrate. A depth of 16µm could be reached, ablating into the glass, with a 70µm width, successfully electrically isolating the film.

so that the electrical test current was confined to a known part of the film whilst the ablated "frame" also made it possible to visually locate where the laser irradiation took place. The latter is important since the films are transparent in the visible range and do not change after irradiation making it difficult to locate the irradiated area without visual cues. Depending on what was being measured before and after irradiation, different sized isolated areas were used. The first areas at 6x1mm were used when only measuring the electrical properties. The area was small which made irradiation times fast and the width of 1mm was sufficient for the 4-point probe to be easily placed within the area. Optical measurements could not be taken with such a small area, and so the 6x6mm size was used for optical measurements. However, containing 6 times the area proportionally increased the irradiation times. The

12x12mm areas were solely used for the Hall voltage measurements, as they were designed to fit the Van der Pauw probe spacings of 12mm.

4.1.3.2 Ytterbium:YAG Laser

The Ytterbium:YAG (Yb:YAG) laser was a Rofin-Sinar USP-100. Operating at a maximum repetition rate of 10MHz and outputting a maximum average power of 120W with pulse durations of the order of 1ps. This laser could be operated in gated mode or pulse on demand. In the former case, optical output follows the internal frequency of the laser for the duration of the TTL signal sent to the laser. For example, a 100µs TTL signal would contain 1000 laser pulses if the internal frequency was set to 10MHz. In the latter case, the laser would output a single pulse for each TTL rising edge. It is important to note that the internal frequency of the laser cavity affected the energy contained in each pulse. It would be expected that setting the laser to 10MHz would have 10x the average power when compared with the frequency set at 1MHz, however this is not the case. As seen from figure 4.17, the average power at 1MHz is roughly the same when compared with 10MHz, i.e. the energy contained per pulse has increased by 10 times at the lower frequency.

The optical arrangement that was used is shown in figure 4.18. The use of an optical isolator was necessary to avoid any unwanted reflections going back into the laser cavity. A rotating half wave plate and a polariser were used as a continuously variable attenuator. The beam expander was added to increase the 3mm beam diameter to 10mm so that the irradiance on the galvo mirrors

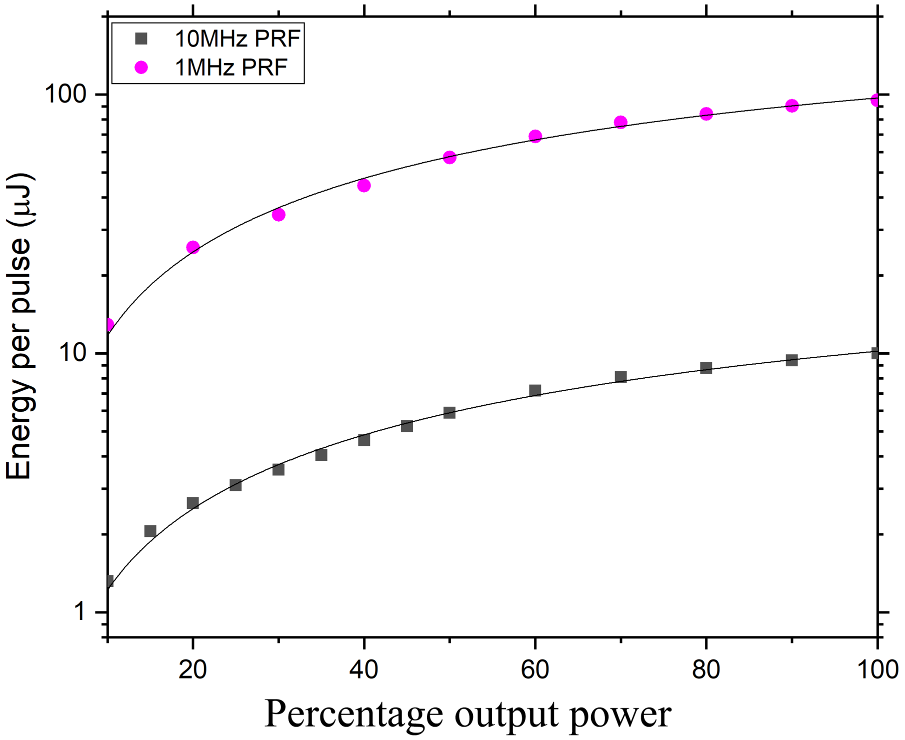

FIGURE 4.17: Energy contained per pulse for the Yb:YAG laser. The percentage output was set by the laser control software, and the energy was calculated from the average power divided by repetition rate.

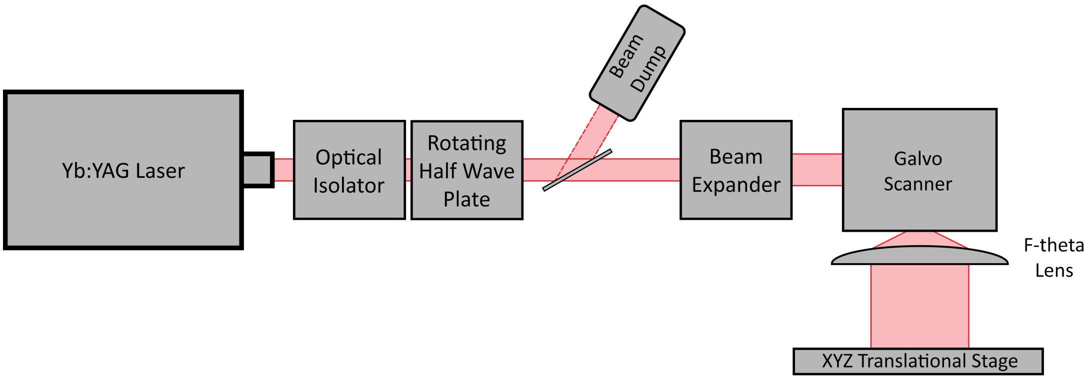

FIGURE 4.18: Optical setup used for the Yb:YAG laser. The rotating half wave plate was used as a variable attenuator with a polariser reflecting unwanted energy into the water-cooled beam dump.

fell below their damage threshold. The galvo scanner was part of an Aerotech Infinite Field Of View (IFOV) system that could be used simultaneously with the XYZ translation stage beneath it. However, the IFOV system experienced various synchronisation problems between the XYZ stages and the galvo scanner, and therefore only the XYZ stages were used in this thesis.

The pulse length of the Yb:YAG laser was measured at the manufacturer and also confirmed with our autocorrelator. The raw data from the autocorrelator at Rofin-Sinar UK is shown in figure 4.19. The autocorrelator had a calibration value of 15.443ps/ms, giving a measurement of 1.19ps. As with our autocorrelator, this is the autocorrelation function, and so correcting for this gives a FWHM pulse length of 841fs. In figure 4.20 the pulse bandwidth was measured at 1.921nm giving a time-bandwidth product of 0.457. An ideal bandwidth limited Gaussian pulse gives a time-bandwidth product of 0.441 indicating that the laser was operating at near the transform limit. [118]

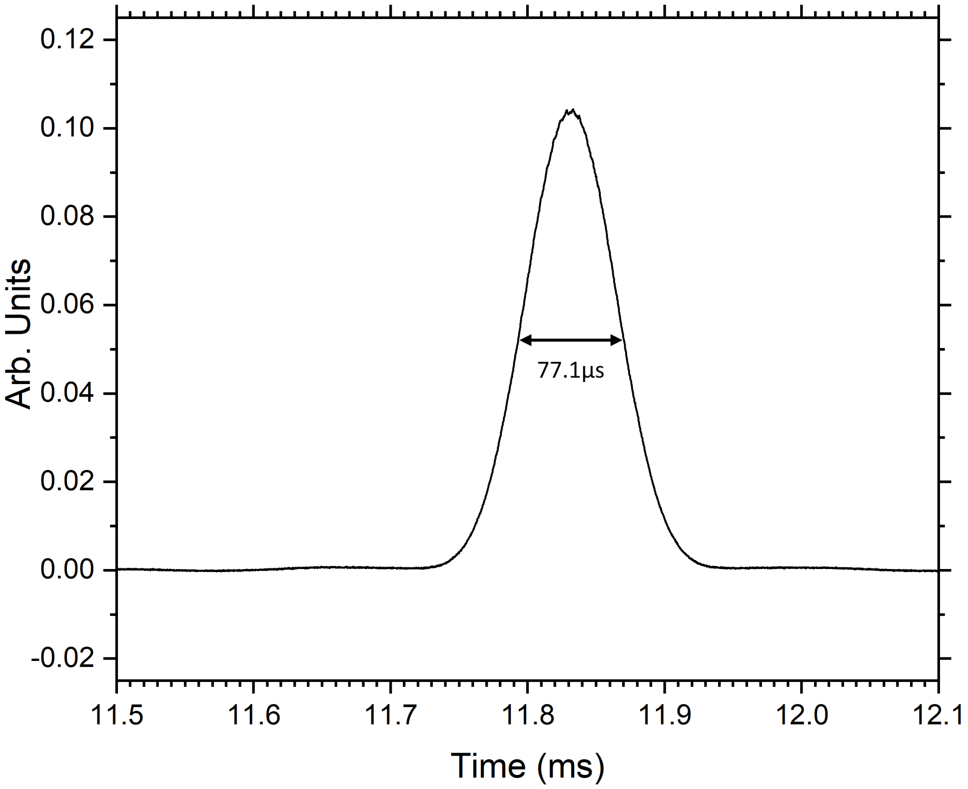

FIGURE 4.19: Plot showing the raw autocorrelator data obtained from the Yb:YAG laser pulse. The data corresponds to a FWHM pulse length of 841fs. [119]

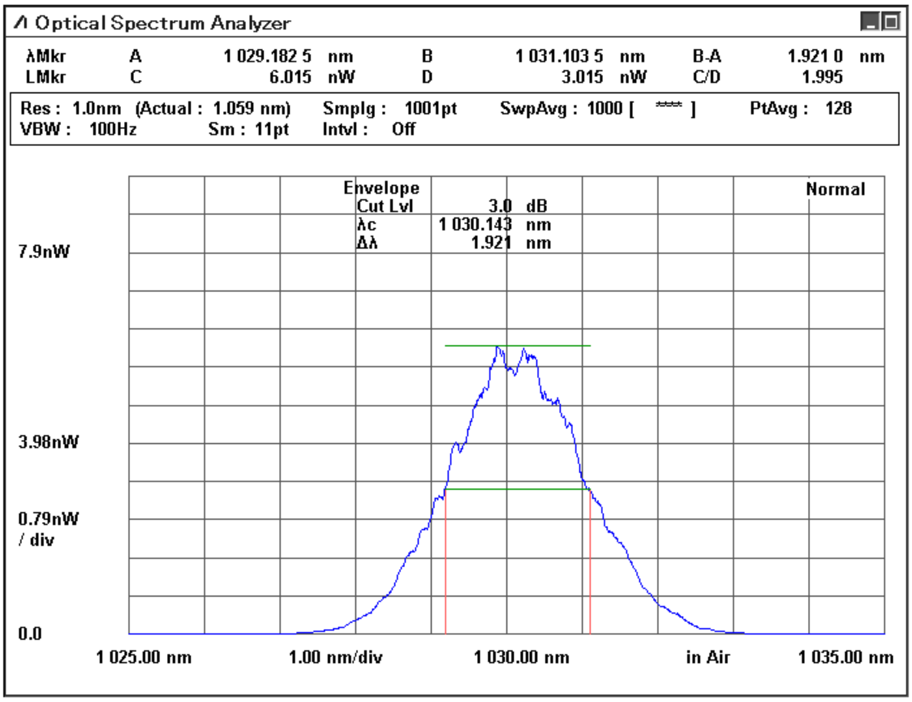

```
λMkr    A    1 029.182 5  nm    B    1 031.103 5  nm    B-A    1.921 0  nm
LMkr    C        6.015  nW      D        3.015  nW      C/D    1.995

Res :  1.0nm  (Actual :  1.059 nm)   Smplg :   1001pt    SwpAvg :  1000 [   ****  ]    PtAvg :   128
VBW :   100Hz           Sm :  11pt   Intvl :    Off

Envelope
Cut Lvl          3.0  dB
λc         1 030.143  nm
Δλ             1.921  nm
```

FIGURE 4.20: Wavelength of the Yb:YAG laser pulse. Measured as being 1030nm with a FWHM $\Delta\lambda = 1.921$nm. [119]

Chapter 5

Ultraviolet Laser Processing of ITO Films

5.1 Introduction

In this chapter, wet processed ITO films manufactured by INM were irradiated with various ultraviolet laser sources to improve the electrical conductivity whilst remaining the optical transparency. ITO films on glass substrates and PET substrates were both irradiated with the laser sources. Initially, the damage thresholds of the film for a particular laser source was determined for the ITO films and/or substrate. When a laser regime was determined, preliminary experiments were conducted to ensure the laser energy could effectively be coupled into the films and improve the electrical conductivity. When it was confirmed that the laser source could process the ITO effectively and improve the conductivity, a complete study for the laser source was conducted. This included more detailed electrical tests, post irradiation optical measurements from the ultraviolet to the infrared and surface morphology measurements.

Ultraviolet laser irradiation is expected to process the films photochemically, not requiring any appreciable temperature increase in order to increase the films electrical conductivity. The high photon energies associated with ultraviolet light can directly affect the chemical structure of the films to increase electrical conductivity in two ways. In the literature review, ultraviolet lasers were mainly used to process ITO films by creating oxygen vacancies within the ITO itself. Oxygen vacancies in the ITO film contribute two free electrons available for electrical conduction, effectively increasing the charge carrier density. In the films considered here, ITO nanoparticles are suspended in an organic binder, 3-(Trimethoxysilyl)propyl methacrylate (MPTS), which can be polymerised under ultraviolet irradiation. [25, 120, 121] When MPTS is irradiated with ultraviolet light at sufficiently high photon energy, the double carbon bond shown in figure 5.1 is broken leaving a free radical. The free radical is then able to react with other nearby molecules, creating a polymer chain of MPTS molecules. During the polymerisation step, the MPTS binder densifies and effectively pulls the ITO nanoparticles closer together. When the ITO nanoparticles are closer together, the non-conductive MPTS barrier between them becomes smaller, and the probability of electron tunnelling through the dielectric barrier is greatly increased resulting in higher current flow.

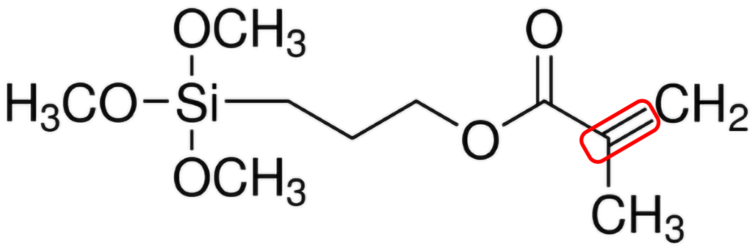

FIGURE 5.1: 3-(Trimethoxysilyl)propyl methacrylate molecule with the double carbon bond outlined in red.

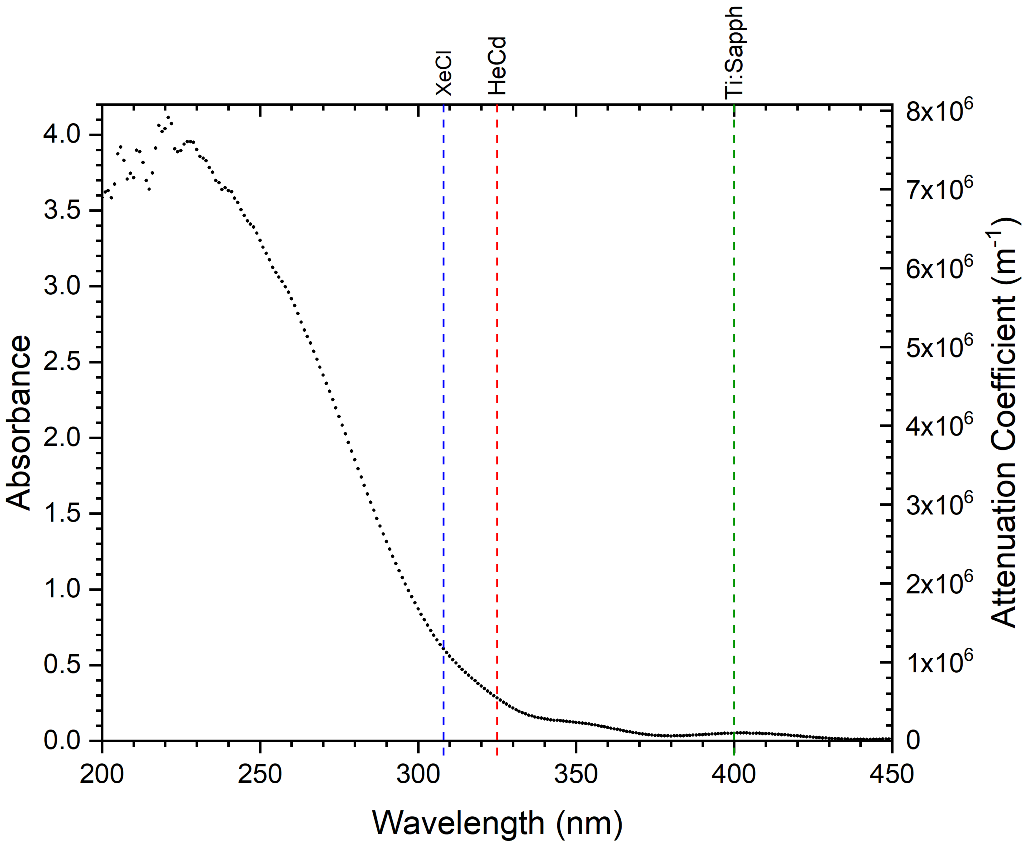

FIGURE 5.2: Absorbance and the respective attenuation coefficient of the ITO films at the wavelengths of the XeCl, HeCd and second harmonic Ti:Sapphire lasers.

5.2 XeCl Laser Irradiation

In Chapter 3, the ultraviolet transmission spectra was measured for the ITO films on fused silica substrates and shown in figure 3.20. From this data, the absorption depth at the XeCl laser wavelength at 308nm can be calculated. Shown in figure 5.2, at a wavelength of 308nm the attenuation coefficient is $1.18 \times 10^6 \mathrm{m}^{-1}$, which corresponds to an absorption depth of 847nm. As the absorption depth is slightly longer than the thickness of the films, the entire film will be affected by the laser energy whilst still being able to absorb a substantial amount of the energy. For example, for a film 522nm thick (Fig. 3.18), the percentage of absorbed light is calculated as follows. The extinction coefficient of the material, k, can be calculated using equation 5.1.

$$k = \frac{\alpha\lambda}{4\pi} \tag{5.1}$$

Where, α, is the absorption coefficient of the material at the wavelength, λ. At a wavelength of 308nm, the absorption coefficient was measured to be $1.18 \times 10^6 \mathrm{m}^{-1}$ (Fig. 5.2). This leads to a value of $k = 0.03$. The refractive index, n, of the ITO films is measured to be 2.4, as shown in section 3.3. Equation 5.2 is used to calculate the reflectivity, R, of the ITO films.

$$R = \frac{(n-1)^2 + k^2}{(n+1)^2 + k^2} \tag{5.2}$$

The reflectivity of the ITO films is calculated to be 17%. Finally, using the values obtained in equations 5.1 and 5.2, the amount of incident laser energy absorbed can be calculated from equation 5.3.

$$\frac{I_z}{I_0} = (1 - R)e^{-\alpha z} \tag{5.3}$$

Setting the thickness, z, at 522nm, leads to a value of 45%. That is, the amount of incident laser energy absorbed into the films is 45%.

5.2.1 Temperature Measurements

Xenon chloride excimer lasers typically have low repetition rates (<100Hz), nanosecond pulse lengths and moderate pulse energies (100's of mJ). As mentioned in the literature review in Chapter 1, this makes XeCl, and other excimer lasers capable of low temperature processing. In the preliminary laser processing trials on PET substrates, no damage to the substrate was observed due to heating. To measure the accumulative temperature rise of the films under irradiation with the XeCl laser, a FLIR A35SC thermal camera was used [122]. To accompany the thermal camera measurements, COMSOL [123] simulations were also run to estimate peak temperature rises on nanosecond time scales by Andrew Clarke. [124]

As the FLIR thermal camera was fitted with a germanium lens, any reflected ultraviolet laser light could not reach the sensor and cause damage. The FLIR camera was aligned so as to visualise the surface of the ITO film with the highest attainable magnification. This ensured that the image of the laser irradiated

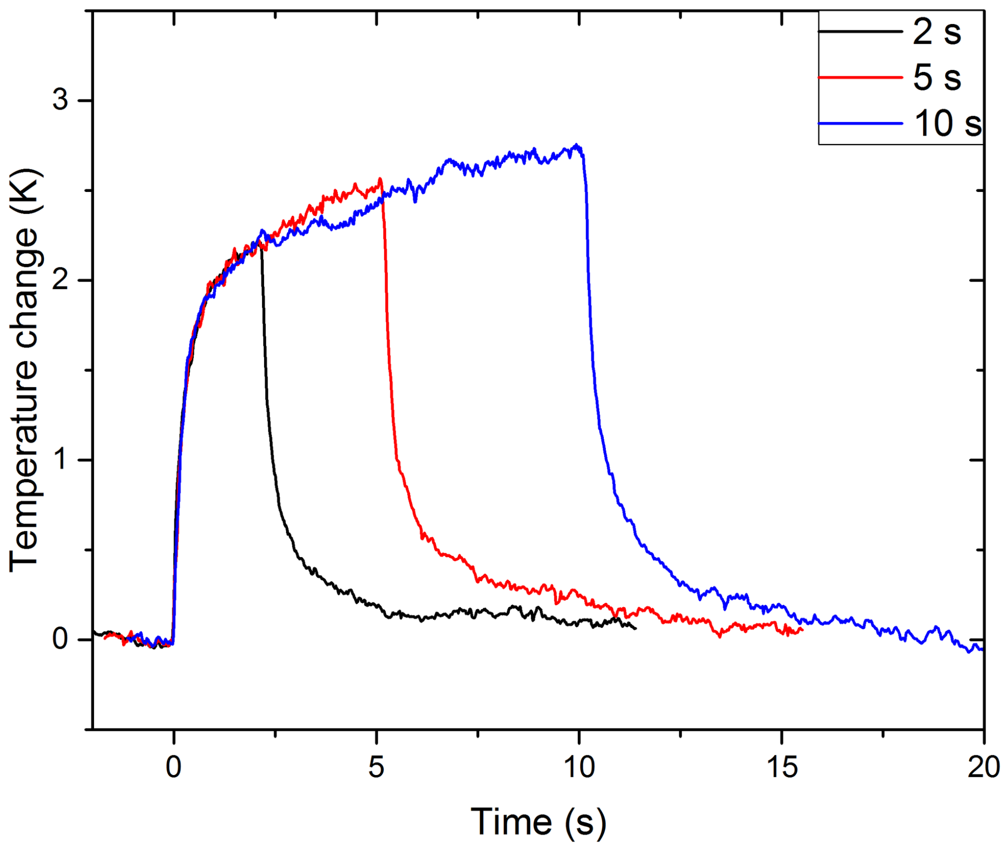

FIGURE 5.3: Temperature change measurement of the ITO film with the FLIR camera for XeCl laser irradiation at 50mJcm^{-2}, 50Hz repetition rate and 1mm diameter beam. Accumulative temperature rises are for 2, 5 and 10 seconds of irradiation.

spot covered as many pixels as possible to improve the spatial average of the measurement. The projection system of the XeCL laser was also adjusted to give a large irradiated area, however, this reduced the maximum reachable fluence to just above 50mJcm^{-2}. To irradiate the sample for temperature measurements, a circular mask with a diameter of 1mm was used with 1:1 imaging to give a fluence of 50mJcm^{-2} and the pulse repetition rate was set to 50Hz. The circular beam was chosen to simplify the COMSOL simulation to match the experiment. Figure 5.3 shows the temperature increases for the XeCl laser irradiation.

As can be seen, the accumulative temperature rises on the ITO films are very

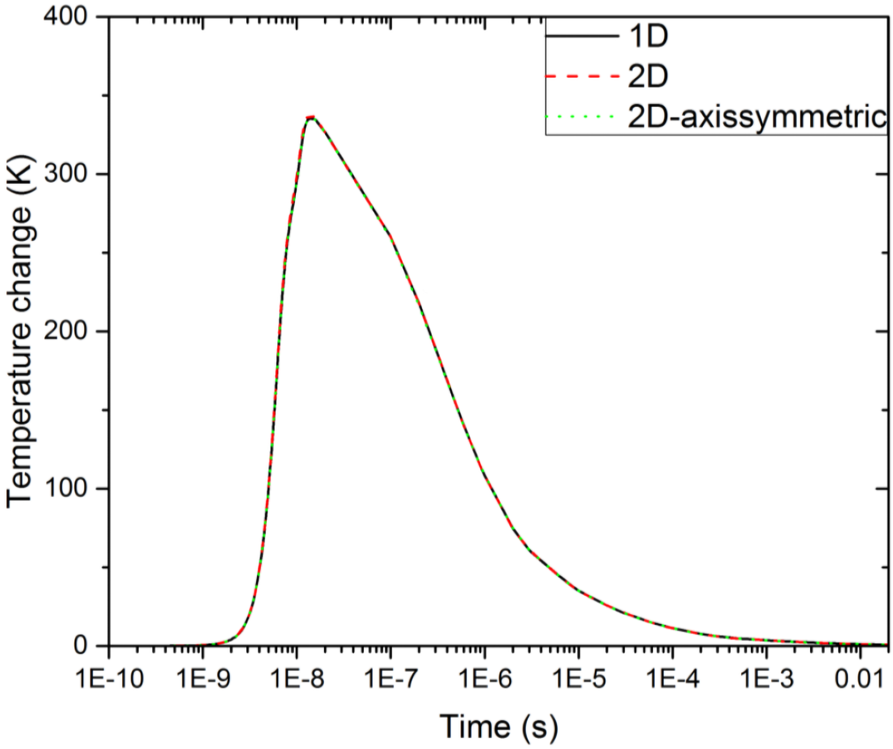

FIGURE 5.4: COMSOL simulation of the temperature rise for 1 pulse of XeCl irradiation at 50mJcm^{-2}, 50Hz repetition rate and 1mm diameter beam. Three different models were used as indicated in the legend.

small, having less than a 3°C rise in temperature over 10 seconds of irradiation. The FLIR thermal camera had a refresh rate of 60Hz, meaning the temperature rise for each frame was averaged over 17ms. The pulse length of the XeCl laser has a FWHM of 4ns, so the heating and cooling rates are expected to be much faster than the 17ms response time of the thermal camera. To estimate the peak temperature rises of the XeCl laser pulse, COMSOL simulations were run with 100ps time steps using the same parameters as the experiment. Figure 5.4 show the simulation results for the temperature rise for a single pulse of the XeCl laser onto the ITO film. [124]

The peak temperature rise of the XeCl laser pulse is around 340°C, and the material returns close to room temperature in 10ms. Due to the low accumulative

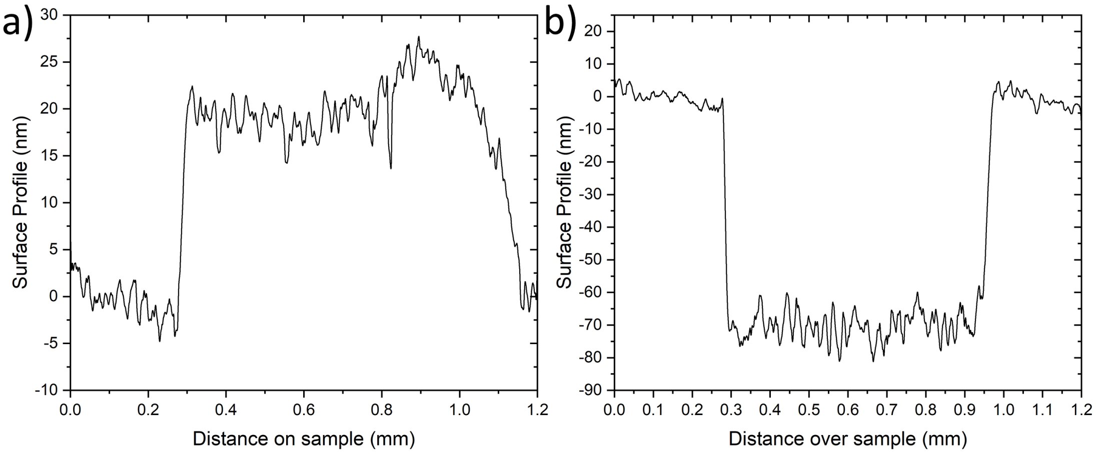

FIGURE 5.5: Dektak surface profiles for ITO films damaged by the XeCl laser at fluences of **a)** 100mJcm^{-2} **b)** 150mJcm^{-2}. Each area was irradiated with 10 pulses.

temperature rises of the XeCl laser, irradiation of ITO films on temperature sensitive PET substrates was possible without damage.

5.2.2 Damage Threshold

To find the damage threshold of the ITO films using the XeCl laser, an approximately 750µm square was imaged onto the surface of the ITO films. The ITO films were irradiated in sets of 10 pulses with increasing fluences, then using the Dektak XT profilometer surface changes which could indicate damage were looked for. Figure 5.5 shows two damage regimes found using this method. At a fluence of 100mJcm^{-2} the ITO films begin to delaminate, raising them above the rest of the unirradiated film. Raising the fluence even higher up to 150mJcm^{-2} we see ablation of the ITO films, removing material and leaving an etched area. With roughly 100 pulses at a fluence of 150mJcm^{-2} the ITO films could be completely removed. Figure 5.5 shows ∼70nm in 10 pulses. Therefore, in 100 pulses we would expect 700nm to be removed which

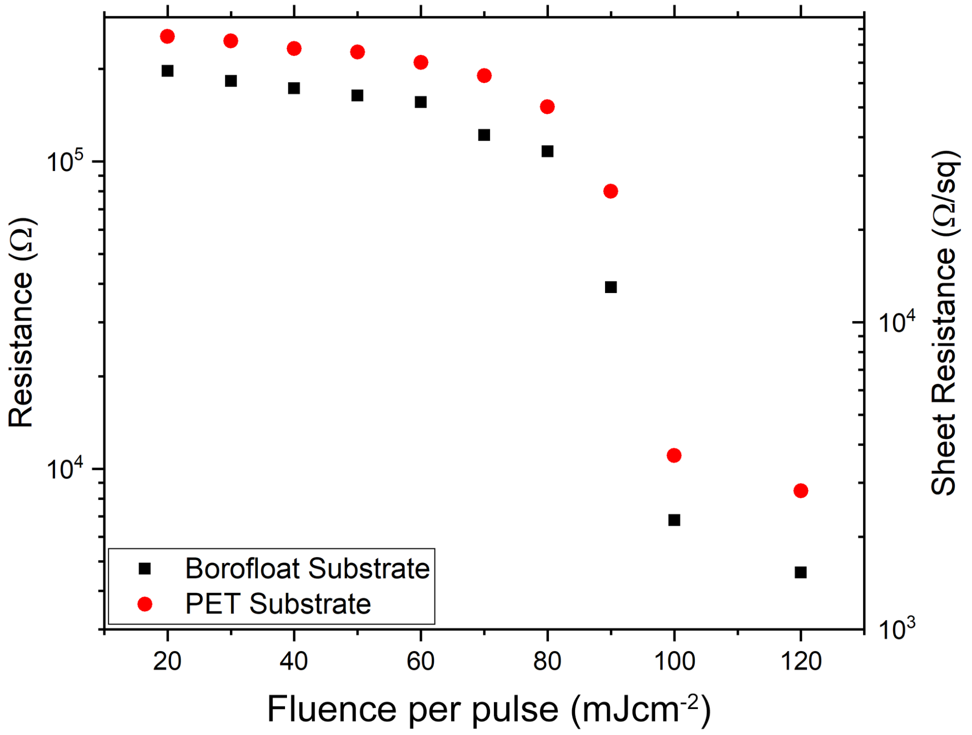

FIGURE 5.6: Sheet resistance measurements on ITO films with glass and PET substrates at varying fluences with the XeCl laser. Each fluence was conducted with 1000 pulses per area, laser operated at 50Hz.

is greater than the thickness of the film as expected. The glass substrates could not be damaged under any fluence attainable by our XeCl laser. The PET substrates have an ablation threshold of 170mJcm^{-2} [125] with the XeCl laser, which is higher than the ITO films so this was not an issue.

5.2.3 Electrical Resistance Measurements

Irradiating the ITO films with the XeCl laser in the preliminary experiments successfully reduced the resistivity of the ITO films significantly, so further studies were conducted.

Irradiating the ITO films on glass and PET substrates at varying fluences and measuring the corresponding sheet resistances was plotted and can be seen in figure 5.6. As seen in figure 5.6, two distinct regimes can be seen. On glass at fluences of 80mJcm^{-2} and below, a steady change in sheet resistance can be seen, dropping from 66kΩ/sq to 36kΩ/sq. When increasing the fluence above 80mJcm^{-2}, the sheet resistance starts to drop significantly down to 2.3kΩ/sq at a fluence of 100mJcm^{-2}, then again appears to start levelling off at 120mJcm^{-2}. The ITO films on PET substrates behave in a very similar way but have a slightly higher sheet resistance value. This is due to the thinner ITO films on the PET substrates. It is important to note that by a fluence of 100mJcm^{-2}, the films started to shows signs of damage. The ITO films became very hazy for the 2 highest fluences, although this did not seem to affect the electrical properties of the film. This might however explain why the sheet resistance levels off at 120mJcm^{-2}, with this very close to the ablation point of the ITO films. When looking at the lowest sheet resistance at 1.53kΩ/sq attained, it is still over 2 orders of magnitude higher than can be achieved with commercial ITO. Before irradiation of the films, the sheet resistance of the ITO was measured to be greater than 1MΩ/sq however, so pulsed laser irradiation at 308nm was still able to reduce the resistivity by around 3 orders of magnitude.

Another parameter chosen to be varied was the accumulated fluence, often termed the "dose" of UV light. This was accomplished by changing the rate at which the translational stages moved and therefore the pulse overlap per unit area for a fixed repetition rate. In the preliminary experiments, changes in electrical resistivity could start having a measurable difference from 500

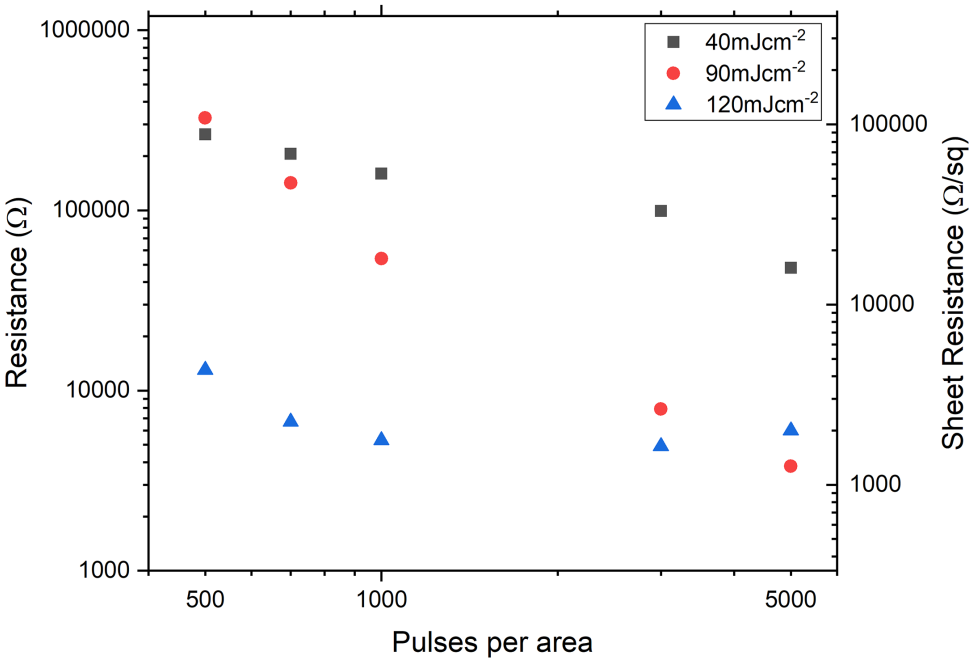

FIGURE 5.7: Sheet resistance measurements on ITO films with glass substrates at varying pulses per area. 3 fluences were used each varying between 500 and 5000 pulses per area.

pulses per area and above. To try achieve a lower sheet resistance value, a higher number of pulses per area were used on the ITO films. Fluences of 40, 90 and 120mJcm^{-2} were chosen, one below damage threshold, one close to it, and one above it, and the ITO films were irradiated with up to 5000 pulses per area. The results can be seen in figure 5.7.

Looking at figure 5.7, it can be immediately seen that a fluence of 120mJcm^{-2} decreases the sheet resistance of the films to a larger extent at lower pulse numbers than the lower fluences. With 500 pulses per area, at 120mJcm^{-2} the sheet resistance is over an order of magnitude lower than the value for 90mJcm^{-2}. However, at 1000 pulses per area the sheet resistance appears to saturate and at 5000 pulses per area starts to increase, probably due to increasing damage to the film. Another important observation from figure 5.7 is at 90mJcm^{-2} increasing the pulses per area continuously decreases sheet resistance until

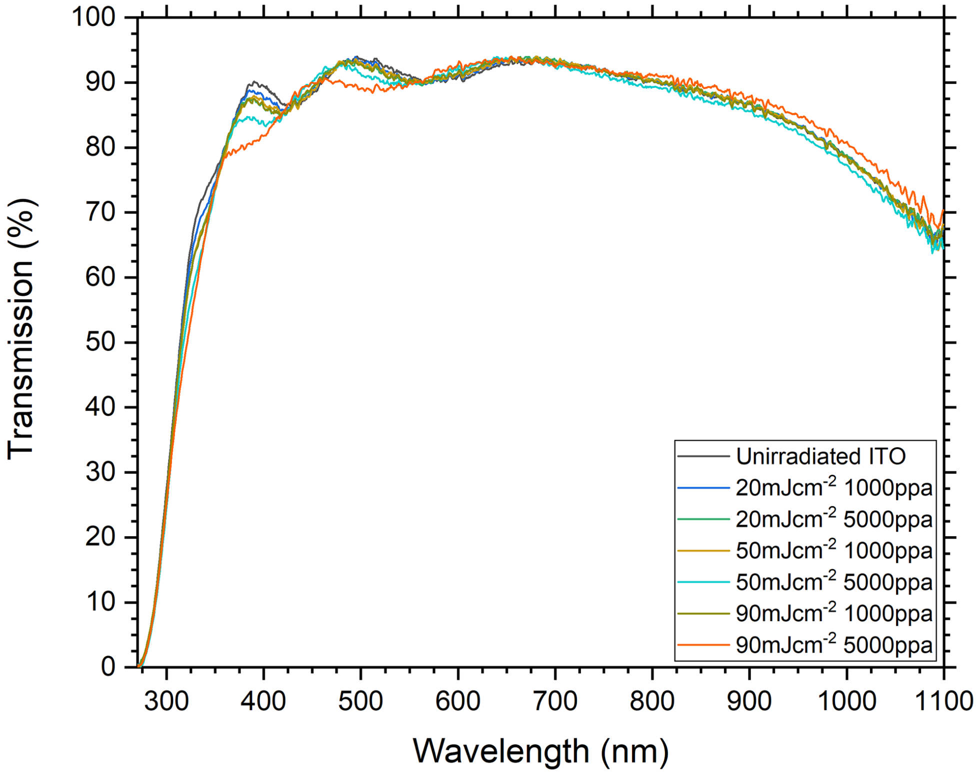

FIGURE 5.8: UV-VIS transmission spectra of ITO films under various levels of irradiation with the XeCl laser. The values at a fluence of 120mJcm^{-2} were not added due to the damage on the films

becoming lower when compared with 120mJcm^{-2}. This is a good result, since the films did not appear to become damaged visually in any way at 90mJcm^{-2}, whilst the optical quality of the films at 120mJcm^{-2} was reduced.

5.2.4 Optical Measurements

5.2.4.1 Transmission

To measure the optical transmission spectra of the ITO films, the larger isolation areas (6mm squares) were used. Optical transmission data were measured from the ultraviolet to the near infrared (190-1100nm). Figure 5.8 shows the transmission spectra for unirradiated and areas irradiated by the XeCl laser.

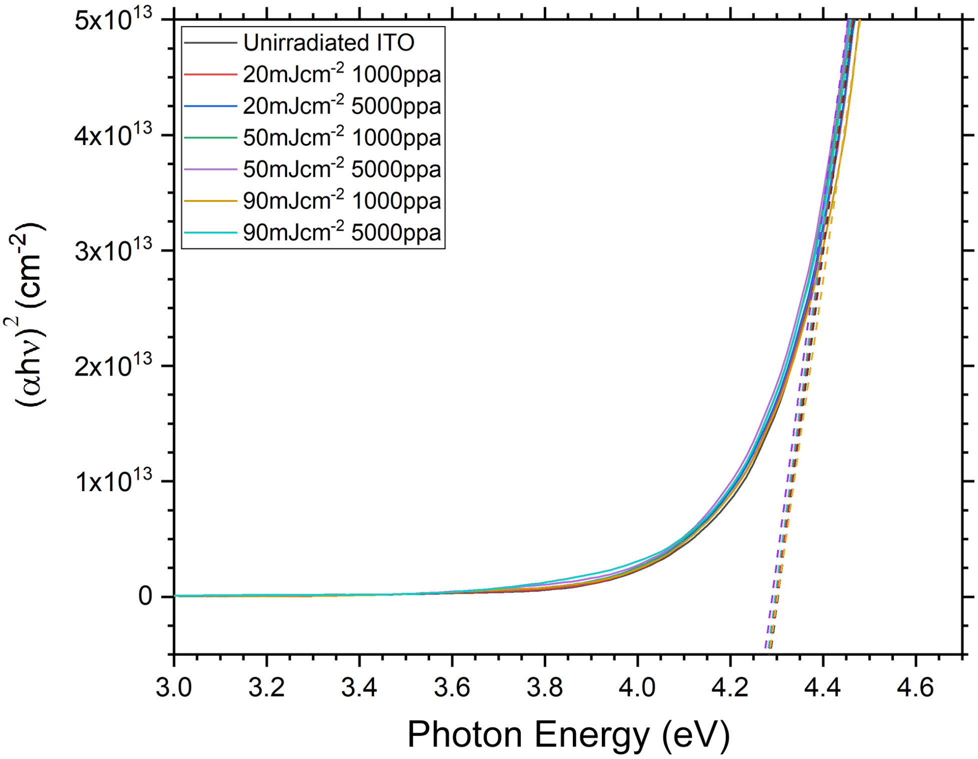

FIGURE 5.9: Tauc plot constructed from the transmission spectra from the ITO films irradiated with the XeCl laser.

As can be seen, the transmission of the ITO films throughout the visible range remains almost the same over the various irradiation regimes, having over 90% transmission throughout a large proportion of it. There is a small change in the thin film interference peaks on the 50 and 90mJcm^{-2} areas with 5000ppa, which is either due to a change in the thickness of the films or a change in the refractive index. One of the important things to notice from this data however, is that the ultraviolet band edge does not change with increasing levels of irradiation. From figure 5.8, a Tauc plot was constructed and is shown in figure 5.9.

The Tauc plot shows that the band gap of the ITO is not changing under increasing of dosage levels. The band gap lies between 4.28±0.04eV for each of

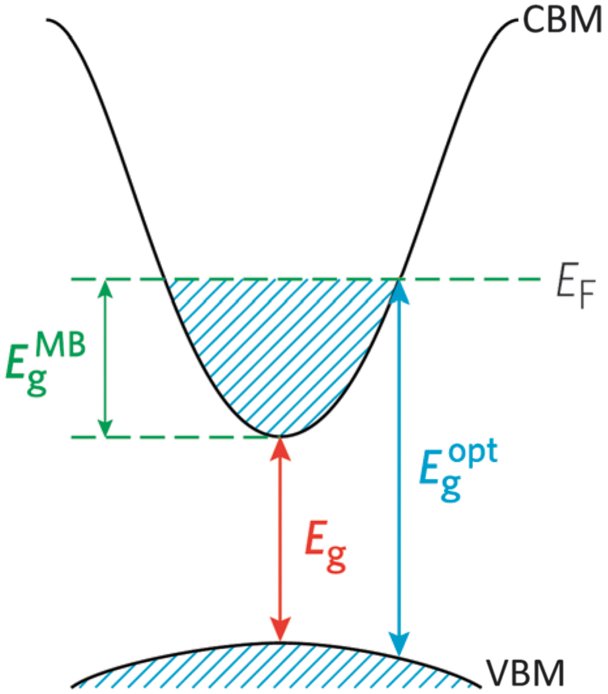

FIGURE 5.10: Example of the Moss-Burstein shift, where the band gap, E_g, is increased in energy by E_g^{MB} due to charge carriers populating the conduction band. [126]

the various fluences used. This result is useful, since even though the electrical resistivity is reducing by 3 orders of magnitude, the band gap is showing no changes. A change to the optical band gap of a semi-conductor material can indicate how the charge carrier density is changing. This is know as the Moss-Burnstein effect, where the band gap of the material appears to change as the conduction band is populated or de-populated with charge carriers, an example of this is shown in figure 5.10. Figure 5.9 implies that the charge carrier densities are staying the same under XeCl irradiation, and instead it is the electron mobility that is increasing.

To further investigate this hypothesis, the plasma edge of the ITO films in the infrared was measured. As shown in Chapter 3, the plasma edge is related to the charge carrier density, as shown in equation 3.13.

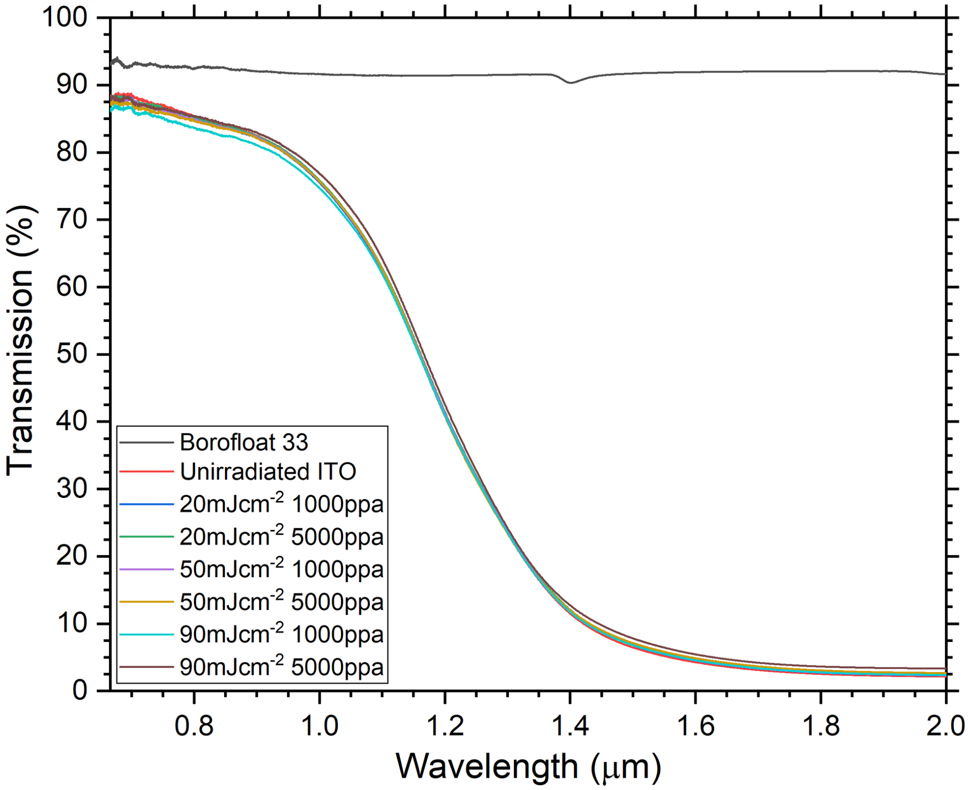

FIGURE 5.11: Infrared transmission spectra of ITO films irradiated with the XeCl laser showing the plasma edge.

If the Tauc plot hypothesis that the charge carrier density is correct, there should not be a change in the plasma edge under irradiation with the XeCl laser. The FTIR results for the ITO results are shown in figure 5.11. Looking at the infrared transmission spectra, we see that there is not a change in the plasma edge under any dosage of XeCl laser irradiation. The plasma edge from this spectra is very similar to the unirradiated sample shown in Chapter 3, and gives a sheet carrier density between 2.98×10^{16} and $6.35 \times 10^{16}\text{cm}^{-2}$. All evidence points towards the charge carrier mobility increasing, whilst the charge carrier density is staying the same as the sample is irradiated. To get a definitive value for the charge carrier density and mobility, using the Hall voltage setup was problematic. Due to the high resistance of the samples after

TABLE 5.1: Table showing haze measurements for ITO films irradiated with the XeCl laser. Each fluence was incident on the sample for 1000 pulses per area.

Fluence ($mJcm^{-2}$)	Haze (%)
0	0.93
20	0.82
30	0.91
40	0.86
50	1.03
60	0.92
70	0.89
80	0.98
90	1.29
100	11.3
120	20.9

irradiation, a suitable current could not be passed through the ITO films without heating the samples significantly. The high voltages needed to supply this current also put the very sensitive nanovoltmeter at risk of damage, so Hall measurements were decided not to be taken.

5.2.4.2 Haze

The haze of the ITO films was measured before laser processing, and again after irradiation. Note that the haze measurements here are for comparison within the thesis only. The light source used did not conform to the broadband standard, as the measurements were taken at a single wavelength using a HeNe laser ($\lambda = 632.8$nm).

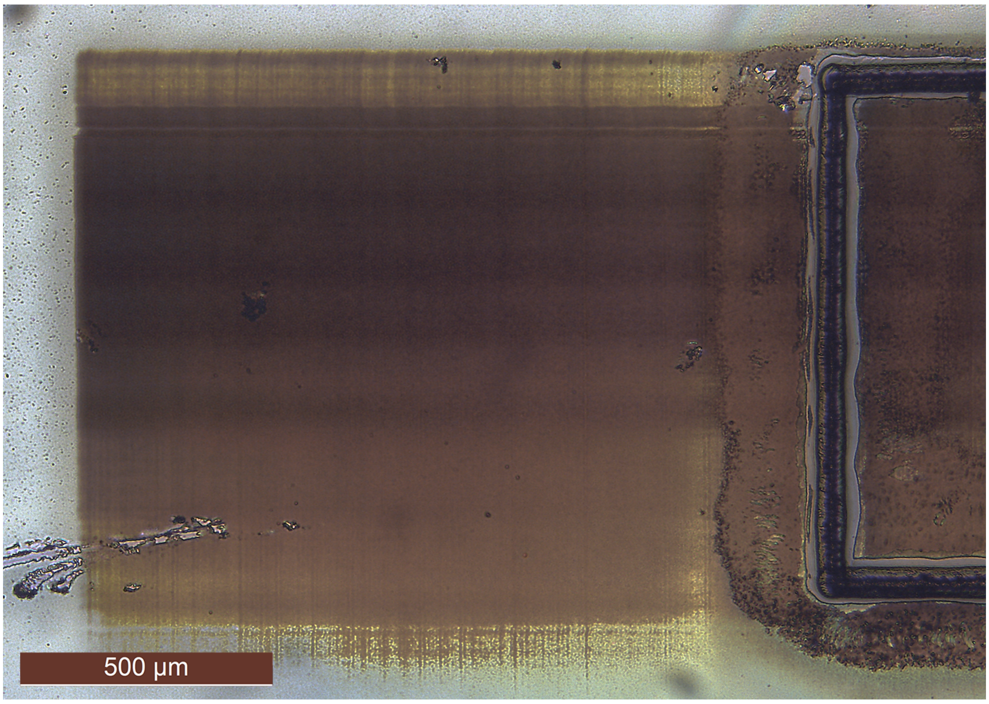

FIGURE 5.12: View at the edge of a XeCl irradiated track on ITO at a fluence of 120mJcm^{-2} with 1000 pulses per area. The dark brown areas indicate where the ITO film has become hazy, but did not look brown to the naked eye.

The haze levels of the ITO films under XeCl irradiation stayed very low, typically below 1% up to a fluence of 90mJcm^{-2}. This value for the haze is the same as the unirradiated ITO films, and remains unchanged for lower fluences. At 100mJcm^{-2} fluence and above, the haze dramatically increases making the films look milky white. A view of the hazy area under the microscope can be seen in figure 5.12. Despite this visible damage, the films remain conductive.

5.2.5 Surface Measurements

The ITO films start to become hazy when irradiated at and above a fluence of 100mJcm^{-2}, but the electrical conductivity is not affected. Irradiating the ITO films at 120mJcm^{-2} and taking a surface profile over the affected area can help

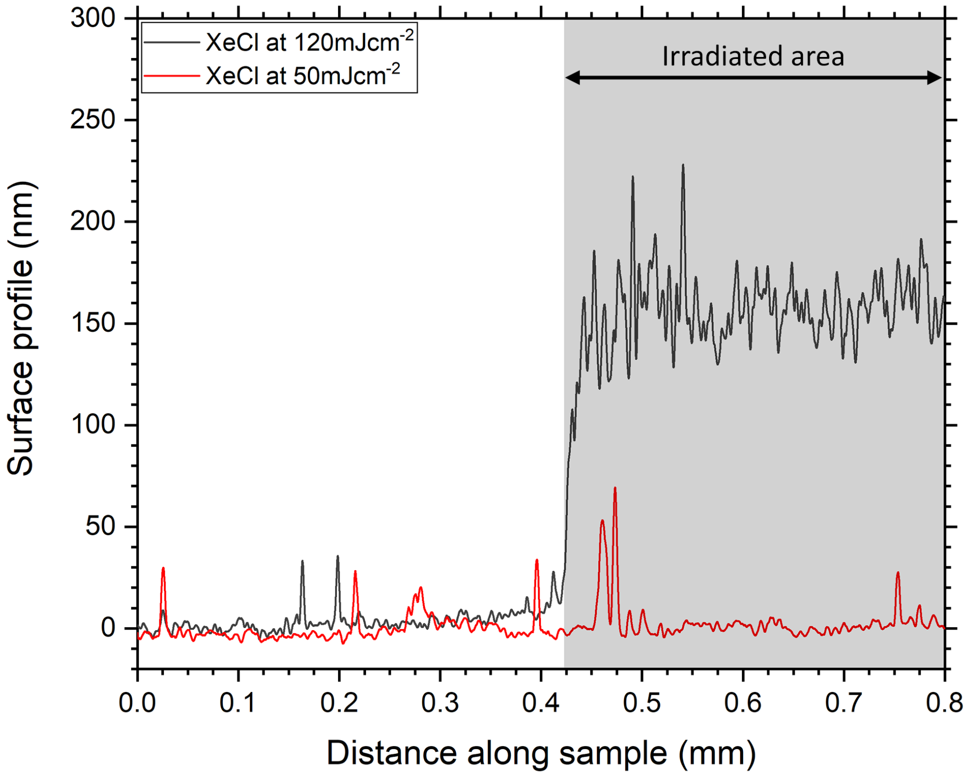

FIGURE 5.13: ITO film surface profile of XeCl irradiated areas with fluences at 50 and 120mJcm^{-2} with 1000 pulses per area. The shaded area indicates where the irradiated area lies. The thickness of the films were 520nm before irradiation.

us understand why. This is shown in figure 5.13. After irradiation at 50mJcm^{-2} which does not cause the ITO films to become hazy, the profile in the irradiated area does not change compared with the unirradiated ITO. When looking at the area irradiated at 120mJcm^{-2}, the surface profile increases in heigh by an average of 170nm above the unirradiated area, whilst the surface roughness also increases. The higher surface roughness of the ITO film will create scattering of any transmitted light, which is the most likely cause of the ITO films becoming hazy in appearance at higher fluences.

As mentioned earlier, ultraviolet irradiation of the ITO ink containing the MPTS binder leads to polymerisation of the MPTS along with densification. Tests

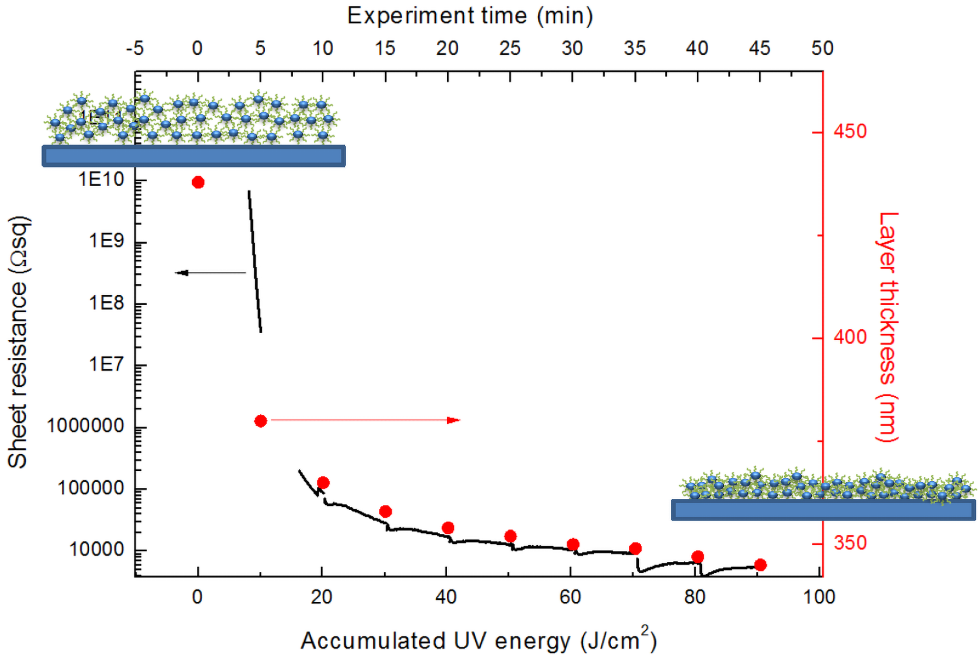

FIGURE 5.14: Sheet resistance and ITO film thickness plotted against accumulated UV energy. In this case, the UV energy was deposited by a mercury lamp.

performed by T.M.Amaral at INM showed that for irradiation under an ultraviolet mercury lamp, the ITO films shrink due to polymerisation. Figure 5.14 shows how sheet resistance and film thickness of the ITO films change under UV irradiation with a mercury lamp. [127] For the same conditions, the XeCl laser was used to irradiate the ITO films then the Dektak XT profilometer was used to check for any film shrinkage at various dosages. For a comparison to figure 5.14, the accumulative UV energy absorbed into the films per unit area was calculated from equation 5.4, taking into account reflection and absorption losses. This integrated fluence is termed the UV dose received.

$$UVDose(Jm^{-2}) = FN(1 - R_{308})(1 - exp(-\alpha_{308}t)) \tag{5.4}$$

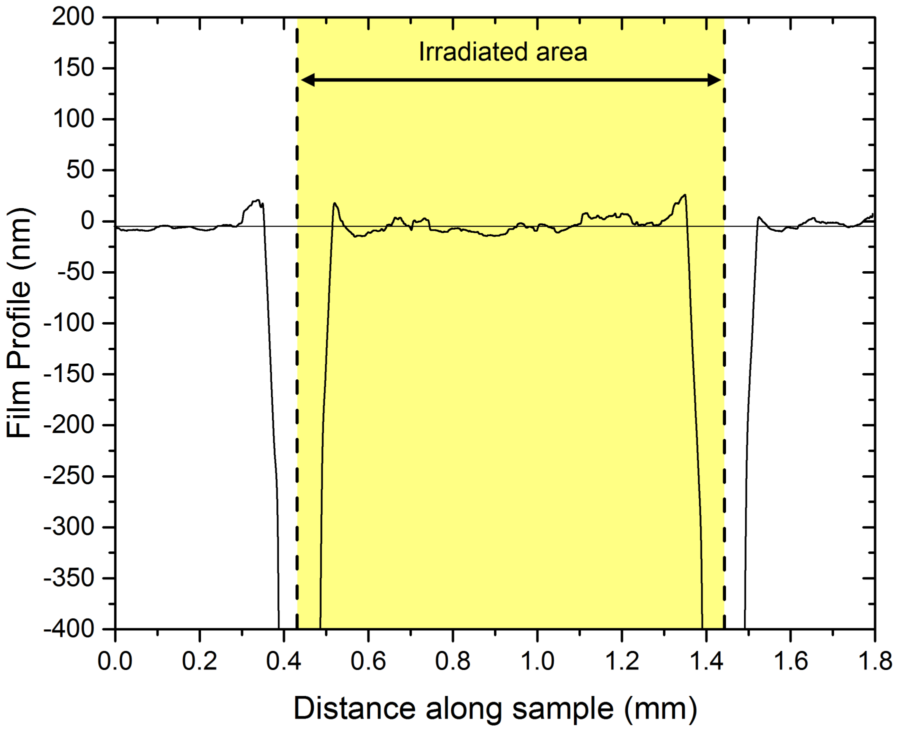

FIGURE 5.15: Dektak surface profile of a XeCl irradiated area on ITO film. The accumulated dosage was 1030Jcm^{-2}, relating to 29000 pulses per area at 50mJcm^{-2}. The two deep trenches (at 0.4 and 1.4mm) relate to the ablated edge of the isolated area.

Where F is the fluence, N is the number of pulses per area, R_{308} is the reflectivity of the film at 308nm, α_{308} is the absorption coefficient at 308nm and t is the thickness of the film.

Measuring the thickness change of the ITO film after XeCl irradiation, even at very high doses, showed no measurable change of film thickness. Shown in figure 5.15 is the film profile across a laser irradiated area. With the accumulated energy dose at more than 10 times higher than the highest dose seen with the mercury lamp, there is no change in film thickness. One explanation for the lack of shrinkage is because of the short pulse nature of the XeCl laser. With nanosecond pulse lengths, the interaction with the films is very different from the continuous ultraviolet light that is given out from the mercury lamp.

In this way, reciprocity, in the sense of photographic exposure is not observed.

5.3 HeCd Laser Irradiation

The HeCd laser used here has a wavelength of 325nm, which from figure 5.2 gives an attenuation coefficient of $5.5\times10^5\text{m}^{-1}$. This corresponds to an absorption depth of 1.83µm. Consequently, the HeCd laser will affect the entire depth of the ITO film, however, it is not as strongly absorbed as the XeCl laser at 308nm. The longer absorption depth allows more ultraviolet light to pass through the ITO film. This transmitted energy will either be absorbed by the substrate or pass straight through into a beam dump.

5.3.1 Temperature Measurements

The HeCd laser outputs continuous wave ultraviolet light. The power reaching the sample after all the optical elements was approximately 46mW. By focussing to different spot sizes a range of irradiances could be generated. As with the XeCl laser, the ultraviolet light from the HeCd can induce photochemical changes within the ITO films without the need for a significant increase in temperature. Using the FLIR thermal camera, the laser-induced temperature rise of the ITO film on glass substrates during irradiation by the HeCd laser was measured. In figure 5.16 the temperature rise due to the HeCd laser with an irradiance of 650kWm^{-2} has a maximum 7°C. The HeCd laser irradiation reached a steady state temperature after $\sim$5 seconds. This temperature rise

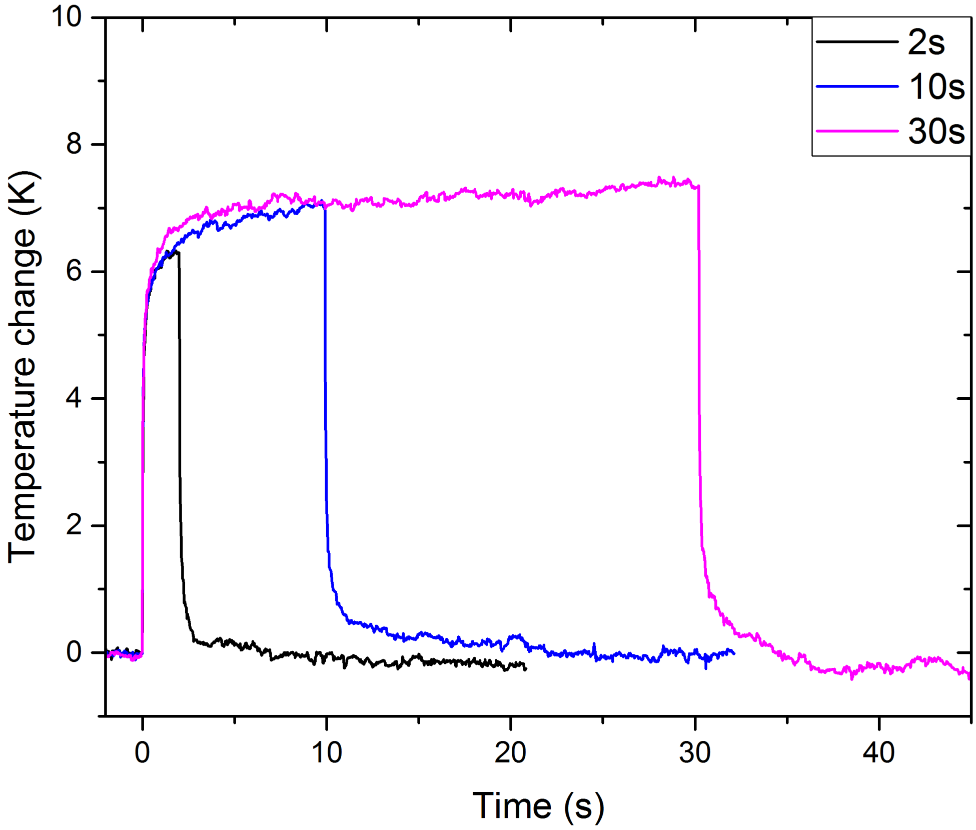

FIGURE 5.16: Temperature rise of ITO films on Borofloat substrates under HeCd irradiation. The laser spot size was 300µm in diameter giving an irradiance of 650kWm^{-2} [124]. To turn the laser beam on and off, a solenoid controlled by a pulse generator opened a mechanical shutter on the laser.

is higher than the XeCl laser, but still low enough so that no photothermal processes could be effecting the ITO films.

To support the temperature measurements on the ITO film irradiation via the HeCd laser, some calculations were made using thermal analysis of the interaction. All the data used in this analysis was taken from Andrew Clarke's thesis [124] or from the glass manufacturers data sheet [93]. For the ITO films, the thermal conductivity, k, was 4.42$\text{Wm}^{-1}\text{K}^{-1}$ and the density, ρ was 7120kgm^{-3}, and the heat capacity, c, was 357.1$\text{Jkg}^{-1}\text{K}^{-1}$. From these values, the thermal diffusivity, D, is calculated from equation 5.5 to be $1.74\times10^{-6}\text{m}^2\text{s}^{-1}$.

$$D = \frac{k}{\rho c} \tag{5.5}$$

As the heat diffusion length is $\delta = \sqrt{Dt}$, then the time taken for the surface absorbed energy to diffuse 520nm is be calculated from equation 5.6 to be $\sim$155ns.

$$t = \frac{\delta^2}{D} \tag{5.6}$$

Therefore, for CW irradiation, the thermal properties of the substrate will dominate very early on in the interaction. In addition, the above estimate assumes surface absorption whereas the real physical situation is a distributed energy loading. This will tend to make the role of the substrate even stronger in determining the steady state temperature rise. Consequently, for the long

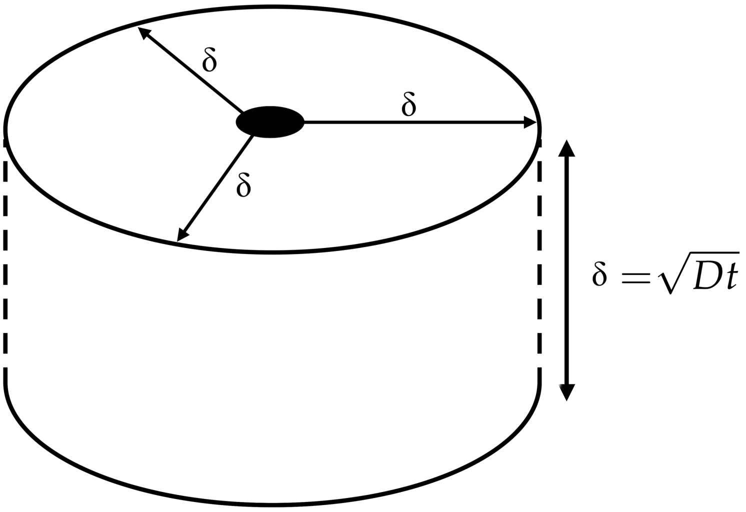

FIGURE 5.17: Schematic diagram of the steady state heat effected volume. The black spot in the centre is the laser beam diameter.

time scale (10's of seconds) laser-induced temperature rises are based on the Borofloat 33 properties.

For a continuous wave laser absorbed in the glass, the heated volume will be primarily determined by heat diffusion (Fig. 5.17).

From figure 5.16, the steady state temperature is reached in $\sim$10 seconds, making $\delta >> \alpha^{-1}$, where α^{-1} is the absorption depth, and so the heated volume is given by $V = \pi\delta^3$. The energy delivered to this volume in time $= t$, is $E = P_a \times t$, where P_a is the absorbed laser power. Considering the heat capacity of the borofloat glass, c, the resulting temperature rise is calculated using equation 5.7.

$$\Delta T = \frac{\Delta E}{mc} = \frac{P_a}{\pi k \sqrt{Dt}} \tag{5.7}$$

Applying the simple analysis above to a timescale of 10 seconds, the absorbed power of the laser was 46mW, the thermal conductivity of the borofloat glass

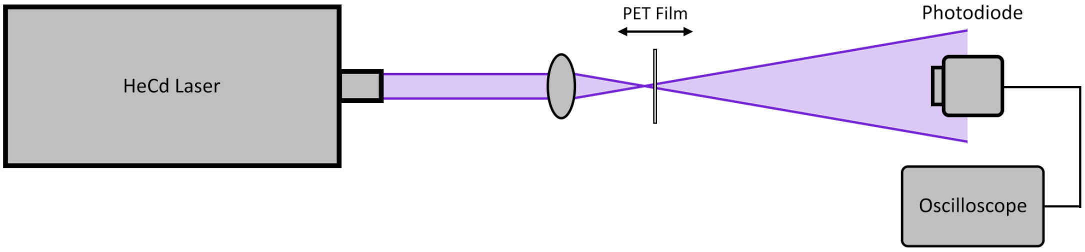

FIGURE 5.18: Optical setup used to measure the damage of PET films caused by the HeCd laser. The PET film was placed at different distances from the lens to change the irradiance.

was 1.1Wm^{-1}K^{-1}, and the diffusion length of the borofloat glass was 2.6mm. The estimated temperature rise calculated to be ~5.1°C. This is closely similar to the experimental value of 7°C (Fig. 5.16) and indicates that the hypothesis that the thermal aspect of the interaction is dominated by the properties of the substrate is correct.

5.3.2 Damage Threshold

To test whether the films could be damaged by the HeCd laser, ITO films on glass substrates were exposed to increasing irradiances up to the maximum at the focal point of the lens. On the glass substrates, the ITO films could not be damaged at any achievable irradiance with our laser setup. The focal point was estimated to be 25µm giving an approximate irradiance of 90MWm^{-2}. On PET substrates, at high enough irradiances, the PET itself could be damaged, leading to a damaged film. The PET had 2 damage regimes. The first signs of damage were discoloring of the PET substrate and it turning milky white, but without signs of catastrophic effects such as holes appearing. The second stage of damage was melting. The experimental setup is shown in figure 5.18.

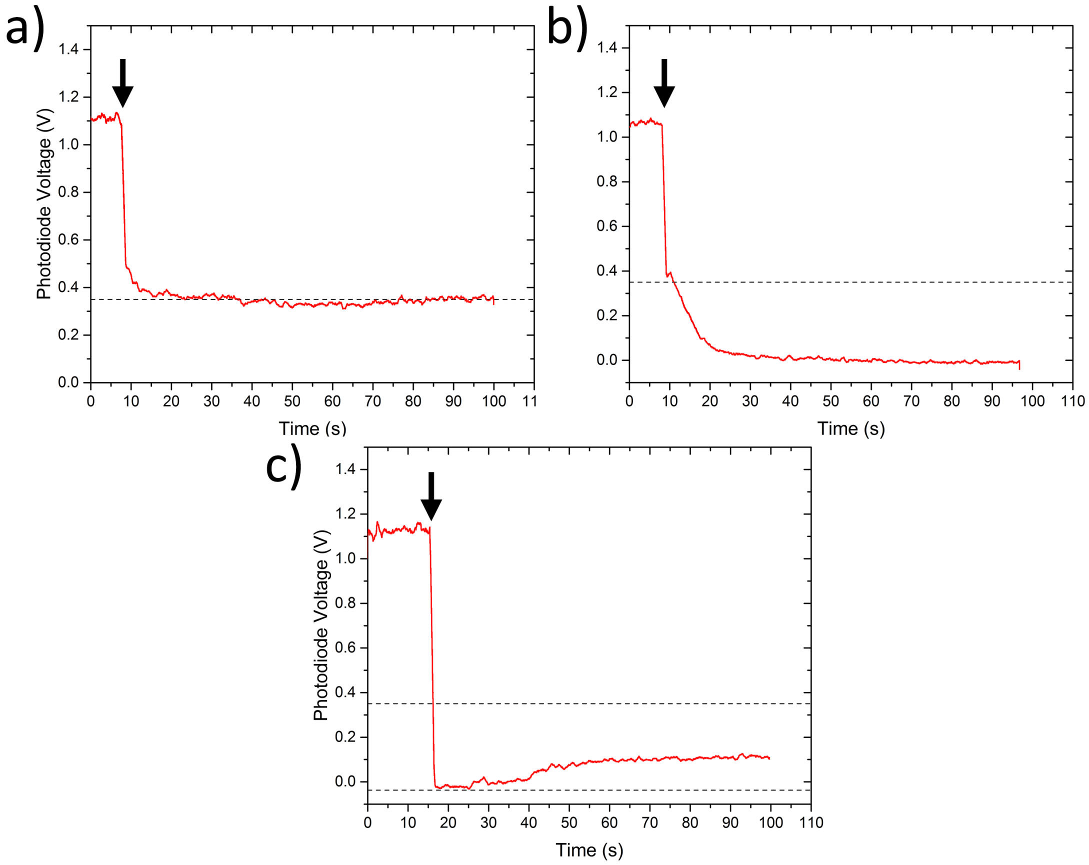

FIGURE 5.19: Photodiode readings from HeCd irradiation of PET at 3 different irradiances: **a)** 210kWm^{-2} **b)** 610kWm^{-2} **c)** 1.5MWm^{-2}. The arrows indicate the moment that the PET was inserted into the beam.

The experimental procedure was simple. The HeCd laser was incident onto the photodiode to start with, making sure not to damage or saturate the detector, then the PET foil was put into the laser beam. As the PET was put into the beam, the photodiode drops in signal measured by the oscilloscope. The resulting data at 3 different irradiances are shown in figure 5.19.

As can be seen, at the lowest irradiance of 210kWm^{-2}, when the PET is placed into the beam the photodiode signal falls due to the reflection losses and absorption of the laser beam. The signal stays at this lower level indefinitely. From this we conclude that this irradiance was insufficient to cause measurable changes in absorption or scattering. Increasing the irradiance to 610kWm^{-2}

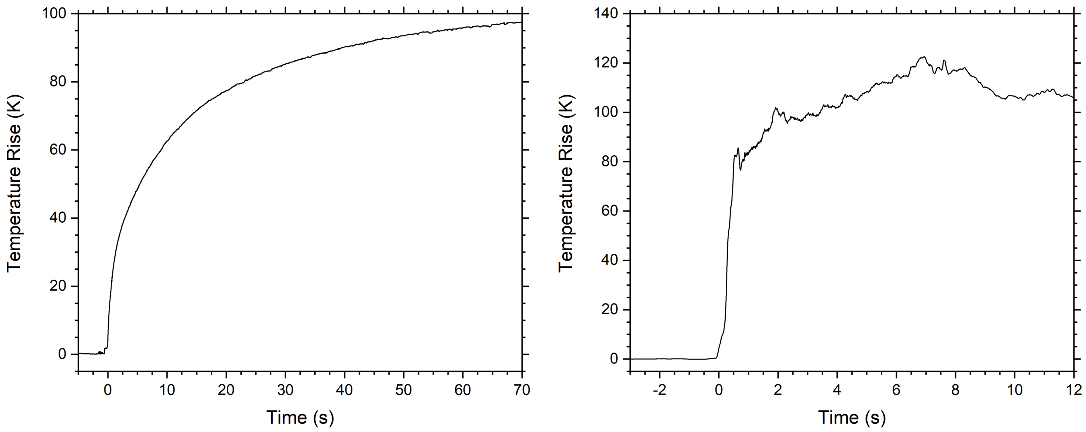

FIGURE 5.20: Temperature measurements using the FLIR thermal camera from HeCd irradiation of PET at 2 irradiances: **left** 610kWm^{-2} **right** 1.5MWm^{-2}.

(Fig. 5.19b) caused the signal drops to around the same level as before, followed by a decrease over time before reaching a minimum at 50 seconds. The decreasing level of signal from the photodiode is because of the increased scattering of light due to damage within the PET. Increasing the irradiance even higher to 1.5MWm^{-2} (Fig. 5.19c) damage occurs much more rapidly. After inserting in the PET the signal drops instantaneously to a very low level, and slowly afterwards an increase in signal can be seen. This is because the PET films were melting, and light from the laser was able to pass unscattered through the hole created.

In figure 5.20, the surface temperature rises of PET for two irradiances is shown. At 610kWm^{-2} a steady increase in temperature up to 100°C is seen. This is a much higher temperature increase that was seen on glass substrates at a similar irradiance. This was due to the increased absorption of the UV light not absorbed or reflected from the ITO films, and also the PET films were only 175µm thick and thus the films did not have as much mass to heat from the

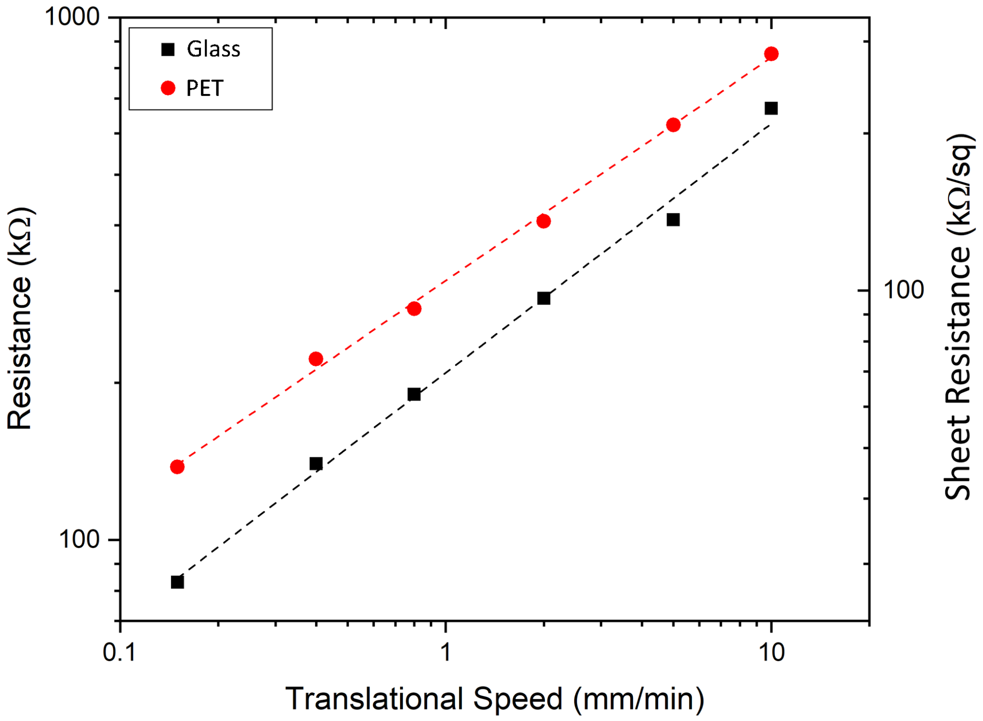

FIGURE 5.21: Sheet resistance measurements of ITO films irradiated by the HeCd laser on glass and PET substrates. The spot size was 1mm leading to an irradiance of 60kWm^{-2}.

substrate. With the higher irradiance of 1.5MWm^{-2}, the temperature rise is almost instantaneous. In under 2 seconds, the temperature of the PET increases to over 100°C. The temperature increases to a peak of 120°C, then starts to decrease. This was most likely due to the PET melting, and hence less material available to absorb the laser light.

5.3.3 Electrical Resistance Measurements

In order to be able to compare the pulsed XeCl laser and the C.W HeCd laser, the concept of integrated fluence or "dose" was used.. The dose was controlled as before, by changing the translational stage speed. The laser spot size was chosen to be 1mm so that a single pass could irradiate the entire width of the 1mm isolated track, as well as keep any possible temperature rises to an absolute minimum. The 1mm diameter circular beam gave an irradiance of 60kWm^{-2}. The sheet resistance values after irradiation with the HeCd laser are shown in figure 5.21. As the translational speed becomes lower, the sheet resistance values also become lower, as we would expect. The difference between the glass and PET substrate sheet resistance is similar to that seen with the XeCl laser irradiation, and is due to the thinner ITO film on the PET substrates. The lowest sheet resistance achievable with the HeCd laser was just under 30kΩ/sq, which is an order of magnitude higher than achievable with the XeCl laser. For a better comparison between the two laser systems, using equation 5.8 we can adjust the absorbed laser dose for each laser system for a more direct comparison.

$$\frac{P_{cw}D_{cw}}{A_{cw}F_pN_pV_{cw}} = \frac{(1-R_p)(1-exp(-\alpha_p t))}{(1-R_{cw})(1-exp(-\alpha_{cw} t))} \tag{5.8}$$

Using equation 5.8, it is possible to match the accumulated energy for both the XeCl and HeCd laser, taking into account the differences in absorption depth at the two wavelengths. Using the parameters used for the experiment from figure 5.21, an experiment was conducted using the XeCl to match the energy dose from the HeCd laser. From the HeCd laser, the power, P_{cw}, was 46mW, the beam diameter, D_{cw}, was 1mm, the beam area, A_{cw}, was 0.785mm^2 and the velocities, V_{cw}, were used from figure 5.21. From the right side of the equation, the absorption coefficients for the HeCd and XeCl, α_{cw} and α_p respectively, were used from figure 5.2 and were 5.5$\times$10^{5}m^{-1} and 1.18$\times$10^{6}m^{-1} respectively. The reflection losses, R_{cw} and R_p, were calculated using refractive

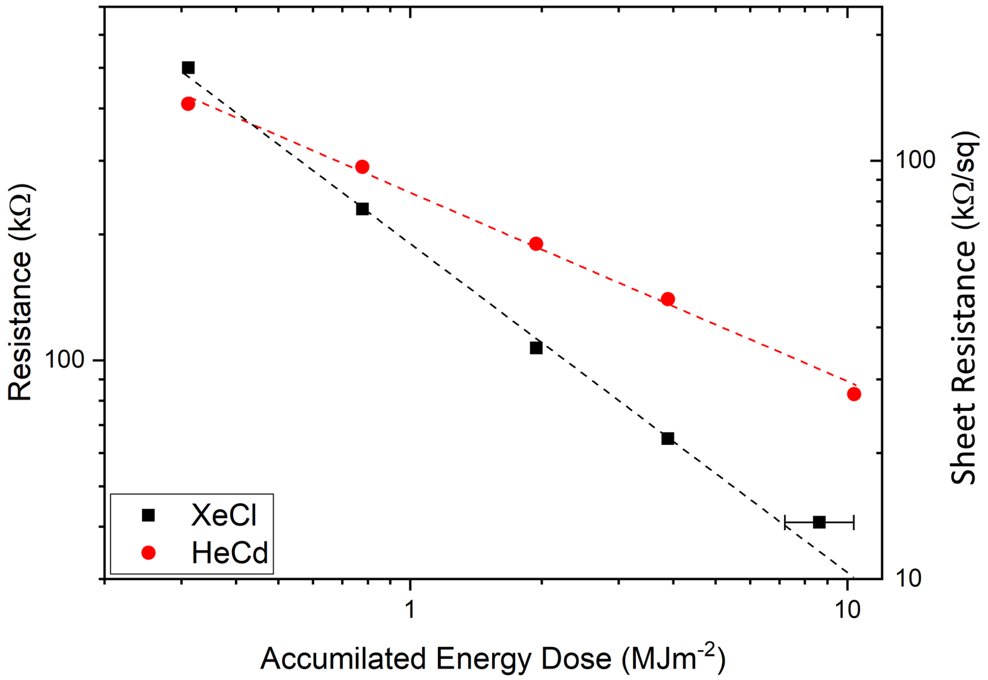

FIGURE 5.22: Sheet resistance measurements of ITO films irradiated with the HeCd and XeCl laser. Fluence of the XeCl laser was 50mJcm^{-2} and the irradiance of the HeCd was 60kWm^{-2}

index data provided by INM. For the XeCl laser, the fluence, F_p, was chosen to be 50mJcm^{-2}, leaving only the number of pulses per area, N_p, to be calculated from the equation to give an experiment with the equivalent dose. Figure 5.22 shows the results from the experiment.

The sheet resistance values from the HeCd laser do not change as quickly as the XeCl laser. Even when the XeCl laser was set to a lower than maximum achievable fluence of 50mJcm^{-2}, the sheet resistance values reduce with accumulated energy does at a faster rate, making the XeCl laser the more suited ultraviolet laser source compared with the HeCd. This effect is provisionally attributed to the higer photon energy of the XeCl laser being more efficient in causing photochemical effects such as cross-linking of the binder and photodecomposition of the solvents.

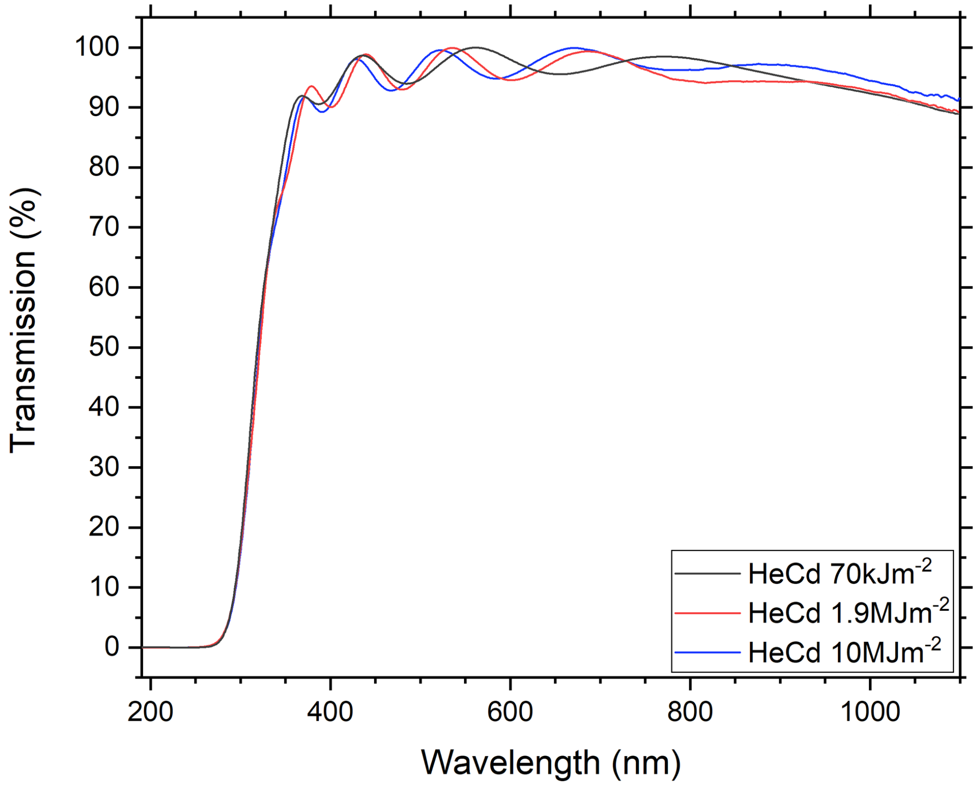

FIGURE 5.23: UV-VIS transmission spectra of the ITO films on fused silica substrates which were irradiated using the HeCd laser at 3 accumulated doses.

5.3.4 Optical Measurements

To measure the optical properties of the ITO films after irradiation with the HeCd laser, the 6mm square isolated areas were used as before. The UV-VIS transmission spectra were taken for 3 doses following irradiation, and the results are shown in figure 5.23. The transmission of the ITO films after irradiation with the HeCd laser does not change significantly over the visible range, and the ultraviolet absorption edge does not appear to alter either. Importantly though, the interference peaks shift slightly between each different irradiation condition, which indicates a change in the thickness of the ITO films or the refractive index. Constructing a Tauc plot from the transmission spectra, shown in figure 5.24, we see again that the bang gap of the material is not

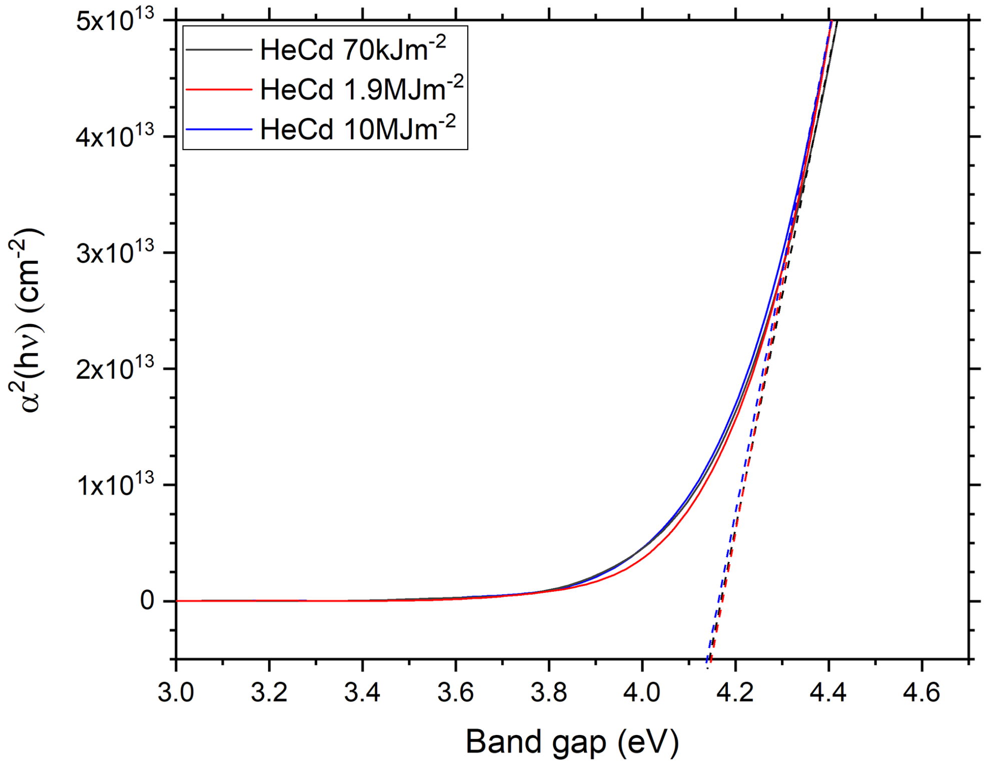

FIGURE 5.24: Tauc plot constructed from figure 5.23 to measure the band gap of the ITO films after various doses from the HeCd laser.

changing significantly.

5.3.5 Surface Measurements

As mentioned, in figure 5.23 the transmission spectra show the interference peaks shifting slightly between different doses. To check whether this is due to a change in refractive index or thickness, the Dektak XT surface profilometer was used to measure across an irradiated track. Figure 5.25 shows the surface profile. The film thickness after irradiation with the HeCd laser shrinks by a maximum value of 40nm in the centre. The film thickness change in the irradiated area is largest at the centre, shrinking less towards the edges. This is to be expected because even though the HeCd laser beam has a uniform

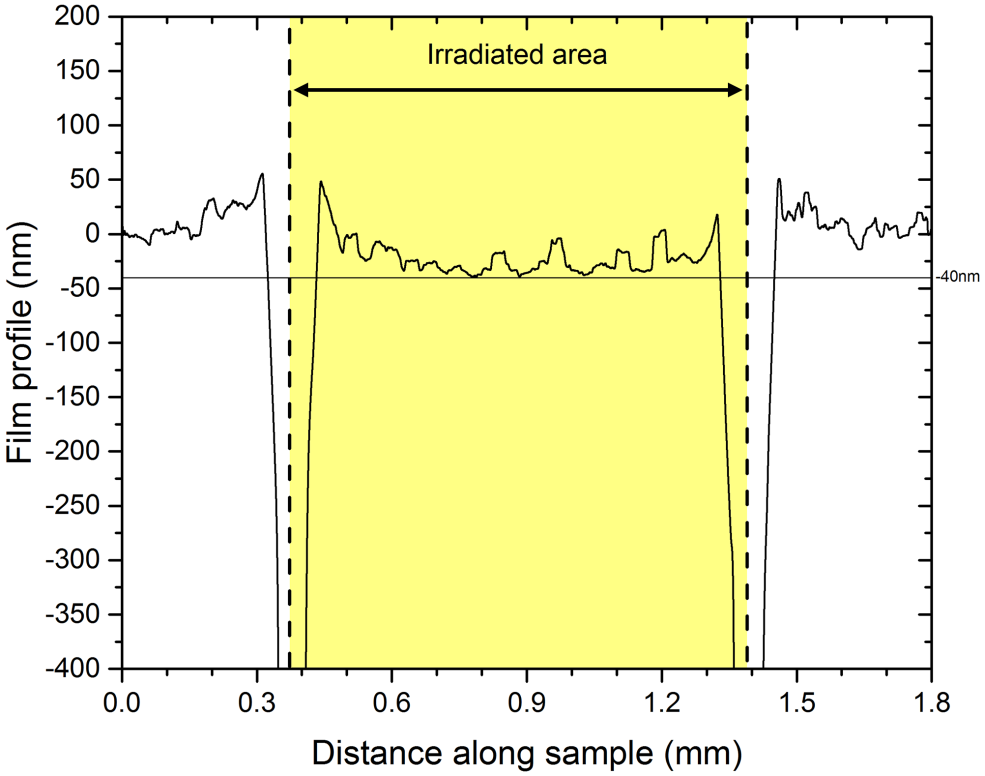

FIGURE 5.25: Dektak surface profile measured across an isolated area irradiated with the HeCd laser at an accumulated energy dose of 10MJm^{-2}, at an irradiance of 60kWm^{-2}.

top hat beam profile, it is circular, and as the beam travels along the track the centre will receive a larger accumulation of laser energy. An example of this is shown in figure 5.26.

The film shrinkage observed from the HeCd irradiation is similar to that seen by INM when cured by a mercury lamp under the same conditions (Fig. 5.14).

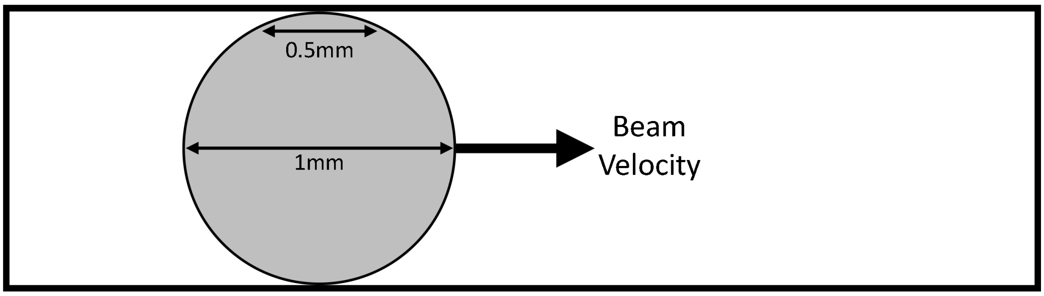

FIGURE 5.26: Example of the difference in accumulated energy dose when a circular beam is used. Nearer the edges of the track, the time exposed by the laser beam is reduced.

The HeCd laser more closely simulates the conditions experienced by the ITO films under an mercury lamp by having a continuous output of ultraviolet light. For the accumulated energy dose of $10\mathrm{MJm}^{-2}$, the HeCd laser beam was continuously irradiating the same spot for approximately 7 minutes. The ITO films at INM were cured for 10 minutes under the mercury lamp. In comparison, for the XeCl laser, the same accumulated energy dose of $10\mathrm{MJm}^{-2}$ took 29000 pulses per area. Each pulse has a FWHM of 4.1ns, meaning the laser was only irradiating the films equivalently for a little over 100µs. As we can expect that any of the photochemical processes will be rate limited, a deviation from exposure reciprocity is also expected.

The ITO film roughness did not change under any achievable irradiance with the HeCd laser on glass substrates, and thus the haze did not change. Under all HeCd irradiation regimes, the haze of the ITO films was measured to be near the same as the unirradiated ITO, at around 1% when measured with the HeNe at 632.8nm.

5.4 ArF Laser Irradiation

For the ArF laser at a wavelength of 193nm, figure 5.2 cannot tell us the absorption depth, as the absorption coefficient is too large to be measured by this equipment. The standard films on glass used throughout the project at a thickness of 520nm were too thick, and so, INM supplied ITO films on a fused silica substrate at a thickness of $\sim$73nm. Taking the transmission spectra of the 73nm ITO films, the absorbance at 193nm was below 1, well within the limits

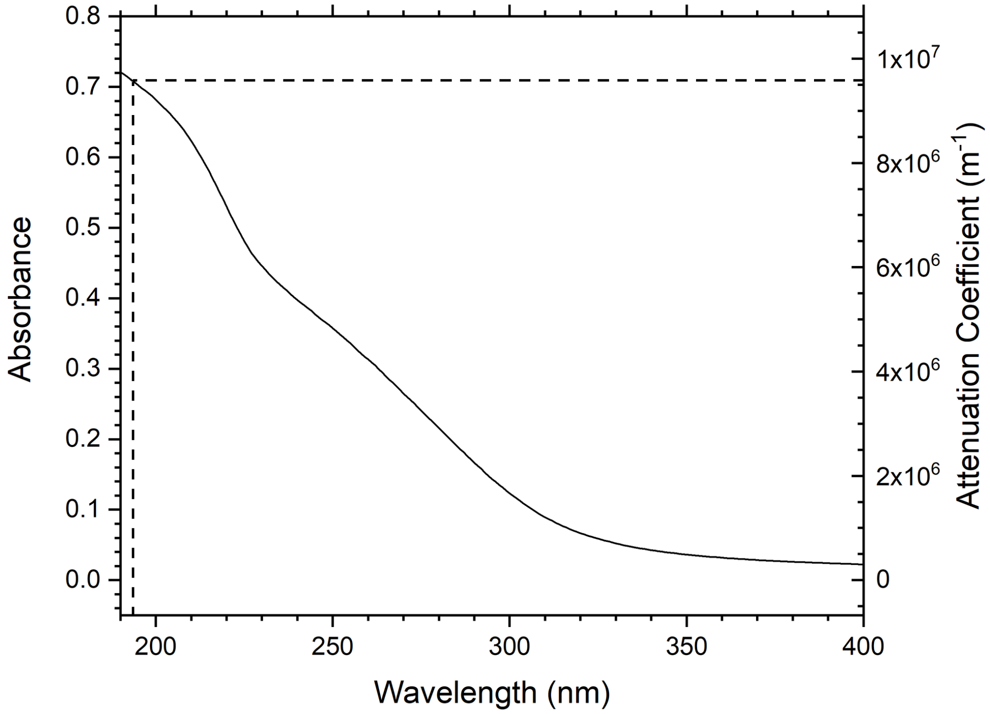

FIGURE 5.27: Attenuation coefficient for the ITO films with 73nm thickness. The absorption depth at 193nm wavelength is 105nm.

of detection as shown in figure 5.27. With a measured absorption coefficient of $9.56\times10^{6}\mathrm{m}^{-1}$, corresponding to an absorption depth of 105nm, the ArF laser will not be able to effectively irradiate the entire thickness of the ITO films, as illustrated in figure 5.28. The measured sheet resistance of the ITO films was therefore predicted to be higher than expected, as only a fifth of the depth of the films was being irradiated.

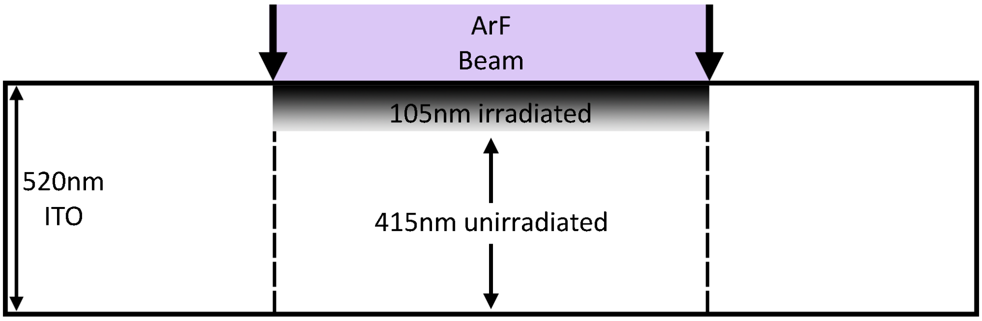

FIGURE 5.28: A demonstration of the absorption depth of the ArF laser beam into the ITO films. Only 20% of the thickness is irradiated.

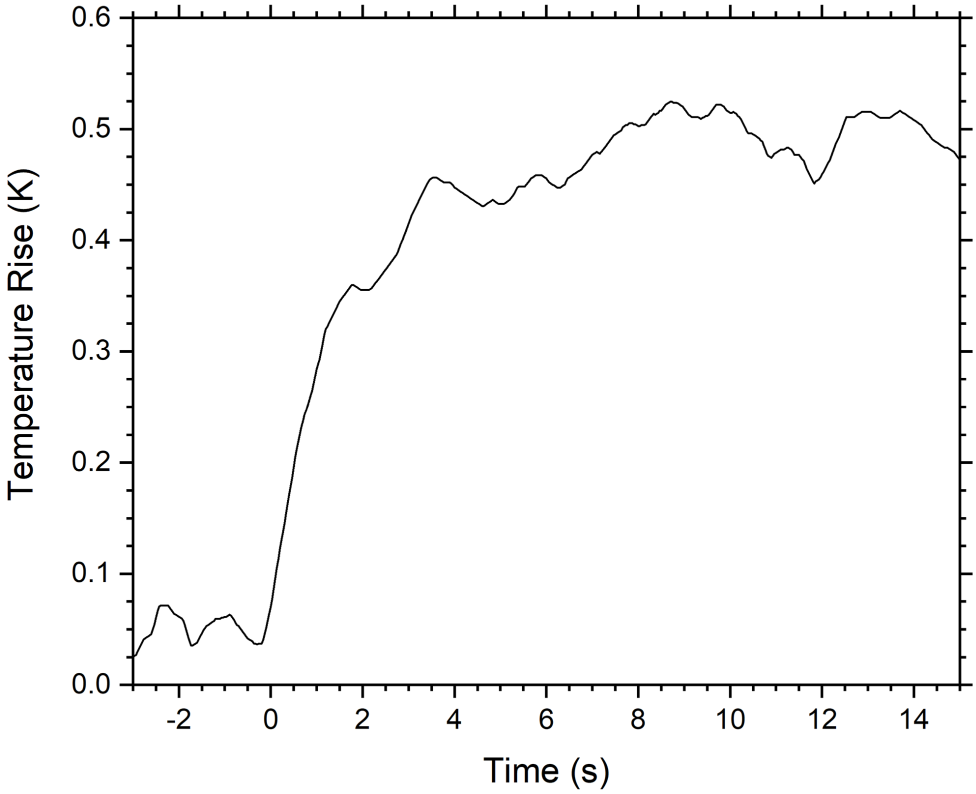

FIGURE 5.29: Temperature rise of the ITO films when irradiated with the ArF laser with a repetition rate of 10Hz and fluence of 50mJcm^{-2}.

5.4.1 Temperature Measurements

The ArF laser behaves very similarly to the XeCl laser, with a shorter wavelength at 193nm. The maximum pulse repetition rate of the system was limited to only 10Hz. The accumulated temperature rise with such a low repetition rate was expected to be very small, and as measured by the FLIR thermal camera in figure 5.29, 15 seconds of irradiation gave a steady state temperature rise of less than 1°C. The data taken from the FLIR camera for such small temperature rises was noisy, and so data smoothing was used on the graph to shown in figure 5.29.

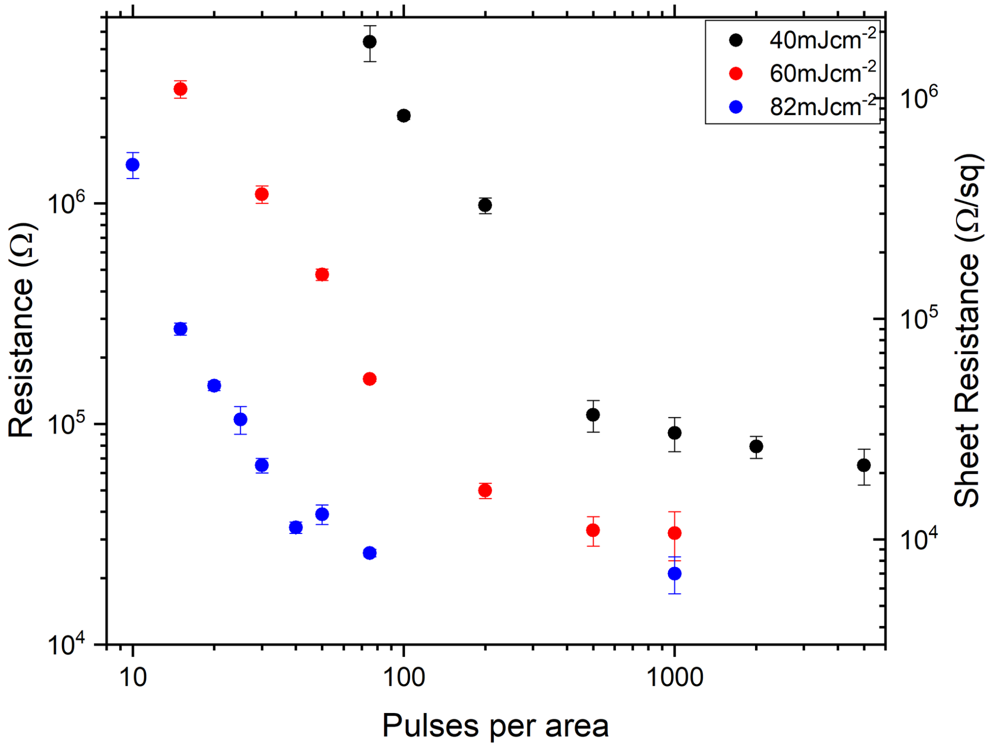

FIGURE 5.30: Temperature rise of the ITO films when irradiated with the ArF laser with a repetition rate of 10Hz and fluence of $50 \mathrm{mJcm}^{-2}$.

5.4.2 Electrical Resistance Measurements

Due to restricted access to the laser, a complete study of the ArF laser irradiation of the ITO films was not possible. Therefore, only electrical measurements were taken on the 520nm ITO films on glass substrates. PET substrates were not tested, but from the temperature measurements it is highly likely that the PET substrates could have been irradiated without problems. Potential UV damage to the PET would also be avoided by the strong absorption of the laser light by the ITO.

Irradiation of the ITO films on glass with the ArF laser gave some promising sheet resistance results, shown in figure 5.30. It is important to note, to measure the resistance for the ArF laser irradiated samples a different setup was used. Because of the time restrictions on the laser system, a simple multimeter and 2 hand-held probes were used to speed up measurements. The multimeter had an upper limit of 10MΩ. The sample beforehand was not measurable on the equipment, i.e. >10MΩ over 3mm. At a fluence of 40mJcm^{-2}, the sheet resistance became measurable after 100 pulses per area, and reached a minimum sheet resistance of around 20kΩ/sq after 5000 pulses per area. At the maximum fluence achievable of 82mJcm^{-2}, the sample was measurable after just 10 pulses per area, and reached a lowest sheet resistance value of 7kΩ/sq. Importantly though, at a fluence of 82mJcm^{-2}, the sheet resistance started to saturate after just 100 pulses per area, which is a huge improvement over the XeCl laser.

Even with the promising results of the ArF laser, the sheet resistance could not get as low as was achievable with the XeCl laser. This could be due to the small absorption depth at 193nm. Resistivity is a better measure of the specific resistance values for materials, which takes into account the thickness. Resistivity, ρ, is calculated from sheet resistance from equation 5.9

$$\rho = R_{sheet} \times thickness \tag{5.9}$$

The XeCl laser at 308nm can irradiated the entire thickness of the 520nm ITO films. The resistivity of the XeCl irradiated films reach a minimum value of 78mΩ cm. If we consider the ArF irradiated films to only be a thickness of 105nm, the corresponding resistivity of the ITO would then be 76mΩ cm. This result agrees with the hypothesis that only a fraction of the ITO films is affected

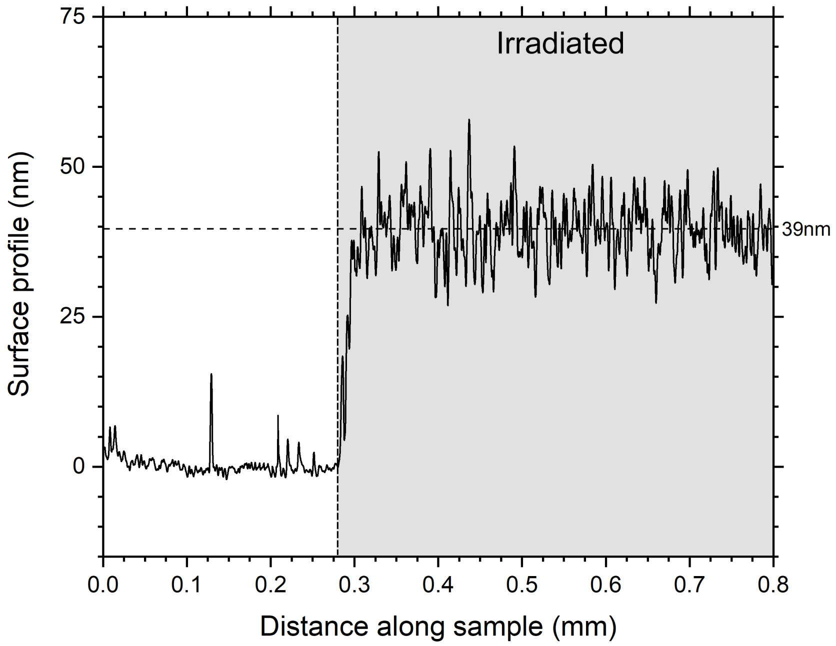

FIGURE 5.31: Dektak XT surface profile going across an area irradiated with the ArF laser at 82mJcm^{-2} with 100 pulses per area.

by the 193nm wavelength radiation. It also shows that the shorter wavelength does not decrease the minimum achievable sheet resistance, but does reduce the amount of time required to reach that minimum compared with the 308nm radiation.

5.4.3 ITO Damage

As seen with the XeCl laser, at a high enough fluence the ArF irradiation could start to damage the films, causing them to become hazy. At the highest fluence used with the ArF laser, 82mJcm^{-2}, the ITO films exhibited the same behaviour as the XeCl laser. Figure 5.31 shows a Dektak surface profile along a damaged area of the ITO films. The ITO films become very rough after irradiation, and begin to increase in thickness. The haze measurements from the ITO films after ArF irradiation were very similar to those following XeCl irradiation. The films stayed at around 1% haze throughout all the irradiated areas, except the ones irradiated at a fluence of 82mJcm^{-2}, where the haze varied between 10 and 20% depending on the number of pulses.

5.5 Conclusions

In this chapter, ITO films containing an ultraviolet curable binder were irradiated with 3 ultraviolet laser sources to reduce the resistivity of the material. The ultraviolet lasers used all had low temperature processing capabilities, below 10°C rises form prolonged periods, which made it possible to irradiate the ITO films on temperature sensitive substrates. Using a continuous wave HeCd laser, a sheet resistance of 30kΩ/sq could be reached with an accumulative energy dose of 10MJm^{-2} at an irradiance of 60kWm^{-2}. This level of sheet resistance is over 3 orders of magnitude higher than commercially available ITO films. Using pulsed excimer laser sources in the ultraviolet gave improved results. The XeCl laser was able to reduce the sheet resistance down to 2kΩ/sq, which was an order of magnitude better than the continuous wave HeCd, but still 2 orders of magnitude higher than commercial ITO. The best result from the ultraviolet laser sources was the ArF laser. Having the highest photon energy at 6.42eV, the ArF laser was able to reduce the sheet resistance of the ITO films to around 7kΩ/sq. Due to the short absorption depth of the ArF laser at 105nm, the corrected resistivity value is very similar to the XeCl irradiated samples, but the lowest resistivity was achieved with much fewer pulses. Still, due to the low repetition rates of the excimer lasers the processing times on an industrial scale would be very large. A better choice would possibly be a 4th harmonic Nb:YAG laser at $\lambda = 266$nm. This would give a higher photon energy than that of the XeCl laser, a larger absorption depth than the ArF laser and a much higher pulse repetition rate. The optical transparency of the ITO films remained above 90% for the majority of the visible wavelength range throughout irradiation with each laser source and the haze remained at around 1% with the exceptions of the highest fluences of the XeCl and ArF lasers which started to induce damage, limiting the transmission and increasing the haze dramatically.

Chapter 6

CO_2 Laser Processing of ITO Films

6.1 Introduction

In this chapter, three different CO_2 laser sources are used to irradiate the wet processed ITO films on glass and PET substrates, investigate laser-induced reduction of electrical resistivity. The same approach was used as the ultraviolet laser processing (Chaper 5). Preliminary experiments were conduced to test if the laser source was able to reduce the resistivity, and if so, a complete study was performed for that source.

As the photon energy of the infrared lasers is $\sim$0.1eV, the interaction with the ITO is thermal, by inducing temperature rises in the films directly, or indirectly from heating the substrate. The process by which the ITO films are expected to increase in conductivity under thermal processing comes in two steps. First, the MPTS binder will be removed under irradiation of the CO_2 laser, followed by sintering of the ITO nanoparticles to form a more continuous film. This means increasing the temperature of the films above the thermal decomposition temperature of the MPTS binder. This poses a problem for the ITO films on flexible substrates, since the melting temperature of PET is only slightly higher than the boiling point of MPTS. [128, 129] To try and minimise the damage induced to the PET substrates, pulsed laser sources will be used to keep accumulated temperature rises as low as possible, whilst still achieving the desired result. It is also possible to raise the temperature above the melting point of materials without damage, as long as the time scales are short enough. [130, 131] However, this relies on the processing step of the ITO films to occur on a faster time-scale than the damage to the substrate.

Measuring the absorption depth at the CO_2 laser wavelength of 10.6µm for the ITO films was not possible. The substrates the ITO films were provided on were not transparent at 10.6µm wavelength, and hence could not measure transmitted light of the samples. Without a reflection attachment for the FTIR, we also could not measure how much of the light the ITO films reflects at 10.6µm due to the low amount of reflected light, so it was assumed all the light is absorbed into the films and/or substrate for the temperature calculations.

6.2 RF:CO_2 Laser Irradiation

6.2.1 Electrical Resistance Measurements

The RF:CO_2 laser used was a continuous wave laser having a maximum output power of 12W. Modulation of the laser was possible via a TTL signal, with

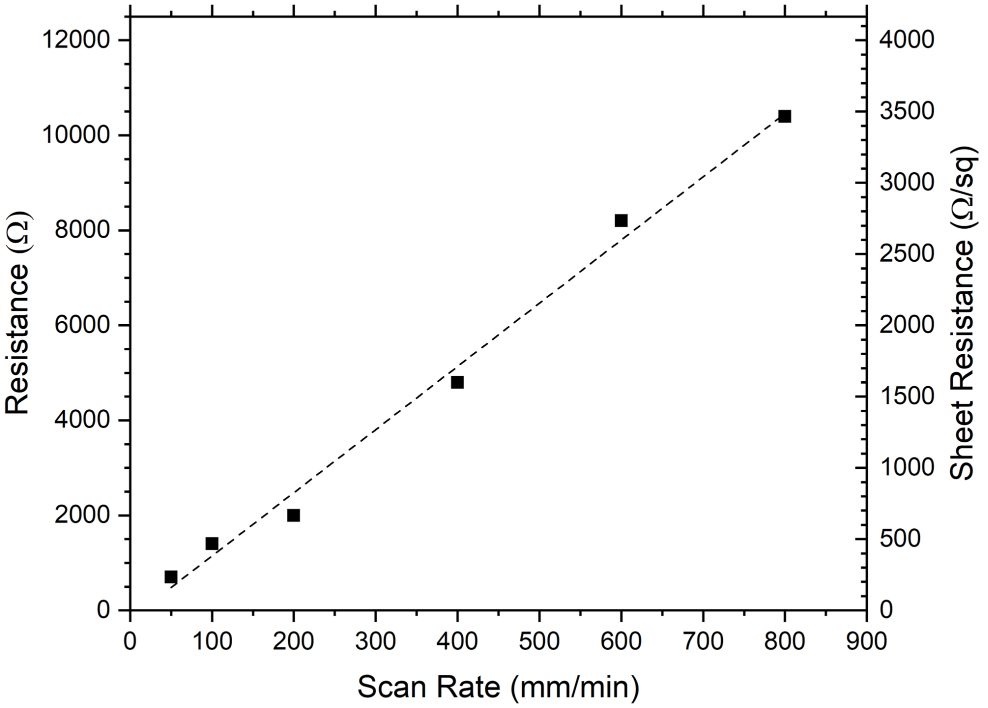

FIGURE 6.1: Sheet resistance measured on the ITO films on glass after irradiation with the RF:CO_2 laser at 12W with an unfocussed 3mm diameter beam.

the shortest response of the laser being around 100µs for a stable output. Irradiation of the ITO films on glass substrates gave very good results. Using the maximum continuous power of the RF:CO_2 laser at 12W, along with the unfocussed beam with a diameter at $1/e^2$ of 3mm (Measured in Fig. 4.13), sheet resistances down to around 250Ω/sq could be reached as shown in figure 6.1.

Translational speeds below 50mm/min resulted in damage to either the films or substrate. The borosilicate glass started to crack and fracture at 25mm/min, making the films discontinuous and non conductive over larger distances. Even though borosilicate glass can withstand thermal stresses better than commonly used soda lime glass, cracking can still be observed due to the large thermal gradient produced by the laser beam.

Measuring the temperature rise of the ITO films under CO_2 irradiation was not

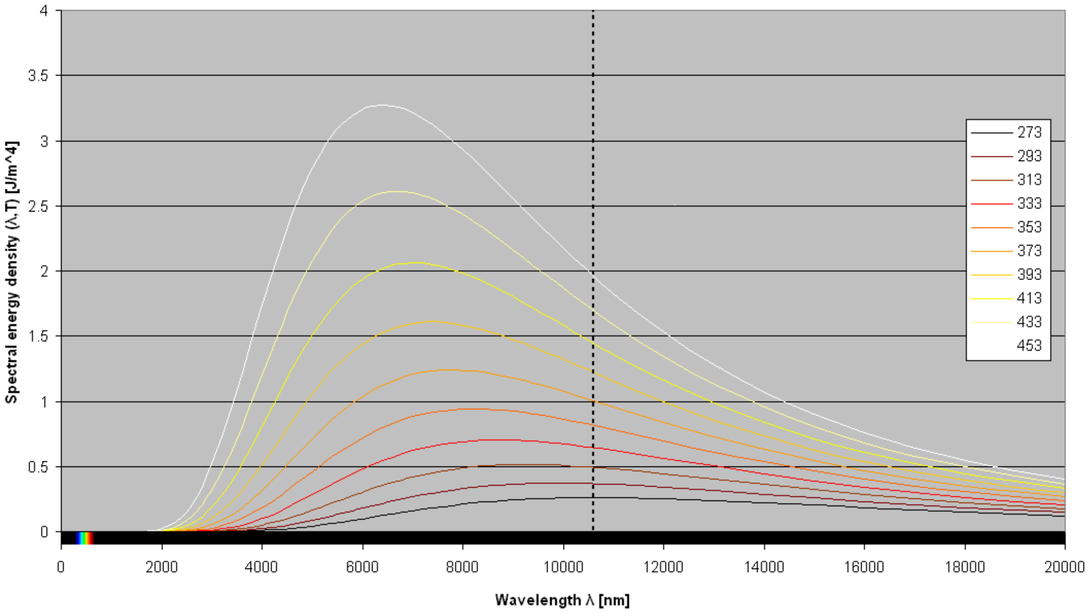

FIGURE 6.2: Blackbody spectrum for temperatures ranging from 273K to 453K. The black dashed line represents the CO_2 laser wavelength of 10.6μm. [132]

possible with the FLIR thermal camera. The FLIR thermal camera used a germanium lens for imaging, which readily transmits the 10.6μm laser radiation onto the sensor. This posed two problems. The main worry was that the CO_2 laser radiation would be too intense for the thermal camera and it would become permanently damaged. The second reason is that the infrared light from the laser could interfere with the camera temperature measurements, since radiation at 10.6μm is present in the blackbody spectrum for a large range of temperatures, as seen in figure 6.2. Having a large peak in the blackbody spectrum at 10.6μm would interfere with the temperature calculations within the camera software, causing errors in the measurements.

The temperature rises have been estimated using the parameters used from the laser with the material properties. Taking the example of the lowest sheet resistance achieved, the translational speed of the laser was 50mm/min. Using this, we can calculate the area the beam irradiated in 1 second. Assuming all the laser energy is absorbed into the sample at the surface of the sample, using equation 2.1 from earlier (also seen below), a heat affected zone can be calculated.

$$\delta = 2\sqrt{D_H \tau} \tag{2.1}$$

From the beam area and heat affected zone, a volume that is heated by the laser is calculated. The ITO films are located on 3mm thick pieces of Schott Borofloat 33 glass substrates, which contribute the vast majority of the sample. For this reason, the temperature rises are assumed to be controlled mainly by the glass parameters. Schott Borofloat 33 has a thermal diffusivity of $6.57 \times 10^{-7} m^2 s^{-1}$, density of $2.2 gcm^{-3}$ and a specific heat capacity of $0.83 Jg^{-1} K^{-1}$. [93] From these parameters, a thermal diffusion length of 0.81mm is calculated, giving an affected volume of $12.3 \times 10^{-3} cm^3$. Using the density of the glass, the affected volume has a mass of 0.028g. Now, using equation 6.1 we can calculate the temperature rise of the sample. Where, Q, is the energy provided by the laser, m, is the mass been heated and c_p is the specific heat capacity of the glass.

$$\Delta T = \frac{Q}{mc_p} \tag{6.1}$$

An estimated temperature rise of 520°C is induced into the sample. From the literature review, ITO films are typically processed at over 500°C, so this estimate gives a comparable temperature rise.

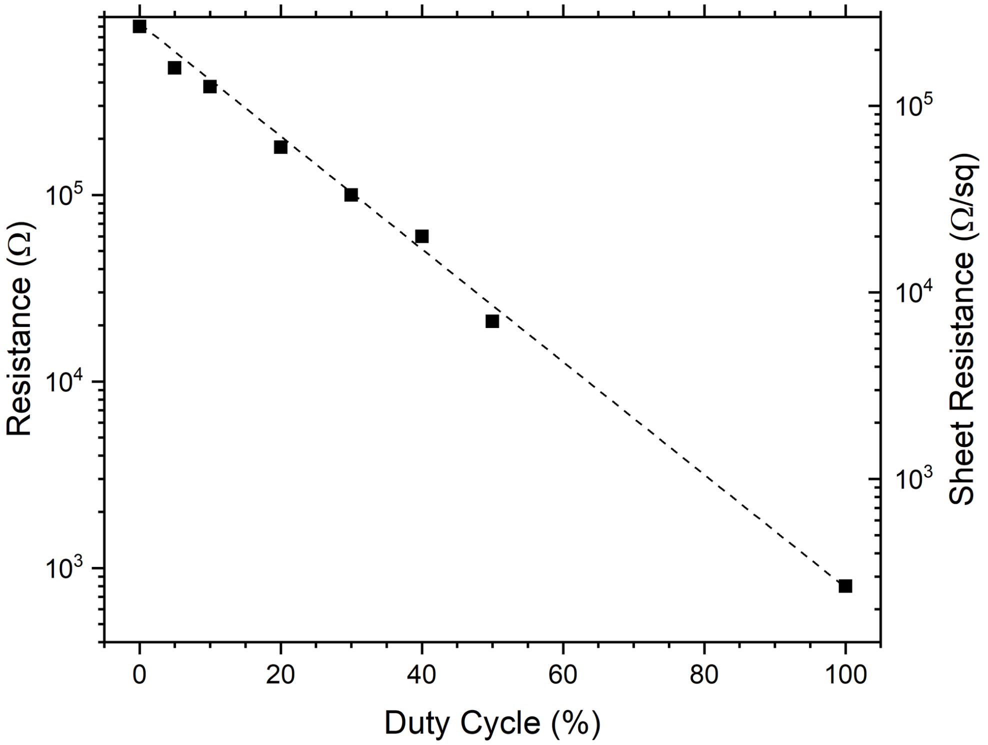

FIGURE 6.3: Sheet resistance measured on the ITO films on glass after irradiation with the RF:CO_2 laser at various TTL duty cycles with an unfocussed 3mm beam. The modulation frequency was 500Hz, and translational stage at 50mm/min

Irradiation of the films on PET substrates at the maximum power of 12W with an unfocussed beam melted the substrate at any speed possible with the translational stages. To try to minimise the damage caused to the substrates, the average power of the RF:CO_2 laser was varied by applying a 500Hz modulation and lowering the duty cycle of the pulses. Figure 6.3 shows how the duty cycle affected the sheet resistance of the films on glass substrates. Reducing the duty cycle of the RF:CO_2 laser significantly increased the achieved sheet resistance value. For the PET substrates, even at a 5% duty cycle with 50mm/min translational speed, damaged was observed making the RF:CO_2 laser an unlikely candidate for processing the ITO films on temperature sensitive substrates.

Most of the irradiation experiments performed with the RF:CO_2 laser were

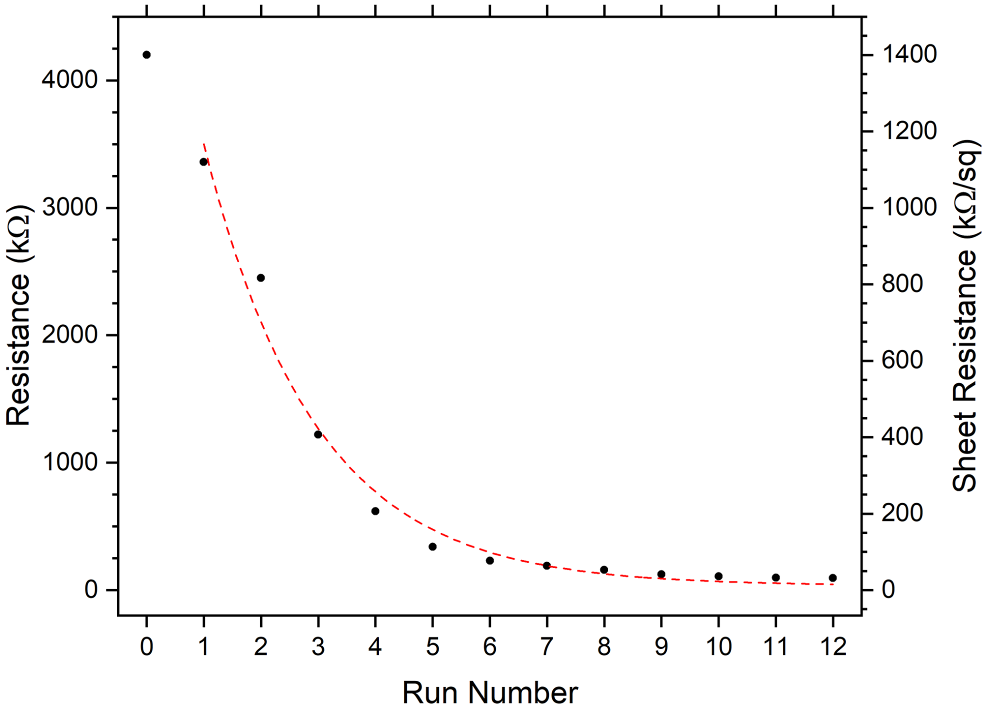

FIGURE 6.4: Sheet resistance values measured from multiple passes of RF:CO_2 laser irradiation with a 10 minute cool down between runs. A 4W beam modulated at 250Hz with a 2mm beam diameter was used, which was translated at a speed of 180mm/min

completed in a single pass along a 1mm track with the unfocussed 3mm beam. An experiment was carried out to see how numerous passes over the same area affected the overall sheet resistance of the ITO films. In this experiment, a single track was irradiated an increasing number of times with a 4W average power beam (2mm diameter), which was modulated at 250Hz. Each run consisted of a single pass over the track at 180mm/min, followed by a 10 minute cool down before measuring the sample. This was repeated 12 times, figure 6.4 shows the results for this experiment.

This experiment gave interesting results. It shows that an accumulative lowering of the sheet resistance can be achieved by repeatedly irradiating the ITO films, even after the films were cooled to room temperature between runs.

Unfortunately, the decrease in sheet resistance between each run becomes less as the number of runs increases, before reaching a stable point where further improvements cannot be made. Whilst the improvements for numerous runs in this experiment gave an order of magnitude lower sheet resistance over the single pass irradiation, it was still 2 orders of magnitude higher than the 250Ω/sq that can be achieved by increasing the power of the laser, and increasing the temperature of the films. This indicates that a higher temperature is required to remove or decompose the binder, and that a lower temperature for longer times has left dielectric material between the ITO nanoparticles.

6.3 TEA:CO_2 Laser Irradiation

The continuous wave RF:CO_2 laser was very good at processing the ITO films on glass substrates, achieving the lowest sheet resistance so far, but was not successful at irradiating the ITO on the temperature sensitive PET substrates without damage. Reducing the irradiance of the laser low enough so that damage did not occur, meant that a change in the electrical conductivity could not be measured. This was likely due to the long pulse lengths of the RF:CO_2 laser, and so a shorter pulse TEA:CO_2 laser was used.

6.3.1 Irradiation of ITO on PET substrates

The pulses from the TEA:CO_2 laser are less than 1µs in duration with a fluence of around 750mJcm^{-2}, and thus should induce higher peak temperatures into

TABLE 6.1: Table showing the sheet resistance of ITO films on PET substrates after TEA:CO_2 laser irradiation at various frequencies. Each spot had 2000 pulses per area at 250mJcm^{-2}

Frequency (Hz)	Sheet Resistance (Ω/sq)
2	>100M
5	>100M
10	>100M
15	>100M
20	>100M

the ITO films, but for shorter periods of time. Putting the ITO films into the non-imaged beam directly from the laser resulted in ablation of the films with a single pulse. A magnification of the beam was required to reduce the fluence of the beam to below the ablation threshold. Visible damage stopped when the fluence was reduced to around 250mJcm^{-2}, so irradiation of the films was conducted at this fluence. The results are shown in Table 6.1. After irradiation of the ITO films on PET substrates, the sheet resistance was unmeasurable on the Tektronix DMM4020, with an upper limit of 100MΩ. This result was not expected, since the films beforehand had a sheet resistance of around 500kΩ/sq. With no visible damage to the films, they were viewed under the microscope. As can be seen in figure 6.5 the films exhibit micro-cracking when irradiated with the TEA:CO_2 laser. At a fluence of 250mJcm^{-2} the cracks make the ITO films discontinuous, causing the resistance between the probes too high to be measured by our equipment. The cracks were too closely packed to be able to measure the resistance of the islands of ITO films in between the cracks, so it is unknown if the films became more conductive or not.

Reducing the fluence to 150mJcm^{-2}, the ITO films were again irradiated with

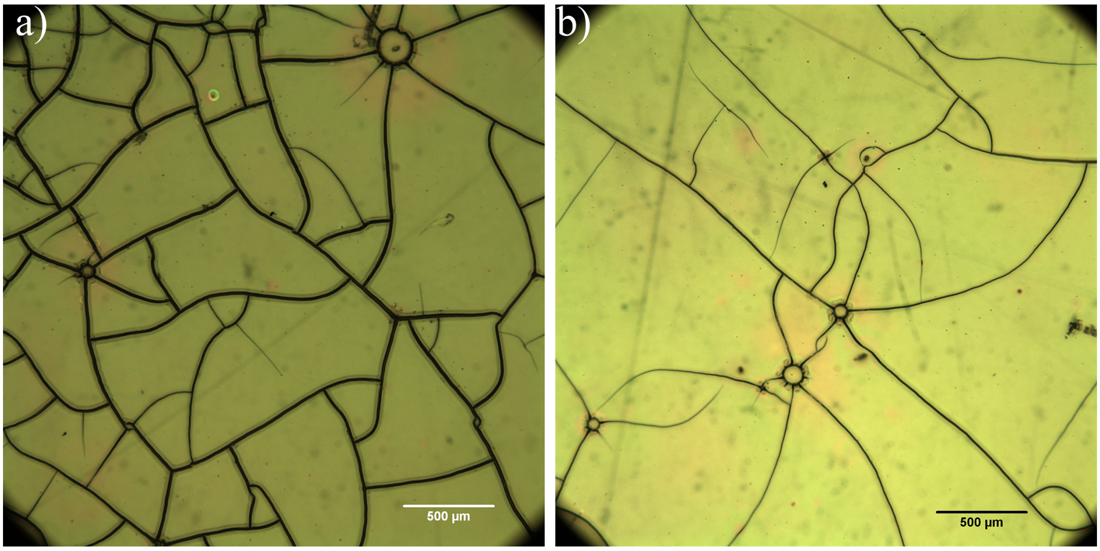

FIGURE 6.5: Micro-cracking observed in the ITO films on PET substrates when irradiated by the TEA:CO_2 laser at **a)** 250mJcm^{-2} and **b)** 150mJcm^{-2}. Each area was irradiated with 2000 pulses per area.

2000 pulses per area at various frequencies. The electrical results were the same as seen in table 6.1 and the resistance could not be measured. Under the microscope, the films were still cracked, but not to the same extent, as seen from figure 6.5b. Measurements could be made within some of the islands, but it was inconclusive whether or not the films were increasing in conductivity due to widely varying readings. The fluence of the TEA:CO_2 laser had to be reduced to a value of 65mJcm^{-2} before the micro-cracking was not observed, at which point, even when the repetition rate of the laser was increased to the maximum of 20Hz no change in the resistance of the films could be measured following irradiation.

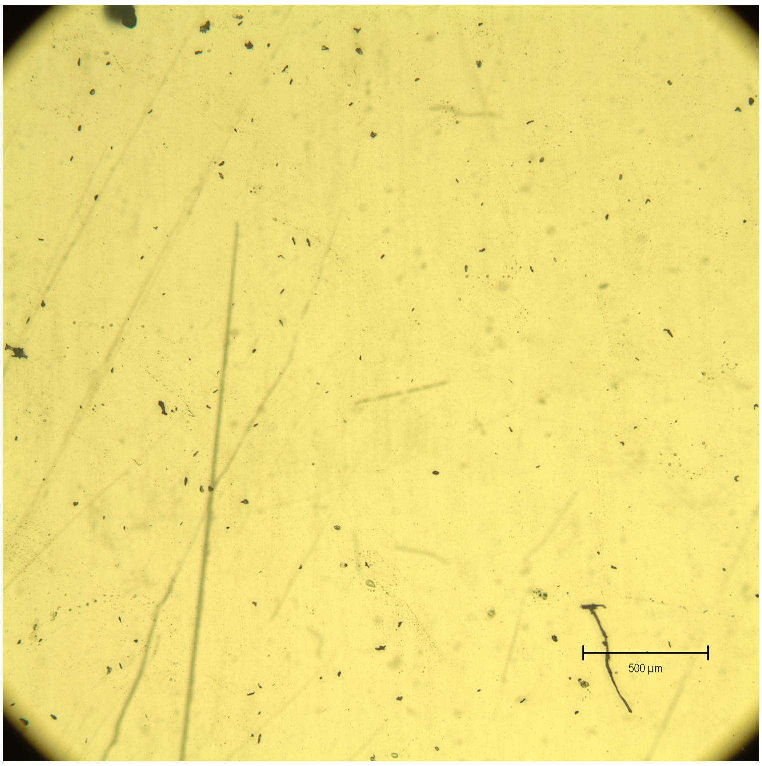

FIGURE 6.6: View of the ITO films irradiated with the TEA:CO_2 laser at a fluence of 250mJcm^{-2} with 2000 pulses per area. No cracking is observed.

6.3.2 Irradiation of ITO on glass substrates

Irradiation of the ITO on glass substrates with the TEA:CO_2 laser was also conducted under the same regimes as for the PET. Irradiation of the ITO in the direct non-imaged beam gave the same results as the PET, ablation of the films. Using the same magnification of the beam to reach a fluence of around 250mJcm^{-2}, following 2000 pulses per area the films had a measurable resistance that had decreased after irradiation. In figure 6.6, it is clear that the ITO films on a glass substrate do not experience micro-cracking in the way observed with the PET substrates.

Further experiments were carried out using the TEA:CO_2 laser to try to reduce the sheet resistance of the ITO films as low as possible using a fluence of

TABLE 6.2: Table showing the sheet resistance of ITO films on glass substrates after TEA:CO_2 laser irradiation at various frequencies. Each spot had 18000 pulses per area at 250mJcm^{-2}

Frequency (Hz)	Sheet Resistance (Ω/sq)
5	85k
10	10k
20	4k

250mJcm^{-2} with 18000 pulses per area at varying pulse repetition rates. The results are shown in table 6.2.

The TEA:CO_2 laser was able to reduce the sheet resistance of the ITO films down to 4kΩ/sq, at the maximum pulse repetition rate of 20Hz with 18000 pulses per area. At lower frequencies, the sheet resistance reached was not as low in comparison, even though the films received the same amount of accumulated energy. This is due to the slower repetition rates of the laser not being able to achieve a high accumulative temperature rise in the films. Further tests were conducted with the TEA:CO_2 laser, however, over longer periods of irradiation the laser started to lose more than 90% of it's output power even with water cooling. It was decided that for the longevity of the laser not to continue any further tests.

6.4 QSW:CO_2 Laser Irradiation

In the studies presented up to this point, the continuous wave RF:CO_2 laser has given the best results on glass substrates, but caused damage to the films on PET substrates. The TEA:CO_2 laser could irradiate the ITO films on the

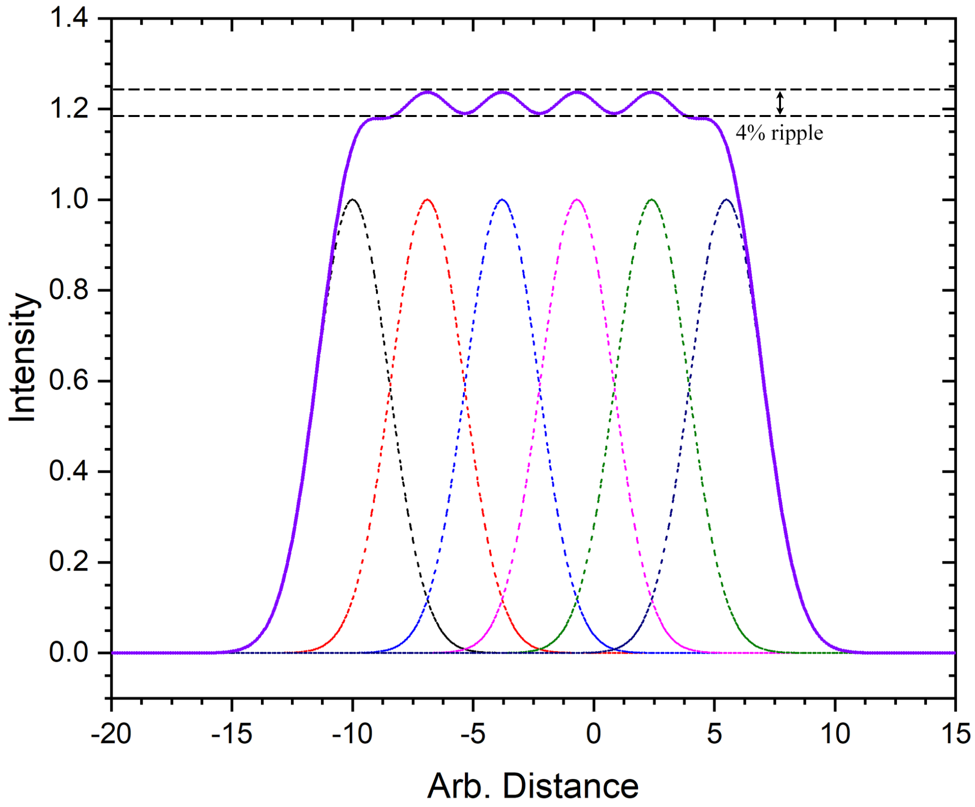

FIGURE 6.7: 6 overlapping Gaussian beams set at 50% $1/e^2$ spacing, along with the resulting overall profile of the overlapped beams. A 4% difference in intensity is seen.

PET substrates without melting them, but due to micro-cracking and a low pulse repetition rate the ITO could not be reduced in resistivity by a measurable amount. The QSW:CO_2 laser is a pulsed laser like the TEA:CO_2, but with much higher repetition rates (up to50kHz), with shorter pulse durations (below 200ns). The QSW:CO_2 laser aims to bridge the gap between generating a low electrical resistivity, whilst being able to irradiate the films on temperature sensitive substrates.

To try and keep temperature rises to a minimum amount of time, a spot size that was small when compared with the thermal diffusion length of the material was used. Due to the Gaussian irradiance profile of the laser, the beam overlap was set at 50% of the $1/e^2$ beam diameter to make sure the entire film

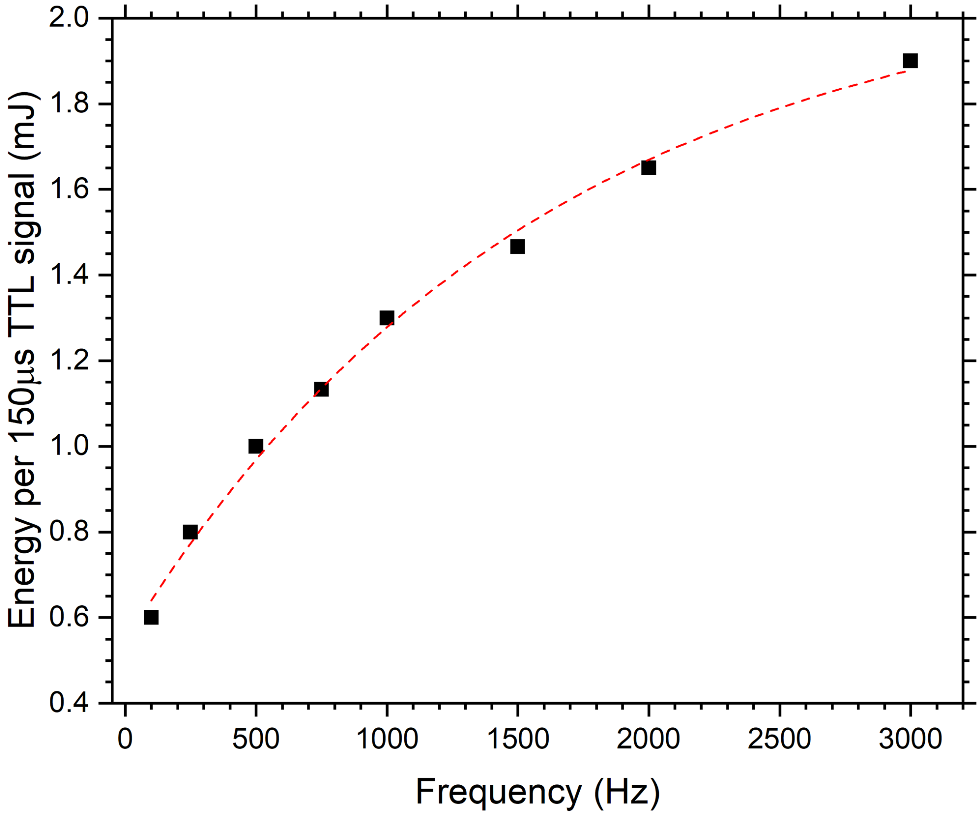

FIGURE 6.8: Average energy per TTL signal for the QSW:CO_2 laser at various modulation frequencies.

had an even coverage of laser irradiation. As seen in figure 6.7, this gives a 4% ripple of intensity for the overlapping beams. To make sure the edges of the irradiated area were evenly irradiated, 500µm outside the isolated area was also irradiated.

After initially characterising the QSW:CO_2 laser, the energy contained per pulse was assumed to be constant across all modulation frequencies. This assumption turned out to be incorrect, and as the modulation frequency of the laser was increased, so did the average pulse energy, as shown in figure 6.8. Measuring the energy for single pulses was a difficult task, since the acousto-optic modulator was constantly running at 50kHz even when the power modulation was turned off. This lead to the acousto-optic modulator and the power modulation for the QSW:CO_2 laser to be out of sync, since they had to be set at different frequencies. The result of this mismatch of frequencies was that the number of pulses emitted from the laser was not consistent. In figure 6.8, 150µs TTL signals applied to the power supply corresponded to a range of 2 to 4 pulses from the laser, depending on when the TTL signal arrived in conjunction with the Q-switch signal. To measure the energy of the laser pulses, the average power was measured and divided by the frequency of the TTL signal. The average power measured over a few seconds gave the average energy per TTL signal, so the uncertainty due to the different number of pulses averaged over 10^5 pulses for each of the measurements was small. The result is a steady increase in pulse energy as the laser modulation frequency is increased (Fig. 6.8).

6.4.1 Damage Threshold on Glass

The QSW:CO_2 laser has pulse durations less than 200ns, with repetition rates up to 50kHz. In comparison with the RF:CO_2 laser, the peak power in the QSW:CO_2 laser beam is over 2 orders of magnitude higher, which was able to ablate the films, as well as damage the glass substrates. At the focal point, the spot size was measured to be approximately 125µm. Irradiating the ITO films on glass substrates resulted in the films being removed, as shown in figure 6.9. The QSW:CO_2 laser can be seen to ablate the ITO films, as well as marking the bare glass. Using the Bruker Dektak, the surface profiles of the two damaged areas were measured. In figure 6.10, the resulting profiles can be seen.

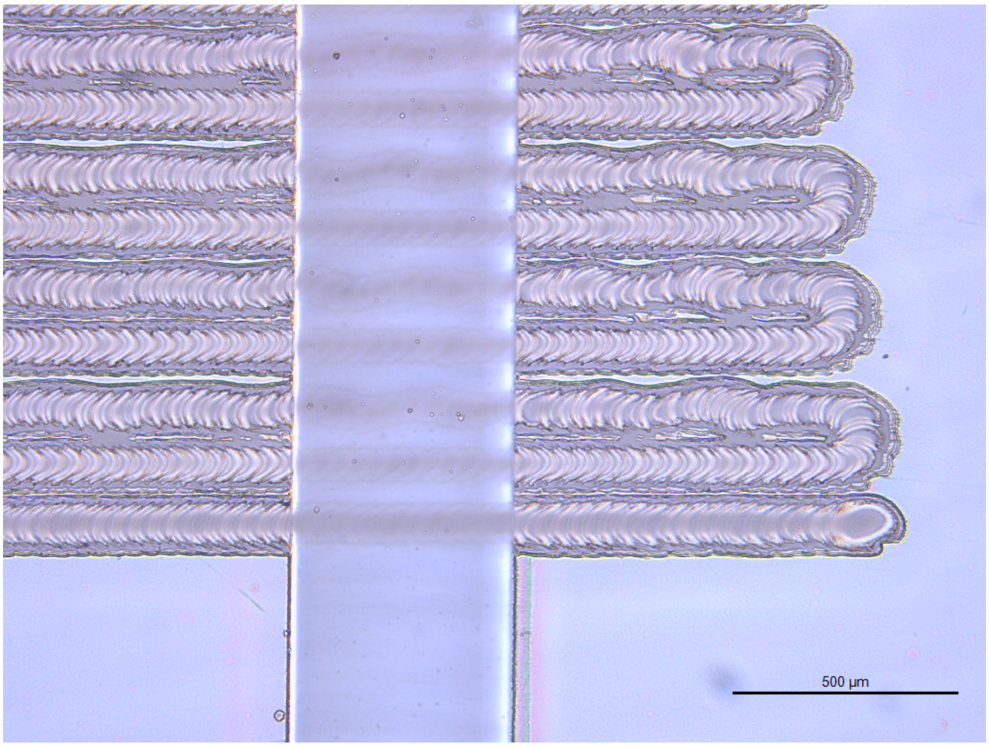

FIGURE 6.9: QSW:CO_2 laser irradiated horizontal tracks. The vertical strip in the centre of the image is bare glass, previously ablated with the XeCl laser.

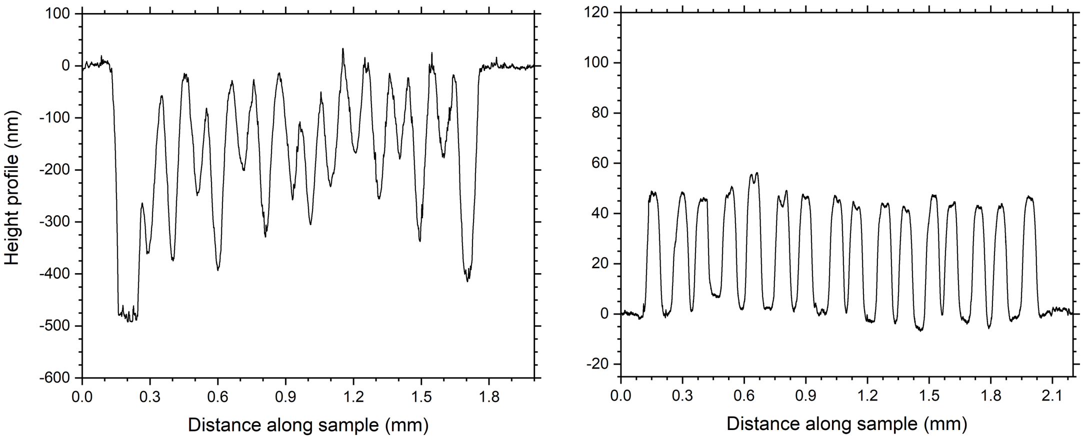

FIGURE 6.10: Dektak surface profiles along the QSW:CO_2 laser damaged areas. **left** The ITO film and, **right** The bare glass

From the surface profile results, it can be seen that the ITO films have been ablated by the laser, but not the entire thickness of the film is removed. The bare glass is seen to become raised under the laser irradiation. This phenomena is reported in literature by T.Shiu *et al.*[133], where CO_2 laser irradiation formed bumps in glass during laser texturing. Due to the damage caused by the QSW:CO_2 laser, the sample was lowered further from the focal point until visible damage could not be seen. At a beam diameter of around 175µm the films and glass could be irradiated without damage, and this beam size was used throughout the following sections unless stated otherwise.

6.4.2 Electrical Resistance Measurements on Glass

For the QSW:CO_2 laser experiments, the usual ITO films were provided by INM with the MPTS binder, along with a set of samples that did not use any binder. If the CO_2 lasers are in fact just removing the MPTS binder to create a more conductive film, then removing the binder should not make a difference when photothermal processes are used. Both of the ITO samples, with and without the binder, were irradiated under the same conditions with the QSW:CO_2 laser. Figure 6.11 shows the sheet resistance results after various dose levels controlled by translational speed and modulation frequency. As can be seen, when using the photothermal processing of the CO_2 laser the MPTS binder does not help reduce the sheet resistance lower as compared to the binder-less ITO films. The films containing no binder still had to have the ITO nanoparticles suspended in a solution containing solvents as well as other organic materials, so material was still been removed with the QSW:CO_2 laser irradiation. This is why the sheet resistance results show very similar behaviour between the different films.

The ITO films containing MPTS and no-binder both reached the same level of sheet resistance at the highest doses, at $\sim 250\Omega/\text{sq}$. At a modulation frequency of 1500Hz, the translational stages could not be operated at a lower speed without the glass starting to fracture, and if the modulation frequency was increased to 1750Hz, fractures were induced into the glass at higher translational speeds. The lowest recorded sheet resistance of $250\Omega/\text{sq}$ is the same as that reached with the RF:CO_2 laser before the glass started to fracture, leading to the conclusion that this is the lowest sheet resistance that can be achieved by heating the films with CO_2 laser sources on borosilicate glass before damage starts to occur.

As calculated previously with the RF:CO_2 laser, the properties of the borosilicate glass substrates can be used along with the parameters of the laser beam to estimate the temperature rise of the ITO films under QSW:CO_2 laser irradiation. The parameters of the glass have not changed between samples, giving the same thermal diffusion length of $\sim$0.81mm for the Schott Borofloat substrates. For the temperature estimation, the QSW:CO_2 laser is assumed to behave as a continuous source laser delivering the average power measured from the pulse train. This estimates the temperature rise over a long time scale, ignoring the peak temperatures induced from the <200ns pulses. The laser beam was focussed to a beam size of 175µm, and for the lowest sheet resistance value achieved, was operated at 1500Hz with a translational speed of

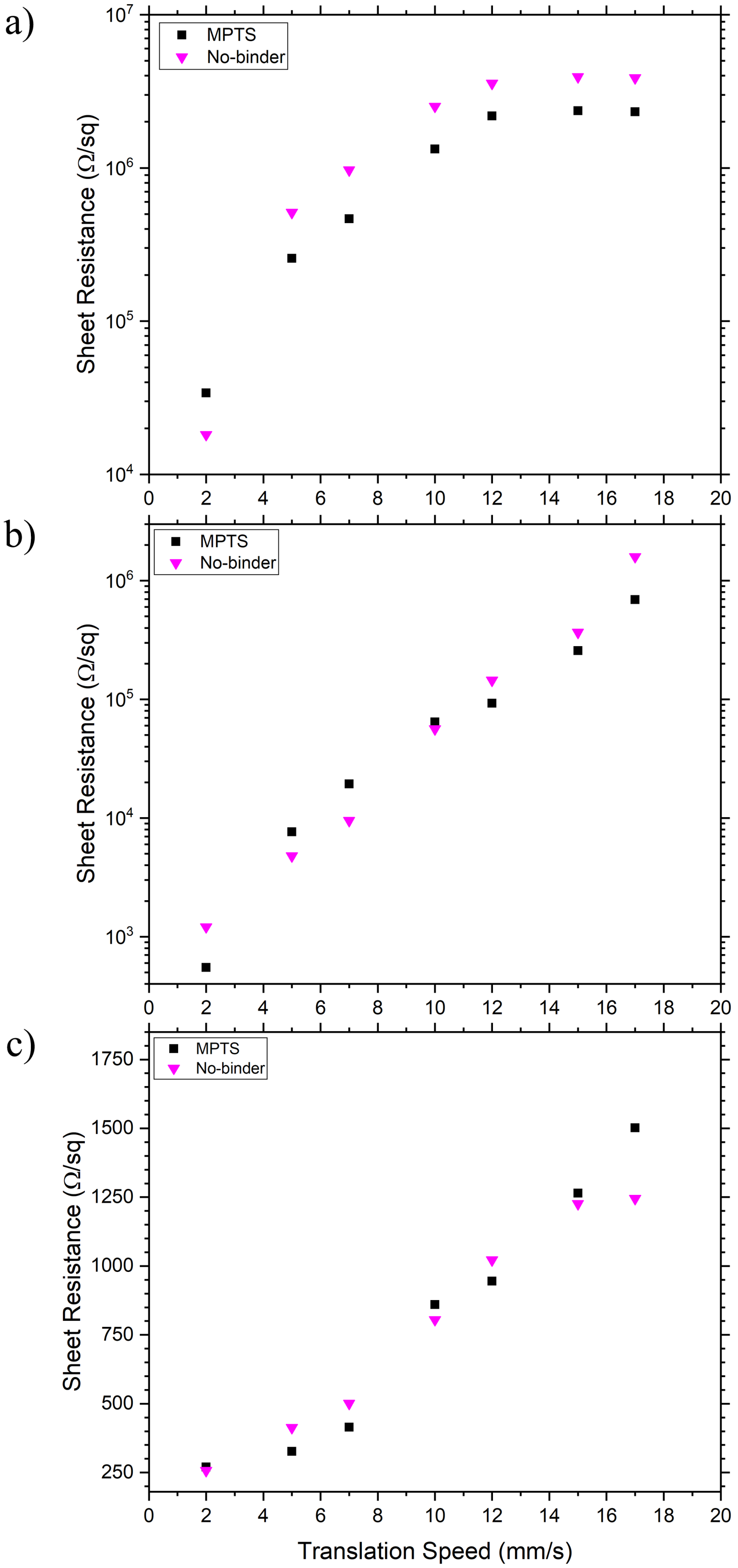

FIGURE 6.11: Sheet resistance of the ITO films with and without the MPTS binder after irradiation with the QSW:CO_2 laser at modulation frequencies **a)** 750Hz **b)** 1000Hz and **c)** 1500Hz, with 150µs TTL width.

2mm/s. From 6.8, we see that at 1500Hz the average energy delivered per TTL signal is around 1.45mJ, corresponding to an average power of 2.2W. Moving at a speed of 2mm/s, with a spot size at 175µm gives an irradiated volume of $2.04\times10^{-3}m^3$. This volume includes the temperature spreading due to the thermal diffusion length calculated earlier. This results in a mass for the heated volume of $4.5\times10^{-3}g$. The specific heat capacity was taken to be $0.83Jg^{-1}K^{-1}$ and the average power supplied by the laser to be 2.2W. This data gives us a temperature rise of 590°C using equation 6.1, which is similar to the temperature rise calculated from the RF:CO_2 laser near the point of glass damage.

6.4.3 Optical Measurements on Glass

To measure the optical properties of the ITO films after irradiation, the same procedure was used as for the ultraviolet irradiated samples. Larger area 6mm squares were irradiated, using the same Gaussian overlapping shown in figure 6.7. Both the ITO films containing MPTS and no binder were irradiated for UV-VIS optical transmission measurements, and the results are shown in figure 6.12. The transmission spectra in the visible stays above 85% throughout the various levels of irradiation by the QSW:CO_2 laser, however, the UV band edge appears to be shifting towards higher wavelengths with higher doses. Constructing a Tauc plot from the UV-VIS transmission data, shown in figure 6.13, confirms that the band gap is reducing.

The band gap shifting towards lower energies was not expected after CO_2 laser irradiation, as this is evidence of a lowering of the charge carrier density, as

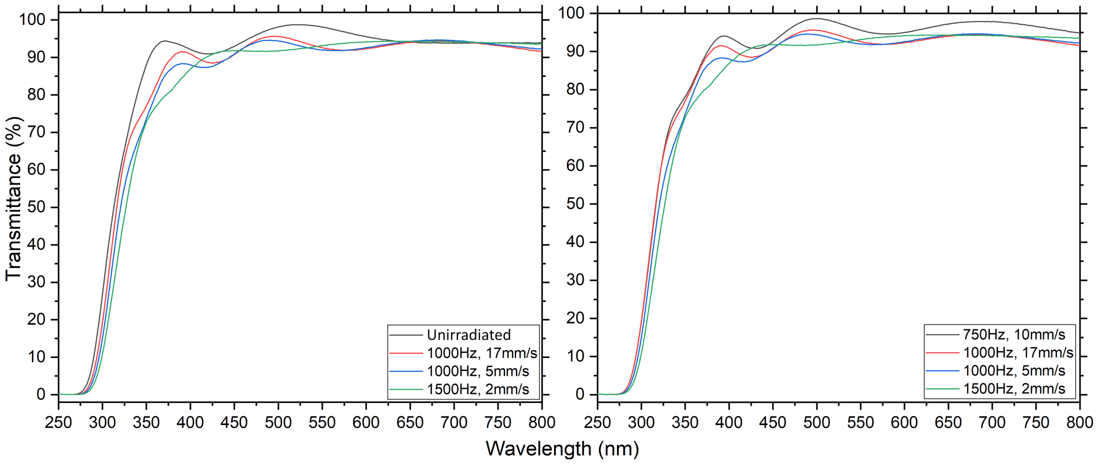

FIGURE 6.12: UV-VIS optical transmission spectra after various doses of QSW:CO_2 laser irradiation. **Left** ITO films containing MPTS binder and **Right** ITO films without a binder.

described by the Moss-Burstein shift shown in section 5.2.4. In the case of the ITO films considered here, the electrical conductivity is increasing by over 4 orders of magnitude, but the bang gap is becoming smaller indicating that the number of charge carriers available in the conduction band is decreasing. If this hypothesis is correct, and the number of charge carriers in the conduction band is decreasing, the plasma edge in the near infrared should also be shifting to lower energies too.

Figure 6.14 shows the near infrared transmission spectra of the ITO films irradiated with the QSW:CO_2 laser. The plasma edge of the ITO films with and without the MPTS binder do shift towards lower energies with increasing levels of irradiation from the QSW:CO_2 laser. This adds further evidence for a reduction in the charge carrier density of the ITO films under CO_2 laser irradiation. To estimate the drop in charge carrier density, the wavelength at which the transmission spectra fall 50% was measured for the lowest and highest dosages from figure 6.14. This value was put into equation 3.13 from earlier,

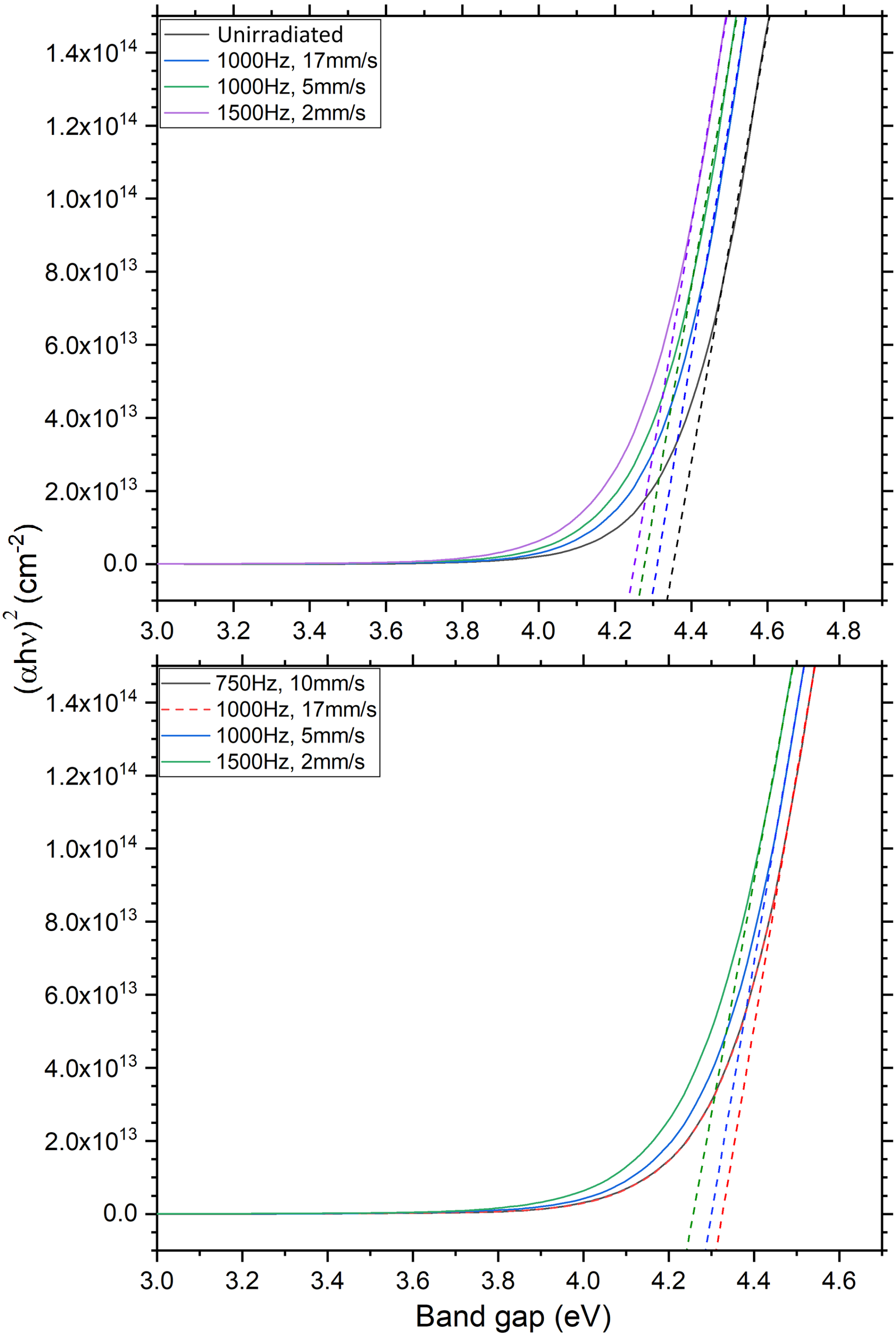

FIGURE 6.13: Tauc plot constructed from UV-VIS absorption data for ITO films irradiated with the QSW:CO_2 laser. **Top** ITO films with MPTS binder, and **Bottom** ITO films without binder.

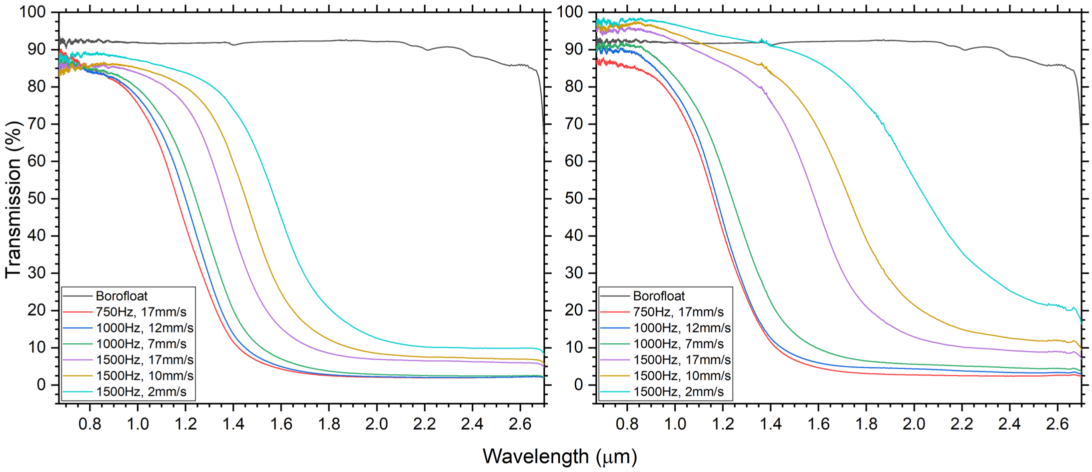

FIGURE 6.14: Near infrared optical transmission spectra after various doses of QSW:CO_2 laser irradiation. **Left** ITO films with MPTS binder, and **Right** ITO films without binder.

also seen below, and an estimated drop in charge carrier density was calculated.

$$\omega_p = \sqrt{\frac{n_e e^2}{m\varepsilon_0}}, [rad/s] \tag{3.13}$$

For the ITO samples containing the MPTS binder, the charge carrier density dropped from 4.3×10^{16}cm^{-2} to 2.4×10^{16}cm^{-2}, a reduction of nearly 50%. The ITO films containing no binder dropped even more, from 4.4×10^{16}cm^{-2} to 1.4×10^{16}cm^{-2}, losing almost 70% of the charge carrier density. Consequently, with a reduction in charge carrier density but an increase in overall conductivity, it was hypothesised that the mobility had greatly improved. As shown in Chapter 3, the equation that related the charge carrier density, η_e, charge carrier mobility, μ_e and the overall conductivity, σ_e, is shown in equation 3.8

$$\sigma_e = \eta_e \mu_e e \tag{3.8}$$

TABLE 6.3: Haze measurements for various irradiated areas at different laser parameters for the ITO films irradiated with the QSW:CO_2 laser.

Laser Paramater	Haze (%)
750Hz, 15mm/s	0.64
1000Hz, 17mm/s	0.35
1000Hz, 10mm/s	0.98
1500Hz, 17mm/s	0.73
1500Hz, 2mm/s	0.58

As can be seen, if the charge carrier density of the ITO film is not to be changing with laser irradiation, but the overall conductivity is increasing, then the only conclusion is that the charge carrier mobility must be increasing.

To measure the haze of the QSW:CO_2 laser irradiated areas, 5 different sites were chosen and the measurements made. After irradiation, each of the areas did not appear to have any visual difference in haziness. As can be seen from table 6.3, throughout a range of irradiation parameters, the haze value for the ITO films does not change significantly and does not follow a trend. Even at the highest dose with a modulation frequency of 1500Hz at 2mm/s the haze stays below 1%. As mentioned before, the haze measurements were only taken at a single wavelength ($\lambda = 632.8$nm) and are only true for this wavelength.

6.4.4 Electron Mobility Measurements

At a sheet resistance of 250Ω/sq, the nanovoltmeter was able to read a voltage drop across the ITO films on the highest scale, up to 200mV. In Chapter 3, the Hall voltage setup seen in figure 3.9 shows current flowing through two corners, 1 and 3, of the square sample, and the voltage drop measured across the other 2 corners, 2 and 4. In an ideal setup, when current is flowing through contacts 1 and 3 on the sample, there would be zero voltage drop across contacts 2 and 4. In our setup, the ITO films irradiated with the QSW:CO_2 laser have an un-even sheet resistance across the sample which varied due to the fluctuating laser output power and film uniformity. Due to the asymmetric nature of the resistance, when current flows through the contacts 1 and 3 there is an offset voltage across contacts 2 and 4, even without the presence of a magnetic field. The offset voltage varied between irradiated samples, but it was always large enough so that the highest scale of the nanovoltmeter had to be used. This made measuring the Hall voltage very difficult. Assuming our ITO films have the same charge carrier density as the commercial ITO films, and using the same current flow, a Hall voltage of the order of 20-40μV was expected. On the 200mV scale, this voltage was within the noise level, making the Hall voltage measurements inconclusive.

6.4.5 MPTS Binder Heating

As part of the CO_2 laser irradiation of the ITO films, the MPTS binder and other solvents were thought to be removed via heating. Using a hot plate, pure MPTS binder was heated on KCl substrates, which are transparent to wavelengths as long as 20μm, as seen in figure 6.15. The FTIR transmission spectrum was taken for various temperature increases. These measurements

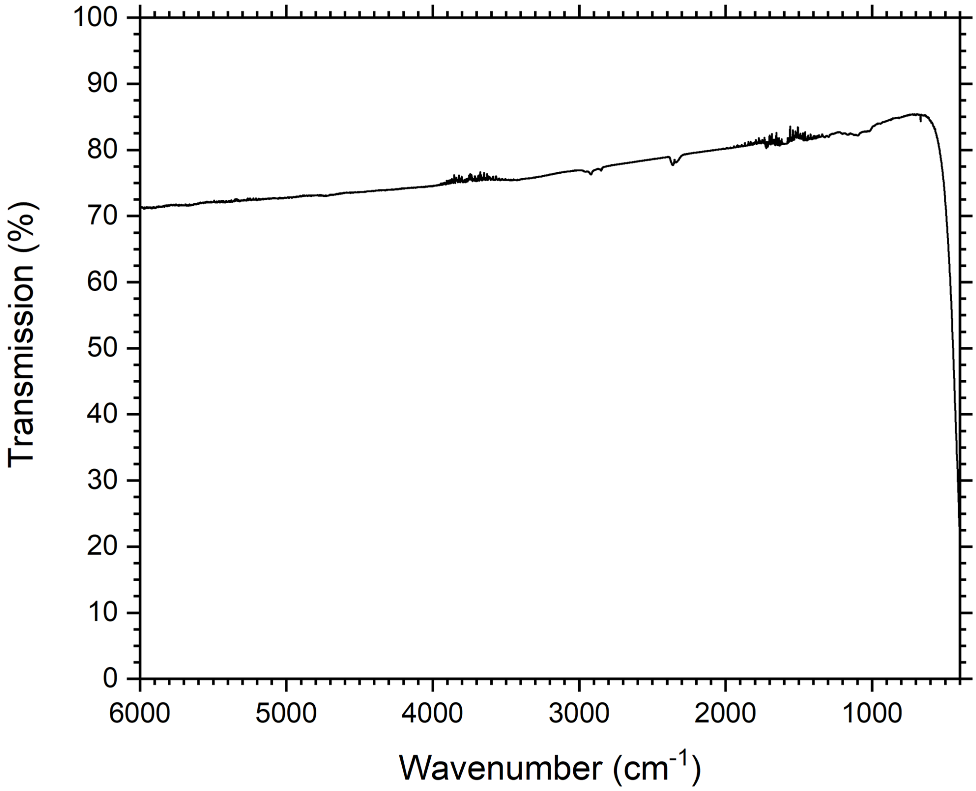

FIGURE 6.15: FTIR spectra for KCl substrates from 6000 to 400cm^{-1}. The noise seen at 4300 and 2400cm^{-1} are peaks due to the air.

were made to ascertain at what temperature changes in the MPTS could be observed by FTIR.

The MPTS was applied to the KCl substrate by applying a 200µl drop in the middle of the KCl substrate, and flattening the drop into a thin film with a piece of glass on top. The film thickness was not measured due to the film still being liquid, so the thickness for different samples was not known to be the same. In the experiment, six temperatures were used on the hotplate for the removal of MPTS ranging from 50 to 300°C, in 50°C steps. The results are shown in figure 6.16.

The FTIR spectra for the MPTS heated on the hot plate showed that the The peak at 1638cm^{-1} related to the carbon double bond located on the vinyl group

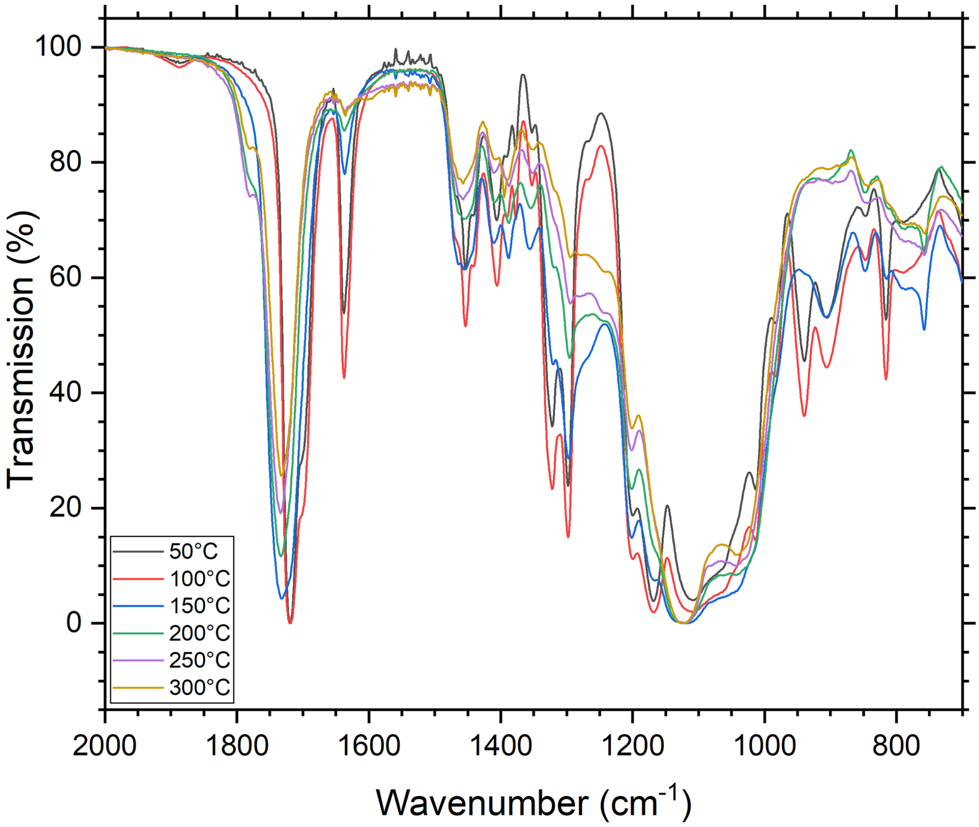

FIGURE 6.16: FTIR transmission spectra for MPTS which had been heated on a hotplate at increasing temperatures between 50°C and 300°C.

decreases significantly with temperature. This represents the polymerisation of the MPTS molecule. [25] This means that the MPTS is polymerising under CO_2 laser irradiation, and not just the ultraviolet laser irradiation. Between wavenumbers 800 and 950cm^{-1} several peaks are disappearing, which could be solvents or other organic materials been removed or decomposed. The FTIR spectra do not show conclusive evidence that the MPTS is being removed. Some of the peaks appear to be lowering in intensity, but this could be due to the chemical changes within the MPTS.

6.4.6 ITO Irradiation on PET Substrates

Using the short pulses from the QSW:CO_2 laser with the high repetition rates gives an irradiation regime between the continuous wave RF:CO_2 laser and the high pulse energy but low repetition rate TEA:CO_2 laser. To irradiate the ITO films on PET substrates, the same spot size was used as with the glass samples (175µm) and sites were irradiated with varying modulation frequencies and translational speeds up until damage started to occur. Following this, the same experiment was run for increasing beam sizes until a suitable regime was found for the irradiation of the ITO on PET substrates without damage.

Starting at a beam diameter of 175µm, damage to the films was seen at all the available frequencies and translation speeds. At a modulation frequency of 750Hz, which is where the sheet resistance of the ITO films on glass started to reduce, the damage done to the PET substrates is severe, as shown in figure 6.17. Melting of the PET could be seen with the naked eye, and no sheet resistance could be measured for the ITO films with our equipment with an upper limit of 100MΩ. Damage was observed for laser frequencies as low as 100Hz, also shown in figure 6.17. Although, in between the damaged sites a continuous path could be seen but the sheet resistance had increased from a value of around 3MΩ/sq to over 10MΩ/sq.

The beam size of the QSW:CO_2 laser was increased until damage could not be seen with the naked eye, which was at a beam size of around 200µm. At 750Hz the films started to melt as with the smaller beam size, but at lower modulation frequencies the damage started to stop, as seen in figure 6.18. No visual damage was seen with the naked eye at a modulation frequency of 300Hz, however, the resistance could not be measured on our equipment. Looking at the films under the microscope, micro-cracks can again be observed as was the case with the TEA:CO_2 laser irradiation. The micro-cracks make the ITO films discontinuous and a measurement could not be made due to the islands created by the cracks. Reducing the modulation frequency to 200Hz stopped the micro-cracks from being produced in the ITO films during irradiation, (fig. 6.18), but because the modulation frequency was only at 200Hz the sheet resistance of the ITO films was not measured to be any lower than before irradiation.

6.5 Conclusions

In this chapter, wet processed ITO films were irradiated with various CO_2 lasers to reduce the sheet resistance. The CO_2 laser irradiation in the infrared

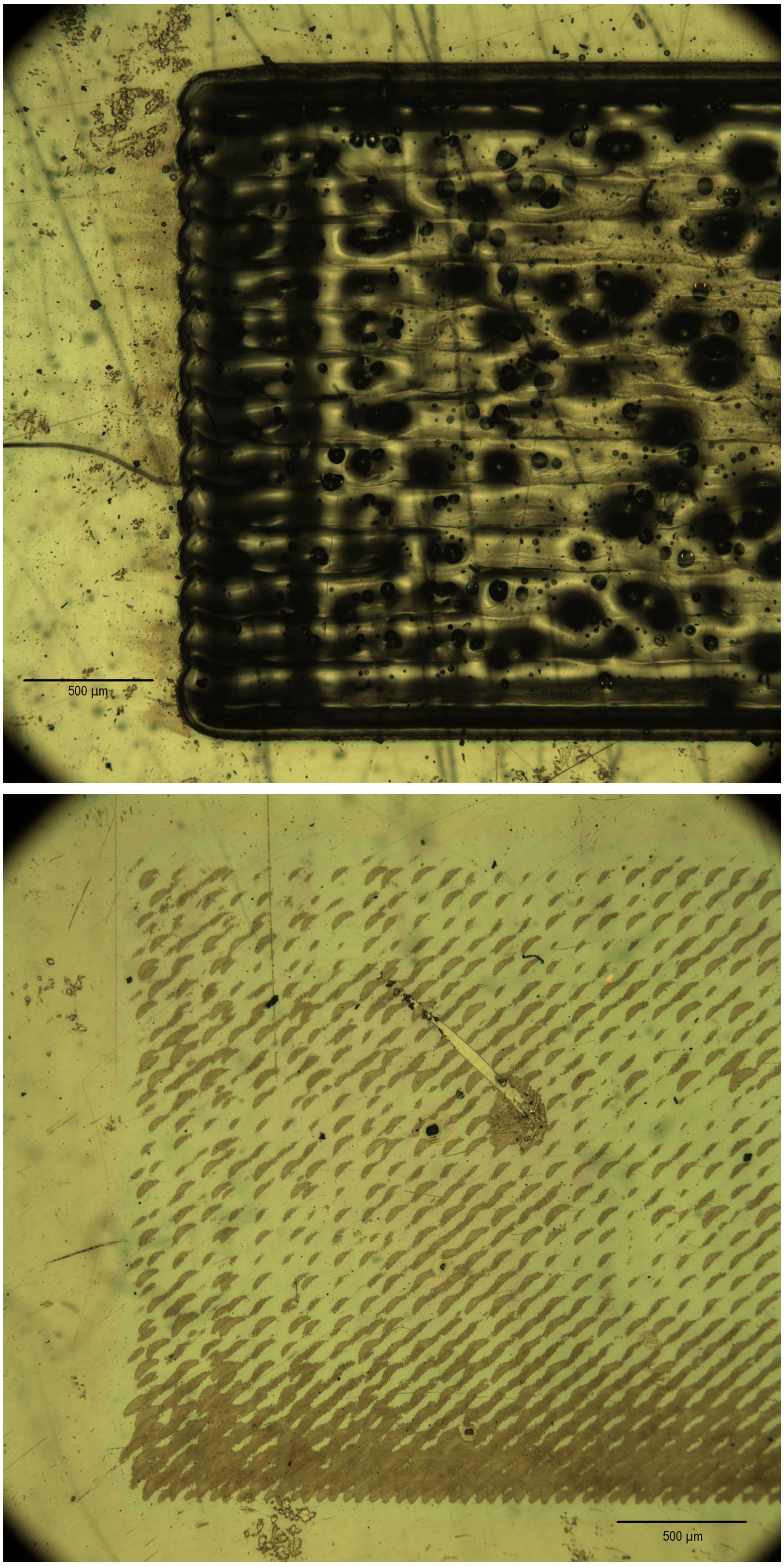

FIGURE 6.17: ITO films on PET substrates irradiated with the QSW:CO_2 laser. **Top** Laser spot size of 175µm, modulation frequency 750Hz at 10mm/s. **Bottom** Laser spot size of 175µm, modulation frequency of 100Hz at 10mm/s.

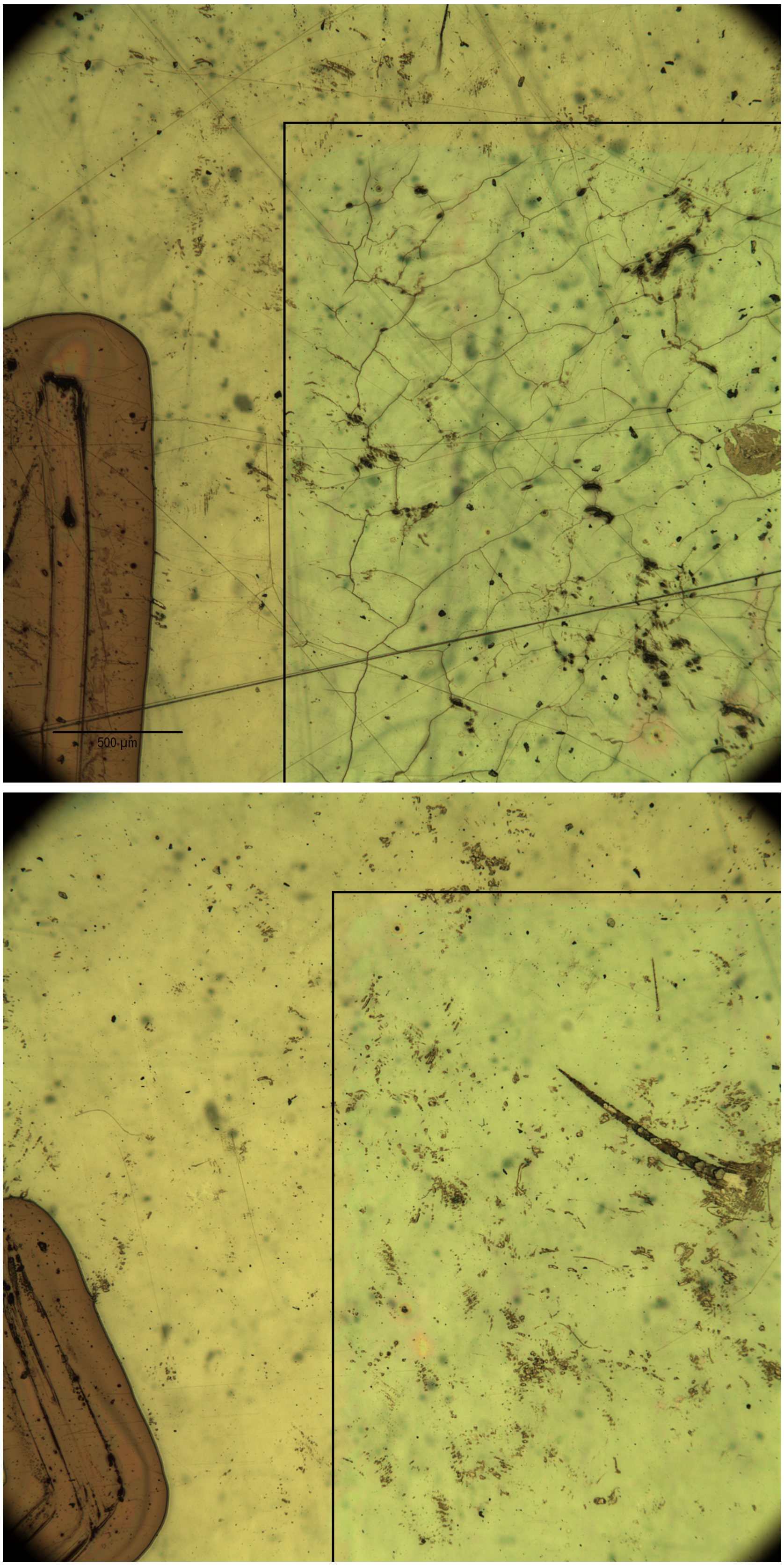

FIGURE 6.18: ITO films on PET substrates irradiated with the QSW:CO_2 laser. **Top** Laser spot size of 200µm, modulation frequency 300Hz at 10mm/s. **Bottom** Laser spot size of 200µm, modulation frequency of 200Hz at 10mm/s.

induced an increase in temperature in the ITO films to process them photothermally. On the glass substrates both the RF:CO_2 and the QSW:CO_2 lasers were able to successfully reduce the sheet resistance of the ITO films down to $250\Omega/\text{sq}$. The process by which the ITO films were reduced in sheet resistance was the removal of non-conducting materials such as solvents and other organic dielectrics. It was found from the FTIR spectra that the MPTS binder was polymerising with increasing temperatures, but this was not increasing the overall conductivity of the ITO films with the binder when compared with the ITO films containing no binder. If the polymerisation of the MPTS binder was having an effect, the conductivity would have been increasing further than the binderless ITO films due to the densification of the ITO films, pulling the ITO nanoparticles together as described in section 5.1.

An interesting result was the apparent reduction of the charge carrier density under increasing temperatures induced by CO_2 laser irradiation, even though the resistivity of the ITO films was reducing by over 4 orders of magnitude. Two hypotheses that require further investigation are proposed. Firstly, an increase in the mobility of the reduced number of charge carriers. This was unable to be verified by the Hall voltage measurements. And secondly, any loss of charge carriers due to oxygen vacancy filling via ITO reactions in air at elevated temperatures.

Irradiation of the ITO films on PET substrates was unsuccessful. The process that reduces the resistivity of the ITO films relies on temperature increases that were beyond the steady-state damage threshold of the PET. Using a low repetition rate TEA:CO_2 laser, we were able to find a regime in which the films were not damaged, but the fluence had to be reduced to the point where a reduction in sheet resistance was not achievable. The same was found for the QSW:CO_2 laser, where the modulation frequency had to be lowered enough so that the accumulative temperature increase did not damage the PET substrates, but again stopped the ITO films been successfully processed to lower sheet resistances.

Chapter 7

Indium-free Film Laser Irradiation

7.1 Introduction

As part of the INFINITY project, indium-free transparent conducting films were to be developed by the partners. These films were based on aluminium doped zinc oxide (AZO) materials. AZO nanoparticles were suspended in a solution containing niobium doped titanium dioxide. The AZO films were provided on glass substrates and PET substrates, with the same thickness as the ITO film counterparts discussed earlier in the thesis at 520nm and 400nm respectively.

Using the techniques learned from the irradiation of the ITO films with ultraviolet and CO_2 laser systems, the AZO films were irradiated in similar ways. The AZO films were first irradiated in the ultraviolet, to try to polymerise the binder and pull the nanoparticles closer together and increase the conductivity. Then the AZO films were irradiated with the QSW:CO_2 laser to remove non conductive material.

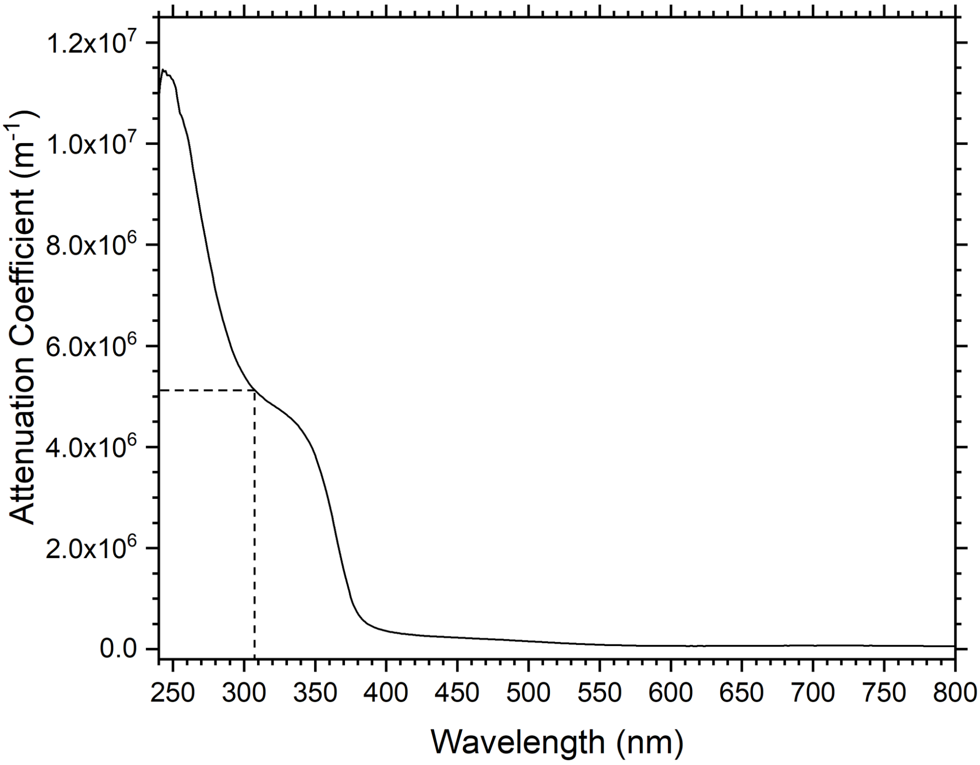

FIGURE 7.1: Attenuation coefficient of the AZO films in the UV to NIR. the absorption depth is approximately 200nm at a wavelength of 308nm.

A preliminary measurement of the resistance of the AZO films before laser irradiation showed them to be non-conductive. With the upper limit of the equipment being 100MΩ, a reading could not be successfully made on the AZO films, even when putting 2 probes very close (<500µm) to each other.

7.2 XeCl Laser Irradiation

7.2.1 Electrical Resistance Measurements

The XeCl laser gave the best results when irradiating the ITO films with ultraviolet radiation, so this laser was used to irradiate the AZO films. From figure 7.1, the absorption depth is approximately 200nm for the XeCl laser at a

TABLE 7.1: Table showing the sheet resistance of AZO films on glass substrates after XeCl laser irradiation at various pulses per area. Each area used a fluence of 30mJcm^{-2}

Pulses Per Area	Sheet Resistance (Ω/sq)
200	>100M
1000	>100M
5000	>100M

wavelength of 308nm. Due to this relatively strong absorption coefficient the entire thickness of the AZO films will not be affected by ultraviolet radiation of significant irradiance, but the laser energy will also not reach the substrate.

The ablation threshold of the AZO films was considerably lower than the ITO films, with visual damage starting at a fluence of ~35mJcm^{-2}. Reducing the fluence to a value of 30mJcm^{-2} stopped damage from occurring, and the AZO films were irradiated with 3 different doses (Table 7.1). Using this fluence close to the damage threshold with the highest dose at 5000 pulses per area, the sheet resistance could not be lowered enough to be measured by our equipment (i.e. >100MΩ). Because the films have such a high resistivity before and after laser irradiation, we were unable to determine if the electrical properties were changing.

7.2.2 Optical Measurements

As seen previously in Chapter 5, a change in electrical properties can sometimes relate to a change in the optical properties of the films too. The same

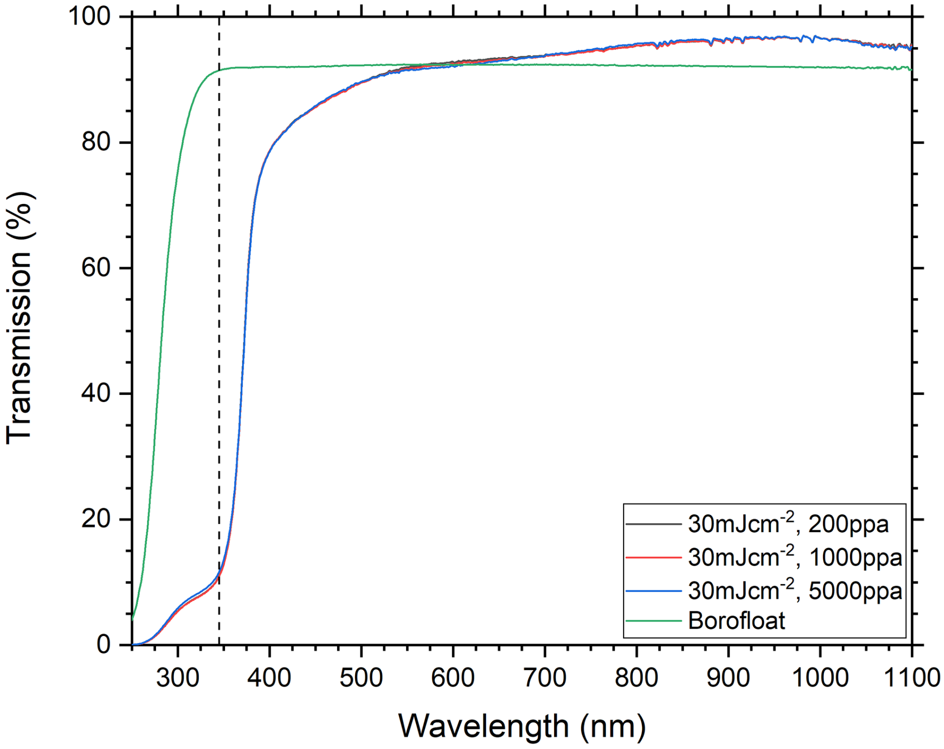

FIGURE 7.2: UV-VIS transmission results for the AZO films irradiated with the XeCl laser at different doses at a fluence of 30mJcm^{-2}. The vertical dashed line represents the start of the Borofloat substrate absorption edge.

measurements were taken for the AZO films from the ultraviolet to the infrared. Seen in figures 7.2 and 7.3 are the optical transmission results from the ultraviolet to the infrared for the AZO films under XeCl irradiation at the highest possible fluence before damage, at 3 different doses.

After the irradiation with the XeCl laser at the 3 irradiation conditions, the optical transmission of the films did not change across the measured wavelength range. In figure 7.2, the optical transmission of the AZO films in the visible part of the spectrum is above 80% from 400nm and longer, and remains at this level of transparency after irradiation with the XeCl laser at all doses. This is an excellent level of transparency for a transparent conductor, however, the electrical properties of the films are very poor. It can be seen that at a wavelength of approximately 350nm, that the transmission curve deviates from a straight absorption edge and exhibits a small bump before reaching effectively zero transmission. This feature in the transmission curve coincides with the absorption edge of the Borofloat substrate. The AZO samples were not provided on fused silica substrates, so it is unknown if this behaviour was caused by the material or the substrate. In figure 7.3, the near infrared transmission for the AZO films irradiated by the XeCl laser can be seen. Again, with increasing doses the infrared transmission does not change. Because the transmission curves are not changing with increasing laser doses, it it not possible to conclude if the XeCl laser is affecting the electrical conductivity of the AZO films. One thing that can be learned from figure 7.3 however, is that the plasma edge does not appear below a wavelength of 3.6µm. This infers that the charge carrier density of the AZO films must be much lower than the ITO films used earlier in this thesis, where the plasma edge was at $\sim$1.5µm. The plasma edge for the AZO films could not be measured, since the Borofloat glass substrate becomes opaque at wavelengths longer than 3.6µm obscuring any transmission data for the films.

The small bump located on the absorption edge made the band gap of the AZO films difficult to measure. Usually, a Tauc plot shows a linear regime which can be extrapolated to find the axis intercept, indicating the optical band gap of the material. In figure 7.4 this is not the case, as the bump causes the line to deviate away from the ideal situation. Assuming that the Borofloat substrate was interfering with the transmission data, we can follow the first small part of the linear section down to the axis intercept. This gives the AZO

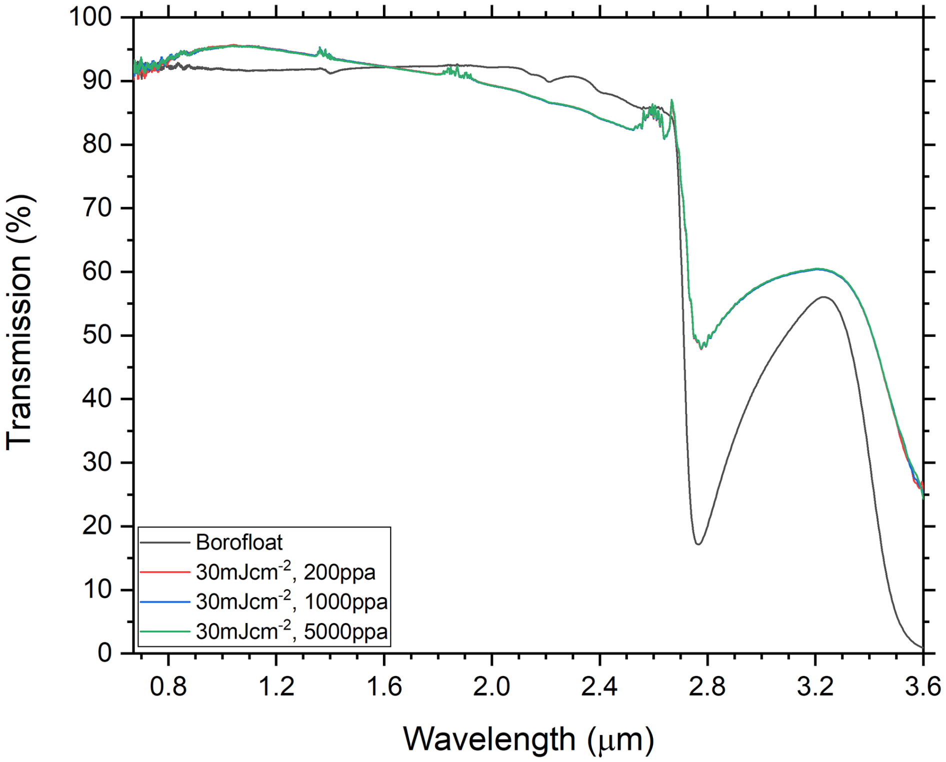

FIGURE 7.3: Near infrared transmission results for the AZO films irradiated with the XeCl laser at different doses at a fluence of 30mJcm^{-2}.

a band gap of ∼4.15eV. The important result from figure 7.4 is that the band gap is not changing with XeCl laser irradiation, giving us a similar result to the ITO films which were irradiated in the same way. Therefore, we cannot infer whether or not the electrical conductivity is increasing under XeCl laser irradiation without improving the sensitivity of the resistance measurement system.

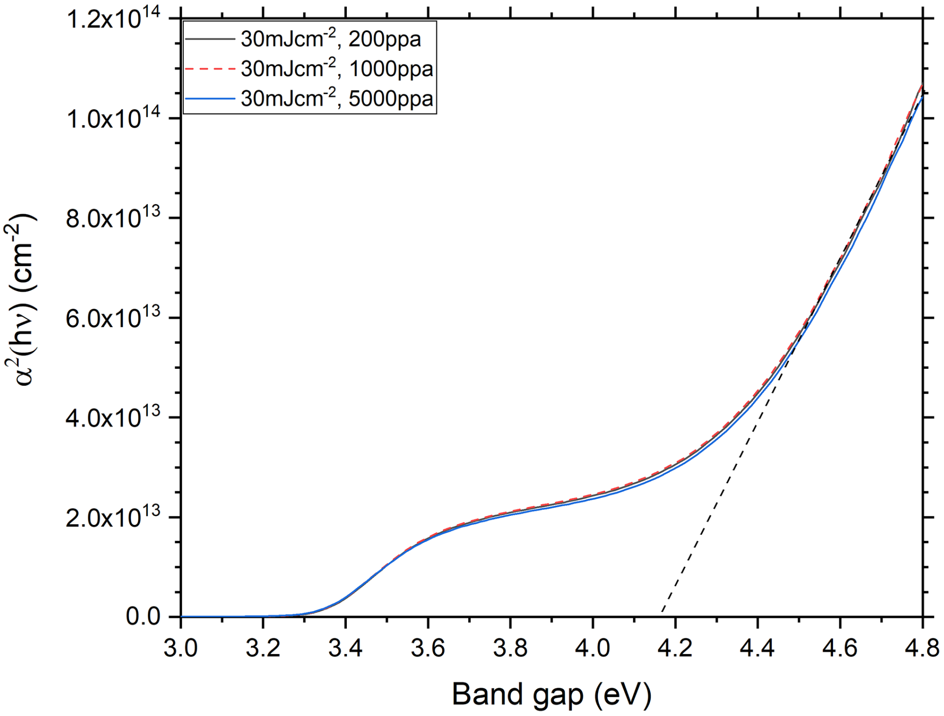

FIGURE 7.4: Tauc plot calculated from the UV-VIS transmission data for AZO irradiated with the XeCl laser at various doses at a fluence of 30mJcm^{-2}.

7.3 QSW:CO$_2$ Laser Irradiation

7.3.1 Electrical Resistance Measurements

Following on from the XeCl irradiation of the AZO films, the QSW:CO$_2$ laser was used to irradiate fresh samples as this laser gave us some of the most promising results with the ITO films earlier in the thesis. The experimental setup used to irradiate the AZO films with the QSW:CO$_2$ laser was the same as in Chapter 5.4, using the same spot size of ∼175µm, since this didn't damage the films in preliminary tests.

Before irradiation with the QSW:CO$_2$ laser the electrical resistivity of the AZO

TABLE 7.2: Table showing the sheet resistances achieved on the AZO films using various parameters with the QSW:CO_2 laser.

Laser parameter	Sheet Resistance
1kHz, 2mm/s	19MΩ/sq
1.5kHz, 17mm/s	9.6MΩ/sq
1.5kHz, 15mm/s	4.7MΩ/sq
1.5kHz, 12mm/s	2.9MΩ/sq
1.5kHz, 10mm/s	2.3MΩ/sq

films was measured, and again, the films could not be measured on our equipment giving us a value greater than the upper limit of 100MΩ. When the laser was modulated at 750Hz, no measurable change in the resistance of the AZO films was observed at any translational speed. With the laser modulated at 1000Hz, all of the irradiated areas except for those at a speed of 2mm/s were not reduced below the 100MΩ limit of the equipment. However, for the 2mm/s speed at a modulation frequency of 1000Hz, a resistance measurement of 19MΩ/sq was recorded. As can be seen in table 7.2, improvements in this sheet resistance can be achieved by modulating the laser at a frequency of 1500Hz, with the lowest sheet resistance achieved measured to be 2.3MΩ/sq when the translation speed was 10mm/s.

This level of sheet resistance is over 4 orders of magnitude higher than is required for a functional device that is currently based on ITO electrodes. It was not possible to reduce this resistivity further, since irradiating the AZO films at any higher doses with the CO_2 laser caused damage to the films. In figure 7.5, the damage to the AZO films can be clearly seen when speeds of 2mm/s and 5mm/s were used at a modulation frequency of 1500Hz. The AZO film cracks

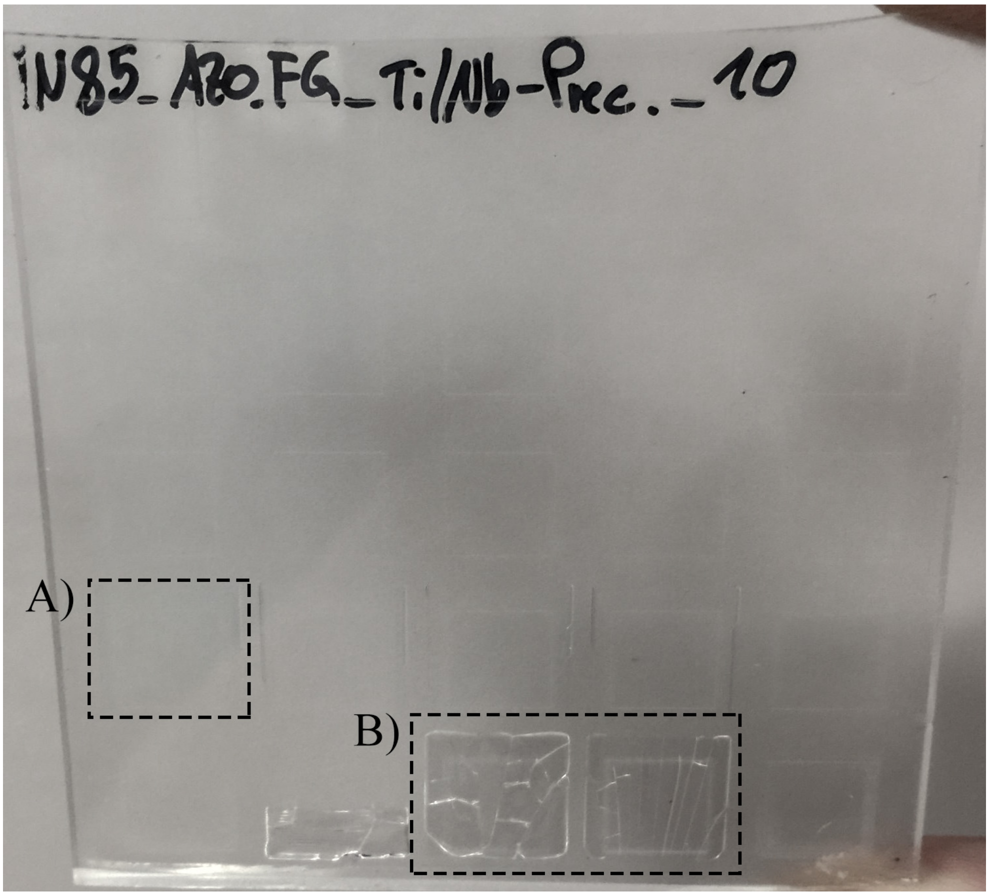

FIGURE 7.5: Image of an AZO sample irradiated with the QSW:CO_2 laser with various parameters. **A)** shows an area irradiated at 1500Hz at 7mm/s and **B)** shows 2 visibly damaged areas which were irradiated at 1500Hz at 2mm/s and 5mm/s respectively.

and delaminates from the glass substrate under these irradiation conditions, making the films discontinuous and having effectively infinite resistance.

Interestingly, the area irradiated at a modulation frequency at 1500Hz with a speed of 7mm/s (fig. 7.5) had a resistance value too high to be measured. This was unexpected, because the area did not appear to contain any damage from the laser irradiation, but had been exposed to a larger amount of laser irradiation than the best result (2.3MΩ/sq). Under the microscope, shown in figure 7.6, it is seen that the irradiated area contained vertical cracks that continued the entire width of the isolated area. These cracks originated from

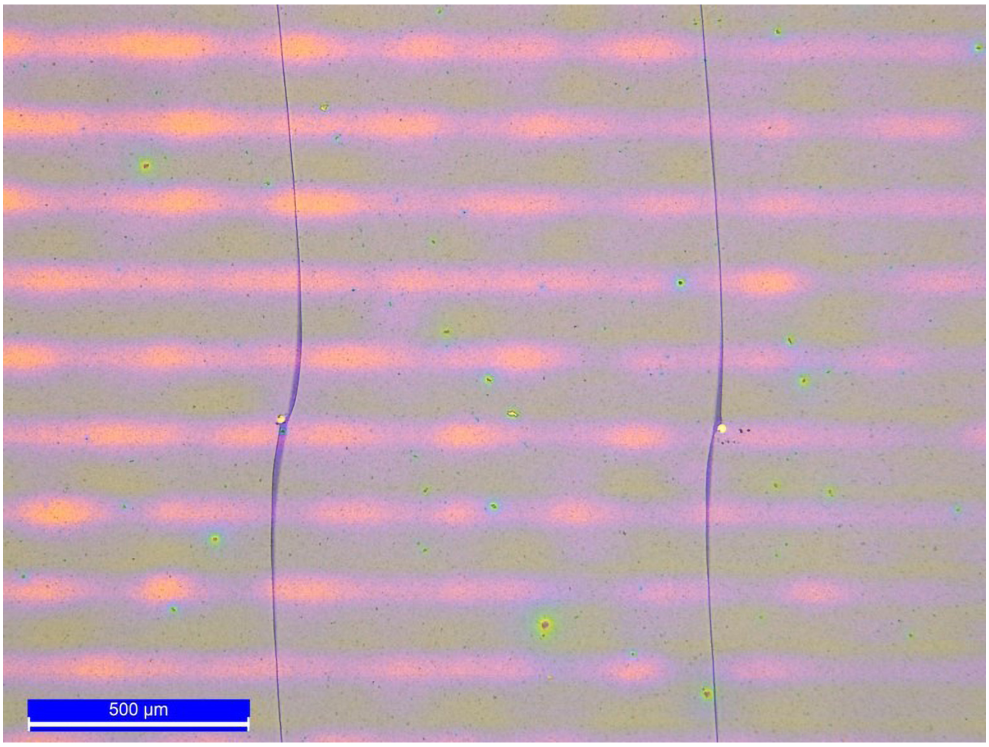

FIGURE 7.6: Microscope image of the AZO films irradiated at 1500Hz at a speed of 7mm/s. The vertical cracks were caused by the measurement probes, which can be seen near the origin of the cracks. The colours were caused by the DIC module on the microscope to show the irradiated paths.

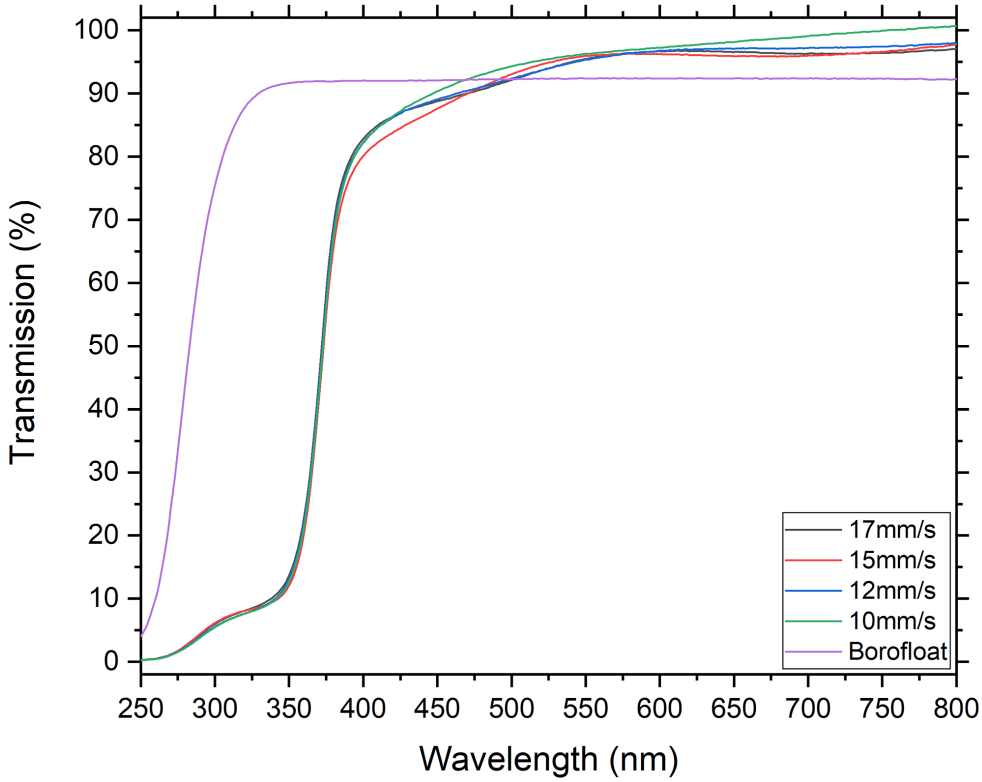

FIGURE 7.7: UV-VIS transmission results for the AZO films irradiated with the QSW:CO_2 laser at different speeds with a modulation frequency of 1500Hz.

the 4-point probe tips that were used to measure the electrical resistivity of the films. The cracks caused the probes to become isolated from each other, and giving a reading of effectively infinite resistance. An attempt to measure the resistivity between the cracks was tried, however, a reading of resistance could not be obtained without causing further cracking in the area.

7.3.2 Optical Measurements

With a measurable reduction in the electrical conductivity of the AZO films under irradiation with the QSW:CO_2 laser, the optical properties were measured after irradiation. Figure 7.7 shows the transmission from the ultraviolet

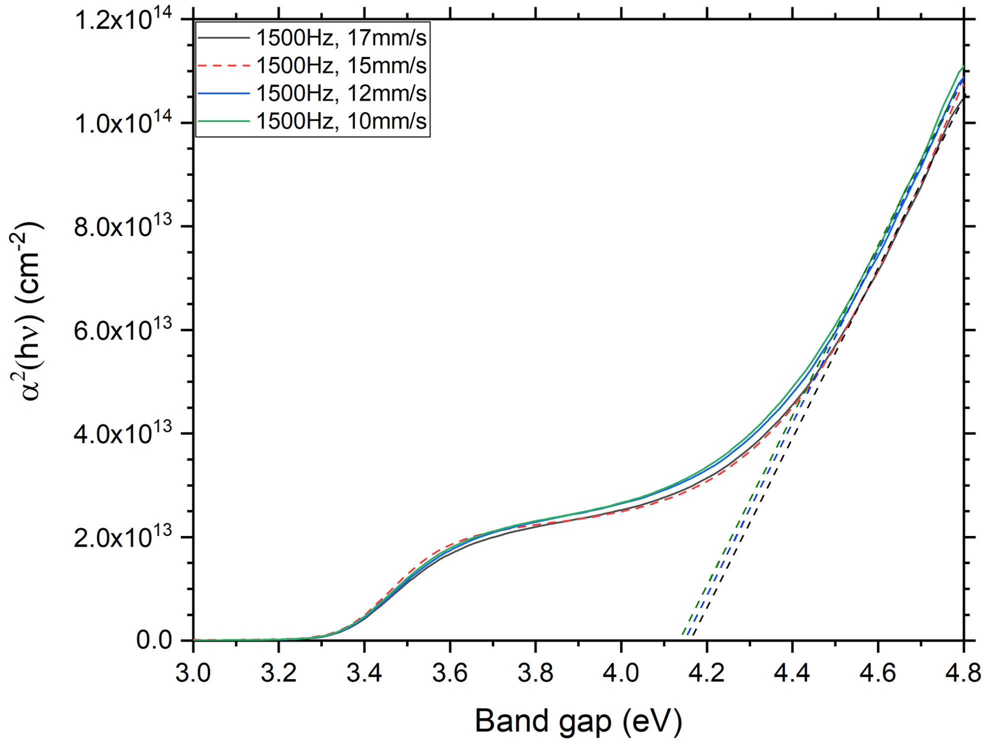

FIGURE 7.8: Tauc plot constructed from the transmission data for the AZO films irradiated with the QSW:CO_2 laser at various speeds, with a modulation frequency of 1500Hz.

and visible parts of the spectrum. The transmission curves change slightly between different translation speeds, but overall stay relatively similar, remaining over 80% transparent over 400nm wavelength. As was seen with the XeCl irradiation of the AZO films, there exists a small bump within the absorption edge of the AZO. Using the same assumptions as before, a Tauc plot was calculated from the transmission data and is shown in figure 7.8.

The Tauc plot shows a slight variation in the optical band gap with increasing CO_2 laser dose. The trend with the AZO films is similar to that seen with the ITO films when they were irradiated with the CO_2 laser, where the bad gap is decreasing as the electrical conductivity increases. The effect is not as pronounced as with the ITO films, but a trend towards a lower optical band gap can be seen from figure 7.8. As mentioned in the previous chapter, the lowering of the band gap with increasing electrical conductivity is the opposite to that expected. This points towards the conclusion that the processes involved in increasing the electrical conductivity in both the ITO and AZO films is the same, and is due to the removal of non conductive material from the films.

With the UV-VIS transmission results pointing towards a reduction in the charge carrier density with increasing laser dose, there should be a visible change in the plasma edge located in the infrared. The infrared transmission results were taken, and are shown in figure 7.9. The plasma edge remains beyond the transparency of the glass substrate, however, at around 3.2μm it can be noticed that with increasing laser doses the transmission is slightly higher. If it is assumed that this trend continues further into the infrared, it could suggest that the plasma edge has been pushed further towards longer wavelengths. This is an extrapolation and to be conclusive, the transmission data would have to be taken with the AZO films deposited on a substrate that was transparent further into the infrared so that the plasma edge could be clearly seen.

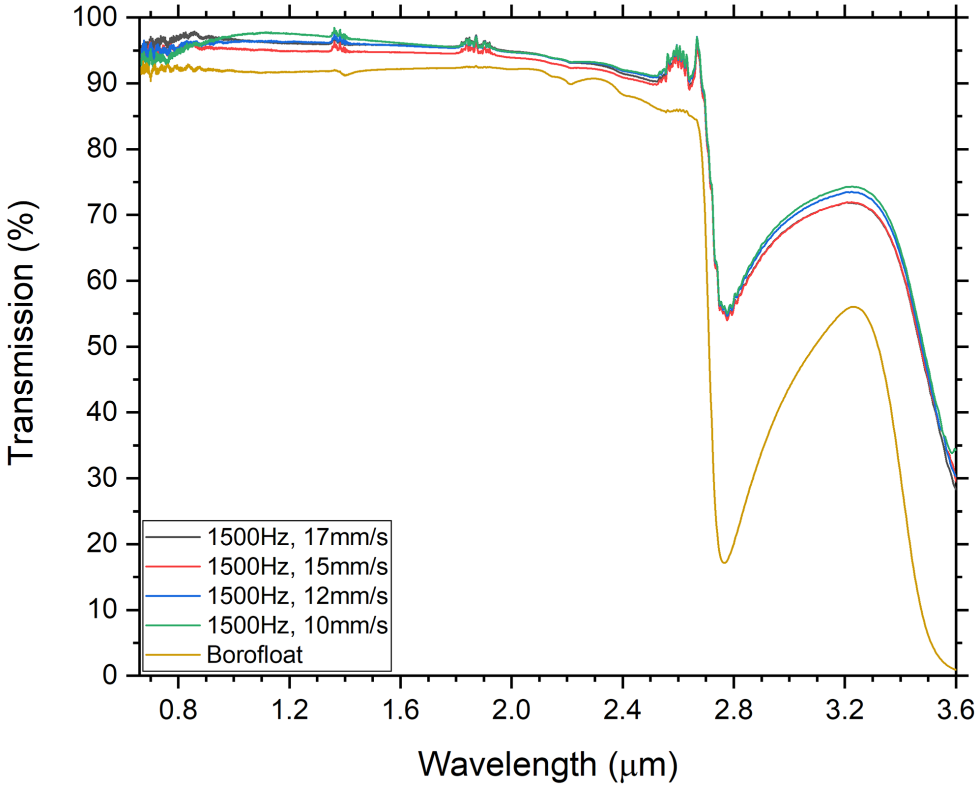

FIGURE 7.9: Infrared transmission results for the AZO films irradiated with the QSW:CO_2 laser at different speeds with a modulation frequency of 1500Hz.

7.4 Silver grids for increased conductivity

As part of a contingency plan in the INFINITY project, patterned silver grids were put in place to help improve the electrical conductivity of the AZO films in the case they were not electrically conductive enough to be used in a demonstrator device. With the best result reaching a sheet resistance value of 2.3MΩ/sq, a working demonstrator device could not be made and the silver grids were implemented to improve this. The idea behind the patterned silver grids was to add a mesh of highly conductive pathways underneath the continuous AZO film. This way, the AZO films only have to transport charge to the nearest silver grid-line. The silver grids are very conductive, so even if the resistance probes are centimetres away the majority of the conduction is coming from the silver grid.

The smaller the grid is be made, the less distance current has to flow through the AZO, making the films appear to become increasingly conductive. The drawback to using the silver grids is that the silver is not transparent, and blocks light from being transmitted. For this reason, the grid lines wanted to be as thin as possible, whist retaining a suitable level of conductivity.

The first attempt at using silver grids was produced by INM in Germany. These grids were created using a research grade ink-jet printer filled with a silver-based solution. An optical microscope image of the printed silver grids can be seen in figure 7.10. The grids are quite large, with 1mm spacing and 200μm wide lines. This made the grid very noticeable by eye, which would have been very poor if used in any display technology. An example of this

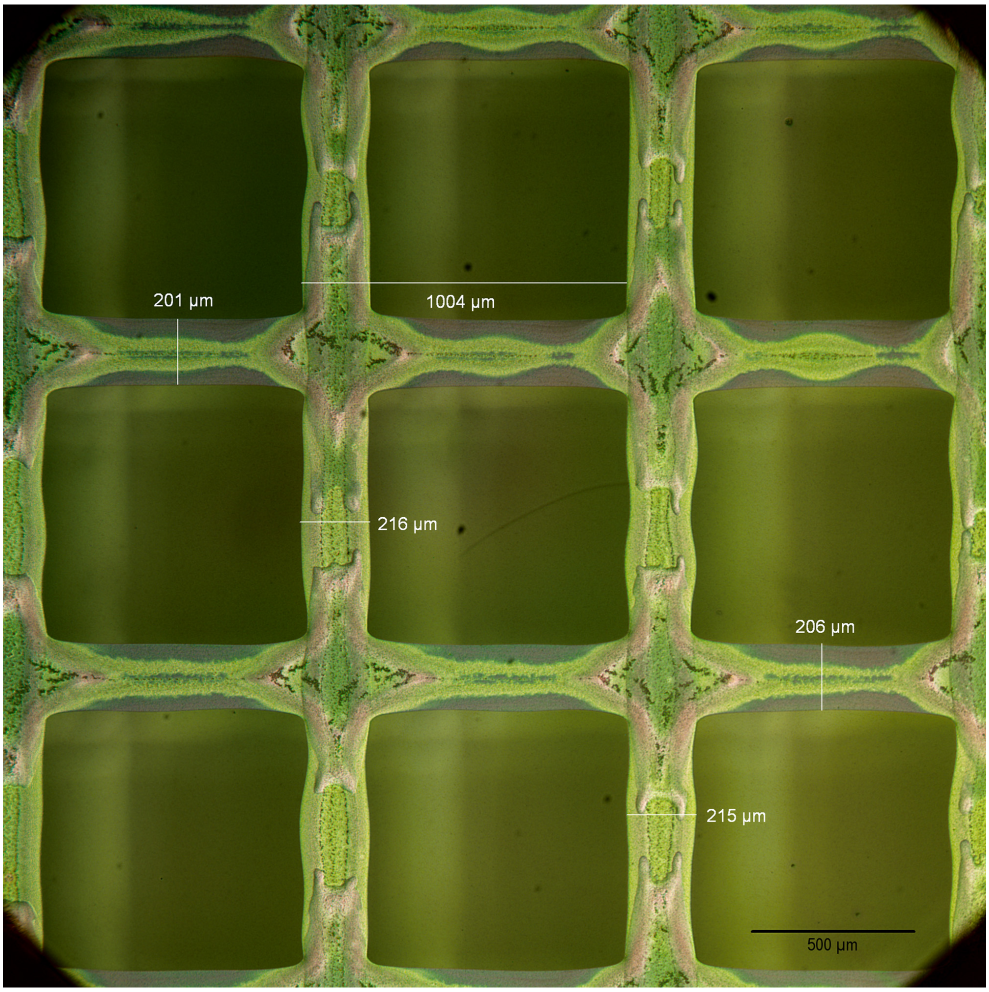

FIGURE 7.10: Image of the ink-jet printed silver grids by INM. The grid is measured as having a spacing of 1mm with grid lines 200µm wide.

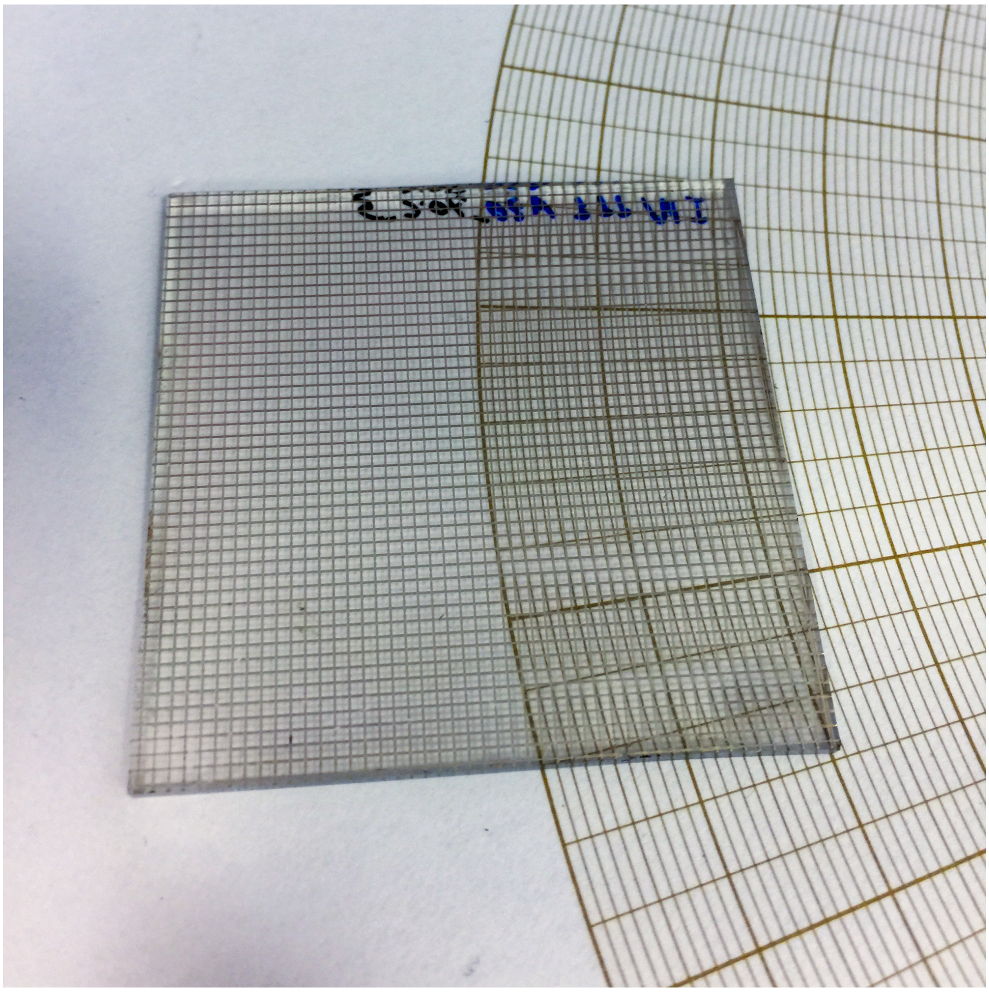

FIGURE 7.11: Image of the ink-jet printed silver grids by INM against a piece of white graph paper to demonstrate the visibility of the grids.

can be seen in figure 7.11. Furthermore, it was calculated by one of the INFINITY partners that the grid spacings were too large when coupled with the AZO films to create a working demonstrator device (either LCD display or photovoltaic panel). The ink-jet printer used to print these grids was already producing the smallest features it could, and so another method of creating small grids with silver was required.

The properties of the ink-jet printed films were measured at INM and the sheet resistance of the silver grids was measured to be 3Ω/sq, which is comparable to the ITO films used in the majority of devices today. The visible light transmission was only 69% however, which is 15-20% lower than ITO films. Even though the ink-jet printed silver grids were too large for use in a display or photovoltaic device, they demonstrated that the concept of using an underlying highly conductive grid for reducing electrical resistivity is achievable and can have some very promising results. Consequently, producing finer silver grids using laser-based techniques was explored

7.4.1 XeCl laser patterned silver grids

In the previous section, the use of silver grids was demonstrated to be a viable option for increasing the conductivity of the AZO film system, at a cost of a slightly reduced visible light transmission. To reduce the size of the grids, the use of laser ablation of silver films was employed. By reducing the size of the grids, we aimed to achieve two things: reduce the spacings between the grid lines in order to decrease the distance current has to flow in the highly resistive AZO film, and secondly to increase or maintain the level of visible light transmission by making the grid lines thinner. To be able to laser ablate silver grids, a 70nm uniform layer of silver was sputtered onto glass and PET substrates at a thickness of around 50nm as measured with the Dektak XT profilometer.

The first laser used to ablate the silver films was the XeCl laser. This laser was chosen because of the high level of absorption silver has at around the wavelength of the laser at 308nm, as shown in figure 7.12. The fact that silver

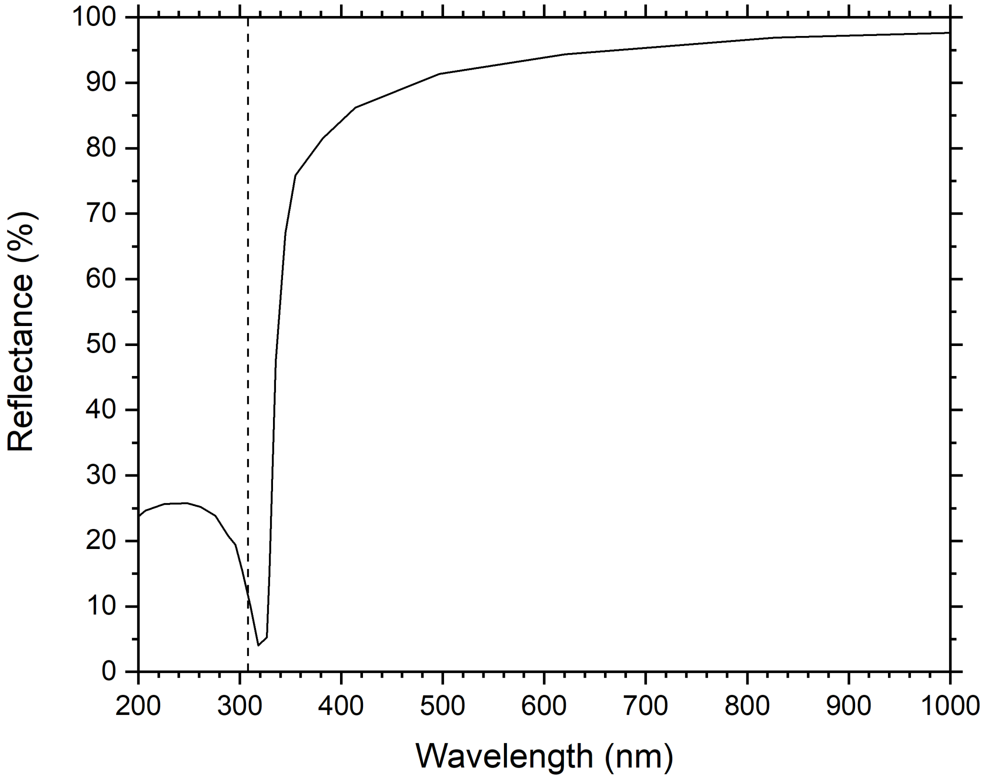

FIGURE 7.12: Graph showing the reflectance of silver from 200nm to 1000nm. The vertical dashed line shows the XeCl wavelength at 308nm.

has a low reflectivity at ~310nm increases the coupling of the laser energy and significantly reduces the ablation threshold fluence.

The experimental setup for ablating the silver films was the same as used in chapter 4, but with a 10x demagnification imaging system to achieve a smaller spot size and higher fluence. With a 1mm square mask, it was possible to produce a 100µm image on the surface of the silver film. It was found that when the fluence was set to around 1.5Jcm^{-2}, the silver films were completely removed in two pulses without damaging the underlying glass. To be able to ablate a grid pattern made from these 100µm square laser generated openings in the film over an area of 50x50mm, each point would require 2 pulses. If the sample translation stages had to stop in between each point then the processing time becomes long. Instead, the laser was synced to the translation stages using Aerotech's position synchronised output (PSO) command, which tells the laser to fire as the stages move a set distance. In this way, the stages could start at a set co-ordinate and move in lines as fast as they could move and request a laser pulse as they reach the set distance. Once the sample had been completely irradiated with single pulses, the stages were put back to the starting co-ordinate, and a second pass was completed using the same parameters to increase the puse count per area to 2, thus completely remove any remaining silver from within the grids. The XeCl laser had a maximum pulse repetition frequency of 50Hz, which was the limiting factor on how fast the patterning could be achieved. With an image size of 100µm, leaving a grid line width of 20µm, gave a travel distance of 120µm to travel between pulses. At 50Hz, it was possible to move at a speed of 6.25mm/s before the laser reaches the maximum pulse repetition frequency. If we assume the stages have zero acceleration time before max speed, and a sample size of 50x50mm, we can expect one single sample to be completed in a time of around 55 minutes.

After patterning the sputtered silver films with the XeCl laser, it was immediately noticeable that the sample had a higher level of transmission in the visible but with a dark tint. As shown in figure 7.13, the apertures in the silver film gave a semi-transparent appearance after patterning with the laser. Because the grid size had become 10x smaller than the ink-jet printed films, it was no longer possible to see the structure with the naked eye unless the sample was very close. Figure 7.14 shows the appearance of the grid under

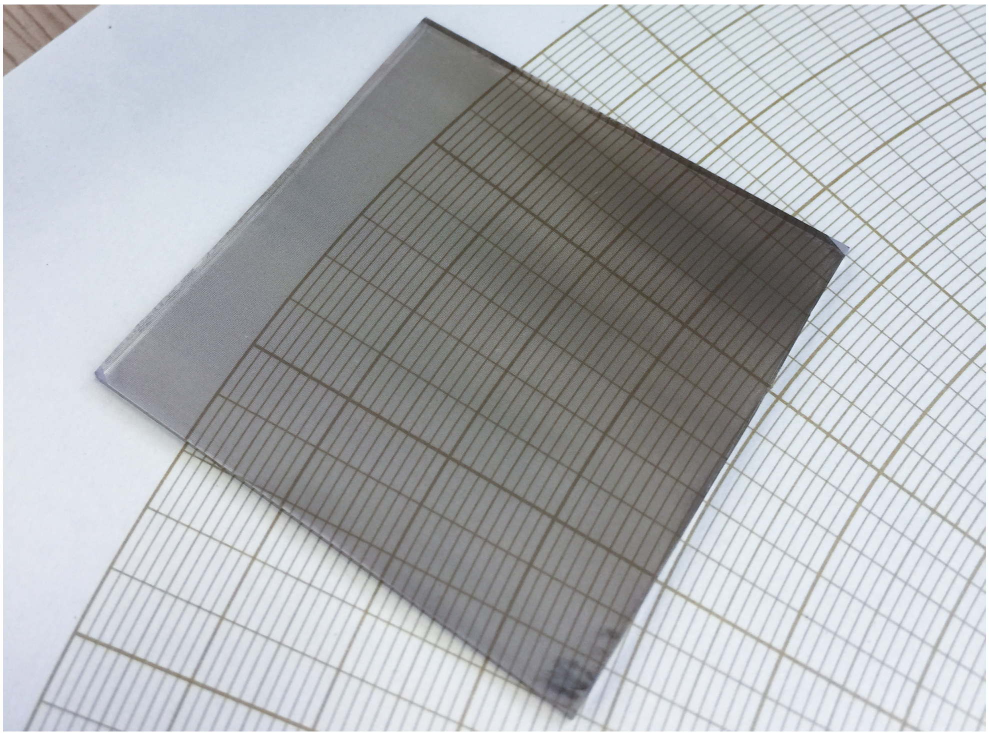

FIGURE 7.13: Picture showing a semi-transparent sputtered silver film after been patterned with the XeCl laser.

the optical microscope. It is shown that with the XeCl laser, it was possible to create 120µm silver grids having a line width of 20µm. It should be noted however, that the XeCl laser could have patterned smaller grids than this if an even higher level of demagnification was used. Unfortunately, the optical setup used here would not allow us to go to a higher demagnification due to space limitations. Furthermore, the time requirements for processing would have been even longer per sample with smaller image sizes.

Another important aspect of the silver grids, was that they had to be as flat as possible. This had to be ensured because if the roughness of the films was high, the sharp peaks could pierce through the stacked electronic layers and create short circuits. To check for surface imperfections, tilted SEM images were taken of the patterned silver films. An SEM image of the XeCl laser patterned silver grids is shown in figure 7.15. The silver grids after XeCl laser

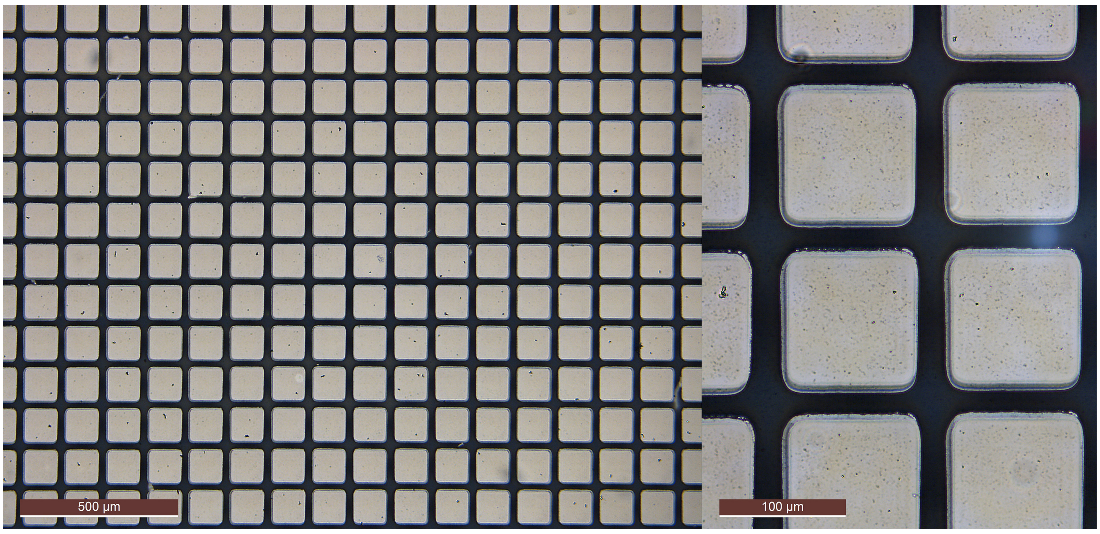

FIGURE 7.14: Optical microscope image taken of the XeCl patterned silver films. On the right is the same area, just at a higher magnification.

patterning did not appear to have become rough. Apart from spots of debris or contamination which could be cleaned off, the ablated areas have sharp edges.

Transmission and electrical measurements were made for the grids before and after the AZO layer was applied by INM in Germany. Before the AZO layer was applied, the optical transmission of the silver grid itself was measured to be 47%, and the sheet resistance was measured to be $11\Omega/\text{sq}$. After the AZO film was applied on top of the silver grid and irradiated with the QSW:CO_2 laser with the highest dosage without damaging the films, the transmission was reduced to a value of 43%, and the sheet resistance reduced to a value of $2\Omega/\text{sq}$. The reduction in visible light transmission was expected, since the AZO films is not perfectly transparent, however, the reduction in sheet resistance was not expected.

The XeCl laser patterned silver grids show promising results for creating highly conductive patterned silver grids. Unfortunately, the visible transmission of

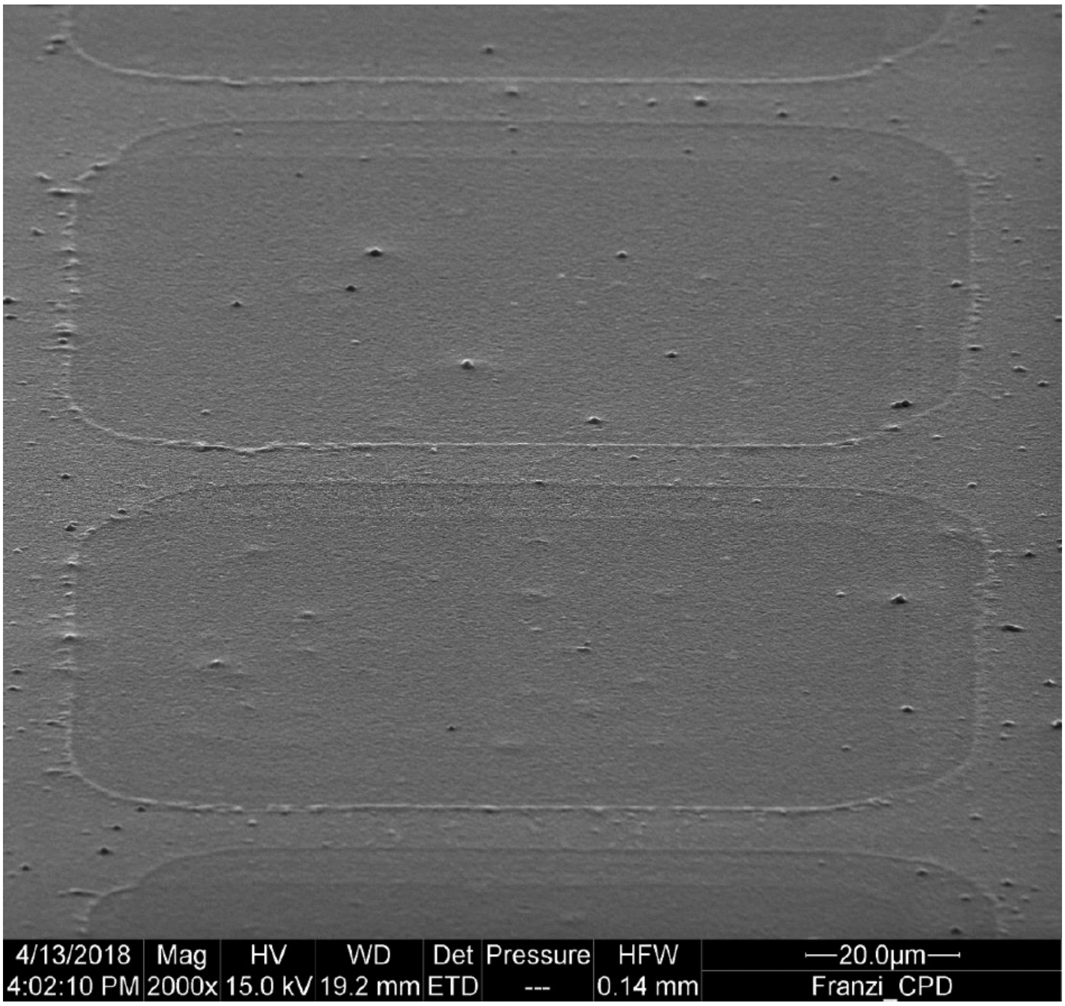

FIGURE 7.15: Scanning electron microscope image of the XeCl laser patterned silver grids.

these films was at best 47%. Whilst the silver grids showed very good electrical conductivity, the low visible transmission would not be ideal for creating a functional device. Additionally, calculations by the INFINITY partners showed that the 100µm spacing between grid lines would still not be small enough for use in their photovoltaic devices when using the poorly conductive AZO film. The processing times when using the XeCl laser were also very long, due to low pulse repetition rate.

7.4.2 Yb:YAG laser patterned silver grids

Following on from the success of the XeCl laser, the Yb:YAG laser was used to pattern the sputtered silver films. The Yb:YAG laser has a maximum pulse repetition rate of 10MHz, and therefore it was expected to be able to pattern the silver films at a much higher rate, thus improving on the XeCl laser processing time. With a pulse length of 841fs, the peak power of the laser pulses from the Yb:YAG laser was high enough to ablate the silver films even though the reflectivity of silver is in excess of 98% at a wavelength of 1030nm wavelength. Experiments were performed on silver films on both glass and PET substrates.

7.4.2.1 Glass Substrates

With a variable energy control for the laser pulses, the ablation threshold for the silver films was measured with the Yb:YAG laser at the focal point of the F-theta scan lens. Because the Yb:YAG laser beam shape was Gaussian, by keeping the beam size the same and varying the pulse energy the diameter

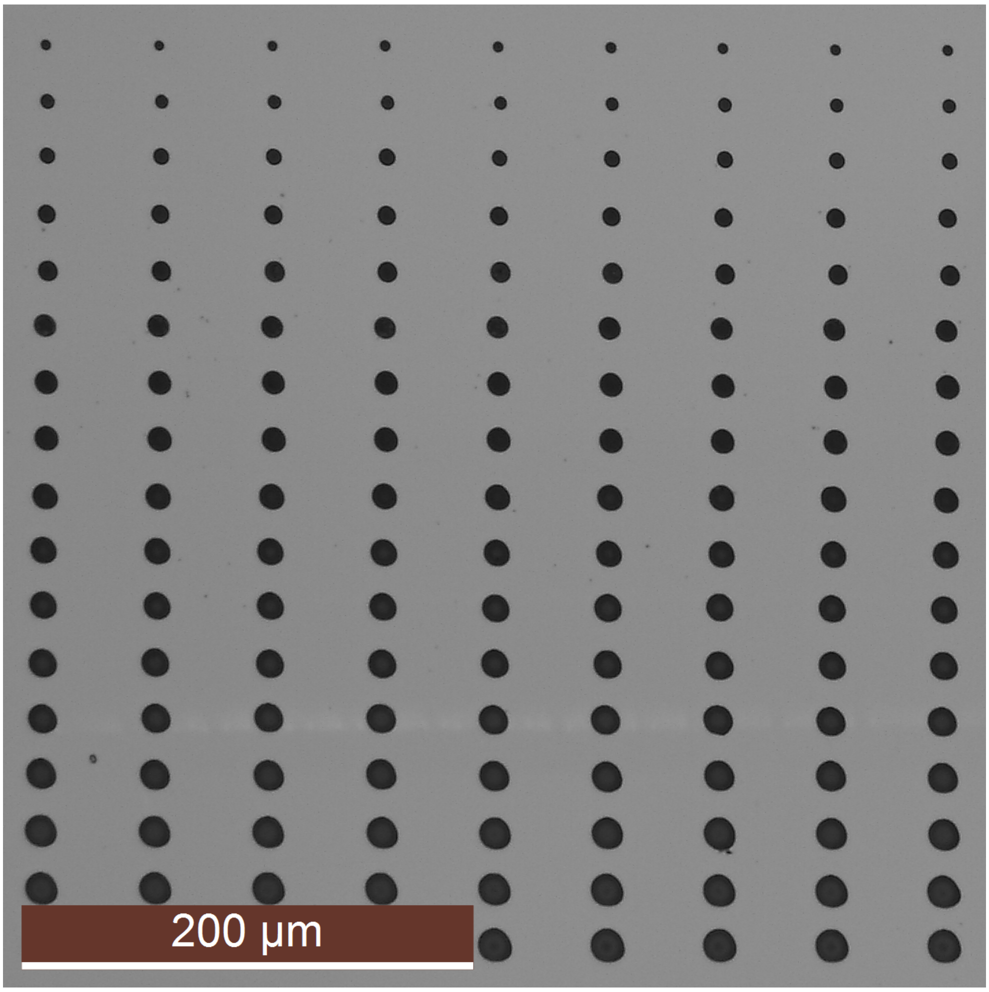

FIGURE 7.16: Optical microscope image of a small section of the 17 damage sites created by the Yb:YAG at various pulse energies.

of the damage sites squared plotted as a function of pulse energy allowed the damage threshold of the silver films to be determined. From this analysis, the spot size of the laser beam through the F-theta lens can also be found. To continuously vary the pulse energy, a rotating half wave plate and Brewster plate was used. To measure the average pulse energy, the average power was recorded over 5 minutes and divided by the pulse repetition rate. Increasing pulse energies were used to create damage sites with single pulses. An optical microscope image of the damage sites is shown in figure 7.16.

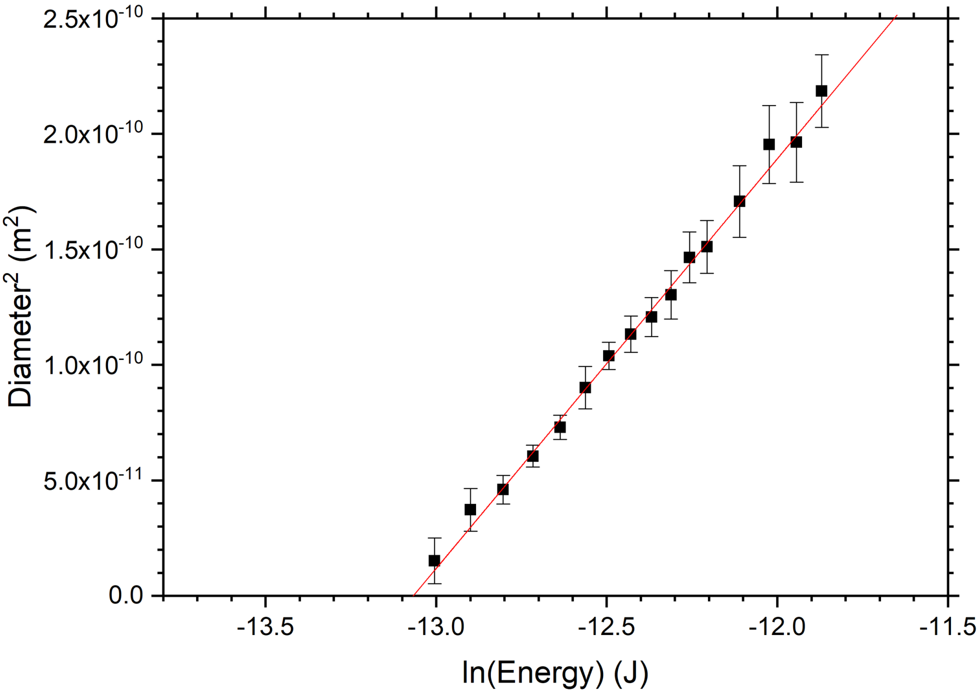

FIGURE 7.17: A graph showing the relationship between the square of the diameter of the damage sites and the log of the pulse energy. The point where the line of best fit intersects the x-axis is the damage threshold energy.

To measure the damage threshold for the silver films, equation 7.1 was used. [134–136]

$$D^2 = 2\omega_0^2 \ln|\frac{E}{E_T}| \tag{7.1}$$

Here, D^2 is the diameter squared of the damage sites, E is the energy of the laser pulse, E_T is the threshold energy for damage, and ω_0 is the beam radius ($1/e^2$ value). To measure the diameter of the damage, a program called ImageJ [137] was used to automatically measure all of the 25 sites as well as the differences between the major and minor axis of the slightly elliptical spots. The results from this procedure are plotted in figure 7.17.

The damage threshold of the silver films was measured to be 2.12μJ. From equation 7.1, we can also measure the spot size of the laser by measuring the gradient of the line of best fit in figure 7.17. The gradient in this case was $1.77 \times 10^{-10} \pm 4 \times 10^{-12}$ m^2. This value gives a spot diameter of 18.8 ± 0.5µm. The damage threshold for the sputtered silver films with the Yb:YAG laser was then calculated to be 6.89kJm^{-2}, averaged over the area of the Gaussian beam. The increasing size of error bars seen in figure 7.17 were due to two reasons: at larger pulse energies the damage site became increasingly elliptical and the difference between the major and minor axis of the circle became larger, and at lower pulse energies the uncertainty was larger were due to the resolution of the optical microscope.

In order to create grids with the Yb:YAG laser with a Gaussian beam profile, packing ratios of circles were investigated to find the best way to pattern the silver films for maximum coverage. We aimed to keep the patterned circles to a maximum of 15µm in diameter, to gives the best possible success of the conductivity being high enough with the AZO deposited on top. This meant that two sized circles in the patterning process could be utilised. Using a dual-sized circle packing technique, with the smaller disk around 60% smaller in diameter, the maximum packing ratio achievable was approximately 92%. [138] Alternatively, using the densest packing ratio with a single sized circle, (hexagonal packing) $\sim$91% can be achieved. [139] It was decided that the single sized circle technique would be used, due to the ease of programming the translation stage movements, not having to change pulse energy during processing and the negligible decrease in packing ratio lost as compared to the dual-sized circle technique.

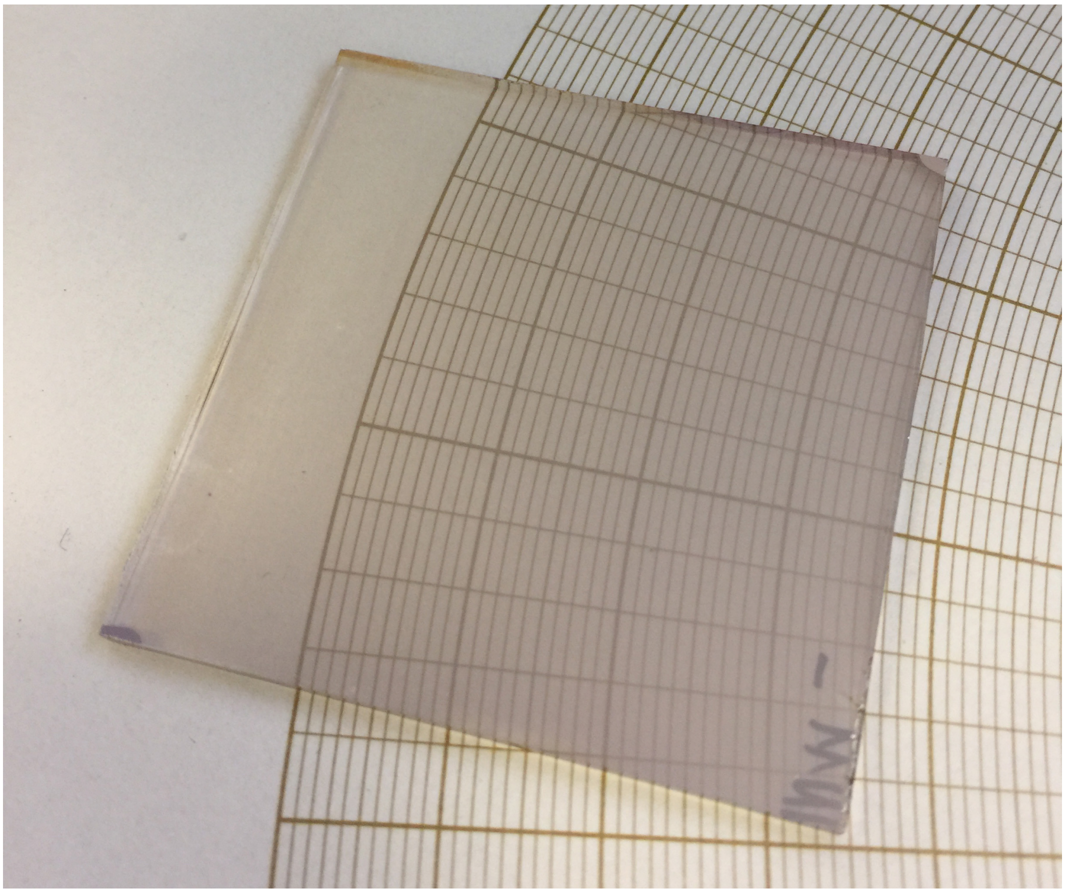

FIGURE 7.18: Photograph showing a silver film after having been patterned with the Yb:YAG laser. The array of circular holes in the silver film gave it a semi-transparent appearance.

After processing the silver films using the Yb:YAG laser, the transparency of the sample had visually improved over the films processed with the XeCl laser, as can be seen in figure 7.18. The patterning of the film could not be seen on the sample because the features were so small. However, diffraction effects could be seen on light passing through the sample.

The Yb:YAG patterned films as viewed under the microscope are shown in figure 7.19. Each circle was measured to be ∼13µm, with a gap between adjacent circles of 5µm. The silver grids were measured before and after the AZO layer was put on top. The silver grids by themselves were measured to have a sheet resistance of 3Ω/sq with a visible transmission of 53%. It is important

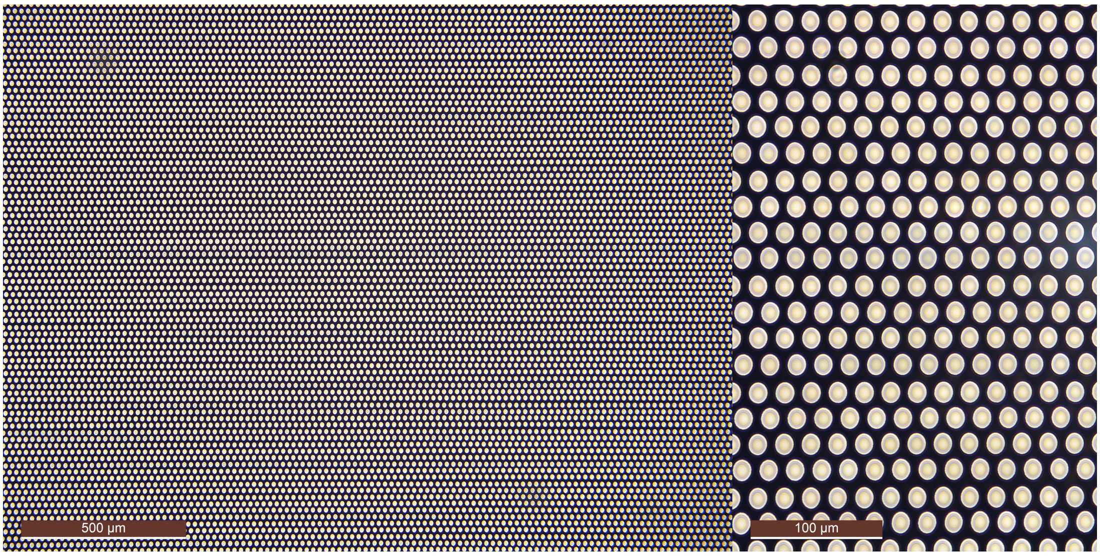

FIGURE 7.19: Optical microscope image taken of the Yb:YAG patterned silver films. On the right is the same area at a higher magnification.

to note that because of the diffractive nature of the patterned films, the visible transmission could have been higher if the measurements were taken closer to the sample. After the AZO layer was put on top of the silver films, the sheet resistance was measured to be 11Ω/sq with a visible transmission of 61%. It is unknown why the visible transmission of the samples increased when the AZO layer was placed on the silver films. The processing times of the silver films using the Yb:YAG were greatly reduced. The 50x50mm samples could be patterned in approximately 8 minutes, and were limited only by the translational stages.

The silver films were viewed using the SEM at an angle to check the surface roughness of the films after patterning. As can be seen from figure 7.20, the roughness of the Yb:YAG patterned silver films was very high. Some features are seen to be over 3µm high, which would be very detrimental when coating the films with an AZO layer that is 500nm thick. The high roughness of the

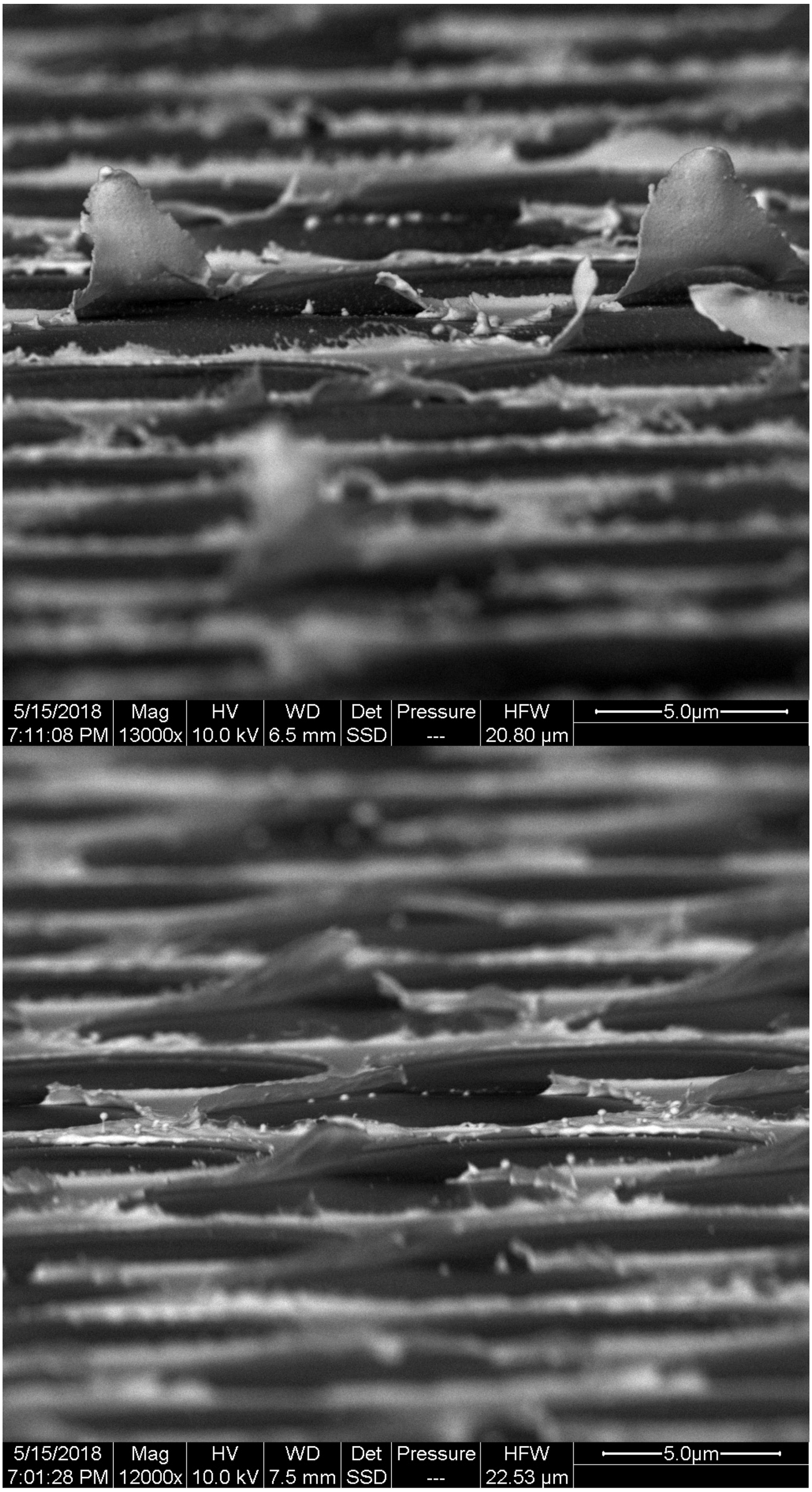

FIGURE 7.20: Tilted SEM images of the Yb:YAG patterned silver films. The roughness of the sample is seen to be very high.

films is likely due to the Gaussian shape of the beam. Since the intensity varies continuously across the beam, there is no clearly defined edge of processing. It is thought that the rough edges of the patterned areas are caused by material which was effected by the laser pulse, but not enough to be completely ablated and detaches from the substrate leaving behind areas which are very rough.

Despite the roughness of the silver films, an AZO layer was spin coated onto the samples to see how much the raised areas would effect the AZO layer on top. In an attempt to make the AZO films as flat as possible, a double layer of AZO was spin coated onto the patterned silver films. The usual AZO coating was applied with a thickness of 500nm, then this was followed by spin coating a much thinner layer on top to try smoothing out any roughness that may have been present after the first layer. The SEM images of the AZO double layer are seen in figure 7.22. The underlying patterned silver films can be seen to be sticking through the AZO films, which would be detrimental to any electronic devices being applied to the AZO films. Despite been able to pattern sputtered silver films into grids of the order of 10µm at very fast rates with sheet resistances as low at 10Ω/sq, the Gaussian nature of the laser beam makes it unsuitable for use in the production of flat enough films for electronic devices. This was due to the continuously varying intensity profile of the Gaussian beam which caused some areas of the beam to be above the ablation threshold, and some to be below. An example of the intensity profile across a Gaussian and a top-hat beam can be seen in figure 7.21. What was left on the surface was half ablated regions of silver which made the roughness too high for commercial devices to function.

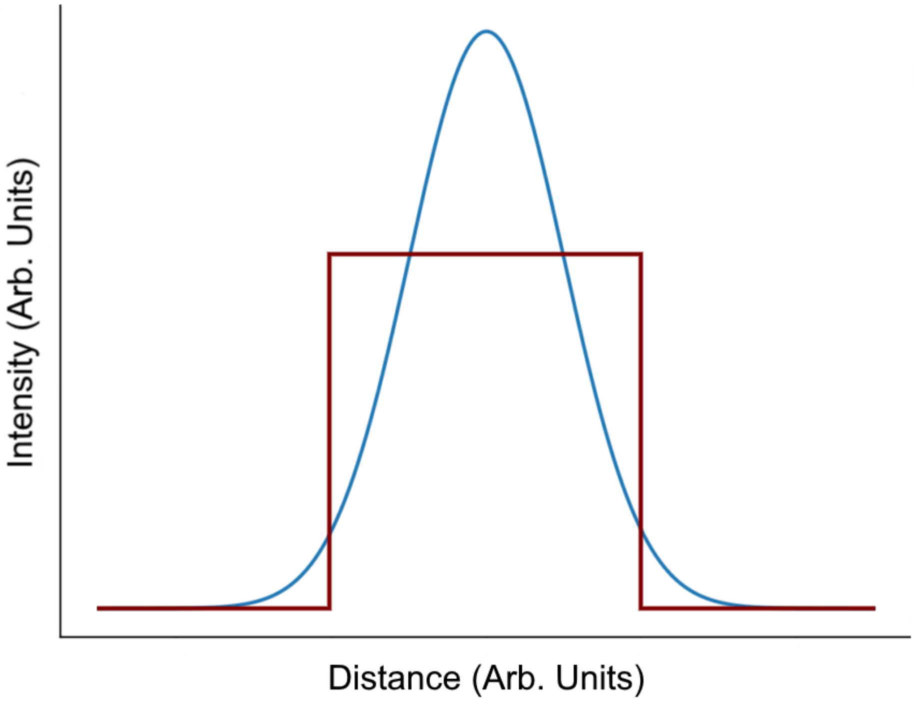

FIGURE 7.21: The intensity profile across a Gaussian laser beam (**Blue**) and a top-hat laser beam (**Red**).

7.4.2.2 PET substrates

As mentioned earlier, the sputtered silver films were also applied to flexible PET substrates for laser patterning. As with the glass substrates, the damage threshold of the silver films was measured on the PET substrates in the same way. The PET films were put at the focal point of the lens, and damage points were created with the Yb:YAG laser at different pulse energies. Figure 7.23 shows the damage points created with the laser at 7 different pulse energies.

Only 7 pulse energies could be taken using the Yb:YAG laser due to a loss in power from the laser itself, as well as a degraded beam shape, as demonstrated in figure 7.23. Even with the poor beam quality, the square of the damage diameter was plotted against $\ln(Energy)$ to measure the damage threshold and

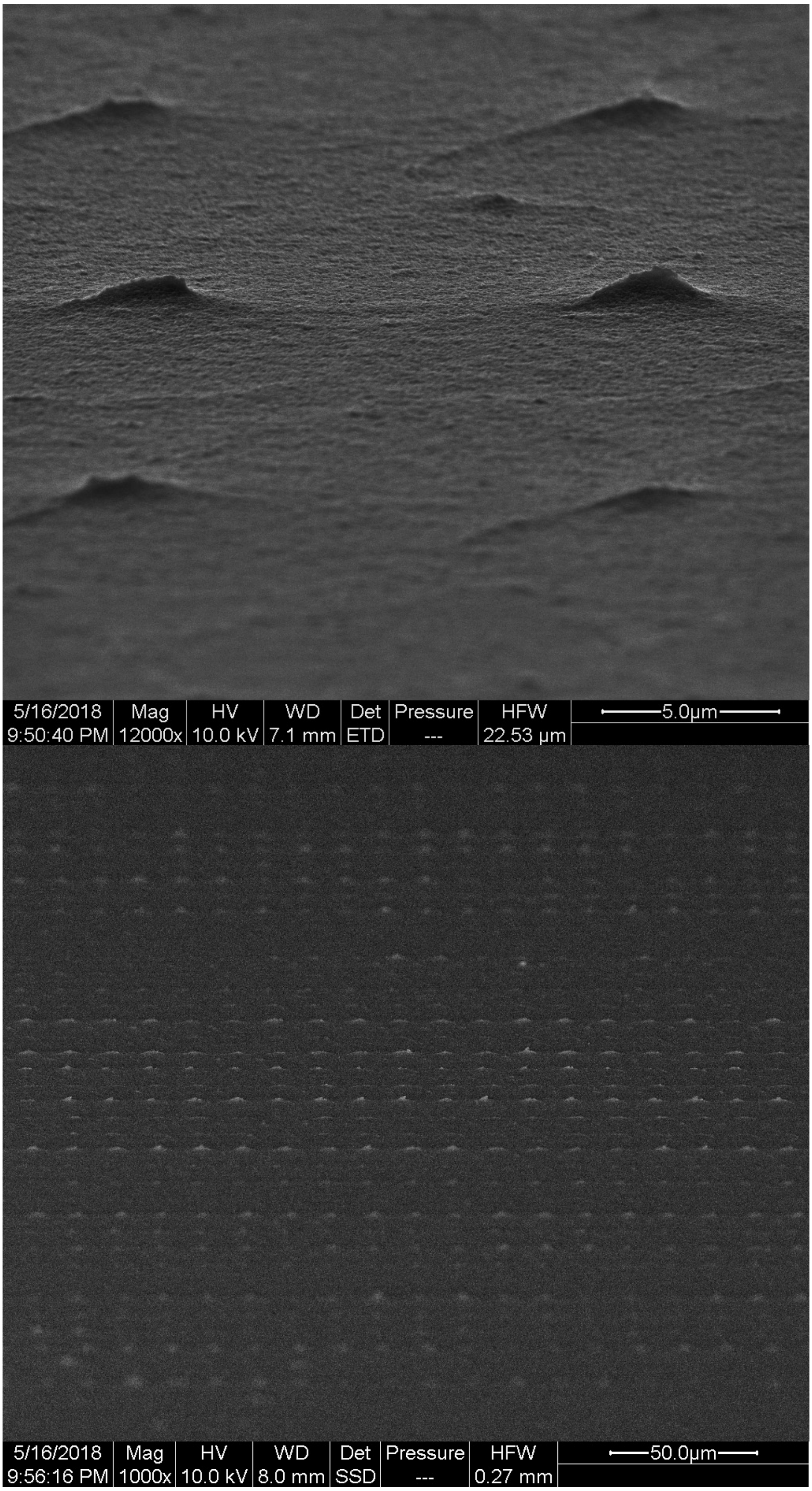

FIGURE 7.22: Tilted SEM images of the Yb:YAG laser patterned silver films with a double layer of AZO applied. Peaks of the underlying silver films can be seen to still be present through the AZO layer.

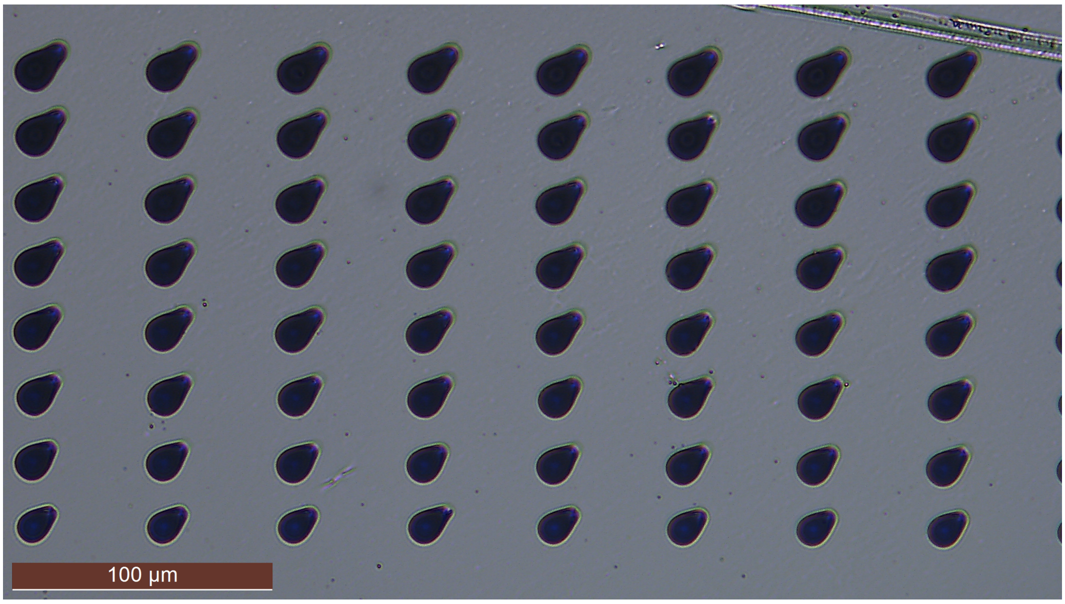

FIGURE 7.23: Optical microscope image of a small section of the 7 damage sites on sputtered silver films created by the Yb:YAG laser at various pulse energies on PET substrates. A poor beam quality had developed from the laser when the damage points were produced.

beam diameter. Due to the large difference in the major and minor axis produced by the laser on the PET, the uncertainties were quite large as seen in figure 7.24. Using the line of best fit, the intersect at the x-axis gives a damage threshold of 4.4µJ at the focus of the lens. The spot size of the laser beam at focus, using the largest and smallest measured gradients, was measured to be 19.5±2.1µm. The beam diameter of the Yb:YAG laser at focus agrees with the beam diameter as measured on the glass substrates within experimental uncertainty. The damage threshold was therefore measured to be a value of 14.7kJm^{-2}, which is over double the threshold measured for the silver films on the glass substrates. It is possible that the increase in threshold represents the better adherence of the silver film to the PET leading to an increase in heat flow to the substrate.

Unfortunately, due to the severe drop in power and beam quality from the

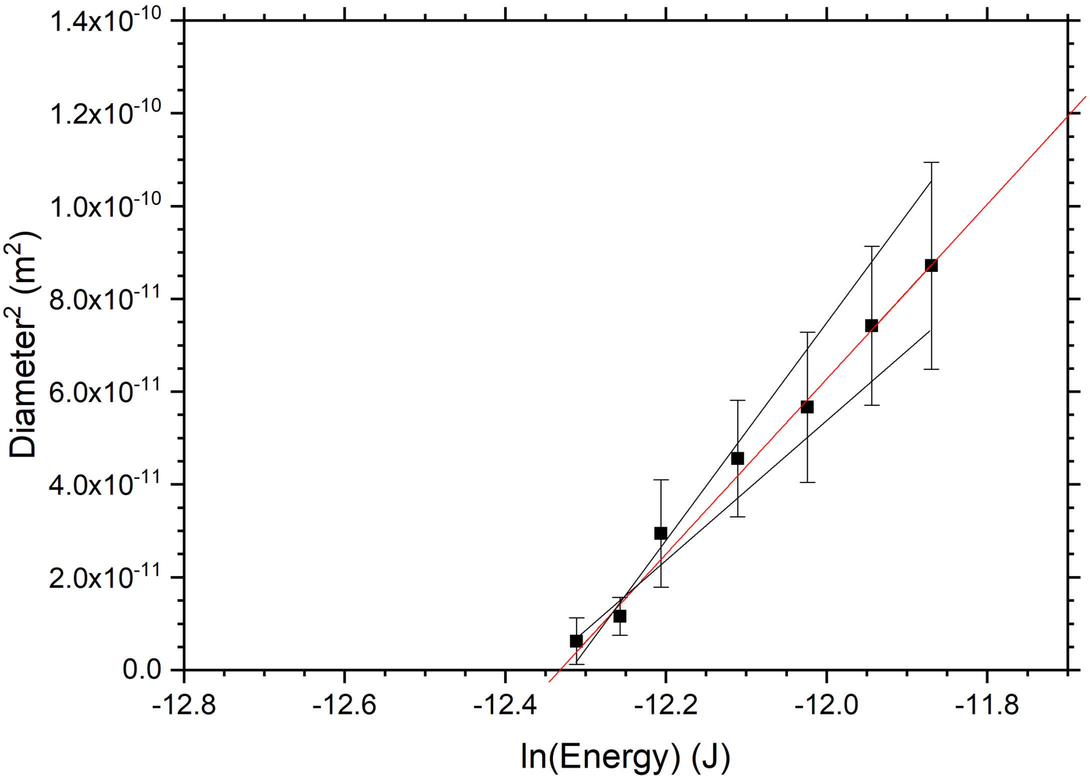

FIGURE 7.24: A graph showing the relationship between the square of the diameter of the damage sites and the logarithm of the pulse energy of the silver films on PET. The red line shows the line of best fit, with the two black lines showing the highest and lowest gradient within the errors.

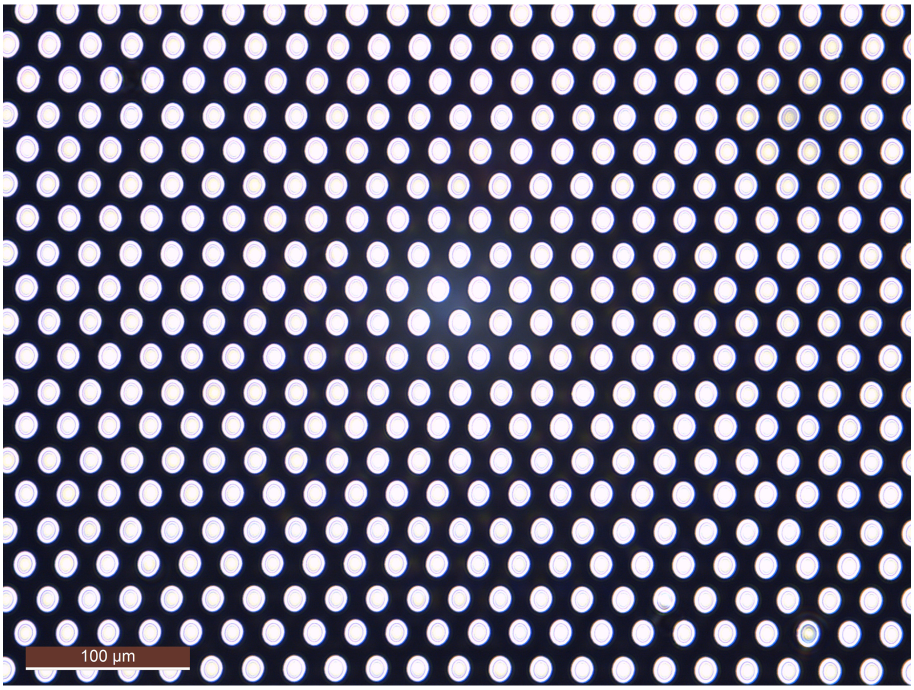

FIGURE 7.25: Optical microscope image taken of the patterned silver films on PET substrates. This was only a preliminary experiment to test for the feasibility of the process.

Yb:YAG laser, a complete sample of the patterned PET was not able to be completed and hence not characterised electrically or optically. An earlier preliminary experiment on the feasibility of patterning the silver films on PET was completed however, and figure 7.25 shows a patterned silver grid on PET substrates. The results were promising, giving very similar results to the silver films on glass substrates. The underlying PET did not appear to be damaged by the single laser pulse, and the silver was completely removed. In figure 7.25 the optimisation of the circle packing had not been performed, and large areas of silver were left. This could have been easily improved by changing the spacing between pulses, however, because the beam shape degraded, packing would have been made very difficult on a full scale sample.

7.5 Conclusions

In this chapter, indium free AZO films were irradiated with the lasers that gave the best results for ITO films in the earlier chapters in this thesis, in the ultraviolet and infrared regimes. The AZO films were intrinsically much lower in electrical conductivity than the ITO films before irradiation. By taking infrared transmission measurements, it was found that this was due to a lack of charge carrier density within the AZO nanoparticles, which severely limited the electrical conductivity achievable with the materials.

By irradiating the AZO films with the XeCl laser in the ultraviolet, a measurable change in the electrical conductivity could not be obtained due to the upper limits of the electrical resistance measurements of our equipment. The optical transparency of the AZO films was very good, having greater than 85% transmission throughout the visible region of wavelengths. The band edges in the ultraviolet and infrared showed no visible change in the charge carrier density in the films following laser irradiation, and without a value for the sheet resistance it was not possible to know if the electrical properties of the films were changing at all.

When the AZO films were irradiated with the QSW:CO_2 laser, for the majority of the irradiation regimes, a value for the electrical conductivity could not be measured due to the resistance being so large. However, for the highest doses of irradiation, the sheet resistance values were lowered enough to be measured. With the QSW:CO_2 laser set to a modulation frequency of 1500Hz and a translational speed of 10mm/s, a sheet resistance value of 2.3MΩ/sq was obtained. If a higher repetition rate or slower translational speed was used, damage of the AZO films was observed, making the sheet resistance effectively infinite due to discontinuities within the films from cracking. The transparency of the AZO films remained above 85% after laser irradiation throughout the visible regime. As with the ITO films, the ultraviolet band edge of the AZO films appeared to decrease with increasing conductivity, which is the opposite of that expected, since this implies the charge carrier density is reducing. This conclusion was partially supported up by the infrared plasma edge appearing to shift further into the infrared, however, because the plasma edge lied beyond the transparency of the glass substrate, this cannot be fully confirmed.

INM performed several experiments on the AZO films alongside the laser irradiation experiments. It was found that the resistivity could not be measured (due to equipment limitations) when cured under an ultraviolet mercury lamp. Treatments in a furnace at 550°C for an hour also lead to an unmeasurable sheet resistance value. Only when the AZO films were heat treated in a furnace in a reducing atmosphere of forming gas (95% N_2, 5% H_2) could the sheet resistance be measured. When baked in a furnace with forming gas at 550°C for an hour, the sheet resistance measured was 2.28MΩ/sq. [140]

Because the AZO films were not able to be reduced in sheet resistance to a suitable level, a contingency plan for the INFINITY project was brought into action. By using a highly conductive underlying silver grid, the AZO films could be spin coated on top to achieve a better long range sheet resistance which could lower the resistance enough to be used in a demonstrator device.

By using an ink-jet printer, INM managed to print silver grids with a spacing of 1mm with 200µm wide grid lines. With the AZO layer spin coated on top of the ink-jet printed layer a sheet resistance of 5Ω/sq was measured, which was a significant improvement over the AZO layer by itself. However, due to the large size of the ink-jet printed grids, the visibility of the grids was very high and the distance between grid lines was too large to make a device work with the poor conductivity of the AZO.

To make smaller grids than that possible with ink-jet printing, laser processing was used. Patterning the sputtered silver films was explored using two laser systems to achieve smaller grids. Firstly, the XeCl laser was used in a projection etching configuration. The UV wavelength of this laser coupled into the silver easily. Using this laser a 10 times improvement was achieved over the ink-jet films by creating a square grid with 100µm spacing and 20µm line thickness. The optical transparency of the patterned silver was ∼43% which, whilst useable in a device, would be ideal if larger. The sheet resistance of the patterned silver was measured to be 11Ω/sq. The top hat nature of the irradiance profile of the beam meant sharp edges were created in the silver, leaving a flat area to spin coat the AZO layer onto. The downside of using the XeCl laser was the low pulse repetition rate ot 50Hz, meaning processing times were very large (∼55 minutes for a 50x50mm sample).

The second laser used to pattern the sputtered silver films was the Yb:YAG ultrashort pulse laser. With a pulse repetition rate of 10MHz the processing times were limited only by the speed of the translation stages. With the Yb:YAG laser, a Gaussian beam was used to create 13µm holes into the silver films with a gap of 5μm between adjacent circles. A single-sized circle packing technique was used, with a hexagonal structure to try to achieve the maximum possible transparency. After the AZO layer was added to the patterned films, a transparency of 61% was achieved, along with a sheet resistance value of 11Ω/sq. By using a Gaussian beam, the edges were no longer sharp as they were with the imaged XeCl top hat beam. This lead to a very rough surface that affected the spin coated AZO layer on top, and would not be suitable for the sensitive electronics in contact with the AZO film. However, the processing times for the 50x50mm sample had been reduced to only 8 minutes.

Chapter 8

Conclusions

8.1 Conclusions

Laser processing of wet-processed transparent conducting films has been studied using ultraviolet and infrared sources to create electrically conductive, yet visibly transparent, films on glass and PET substrates.

The ITO films manufactured by INM were characterised before laser irradiation to get a benchmark for how the films initially compared to commercially available transparent conducting films. The ITO tracks which were ink-jet printed on glass substrates were measured to be 500μm wide and had a variable thickness across the track with two spikes of thickness near the edge caused by the coffee ring effect. Measuring the optical properties of these tracks would have been difficult due to the small width and variable thickness, and it was chosen to measure the properties of the ITO films on spin coated, larger area, samples. The ITO films produced via spin coating on glass substrates were measured using stylus profilometry to have a thickness of $\sim$520nm. Measuring the optical transmission of the ITO films showed promising results, having greater than 90% transparency throughout the visible range. From the transmission data it was also possible to measure the refractive index of the films via the thin film interference pattern observed. The value obtained of the visible region was $n = 2.4$. The electrical resistivity of the ITO films were measured to be in excess of 100Ω cm, equating to a sheet resistance greater than 2MΩ/sq in this case. The sheet resistance of commercially available ITO films is typically around 10Ω/sq, making the unirradiated ITO films over 5 orders of magnitude less conductive. The infrared transmission spectra was taken via FTIR enabling the discovery of the NIR plasma edge, which can be used to measure the charge carrier density of the films. Using the range of values observed for the plasma edge wavelength, a charge carrier density between 2.8×10^{16} and 5.2×10^{16}cm^{-2} was inferred, which lies in the range for commercially sputtered ITO films. This leads to the conclusion that the unirradiated ITO films have a high charge carrier density, but a low charge carrier mobility results in a poor overall conductivity is. The same ITO films were also provided to us on flexible PET substrates which were deposited via gravure printing. These films were identical to the ones on glass substrates, but had a smaller thickness of 400nm. The experiments then followed aimed at improving the electrical properties of these samples through laser irradiation.

The laser systems use were characterised, and the beam delivery systems were described. For the pulsed laser systems, pulse durations were measured using either photodetectors for pulses greater than 1ns or via autocorrelation for the ultrafast laser systems having pulse durations less than 1ps. The laser systems that produced large multimode beams used beam delivery systems containing an imaging setup to irradiate areas with a known area with uniform energy distribution. For the lasers generating smaller gaussian or circular beams, a simple focussing lens was used to deliver the energy to the samples.

The ITO films were irradiated with ultraviolet radiation from three laser sources. Using a pulsed XeCl laser with a wavelength of 308nm it was possible to reduce the sheet resistance of the ITO films down to $\sim$1.5kΩ/sq (78mΩ cm); a reduction in sheet resistance of 3 orders of magnitude. The absorption coefficient of the ITO films at $\lambda = 308$nm was measured to be 1.18×10^{6}m^{-1}, which equates to 45% of the incident energy being absorbed throughout the film. Irradiation of the ITO films with the pulsed ArF laser at a wavelength of 193nm reduced the sheet resistance of the ITO films down to $\sim$7kΩ/sq (380mΩ cm). However, as the absorption depth at $\lambda = 193$nm was only 105nm, the majority of the depth of the 520nm thick films were unirradiated. Taking into account the absorption depth of the laser energy as being 105nm, the resistivity of the irradiated part of the ITO films is estimated to be $\sim$76mΩ cm which is similar to the lowest achievable resistivity with the XeCl laser. Using a CW HeCd laser to irradiate the ITO films, the best result achieved was a sheet resistance value of 30kΩ/sq (1.5Ω cm). The higher resistivity value obtained with the HeCd laser is likely due to the low power of the laser as well as the high absorption depth at $\lambda = 325$nm at a depth of 1.8µm. The optical properties of the

ITO films did not change significantly after irradiation with any of the ultraviolet laser sources, staying greater than 85% transparent throughout the visible range. The ultraviolet laser sources used photochemical processes to reduce the resistivity of the ITO films, and during irradiation with these sources small temperature rises were seen. The highest temperature rise was seen using the HeCd laser with a $\Delta T = 7°\text{C}$ on glass substrates, enabling the irradiation of the ITO films on temperature sensitive substrates such as PET. With the higher absorbance of the ultraviolet light from the HeCd in the PET substrates, higher temperature rises were seen, but the PET substrates could still be irradiated without damage. The mechanism for the reduction in resistivity is thought ot be shrinkage of the binder in the ink (due to photopolymerisation) causing the ITO nanoparticles to become more closely packed.

Three types of CO_2 lasers were used to irradiate the ITO films with infrared radiation at $\lambda = 10.6\mu\text{m}$. Both the RF:$CO_2$ and the QSW:CO_2 laser operated under similar conditions, and both were able to reduce the resistivity of the ITO films on glass substrates down to $\sim$250Ω/sq (13mΩ cm). This is a reduction in resistivity of 4 orders of magnitude due to laser irradiation, and an order of magnitude lower than could be achieved with the best ultraviolet laser source. The optical properties of the ITO films after irradiation remained very similar in the visible, however, the UV and NIR absorption edges were changed. With increasing conductivities achieved, both the optical band gap and the plasma edge indicated that the charge carrier density was decreasing, which was an unexpected result. Due to the large temperature increases of the ITO films and substrates involved with the RF:CO_2 and QSW:CO_2 laser irradiation, it was not possible to reduce the resistivity of the ITO films to a measurable degree before the temperature sensitive PET substrates were damaged. The TEA:CO_2 laser was used due to the low repetition rate of 10Hz and large achievable fluences at up to 750mJcm^{-2}. The ITO films on PET substrates were irradiated with the TEA:CO_2 laser in an attempt to reduce the accumulated temperature rise of the substrate, whilst still reducing the electrical resistivity of the films. The irradiation did reduce the ΔT enough so that the PET remained undamaged, however, the ITO films exhibited micro cracking throughout the irradiated area, making the resistivity effectively infinite. This behaviour was not seen when irradiating the films on glass substrates at the same fluence. The thermal mechanism for increasing the conductivity is thought to be removal of organic, dielectric, material from the ink. In addition, FTIR absorption spectra measured here indicate that thermally driven polymerisation is also occurring resulting in the same mechanism as the UV lasers.

Using the most promising results from the laser irradiation of the ITO films, indium-free AZO films were laser processed to increase their electrical conductivity. The films were manufactured in the same way as the ITO films, having the same thickness and deposited on the same substrates. Initial characterisation of the AZO films showed that they had a very high resistivity, higher than our instrument could measure. The optical transparency for the AZO films was high though, having greater than 85% transmission throughout the majority of the visible spectrum. Irradiation of the AZO films with the XeCl laser could not reduce the resistivity to a level that could be measured by our instruments, and the optical data could not provide any insights on whether or not the resistivity was reducing or not. Irradiation of the AZO films using the QSW:CO_2 laser at high enough doses of accumulated energy did reduce the resistivity enough to be measured, and the lowest achievable resistivity before the films became damaged was 2.3MΩ/sq (120Ω cm). The optical data suggests that the charge carrier density of the AZO films is very low, with the plasma edge lying outside the transparency of the glass substrates. Therefore, it can be concluded that the low conductivity of the films is intrinsic to the materials used and not the laser processing. This was confirmed by thermal and UV treatments of the raw materials by a project partner.

Finally, to overcome the poor conductivity of the indium-free AZO films, patterned silver grids were produced via laser ablation. These were to lie beneath the AZO films and increase the electrical conductivity. Initially, silver grids were ink-jet printed by INM and proved the concept that they could greatly reduce the resistivity down to a value of 3Ω/sq. The ink-jet printed silver grids were quite large however, with 1mm spaced 200µm wide tracks, making them undesirable due to the visibility to the eye. Using the XeCl laser, it was possible to use a 10x demagnification setup to create 120µm spaced 20µm wide tracks in sputtered silver films. These grids were much less visible to the eye, but were not small enough to be used due to the poor conductivity of the AZO films. A Yb:YAG picosecond laser source was used to create smaller grid patterns, and was able to produce repeatable 13µm circular spots in sputtered silver films, with the largest gaps at $\sim$5µm. It was found however, that the patterned films generated by the Yb:YAG laser were uneven due to partially ablated areas of silver and were unable to be used for device fabrication.

8.2 Future Work

The aim of this thesis was to be able to produce transparent electrically conductive films on flexible substrates. Using ultraviolet radiation the electrical resistivity of as-deposited films was reduced by 3 orders of magnitude on flexible PET substrates without damage, but the resistivity was still too high for use in displays and photovoltaic devices. The use of CO_2 lasers reduced the resistivity by another order of magnitude, which is encouraging for application in some devices, but this was not possible on flexible substrates due to the laser-induced temperature exceeding the materials upper working limit. One possible way to solve this problem would be to selectively deposit energy into the ITO/AZO films and not into the substrate. By selecting a wavelength that is absorbed into the films but transparent to the substrate, it would be possible to concentrate the energy in the film, increasing its temperature whilst leaving the substrate at a lower temperature. Some further work has already been completed on this idea, and was carried out by A.A.Serkov *et al.*using a filtered white light laser with picosecond pulses. [141] The ultrashort pulses also limit the timescale of the interaction and therefore heat flow into the substrate.

It was hypothesised that the roughness of the patterned silver films when using the Yb:YAG laser was due to the wings of the Gaussian irradiance profile causing delamination rather than ablation. Consequently, it would be interesting to explore the use of optical systems that transform the irradiance profile into a flat, top-hat, distribution. A diffractive optic has been purchased for use with the Yb:YAG laser and will be trialled.

References

[1] R. Das and K. Ghaffarzadeh, “Transparent Conductive Films (TCF) 2017-2027: Forecasts, Markets, Technologies”, Tech. Rep., 2017.

[2] C. Brabec, V. Dyakonov, and U. Scherf, Eds., *Organic Photovoltaics: Materials, Device Physics, and Manufacturing Technologies*. Wiley VCH, 2008, pp. 426–427.

[3] C Markert, D Hecht, and R Frahm, “Structural and electrical properties of thin d.c. magnetron-sputtered gold films deposited on float glass”, *Surface and Interface Analysis*, vol. 38, no. 4, pp. 715–718, 2006, file:///C:/Users/Olivier/Documents/Work/Papers/DINAMIC 0651.pdf. DOI: `10.1002/sia.2258`.

[4] M. Avrekh, B. M. Thibadeau, O. R. Monteiro, and I. G. Brown, “Transparent, conducting, metallic thin films”, *Review of Scientific Instruments*, vol. 70, no. 11, pp. 4328–4330, 1999. DOI: `10.1063/1.1150075`.

[5] J. Yun, “Ultrathin Metal films for Transparent Electrodes of Flexible Optoelectronic Devices”, *Advanced Functional Materials*, vol. 27, no. 18, 2017. DOI: `10.1002/adfm.201606641`.

[6] J. E. Medvedeva, “Combining Optical Transparency with Electrical Conductivity: Challenges and Prospects”, in *Transparent Electronics: From Synthesis to Applications*, 2010, pp. 1–29. DOI: `10.1002/9780470710609.ch1`.

[7] E. Nam, Y.-H. Kang, D.-J. Son, D. Jung, S.-J. Hong, and Y. S. Kim, “Electrical and surface properties of indium tin oxide (ITO) films by pulsed DC magnetron sputtering for organic light emitting diode as anode material”, *Surf. Coat. Technol.*, vol. 205, S129–S132, 2010, http://linkinghub.elsevier.com/retrieve/pii/S0257897210005013. DOI: `10.1016/j.surfcoat.2010.06.060`.

[8] H. Morikawa and M. Fujita, “Crystallization and decrease in resistivity on heat treatment of amorphous indium tin oxide thin films prepared by d.c. magnetron sputtering”, *Thin Solid Films*, vol. 339, no. 1–2, pp. 309–313, 1999, http://www.sciencedirect.com/science/article/pii/S0040609098011560. DOI: `http://dx.doi.org/10.1016/S0040-6090(98)01156-0`.

[9] A. Suzuki, T. Matsushita, T. Aoki, A. Mori, and M. Okuda, “Highly conducting transparent indium tin oxide films prepared by pulsed laser deposition”, *Thin Solid Films*, vol. 411, no. 1, pp. 23–27, 2002. DOI: `10.1016/S0040-6090(02)00167-0`.

[10] S. Ishibashi, Y. Higuchi, Y. Ota, and K. Nakamura, “Low resistivity indium–tin oxide transparent conductive films. II. Effect of sputtering voltage on electrical property of films”, *Journal of Vacuum Science & Technology A: Vacuum, Surfaces, and Films*, vol. 8, no. 3, pp. 1403–1406,

1990, http://avs.scitation.org/doi/10.1116/1.576890. DOI: `10.1116/1.576890`.

[11] M. Baum, J. Strauß, F. Grüßel, I. Alexeev, and M. Schmidt, "Generation of phase-only holograms by laser ablation of nanoparticulate ITO layers", *Journal of Optics (United Kingdom)*, vol. 16, no. 12, 2014. DOI: `10.1088/2040-8978/16/12/125706`.

[12] Q. Wang, I. Masao, M. Tan, P. Dai, Y. Wu, S. Lu, and H. Yang, "High quality non-rectifying contact of ITO with both Ni and n-type GaAs", *Journal of Semiconductors*, vol. 36, no. 5, pp. 1–5, 2015. DOI: `10.1088/1674-4926/36/5/053003`.

[13] G. Phipps, C. Mikolajczak, and T. Guckes, "Indium and Gallium: long-term supply", *Renewable Energy Focus*, vol. 9, no. 4, 2008. DOI: `10.1016/S1471-0846(08)70140-9`.

[14] O. Tuna, Y. Selamet, G. Aygun, and L. Ozyuzer, "High quality ITO thin films grown by dc and RF sputtering without oxygen", *Journal of Physics D: Applied Physics*, vol. 43, no. 5, 2010. DOI: `10.1088/0022-3727/43/5/055402`.

[15] B. G. Lewis and D. C. Paine, "Applications and processing of transparent conducting oxides", *MRS Bulletin*, vol. 25, no. 8, pp. 22–27, 2000. DOI: `10.1557/mrs2000.147`.

[16] M. J. Van Bommel, T. N. M. Bernards, and W. Talen, "Wet-Chemical Processing of Tin-Doped Indium Oxide Layers", in *Better Ceramics through Chemistry VI*, vol. 346, 1994, pp. 469–474.

[17] M. S. Tsai, C. L. Wang, and M. H. Hon, "The preparation of ITO films via a chemical solution deposition process", *Surface and Coatings Technology*, vol. 172, no. 1, pp. 95–101, 2003. DOI: `10.1016/S0257-8972(03)00314-1`.

[18] S. J. Hong and J. I. Han, "Indium tin oxide (ITO) thin film fabricated by indium-tin-organic sol including ITO nanoparticle", *Current Applied Physics*, vol. 6, no. SUPPL. 1, pp. 206–210, 2006. DOI: `10.1016/j.cap.2006.01.041`.

[19] C. Goebbert, H. Bisht, N. Al-Dahoudi, R. Nonninger, M. A. Aegerter, and H. Schmidt, "Wet chemical deposition of crystalline, redispersable ATO and ITO nanoparticles", *Journal of Sol-Gel Science and Technology*, vol. 19, no. 1-3, pp. 201–204, 2000. DOI: `10.1023/A:1008728103512`.

[20] L. I. Jing and Z. Xiao-dong, "Investigation of annealing effect on the electrical and optical properties of ITO film prepared by sol-gel process", *Applied Mechanics and Materials*, vol. 85, pp. 431–435, 2011. DOI: `10.4028/www.scientific.net/AMM.84-85.431`.

[21] T. M. Hammad, "Effect of annealing on electrical, structural, and optical properties of sol-gel ITO thin films", *Physica Status Solidi (a)*, vol. 206, no. 9, pp. 2128–2132, 2009, http://doi.wiley.com/10.1002/pssa.200881781. DOI: `10.1002/pssa.200881781`.

[22] M. S. Hwang, B. Y. Jeong, J. Moon, S. K. Chun, and J. Kim, "Inkjet-printing of indium tin oxide (ITO) films for transparent conducting electrodes", *Materials Science and Engineering B: Solid-State*

Materials for Advanced Technology, vol. 176, no. 14, pp. 1128–1131, 2011, http://dx.doi.org/10.1016/j.mseb.2011.05.053. DOI: `10.1016/j.mseb.2011.05.053`.

[23] M. A. Aegerter and N. Al-Dahoudi, "Wet-chemical processing of transparent and antiglare conducting ITO coating on plastic substrates", *Journal of Sol-Gel Science and Technology*, vol. 27, no. 1, pp. 81–89, 2003. DOI: `10.1023/A:1022636112130`.

[24] N. Al-Dahoudi and M. A. Aegerter, "Wet coating deposition of ITO coatings on plastic substrates", *Journal of Sol-Gel Science and Technology*, vol. 26, no. 1-3, pp. 693–697, 2003. DOI: `10.1023/A:1020777500940`.

[25] N. Al-Dahoudi, "Wet chemical deposition of transparent conducting coatings made of redispersable crystalline ITO nanoparticles on glass and polymeric substrates", PhD thesis, Saarland University - Leibniz Institut für neue Materialien, 2003.

[26] A. Stadler, "Transparent Conducting Oxides—An Up-To-Date Overview", *Materials*, vol. 5, no. 4, pp. 661–683, 2012. DOI: `10.3390/ma5040661`.

[27] T. Minami, "Transparent conducting oxide semiconductors for transparent electrodes", *Semiconductor Science and Technology*, vol. 20, no. 4, 2005. DOI: `10.1088/0268-1242/20/4/004`. arXiv: `arXiv:0804.0063`.

[28] M. Yan, M. Lane, C. R. Kannewurf, and R. P. H. Chang, "Highly conductive epitaxial Cdo thin films prepared by pulsed laser

deposition", *Applied Physics Letters*, vol. 78, no. 16, pp. 2342–2344, 2001. DOI: `10.1063/1.1365410`.

[29] Y. Zhu, R. J. Mendelsberg, J. Zhu, J. Han, and A. Anders, "Transparent and conductive indium doped cadmium oxide thin films prepared by pulsed filtered cathodic arc deposition", *Applied Surface Science*, vol. 265, pp. 738–744, 2013, http://dx.doi.org/10.1016/j.apsusc.2012.11.096. DOI: `10.1016/j.apsusc.2012.11.096`.

[30] H. Search, C. Journals, A. Contact, M. Iopscience, and I. P. Address, "Transparent conducting CdO films formed", vol. 750, pp. 750–752, 1993. DOI: `10.1088/0268-1242/8/5/024`.

[31] T. J. Coutts, X. Wu, W. P. Mulligan, and J. M. Webb, "High-performance, transparent conducting oxides based on cadmium stannate", *Journal of Electronic Materials*, vol. 25, no. 6, pp. 935–943, 1996. DOI: `10.1007/BF02666727`.

[32] A. Wang, J. R. Babcock, N. L. Edleman, A. W. Metz, M. A. Lane, R. Asahi, V. P. Dravid, C. R. Kannewurf, A. J. Freeman, and T. J. Marks, "Indium-cadmium-oxide films having exceptional electrical conductivity and optical transparency: Clues for optimizing transparent conductors", *Proceedings of the National Academy of Sciences*, vol. 98, no. 13, pp. 7113–7116, 2001, http://www.pnas.org/cgi/doi/10.1073/pnas.121188298. DOI: `10.1073/pnas.121188298`.

[33] World Health Organization, "Exposure to cadmium: a major public health concern", *Preventing Disease Through Healthy Environments*, pp. 3–6, 2010, http://www.who.int/ipcs/features/cadmium.pdf.

[34] A. Chen, K. N. Dietrich, X. Huo, and S. M. Ho, "Developmental neurotoxicants in e-waste: An emerging health concern", *Environmental Health Perspectives*, vol. 119, no. 4, pp. 431–438, 2011. DOI: `10.1289/ehp.1002452`.

[35] E. Shanthi, V. Dutta, A. Banerjee, and K. L. Chopra, "Electrical and optical properties of undoped and antimony-doped tin oxide films", *Journal of Applied Physics*, vol. 51, no. 12, pp. 6243–6251, 1980. DOI: `10.1063/1.327610`.

[36] T Kololuoma and J. T. Rantala, "Effect of Argon Plasma Treatment on Conductivity of Sol-Gel Fabricated Sb-Doped SnO2 Thin Films", *Electronics Letters*, vol. 36, no. 2, pp. 172–173, 2000. DOI: `10.1049/el:20000174`.

[37] E. Elangovan and K. Ramamurthi, "A study on low cost-high conducting fluorine and antimony-doped tin oxide thin films", *Applied Surface Science*, vol. 249, no. 1-4, pp. 183–196, 2005. DOI: `10.1016/j.apsusc.2004.11.074`.

[38] S. M. Ali, S. T. Hussain, S. A. Bakar, J. Muhammad, and N. ur Rehman, "Effect of doping on the Structural and Optical Properties of SnO2 Thin Films fabricated by Aerosol Assisted Chemical Vapor Deposition", *Journal of Physics: Conference Series*, vol. 439, p. 012 013,

2013, http://stacks.iop.org/1742-6596/439/i=1/a=012013?key=crossref.a754d755764c410556ac-294027b8448d. DOI: `10.1088/1742-6596/439/1/012013`.

[39] T. Minami, H. Sato, H. Nanto, and S. Takata, "Highty Conductive and Transparent Silicon Doped Zinc Oxide Thin Films Prepared by RF Magnetron Sputtering", *Japanese Journal of Applied Physics*, vol. 25, no. Part 2, No. 9, pp. L776–L779, 1986, http://stacks.iop.org/1347-4065/25/i=9A/a=L776. DOI: `10.1143/JJAP.25.L776`.

[40] T. Minami, H. Sato, T. Sonoda, H. Nanto, and S. Takata, "Influence of substrate and target temperatures on properties of transparent and conductive doped ZnO thin films prepared by r.f. magnetron sputtering", *Thin Solid Films*, vol. 171, no. 2, pp. 307–311, 1989. DOI: `10.1016/0040-6090(89)90637-8`.

[41] K Ellmer, "Resistivity of polycrystalline zinc oxide films: current status and physical limit", *Journal of Physics D: Applied Physics*, vol. 34, no. 21, pp. 3097–3108, 2001. DOI: `10.1088/0022-3727/34/21/301`.

[42] L. Gomez De Arco, Y. Zhang, C. W. Schlenker, K. Ryu, M. E. Thompson, and C. Zhou, "Continuous, highly flexible, and transparent graphene films by chemical vapor deposition for organic photovoltaics", *ACS Nano*, vol. 4, no. 5, pp. 2865–2873, 2010. DOI: `10.1021/nn901587x`.

[43] P. K. Nayak, “Pulsed-grown graphene for flexible transparent conductors”, *Nanoscale Advances*, vol. 1, no. 3, pp. 1215–1223, 2019. DOI: `10.1039/c8na00181b`.

[44] I. Khrapach, F. Withers, T. H. Bointon, D. K. Polyushkin, W. L. Barnes, S. Russo, and M. F. Craciun, “Novel highly conductive and transparent graphene-based conductors”, *Advanced Materials*, vol. 24, no. 21, pp. 2844–2849, 2012. DOI: `10.1002/adma.201200489`. arXiv: `1206.0001`.

[45] C. J. Lee, H. K. Lin, C. H. Li, L. X. Chen, C. C. Lee, C. W. Wu, and J. C. Huang, “A study on electric properties for pulse laser annealing of ITO film after wet etching”, *Thin Solid Films*, vol. 522, pp. 330–335, 2012. DOI: `10.1016/j.tsf.2012.09.010`.

[46] L. Schade, S. Franzka, S. Hardt, H. Wiggers, and N. Hartmann, “Sintering of thin titanium dioxide nanoparticle films via photothermal processing with ultraviolet continuous-wave lasers”, *Applied Surface Science*, vol. 278, pp. 336–340, 2013, http://dx.doi.org/10.1016/j.apsusc.2012.11.077. DOI: `10.1016/j.apsusc.2012.11.077`.

[47] W. T. Hsiao, S. F. Tseng, K. C. Huang, and D. Chiang, “Electrode patterning and annealing processes of aluminum-doped zinc oxide thin films using a UV laser system”, *Optics and Lasers in Engineering*, vol. 51, no. 1, pp. 15–22, 2013, http://dx.doi.org/10.1016/j.optlaseng.2012.08.003. DOI: `10.1016/j.optlaseng.2012.08.003`.

[48] C. K. Rhodes, C. A. Brau, H. Egger, A. Gallagher, P. W. Hoff, K. Hohla, D. L. Huestis, M. Krauss, G. Marowsky, M. V. McCusker, F. H. Mies, H. Pummer, and F. K. Tittel, *Excimer Lasers*. 1984, p. 276.

[49] K. Shinoda, T. Nakajima, and T. Tsuchiya, "In situ monitoring of excimer laser annealing of tin-doped indium oxide films for the development of a low-temperature fabrication process", *Applied Surface Science*, vol. 292, pp. 1052–1058, 2014, http://linkinghub.elsevier.com/retrieve/pii/S0169433213023908. DOI: `10.1016/j.apsusc.2013.12.101`.

[50] W. M. Cranton, S. L. Wilson, R. Ranson, D. C. Koutsogeorgis, K. Chi, R. Hedgley, J. Scott, S. Lipiec, A. Spiller, and S. Speakman, "Excimer laser processing of inkjet-printed and sputter-deposited transparent conducting SnO2:Sb for flexible electronics", *Thin Solid Films*, vol. 515, pp. 8534–8538, 2007. DOI: `10.1016/j.tsf.2007.03.118`.

[51] W. Chung, M. O. Thompson, P. Wickboldt, D. Toet, and P. G. Carey, "Room temperature indium tin oxide by XeCl excimer laser annealing for flexible display", *Thin Solid Films*, vol. 460, no. 1-2, pp. 291–294, 2004. DOI: `10.1016/j.tsf.2004.01.050`.

[52] S. O. El Hamali, W. M. Cranton, N. Kalfagiannis, X. Hou, R. Ranson, and D. C. Koutsogeorgis, "Enhanced electrical and optical properties of room temperature deposited Aluminium doped Zinc Oxide (AZO) thin films by excimer laser annealing", *Optics and Lasers in Engineering*, vol. 80, pp. 45–51, 2016,

http://dx.doi.org/10.1016/j.optlaseng.2015.12.010. DOI: `10.1016/j.optlaseng.2015.12.010`.

[53] M. Y. Zhang and G. J. Cheng, “Highly conductive and transparent alumina-doped ZnO films processed by direct pulsed laser recrystallization at room temperature”, *Applied Physics Letters*, vol. 99, no. 5, pp. 2009–2012, 2011. DOI: `10.1063/1.3622645`.

[54] N. Asakuma, T. Fukui, and M. Toki, “Low-Temperature Synthesis of ITO Thin Films Using an Ultraviolet Laser for Conductive Coating on Organic Polymer Substrates”, pp. 91–95, 2003.

[55] R. Delmdahl and R. Pätzel, “Excimer laser technology trends”, *Journal of Physics D: Applied Physics*, vol. 47, no. 3, 2014. DOI: `10.1088/0022-3727/47/3/034004`.

[56] M. von Allmen and A. Blatter, *Laser-Beam Interactions with Materials*, 2nd Editio. Berlin: Springer-Verlag, 1998, vol. 2, http://link.springer.com/10.1007/978-3-642-57813-7. DOI: `10.1007/978-3-642-57813-7`.

[57] D. Bäuerle, *Laser Processing and Chemistry*, 2nd Editio. Berlin: Springer-Verlag, 2000, http://link.springer.com/10.1007/978-3-642-17613-5. DOI: `10.1007/978-3-642-17613-5`. arXiv: `1011.1669`.

[58] R. Weber, T. Graf, P. Berger, V. Onuseit, M. Wiedenmann, C. Freitag, and A. Feuer, “Heat accumulation during pulsed laser materials processing”, *Optics Express*, vol. 22, no. 9, p. 11 312, 2014,

https://www.osapublishing.org/oe/abstract.cfm?uri=oe-22-9-11312. DOI: `10.1364/OE.22.011312`.

[59] R. Weber, T. Graf, C. Freitag, A. Feuer, T. Kononenko, and V. I. Konov, "Processing constraints resulting from heat accumulation during pulsed and repetitive laser materials processing", *Optics Express*, vol. 25, no. 4, p. 3966, 2017, https://www.osapublishing.org/abstract.cfm?URI=oe-25-4-3966. DOI: `10.1364/OE.25.003966`.

[60] P. Dyer, "Excimer laser polymer ablation: twenty years on", *Applied Physics A*, vol. 173, pp. 167–173, 2003, http://link.springer.com/article/10.1007/s00339-003-2137-1. DOI: `10.1007/s00339-003-2137-1`.

[61] W. T. Silfvast, *Laser Fundamentals*, 2nd Ed. Cambridge University Press, 2004, http://aapt.scitation.org/doi/10.1119/1.18690. DOI: `10.1119/1.18690`.

[62] M. Thirumoorthi and J. Thomas Joseph Prakash, "Structure, optical and electrical properties of indium tin oxide ultra thin films prepared by jet nebulizer spray pyrolysis technique", *Journal of Asian Ceramic Societies*, vol. 4, no. 1, pp. 124–132, 2016, http://dx.doi.org/10.1016/j.jascer.2016.01.001. DOI: `10.1016/j.jascer.2016.01.001`.

[63] V. Senthilkumar, P. Vickraman, M. Jayachandran, and C. Sanjeeviraja, "Structural and optical properties of indium tin oxide (ITO) thin films with different compositions prepared by electron beam evaporation",

Vacuum, vol. 84, no. 6, pp. 864–869, 2010, http://dx.doi.org/10.1016/j.vacuum.2009.11.017. DOI: `10.1016/j.vacuum.2009.11.017`.

[64] C. Goebbert, G. Gasparro, and T. Schuler, "Influence of the layer morphology on the electrical properties of sol gel transparent conducting oxide coatings", *Journal of Sol-Gel Science and Technology*, vol. 19, pp. 435–439, 2000, http://www.springerlink.com/index/R115P782100R84U3.pdf.

[65] F. H. Alsultany, N. M. Ahmed, M. Z. Matjafri, and F. H. Alsultany, "Effects of CW CO 2 Laser Annealing on Indium Tin Oxide Thin Films Characteristics", *Soft Nanoscience Letters*, vol. 4, no. 4, pp. 83–89, 2014, http://www.scirp.org/journal/snl%5Cnhttp://dx.doi.org/10.4236/snl.2014.44012%5Cnhttp://creativecommons.org/licenses/by/4.0/. DOI: `10.4236/snl.2014.44012`.

[66] T. Königer, T. Rechtenwald, I. Al-Naimi, T. Frick, M. Schmidt, and H. Münstedt, "CO2-laser treatment of indium tin oxide nanoparticle coatings on flexible polyethyleneterephthalate substrates", *Journal of Coatings Technology Research*, vol. 7, no. 2, pp. 261–269, 2010. DOI: `10.1007/s11998-009-9181-5`.

[67] X. Y. Tao, I. Fsaifes, V. Koncar, C. Dufour, C. Lepers, L. Hay, B. Capoen, and M. Bouazaoui, "CO2 laser-induced crystallization of sol-gel-derived indium tin oxide films", *Applied Physics A: Materials Science and Processing*, vol. 96, no. 3, pp. 741–749, 2009. DOI: `10.1007/s00339-009-5157-7`.

[68] D. Ganz, G. Gasparro, and M. a. Aegerter, "Laser Sintering of SnO2:Sb Sol-Gel Coatings", *Journal of Sol-Gel Science and Technology*, vol. 13, pp. 961–967, 1998.

[69] H. Salar Amoli and B. Fathi, "Effect of pulse Nd-YAG laser beam interaction on annealing of nanopowder ITO using spin-on-glass", *Journal of Sol-Gel Science and Technology*, vol. 59, no. 1, pp. 32–35, 2011. DOI: `10.1007/s10971-011-2457-0`.

[70] M. F. Chen, K. M. Lin, and Y. S. Ho, "Effects of laser-induced recovery process on conductive property of SnO2:F thin films", *Materials Science and Engineering B: Solid-State Materials for Advanced Technology*, vol. 176, no. 2, pp. 127–131, 2011, http://dx.doi.org/10.1016/j.mseb.2010.10.011. DOI: `10.1016/j.mseb.2010.10.011`.

[71] Q. Xu, R. Hong, H. Huang, Z. Zhang, M. Zhang, X. Chen, and Z. Wu, "Laser annealing effect on optical and electrical properties of Al doped ZnO films", *Optics & Laser Technology*, vol. 45, pp. 513–517, 2013, http://www.sciencedirect.com/science/article/pii/S0030399212002691. DOI: `10.1016/j.optlastec.2012.06.001`.

[72] I. Hamberg and C. G. Granqvist, "Transparent and infrared-reflecting indium-tin-oxide films: quantitative Modeling of the Optical Properties", *Applied Optics*, vol. 24, no. 12, pp. 1815–1819, 1985.

[73] H. Askari, H. Fallah, M. Askari, and M. C. Mohmmadieyh, "Electrical and optical properties of ITO thin films prepared by DC magnetron

sputtering for low-emitting coatings", pp. 1–8, 2014, http://arxiv.org/abs/1409.5293. arXiv: `1409.5293`.

[74] P. K. Biswas, A. De, N. C. Pramanik, P. K. Chakraborty, K. Ortner, V. Hock, and S. Korder, "Effects of tin on IR reflectivity, thermal emissivity, Hall mobility and plasma wavelength of sol-gel indium tin oxide films on glass", *Materials Letters*, vol. 57, no. 15, pp. 2326–2332, 2003. DOI: `10.1016/S0167-577X(02)01220-X`.

[75] A. Shimamoto, K. Yamashita, H. Inoue, S.-M. Yang, M. Iwata, and N. Ike, "A Nondestructive Evaluation Method: Measuring the Fixed Strength of Spot-Welded Joint Points by Surface Electrical Resistivity", *Journal of Pressure Vessel Technology*, vol. 135, no. 2, pp. 0 215 011–215 017, 2013, http://www.pubmedcentral.nih.gov/articlerender.fcgi?artid=3994754&tool=pmcentrez&rendertype=abstract. DOI: `10.1115/1.4007957`.

[76] F. Smits, "Measurement of Sheet Resistivities With the 4-Point Probe", *Bell System Technical Journal*, pp. 711–718, 1958.

[77] P. O.F.T.H. E. I-r e, "Measurements Transistors*", *procedding of the I.R.E*, vol. 29, pp. 1429–1434, 1952. DOI: `10.1109/JRPROC.1954.274680`.

[78] J. R. Ehrstein, C. M. Croarkin, and H. K. Liu, "NIST Special Publication 260-131", *National Institute of Standards and Technology*, 2006, http://scholar.google.com/scholar?hl=en&btnG=Search&q=intitle:NIST+Special+Publication+829#1.

[79] J.-h. Kang, Y.-c. Cheng, C.-s. Kim, and S.-h. Lee, "An international Comparison Measurement of Silicon Wafer Sheet Resistance using the

Four-point Probe Method", vol. 10, pp. 742–747, 2015.

[80] S. Thorsteinsson, F. Wang, D. H. Petersen, T. M. Hansen, D. Kjr, R. Lin, J. Y. Kim, P. F. Nielsen, and O. Hansen, "Accurate microfour-point probe sheet resistance measurements on small samples", *Review of Scientific Instruments*, vol. 80, no. 5, 2009. DOI: `10.1063/1.3125050`.

[81] W. Conshohocken, "Standard Test Method for Sheet Resistance Uniformity Evaluation by In-Line Four- Point Probe with the Dual-Configuration Procedure", *American Society for Testing and Materials*, pp. 1–12, 1997.

[82] *Thermo Scientific Evolution 201 and 220 UV-Visible Spectrophotometers PDF - Thermo Fisher Scientific Inc.* http://www.thermofishersci.in/lit/Thermo Scientific Evolution 201.pdf.

[83] *IFS 66v/S Vacuum FT-IR (Bruker Optics) | EVISA's Instruments Database*, http://www.speciation.net/Database/Instruments/Bruker-Optics/IFS-66vS-Vacuum-FTIR-;i650.

[84] "Standard test method for haze and luminous transmittance of transparent plastics", *ASTM International*, vol. 1, pp. 1–7, 2012. DOI: `10.1520/D1003-11.2`.

[85] *Jandel Engineering - Jandel Four Point Probes - Veeco*, http://www.jandel.co.uk/products/four-point-probes.html, 2018.

[86] *Resistivity and Hall Measurements - National Institute of Standards and Technology*,

https://www.nist.gov/pml/engineering-physics-division/popular-links/hall-effect/resistivity-and-hall-measurements.

[87] T. M. Amaral, *ISOTAN Calibration Sample - INM – Leibniz Institute for New Materials, Campus D2 2, 66123, Saarbrücken, Germany*, 2017.

[88] Z. I. C. Hen, Y. I. Z. Huo, W. T. U. Enbin, Z. L. I. Eqi, X. M. A. Uejin, Y. A. P. Ei, and G. A.N.G. W. Ang, "High mobility indium tin oxide thin film and its application at infrared wavelengths : model and experiment", vol. 26, no. 17, pp. 1273–1276, 2018. DOI: `10.1364/OE.26.022123`.

[89] S. Q. Hussain, W. K. Oh, S. Ahn, A. H. T. Le, S. Kim, Y. Lee, and J. Yi, "RF magnetron sputtered indium tin oxide films with high transmittance and work function for a-Si:H/c-Si heterojunction solar cells", *Vacuum*, vol. 101, pp. 18–21, 2014, http://dx.doi.org/10.1016/j.vacuum.2013.07.004. DOI: `10.1016/j.vacuum.2013.07.004`.

[90] *INM – Leibniz Institute for New Materials, Campus D2 2, 66123, Saarbrücken, Germany*.

[91] N. Al-Dahoudi and M. A. Aegerter, "Wet chemical deposition of multifunctional conducting coatings made with a nanocomposite suspension", *Surface Coatings Interational Part B*, vol. 88, pp. 257–261, 2005.

[92] N. Al-Dahoudi, H. Bisht, C. Göbbert, T. Krajewski, and M. A. Aegerter, "Transparent conducting, anti-static and anti-static-anti-glare coatings

on plastic substrates", *Thin Solid Films*, vol. 392, no. 2, pp. 299–304, 2001. DOI: `10.1016/S0040-6090(01)01047-1`.

[93] *BOROFLOAT® 33 - Borosilicate Glass - SCHOTT AG*, https://www.schott.com/borofloat/english/index.html.

[94] *Spectrosil® 2000 Datasheet PDF - Heraeus*, www.heraeus.com/media/media/hqs/doc_hqs/products_and_solutions_8/optics/Spectrosil_EN.pdf.

[95] M. A. Mohsin, T. Abdulrehman, and Y. Haik, "Reactive Extrusion of Polyethylene Terephthalate Waste and Investigation of Its Thermal and Mechanical Properties after Treatment", *International Journal of Chemical Engineering*, vol. 2017, pp. 15–18, 2017. DOI: `10.1155/2017/5361251`.

[96] *Tekra - Melinex® ST Heat Stabilized PET Films*, https://www.tekra.com/products/films/polyester-films/heat-stabilized-pet.

[97] C. M. Lopes and M. I. Felisberti, "Thermal conductivity of PET/(LDPE/AI) composites determined by MDSC", *Polymer Testing*, vol. 23, no. 6, pp. 637–643, 2004. DOI: `10.1016/j.polymertesting.2004.01.013`.

[98] V. Prajzler, P. Nekvindova´, P. Hypsˇ, O. Lyutakov, and V. Jerˇa´bek, "Flexible polymer planar optical waveguides", *Radioengineering*, vol. 23, no. 3, pp. 776–782, 2014.

[99] S. G. Prasad, A. De, and U. De, "Structural and Optical Investigations of Radiation Damage in Transparent PET Polymer Films", *International Journal of Spectroscopy*, vol. 2011, no. March, pp. 1–7, 2011. DOI: `10.1155/2011/810936`.

[100] *Microdrop Technologies GmbH - AD-P-8000 Ink-Jet Printer*, https://www.microdrop.de/positioning-system.html?file=files/downloads/Printing System Autodrop Professional 1017.pdf. (visited on 09/20/2006).

[101] R. D. Deegan, O. Bakajin, T. F. Dupont, G. Huber, S. R. Nagel, and T. A. Witten, "Capillary flow as the cause of ring stains from dried liquid drops", *Nature*, vol. 389, no. 6653, pp. 827–829, 1997. DOI: `10.1038/39827`.

[102] D. Soltman and V. Subramanian, "Inkjet-printed line morphologies and temperature control of the coffee ring effect", *Langmuir*, vol. 24, no. 5, pp. 2224–2231, 2008. DOI: `10.1021/la7026847`.

[103] J. Tauc, R. Grigorovici, and A. Vancu, "Optical Properties and Electronic Structure of Amorphous Germanium", in *Physica Status Solidi (B)*, http://dx.doi.org/10.1002/pssb.19660150224, vol. 15, 1966, pp. 627–637. DOI: `10.1002/pssb.19660150224`. arXiv: `pssb.19660150224 [10.1002]`.

[104] L. Gupta, A. Mansingh, and P. K. Srivastava, "Band gap narrowing and the band structure of tin-doped indium oxide films", *Thin Solid Films*, vol. 176, no. 1, pp. 33–44, 1989. DOI: `10.1016/0040-6090(89)90361-1`.

[105] H. Han, J. W. Mayer, and T. L. Alford, “Band gap shift in the indium-tin-oxide films on polyethylene napthalate after thermal annealing in air”, *Journal of Applied Physics*, vol. 100, no. 8, 2006. DOI: `10.1063/1.2357647`.

[106] J. Du, X.-l. Chen, C.-c. Liu, J. Ni, G.-f. Hou, Y. Zhao, and X.-d. Zhang, “Highly transparent and conductive indium tin oxide thin films for solar cells grown by reactive thermal evaporation at low temperature”, *APPLIED PHYSICS A-MATERIALS SCIENCE & PROCESSING*, vol. 117, no. 2, pp. 815–822, 2014. DOI: `10.1007/s00339-014-8436-x`.

[107] S. H. Brewer and S. Franzen, “Indium tin oxide plasma frequency dependence on sheet resistance and surface adlayers determined by reflectance FTIR spectroscopy”, *Journal of Physical Chemistry B*, vol. 106, no. 50, pp. 12 986–12 992, 2002. DOI: `10.1021/jp026600x`.

[108] H. Kim, C. M. Gilmore, A. Piqué, J. S. Horwitz, H. Mattoussi, H. Murata, Z. H. Kafafi, and D. B. Chrisey, “Electrical, optical, and structural properties of indium-tin-oxide thin films for organic light-emitting devices”, *Journal of Applied Physics*, vol. 86, no. 11, pp. 6451–6461, 1999. DOI: `10.1063/1.371708`.

[109] F Wooten, *Optical Properties of Solids*, 1st. London: Academic Press Inc., 1972, p. 272, https://www.elsevier.com/books/optical-properties-of-solids/wooten/978-0-12-763450-0.

[110] J. S. Kim, F. Cacialli, A. Cola, G. Gigli, and R. Cingolani, “Increase of charge carriers density and reduction of Hall mobilities in

oxygen-plasma treated indium-tin-oxide anodes", *Applied Physics Letters*, vol. 75, no. 1, pp. 19–21, 1999. DOI: `10.1063/1.124263`.

[111] I. Hamberg and C. G. Granqvist, "Evaporated Sn-doped In2O3films: Basic optical properties and applications to energy-efficient windows", *Journal of Applied Physics*, vol. 60, no. 11, 1986. DOI: `10.1063/1.337534`.

[112] P. Fuchs, A. Paracchino, H. Hagendorfer, L. Kranz, T. Geiger, Y. E. Romanyuk, A. N. Tiwari, and F. Nuësch, "Indium-Free PTB7/PC71BM Polymer Solar Cells with Solution-Processed Al:ZnO Electrodes on PET Substrates", *International Journal of Photoenergy*, vol. 2016, no. March, 2016. DOI: `10.1155/2016/2047591`.

[113] J. Puetz and M. A. Aegerter, "Direct gravure printing of indium tin oxide nanoparticle patterns on polymer foils", *Thin Solid Films*, vol. 516, no. 14, pp. 4495–4501, 2008. DOI: `10.1016/j.tsf.2007.05.086`.

[114] *E G & G Judson - FND100Q PDF Datasheet*, https://www.datasheets360.com/pdf/8760177735916111860. (visited on 08/29/2018).

[115] A. L. Marchant and H. V. Snelling, "Reciprocity in long pulse duration laser interactions with polymers", *Journal of Physics D: Applied Physics*, vol. 45, no. 21, p. 215 402, 2012, http://stacks.iop.org/0022-3727/45/i=21/a=215402?key=crossref.a8ced0a9646ea70b82a4553c4115bd72. DOI: `10.1088/0022-3727/45/21/215402`.

[116] I. Ursu, I. N. Mihailescu, I. Apostol, M. Dinescu, A. Hening, M. Stoica, A. M. Prokhorov, V. P. Ageev, V. I. Konov, and V. N. Tokarev, "On the

behaviour of aluminium under microsecond pulsed TEA CO2laser radiation in vacuum", *Journal of Physics D: Applied Physics*, vol. 17, no. 6, pp. 1315–1324, 1984. DOI: `10.1088/0022-3727/17/6/027`.

[117] L Sarger and J Oberlé, "How to measure the characteristics of laser pulses", in *Femtosecond Laser Pulses: Principles and Experiments*, C Rulliére, Ed., Second, Springer, New York, 2003, ch. 7.

[118] E. G. Arthurs, D. J. Bradley, and A. G. Roddie, "Frequency-Tunable Transform-Limited Picosecond Dye-Laser Pulses", *Applied Physics Letters*, vol. 19, no. 11, pp. 480–482, 2004. DOI: `10.1063/1.1653781`.

[119] J. Lee and B. Fulford, *Private Communication: Rofin-Sinar UK Ltd. September 2018*.

[120] T. Uehara, M. Nakagawa, and O. Sugihara, "Preparation of UV-cured organic–inorganic hybrid materials with low refractive index for multilayer film applications", *Optical Materials Express*, vol. 3, no. 9, p. 1351, 2013, https://www.osapublishing.org/ome/abstract.cfm?uri=ome-3-9-1351. DOI: `10.1364/OME.3.001351`.

[121] F. Pardal, V. Lapinte, J.-j. Robin, F. Pardal, V. Lapinte, J.-j. Robin, I. Charles, G. Montpellier, and U. M.R.C.-u.-e.-u. Equipe, "Kinetics of cotelomerization of 3- (trimethoxysilyl) propylmethacrylate and perfluorodecylacrylate Kinetics of cotelomerization of 3- (trimethoxysilyl) propyl methacrylate and perfluorodecylacrylate", 2009.

[122] *FLIR A35SC Thermal Camera Test Kit*, https://www.flir.co.uk/products/a35sc-test-kit/.

[123] *COMSOL Multiphysics® Modeling Software*, https://uk.comsol.com/comsol-multiphysics.

[124] A. Clarke, "Comparison of calculated and measured temperature fields in laser-heated thin film systems", PhD thesis, University of Hull, 2017.

[125] P. E. Dyer and J. Sidhu, "Excimer laser ablation and thermal coupling efficiency to polymer films", *Journal of Applied Physics*, vol. 57, no. 4, pp. 1420–1422, 1985. DOI: `10.1063/1.334503`.

[126] S. C. Dixon, D. O. Scanlon, C. J. Carmalt, and I. P. Parkin, "N-Type doped transparent conducting binary oxides: An overview", *Journal of Materials Chemistry C*, vol. 4, no. 29, pp. 6946–6961, 2016, http://dx.doi.org/10.1039/C6TC01881E. DOI: `10.1039/c6tc01881e`.

[127] T. M. Amaral and S. Heusing, *Private Communication - Institute for New Materials, Saarbrücken*, 2017.

[128] *3-(Trimethoxysilyl)propyl methacrylate 98% | Sigma-Aldrich*, https://www.sigmaaldrich.com/catalog/product/aldrich/440159 ?lang=en&region=GB. (visited on 09/20/2018).

[129] A. van der Vegt and L. Govaert, *Polymeren: van keten tot kunststof*. 2003, p. 279.

[130] L Plevert, S Mottet, M Bonnel, and N Duhamel, "Mimimal Glass Deformations with rapid thermal annealing control", *Journal of Applied*

Physics, vol. 34, no. 2A, p. 439, 1995.

[131] S. E. Rosenberg, P. Y. Wong, and I. N. Miaoulis, “Rapid Thermal Annealing of High-Melting-Point Films on Low-Melting-Point Substrates”, *Dept. of Mech. Eng*, vol. 9, no. 2, pp. 249–256, 1996.

[132] *Black body radiation and color temperature*, http://www.giangrandi.ch/optics/blackbody/blackbody.shtml. (visited on 10/01/2018).

[133] T. R. Shiu, C. P. Grigoropoulos, D. G. Cahill, and R. Greif, “Mechanism of bump formation on glass substrates during laser texturing”, *Journal of Applied Physics*, vol. 86, no. 3, pp. 1311–1316, 1999. DOI: `10.1063/1.370887`.

[134] J. E. Decker, W. Xiong, F. Yergeau, and S. L. Chin, “Spot-size measurement of an intense CO2 laser beam”, *Applied Optics*, vol. 31, no. 12, pp. 1912–1913, 1992.

[135] J. M. Liu, “Simple technique for measurements of pulsed Gaussian-beam spot sizes”, *Optics Letters*, vol. 7, no. 5, p. 196, 1982. DOI: `10.1364/ol.7.000196`.

[136] F. Yergeau, S. L. Chin, and P. Lavigne, “Multiple ionisation of rare-gas atoms by an intense CO2 laser (1014 W cm-2)”, *Journal of Physics B: Atomic and Molecular Physics*, vol. 20, no. 4, pp. 723–739, 1987. DOI: `10.1088/0022-3700/20/4/013`.

[137] *ImageJ - An open platform for scientific image analysis*, https://imagej.net/Welcome. (visited on 09/20/2007).

[138] A. Heppes, "Some Densest Two-Size Disc Packings in the Plane", in *Discrete and Computational Geometry*, vol. 30, 2003, pp. 241–262. DOI: `10.1007/s00454-003-0007-6`.

[139] H.-C. Chang and L.-C. Wang, "A Simple Proof of Thue's Theorem on Circle Packing", pp. 1–4, 2010, http://arxiv.org/abs/1009.4322. arXiv: `1009.4322`.

[140] T. M. Amaral and S. Heusing, *H2020 - INFINITY Project Deliverable Report*, https://infinity-h2020.eu/, 2018.

[141] A. A. Serkov, H. V. Snelling, S. Heusing, and T. M. Amaral, "Laser sintering of gravure printed indium tin oxide films on polyethylene terephthalate for flexible electronics", *Scientific Reports*, vol. 9, no. 1, pp. 1–8, 2019. DOI: `10.1038/s41598-018-38043-y`.